



Doctoral School "Vito Volterra"

PhD Thesis in Earth Sciences

“Structural, tectonic and geodynamic significance of Middle Triassic igneous activity in the Dolomites, NE Italy”

Hassan Sayed Hassan Abbas

Supervisors

Prof. Eugenio Carminati

Prof. Michele Lustrino

Doctoral Program Coordinator

Prof. Silvio Mollo

ACKNOWLEDGEMENTS

First, I would like to express my deep sense of gratitude to my supervisors, Prof. Eugenio Carmainti and Prof. Michele Lustrino for their support, fruitful discussions, guidance, encouragement, efforts and patience during this project.

I would like to show my gratitude to Prof. Piero Gianolla, Prof. Massimo Mattei, Prof. Francesca Cifelli, Dr. Samuele Agostini, Dr. Maria Michail, and Dr. Marcello Caggiati for their efforts and contribution in this work.

Erasmus Mundus European Commission is gratefully acknowledged for providing financial support my PhD program project in the framework of EU METALIC II project (Erasmus Mundus Action 2). Also, financial support from PRIN2015-Project 2015EC9PJ5_001 and Progetti di Ateneo Sapienza 2017 (Prof. Eugenio Carminati) is acknowledged.

I would like to thank Prof. Giovanni B. Andreozzi (Ph.D. coordinator), for his support and guidance.

Thanks also to Marcello Serracino (CNR-IGAG, Rome) for his assistance during the electron microprobe analyses. Great thanks also to Domenico Mannelta (Mimmo) for his help during the thin section production, to Paolo Di Giuseppe for his assistance during the isotope analyses and to Prof. Massimo Coltorti for his invaluable help in the field.

The Trento province is thanked for providing permissions for sampling in the Dolomites, that are an UNESCO protected site.

Finally, I would like to express my deepest thanks to my family especially to my wife (Hanna Mohamoud), my son (Zeyad) and my daughter (Salma) for love, patient and support.

Table of Contents	Page n.
Abstract	iii
CHAPTER ONE- INTRODUCTION	
	1
CHAPTER TWO- GEOLOGICAL SETTING	
	10
2.1. Introduction	10
2.2. Permian and Middle Triassic stratigraphy of the Dolomites	14
2.3. Pre-Cenozoic magmatism in the Southern Alps and adjoining areas	22
2.3.1. Permian magmatism	22
2.3.2. Triassic magmatism	22
2.4. Tectonic evolution of the Southern Alps	25
2.4.1. Pre-Alpine evolution of the Southern Alps	25
2.4.2. Alpine Orogeny in the Southern Alps	26
2.5. Tectonic evolution of the Dolomites	27
2.5.1. Middle Triassic Tectonics in the Dolomites	30
2.3. The Predazzo intrusive complex	32
2.4. The Monzoni intrusive complex	33
CHAPTER THREE- SAMPLING AND METHODS	
	35
3.1. Sampling strategy	35
3.2. Methods	37
3.2.1. Petrographic descriptions	37
3.2.2. Whole-rock major and trace element analyses	37
3.2.3. Mineral chemistry analyses	37
3.2.4. Isotope analyses	38
3.2.5. Microstructural analysis	40
3.2.6. Magnetic mineralogy	41
3.2.7. Anisotropy of low-field magnetic susceptibility (LF-AMS)	44
3.2.8. Anisotropy of high-field magnetic susceptibility (HF-AMS)	45
CHAPTER FOUR- PETROLOGICAL AND GEOCHEMICAL STUDIES	
	46
4.1. Petrographic description	46
4.1.1. Dolomites massive volcanic rocks	48
4.1.2. Dolomites pyroclastic rocks	50
4.1.3. Vicentinian Alps rocks	51
4.1.4. Predazzo plutonic rocks	51
4.1.5. Monzoni plutonic rocks	53
4.2. Mineral chemistry	56
4.3. Whole-rock chemistry	60
4.4. Sr-Nd-Pb isotopic ratios	80

CHAPTER FIVE- STRUCTURAL AND AMS STUDIES	85
5.1. Microstructural and petrographic description	85
5.1.1. Predazzo pluton	90
5.1.2. Monzoni pluton	99
5.2. Magnetic susceptibility	104
5.3. Magnetic Properties	104
5.4. AMS Shape Parameters (T)	111
5.5. Degree of anisotropy (Pj)	111
5.6. AMS foliation and lineation	117
5.7. HF-AMS fabric	125
CHAPTER SIX- DISCUSSION	127
6.1. Petrological analysis	127
6.1.1. Inter- and intra-district geochemical variations.	127
6.1.2. Constraints on the mantle source(s)	134
6.1.3. Geodynamic and tectonic setting. Geochemistry vs. geology	141
6.2. Structural analysis	144
6.2.1. The origin of magnetic fabric in the Predazzo and Monzoni rocks	144
6.2.2. Emplacement modes of the Dolomites igneous bodies	146
6.2.2.1. Emplacement mode of the Predazzo pluton	146
6.2.2.2. Emplacement mode of the Monzoni pluton	150
CHAPTER SEVEN- CONCLUSIONS	154
APPENDIX	159
Appendix 1	159
Appendix 2	168
Appendix 3	176
Appendix 4	189
Appendix 5	192
REFERENCES	197

ABSTRACT

At the Middle-Late Triassic boundary (~244-235 Ma) a diffuse igneous activity developed in Southern Alps, a wide area where the recently agglutinated Pangea super-continent had begun to disrupt. Sparse remnants of these products now crop out in the Brescian pre-Alps, the Vicentinian Alps (Recoaro-Schio-Posina), Non Valley, Dolomites and Tarvisian Alps. The igneous activity is concentrated mainly in the Dolomites mostly as lava flow and pyroclastic successions, with rare intrusive bodies cropping out at Predazzo, Monzoni, and Cima Pape.

The Triassic igneous rocks show a wide compositional spectrum with compositions ranging from metaluminous (basalt/gabbros) to peraluminous (rhyolites/leucogranites) and including also cumulitic lithologies (cumulitic gabbros and clinopyroxenites).

The study of Triassic magmatism in the Southern Alps is the special interest due to contrasting models proposed to define the geodynamic and tectonic setting.

The petrographic, mineral chemistry and geochemical investigations have been performed for Triassic igneous rocks from different localities in the Dolomites and Vicentinian Alps to understand the origin of this magmatism and the main magmatic processes that controlled the evolution of these rocks.

We investigated the magnetic and magmatic fabric of Predazzo and Monzoni plutons by means of anisotropy of magnetic susceptibility (AMS) and microstructural data coupled with a field geological study. The AMS technique aimed at revealing the internal fabric of Predazzo and Monzoni plutons and

defines the magnetic foliation and magnetic lineation (magmatic flow). Also, this technique is used to study magma migration and emplacement in the upper crust and define the model of emplacement of igneous bodies. Furthermore, the AMS method is aimed to constraining and define the relationship between magma emplacement and Middle Triassic tectonics.

Finally, the integration between structural and petrological analyses allowed to constrain the geodynamic and tectonic setting of Middle Triassic magmatism in the Dolomites and Southern Alps.

The major findings and contribution of this study are the following: 1) The Triassic magmatism in the Southern Alps has mainly shoshonitic affinity followed by high-K calcalkaline. 2) The studied rocks show a sharp correlation (SiO_2 , $\text{Na}_2\text{O}+\text{K}_2\text{O}$) and negative correlation (TiO_2 , $\text{Fe}_2\text{O}_{3\text{tot}}$, MnO , MgO , CaO , $\text{CaO}/\text{Al}_2\text{O}_3$) with differentiation index (D.I.). 3) The Dolomites lavas exhibit enrichment of large ion lithophile elements (LILE) relative to high field strength elements (HFSE) and shows high Ba/Nb (32.8-93.9), low Ce/Pb (1.8-10.4) and low U/Nb (0.11-0.33) coupled with low HFSE (e.g., Nb = 6-12 ppm) with low Nb/Nb* $[(\text{Nb}/0.46)/((\text{O}980/0.023)*(\text{U}980/0.017))^{0.5}]$ ratio (0.1-0.35), resembling the typical characteristics of magmas generated by subduction-modified mantle sources. 4) The fractional crystallization of Mg-bearing phases such as olivine and clinopyroxene with only a minor role of plagioclase controlled Dolomites volcanic rocks evolution. 5) The $^{87}\text{Sr}/^{86}\text{Sr}$ for the Dolomites volcanic rocks ranges from 0.70432 to 0.70577 and do not show any correlation with D.I., with SiO_2 or MgO which indicates that the mantle sources, only little modified, if any, by interaction with the local crust. 6) The $^{143}\text{Nd}/^{144}\text{Nd}_{(i)}$ ranges

from 0.51227 to 0.51237, with $\epsilon\text{Nd}_{(i)}$ values slightly lower to slightly higher than $\text{ChUR}_{(230 \text{ Ma})}$ (from -1.4 to +0.5). The Pb isotopic compositions are homogeneous, with $^{206}\text{Pb}/^{204}\text{Pb}$ clustered around 18.26 and 18.41, $^{207}\text{Pb}/^{204}\text{Pb}$ from 15.62 to 15.67 and $^{208}\text{Pb}/^{204}\text{Pb}$ from 38.36 to 38.89. 7) The isotopic variation of the Southern Alps Triassic rocks is related to mantle source heterogeneities rather than interaction with upper crustal lithologies. 8) The mildly to strongly evolved rocks are genetically linked with the least differentiated terms by closed system fractional crystallization of gabbroic to monzonitic assemblages. 9) According to results of ABS5 software modelings of the less evolved basaltic sample, the origin of these rocks is a peridotitic mantle wedge source at typical subduction settings. 10) Finally, the mantle sources of Triassic igneous rocks reflect previous subduction metasomatism (likely developed during Hercynian times) when continental rifting caused raising of the geotherms and passive upwelling of asthenospheric mantle. 11) The study is a new evidence of the validity of the AMS method for unraveling the mode of emplacement of igneous bodies. 12) AMS, microstructural and petrographic data from the Predazzo body are consistent with a multistage ring-dyke emplacement mode. 13) The Predazzo sheets were emplaced via either upward magma flow or along-strike lateral magma transport. 14) The ENE-WSW elongated shape of the Monzoni body was controlled by the occurrence of strike-slip faults associated with Ladinian-tectonics. 15) The feeder zones are located at the NE and SW part of the Predazzo intrusion and at the NE edge of the Monzoni intrusion. 16) The low degree of anisotropy (P_j) values indicate the existence of low strain during the emplacement of Predazzo and Monzoni. 17) The Predazzo and Monzoni plutons emplacement followed the main Triassic tectonic phase (post-tectonic). 18)

Ladinian strike-slip tectonics providing a preferential pathway for post-tectonic magma.

**CHAPTER ONE
INTRODUCTION**

During Middle-Late Triassic, igneous activity took place in the Alpine chain as well as in the Po Plain, Adriatic Sea, Dinarides and the Hellenides. The igneous activity in the Southern Alps is recorded in the Dolomites, Non-valley area, Tarvisian Alps, Vicentinian Alps, and Brescian Alps.

The Middle Triassic igneous activity in the Dolomites (Eastern Southern Alps, Italy) is well known from nearly two centuries (e.g., von Richthofen, 1860; Hansel, 1878). The Dolomites represent a worldwide reference area for the relationships between magmatism, sedimentation and tectonics (e.g., Ogilvie-Gordon, 1902, 1903; Hörnes, 1912; Penck, 1911; Vardabasso, 1929, 1930; Leonardi, 1967; Castellarin et al., 1982, 1982b; Visonà, 1997).

In the Dolomites area, Middle Triassic igneous rocks are mostly pyroclastic, but abundant submarine and subaerial lava and dyke swarms also occur, with magma chambers eroded to shallow-depth intrusive body levels, cropping out only at Predazzo, Monzoni and Cima Pape. Several contrasting geodynamic/tectonic models were proposed to explain the Triassic igneous activity in the Southern Alps::

- 1) An aborted continental rifting, based on the association of extensional structures and volcanism (Bechstädt et al., 1977).
- 2) Northward subduction and delamination of lower continental crust in the upper mantle, based on the calcalkaline and shoshonitic magmatic association

and on local compressional structures of Middle Triassic age (Castellarin et al., 1980, 1988; Casetta et al., 2017).

3) Sinistral strike-slip tectonics associated with local compressional and extensional structures (“rhomb-horsts” and “pull-apart basins”) generating magma extrusion and subsidence as result of the collapse of magma chamber roofs (Blendinger, 1985; Doglioni, 1987, 1988).

4) Marginal back-arc basin associated with the post-Variscan evolution of the Alpine sector (Marinelli et al. 1980; Viel, 1982).

5) Partial melting of a mantle source modified during the preceding Variscan orogeny and contaminated by the incorporation of large portions of crustal material (Crisci et al., 1984; Sloman, 1989; Bonadiman et al., 1994).

6) Intra-Pangea dextral megashear system with lithosphere-scale extension enabling hybridization between mantle melts and lower crust lithologies (Brandner and Keim, 2011).

7) Rifting related with the opening of the Neotethys (Beltran-Trivinõ et al., 2016).

8) Active upwelling of hot asthenospheric mantle due to the insulating thermal effect of the huge Pangea landmass (Stahle et al., 2001),

9) Subduction of a small Permian back-arc oceanic domain (Garzanti 1985; Zanetti et al. 2013).

10) Active arc/back-arc development following the NNW-directed subduction of the Paleotethys oceanic lithosphere beneath the south-eastern European paleo-margin – assuming the Brescian sector of the Southern Alps as the western continental lateral termination of the Meliata oceanic back-arc basin (Cassinis et al., 2008).

11) The existence of Palaeozoic rifted continental basin or a narrow oceanic basin between the South Alpine and Austroalpine continental blocks, closed by a subduction dipping beneath South Alpine (Bianchini et al., 2018).

The major goal of this thesis is to constrain the tectonic and geodynamic setting in which Triassic magmatism occurred.

Magmas generated in active subduction settings usually show peculiar volcanological, petrographic, mineral chemical, geochemical and isotopic characteristics, commonly very different from those emplaced in mid-plate settings and along passive plate margins (e.g., Lustrino et al., 2011; Turner and Langmuir, 2015; Di Giuseppe et al., 2017; Kimura, 2017; Schmidt and Jagoutz, 2017; Zheng and Zhao, 2017). The identification of a given tectonic setting on the basis of geochemical data and petrological arguments is a common but dangerous approach. For example, the typical compositions found along active plate margins, falling in the calcalkaline, high-K calcalkaline and potassic-ultrapotassic clans are also recorded in mid-plate settings and in extensional areas post-dating subduction processes (Davidson, 1996; Turner et al., 1996; Liegeois et al., 1998; Fan et al., 2003; Moghazi, 2003; Lan et al., 2012; Lustrino et al., 2016).

If geological and geophysical data (e.g., earthquake distribution, focal mechanisms, mantle tomography and so on) can help unravelling the geodynamic setting of active to recent magmatism, similar straight considerations are hard to obtain for the geological past. Thus, when dealing with ancient remnants of igneous activities, Earth scientists are forced to work mostly with geochemical data, using petrographic evidence and inferring petrological reasoning, helped by geological and structural constraints. This

could drive to non-unique definitions of the geodynamic processes responsible for magmatism in the past.

A case study is represented by the Middle-Late Triassic igneous activity recorded in the Southern Alps (Italy) during continental rifting stages (e.g., Doglioni, 1992; Bertotti et al. 1993; Gianolla et al., 2010; Abbas et al., 2018). Indeed, at odd with geological evidence, Ladinian magmatic rocks in Southern Alps are characterized by calcalkaline to shoshonitic affinities, rendering their origin still a matter of discussion in a global geodynamic framework. Furthermore, the Predazzo, Monzoni and Cima Pape Middle Triassic intrusive bodies in the Dolomites crop out close to the Middle Triassic strike-slip faults (e.g., Stava line), suggesting a potential role for strike-slip tectonics in the emplacement of these plutons. The generation, ascent and emplacement of magma through the crust and its relation to strike-slip faulting is still a matter of debate (Castro 1987; Tikoff and Teyssier 1992; Paterson and Fowler 1993; Roman-Berdiel et al. 1997; Rosenberg 2004). The emplacement of intrusive bodies can be considered either as controlled by regional tectonics (syntectonic) if the magmatic fabric is consistent with the regional strain field, or caused by the internal dynamics of the magma chamber if the magmatic fabric patterns are independent from the regional tectonic structures (Hutton, 1988; Paterson et al., 1998; Rosenberg, 2004).

In the past years, several structural studies on intrusive bodies have been carried out using the anisotropy of magnetic susceptibility (AMS) technique (e.g., Van der Voo and Klootwijk 1972; Bouchez et al. 1990; Raposo and Gastal 2009, Cifelli et al., 2012). The magnetic fabric in a pluton is affected by several factors, such as the flow of the magma, the changes in its effective viscosity and the finite

deformation it undergoes before complete crystallization. Assuming a direct relationship between mineral and magnetic fabrics (e.g., Graham 1954), the analysis of the AMS in igneous bodies can be used to define the relationship between magma emplacement and tectonics. This is particularly crucial for rocks that often appear isotropic and where magmatic foliation and lineation are difficult to observe and measure at the outcrop scale, such as granites (e.g., Knight and Walker, 1988, Tarling and Hrouda 1993).

In this work we provide a petrographic, mineral chemical, whole-rock chemical and Sr-Nd-Pb isotope data from Ladinian lava flows, dykes and plutonic rocks from the Dolomites and Vicentinian Alps (Recoaro area), with the aim of characterizing them from a petrological point of view to better constrain the geodynamic framework in which they were emplaced. A general review of the entire Triassic igneous activity of the Southalpine area is also provided, presenting a comprehensive dataset containing more than 1066 whole-rock data. Moreover, we investigate the space and time relationship between the Ladinian Predazzo and Monzoni plutons and Middle Triassic strike-slip faulting in the Dolomites using AMS techniques, coupled with petrographic and field studies. In addition to this regional significance, our work can contribute to the understanding of magma migration and emplacement in the upper crust. A few exposed subvolcanic and caldera-related plutons have been reported worldwide and magma-plumbing systems of active volcanic areas cannot be directly studied. Therefore, developing and testing models for the emplacement mechanisms of the ancient exposed sheet intrusions can contribute to the assessment of volcanic hazard and risk in active volcanic areas (Sparks, 2003; Tibaldi and Pasquarè, 2008; Cashman and Sparks, 2013).

Structural studies with field work and petrological studies were conducted to constrain the tectonic and geodynamic setting in which Triassic magmatism occurred.

The following methods were used in this study:

- Petrographic description of microscopic thin sections (performed in the Department of Earth Science, Sapienza University).
- Whole-rock major and trace element analyses of selected samples (performed in Actlabs Laboratories, Canada).
- Electron microprobe analyses with Cameca SX50 microprobe (performed in the CNR-IGAG Laboratories, Sapienza University).
- Sr-Nd-Pb isotopic study on selected samples (performed in the CNR-IGG Laboratories, Pisa).
- Microstructure analysis for the microscopic thin sections.
- Anisotropy of low-field magnetic susceptibility (LF-AMS) technique has been performed on samples from the Predazzo and Monzoni plutons. AMS has been measured in the paleomagnetic laboratory at Roma Tre University in cooperation with Prof. Massimo Mattei and Prof. Francesca Cifelli.
- Anisotropy of high-field magnetic susceptibility (HF-AMS) technique was performed on samples from the Predazzo and Monzoni pluton (analyses were done in the paleomagnetic laboratory, ETH Zürich, in collaboration with Prof. Dr. Ann Marie Hirt).
- Magnetic mineralogy analyses were carried out in order to constrain the AMS carriers in the sampled sites. Analyses were performed in the paleomagnetic laboratory of Roma Tre University and in INGV (Istituto Nazionale di Geofisica e Vulcanologia, Roma, in collaboration with Dr. Aldo Winkler).
- Fieldwork has been done in cooperation with the University of Ferrara.

The following specific research objectives were pursued:

- Studying the petrographic features of the microscopic thin sections and define the mineralogical composition and textures of the rocks.
- Determining the minerals and groundmass chemistry for the studied rocks.
- Studying the petrological and geochemical characteristics of the middle Triassic rocks in the Dolomites and Vicentinian Alps (Recoaro-Schio-Posina).
- Identifying the igneous rock series.
- Understanding the relationships among the magmatic rocks from different sectors of the Dolomites and Vicentinian Alps (Recoaro-Schio-Posina).
- Identifying the role of the main petrogenetic processes such as fractional crystallization, and crustal contamination in the evolution of these rocks.
- Addressing the origin and the mantle source(s) of these rocks.
- Defining the space and time relationship between the Ladinian Predazzo and Monzoni plutons and Middle Triassic strike-slip faulting in the Dolomites.
- Defining the origin of the microstructural features in the microscopic thin sections.
- Determining the contribution of ferromagnetic and paramagnetic minerals to the magnetic anisotropy of the studied rocks.
- Defining the magma flow patterns in the two Dolomites plutons (Predazzo and Monzoni).
- Testing models for the emplacement mechanisms for the two plutons and its relation to the Middle Triassic structures.

1.1 Organization of the thesis and presentation of data and results

A brief description of the contents of the following thesis chapters is here provided. Part of the data presented in this thesis have been published in the Journal of Structural Geology, whereas other data appear in a manuscript submitted to Gondwana Research.

Chapter 2- Geological setting

In this chapter, a summary of the evolution of the Southern Alps is provided, with special reference to the Triassic magmatism in the whole Southern Alps and in the Dolomites.

Chapter 3- Sampling and Methods

In this chapter, the sampling strategy, samples preparation and a description of the adopted (petrological and structural) methods are presented.

Chapter 4- Petrological and geochemical studies

In this chapter, the results obtained by petrological analyses from Ladinian lava flows, dykes and plutonic rocks from the Dolomites and Vicentinian Alps (petrographic, mineral chemical, whole-rock chemical and Sr-Nd-Pb isotope data) are shown and a review of the entire Middle Triassic igneous activity of the whole Southern Alps is presented.

Chapter 5- Structural and AMS studies

In this chapter, the results obtained by structural analyses for the Predazzo and Monzoni plutons (AMS, microstructural, petrographic analyses and field studies) are shown.

Chapter 6- Discussion

In this chapter, a discussion of the significance of petrological and structural results presented in the previous two chapters is provided, in order to constrain

the geodynamic and tectonic setting in which magmatic rocks were emplaced, determine the mantle source(s) and the main magmatic processes which produced these rocks. Moreover, the relationship between the Ladinian Predazzo and Monzoni plutons and Middle Triassic strike-slip faulting in the Dolomites is discussed. Also, models for the emplacement mechanisms for the two plutons are presented.

Chapter 7- Conclusions

Appendix

References



**CHAPTER TWO
GEOLOGICAL SETTING**

2.1. Introduction

The Southern Alps (Fig. 2.1) are located south of the Neogene Periadriatic Line, an S-shaped NE-SW-trending dextral mylonitic shear zone separating Europe-verging thrusts from Adria-verging thrusts in the Alpine Chain (Handy et al., 2010). The Southern Alps are considered in literature as the retro-wedge of the double-verging Alpine Chain, developed during the Cretaceous-Paleogene subduction of an eastern branch of the Alpine Tethys, a belt that widened after the Eocene Europe-Adria collision (Handy et al., 2010; Carminati et al., 2012; Carminati and Doglioni, 2012).

The Southern Alps consist of a well-preserved Mesozoic passive continental margin (e.g., Bertotti et al., 1993) inverted during the Alpine Orogenesis (Doglioni, 1987; Handy et al., 2010). The Dolomites (Fig. 2.1, 2.2) consist of a large-scale Neogene pop-up structure bounded by two main tectonic lineaments belonging to the Periadriatic Line: the dextrally transpressive Pusteria Line to the north, and the SSE-verging thrust of the Valsugana Line to the south. The Recoaro area lies in a more external wedge of the Southern Alps (Fig. 2.1), separated from the Veneto magmatic province to the south by the Cima Marana thrust, and affected to the east by the post-Miocene Schio-Vicenza and Val d'Astico sinistral strike-slip fault system (Castellarin et al., 2006, Fondriest et al., 2012).

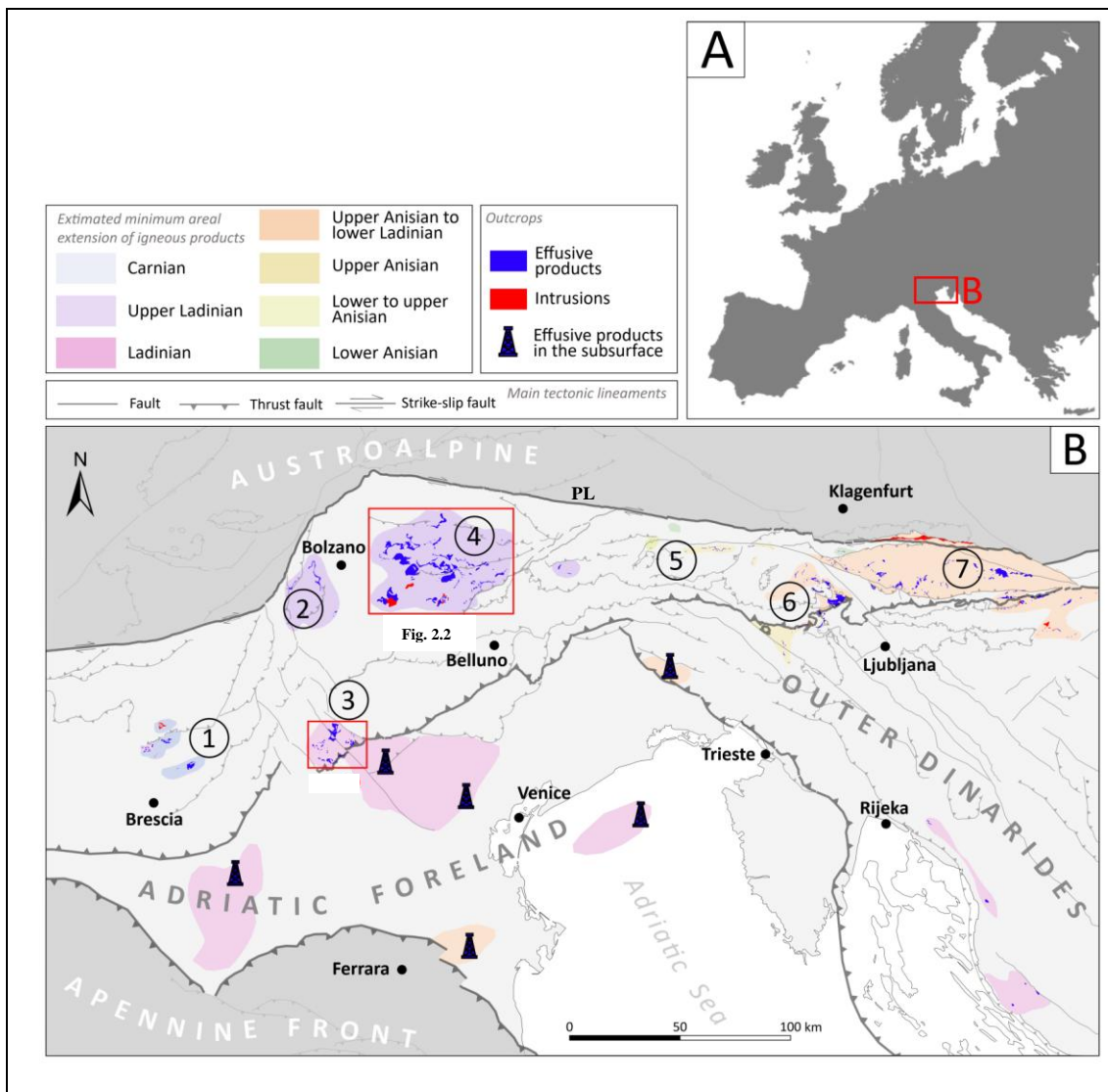
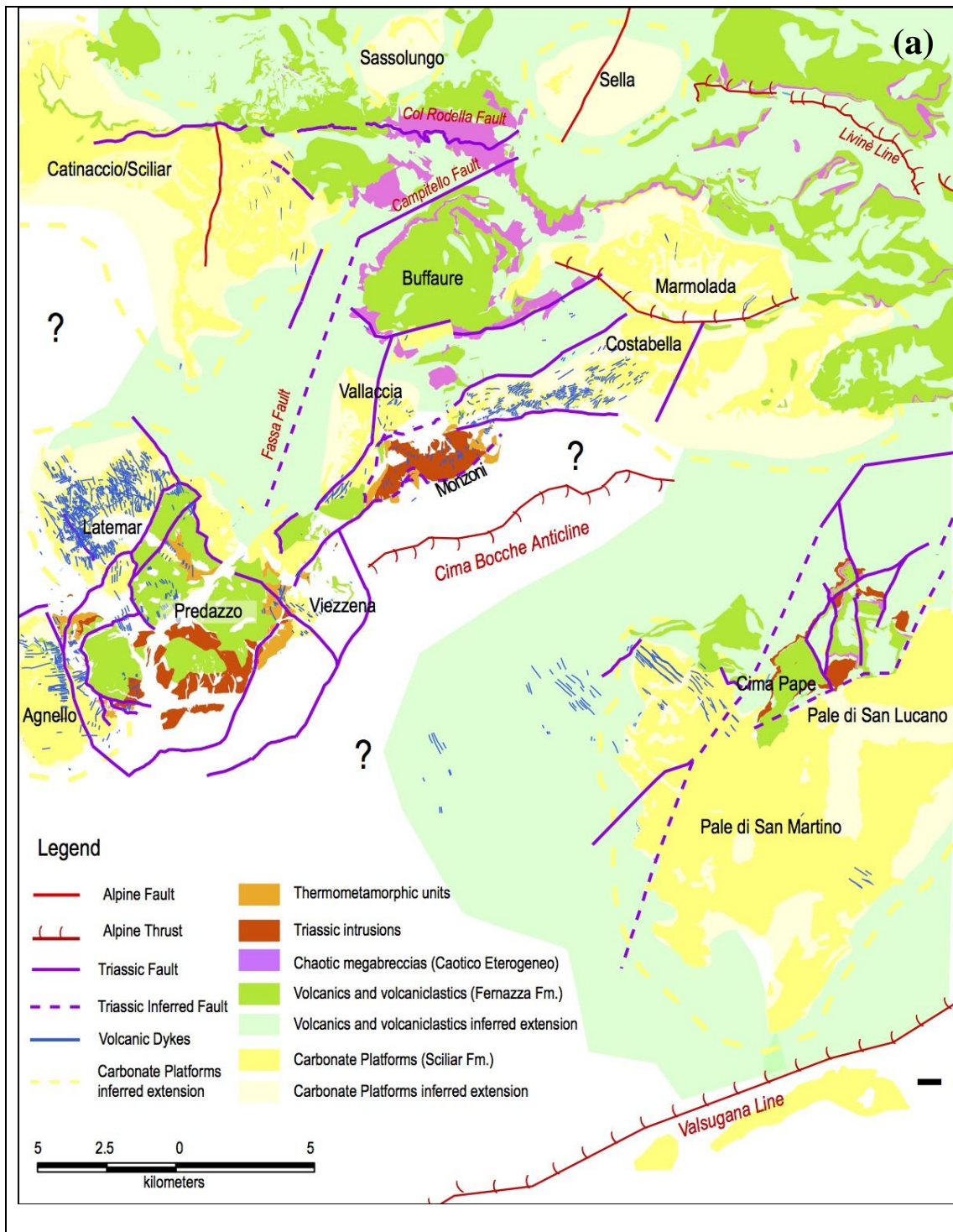
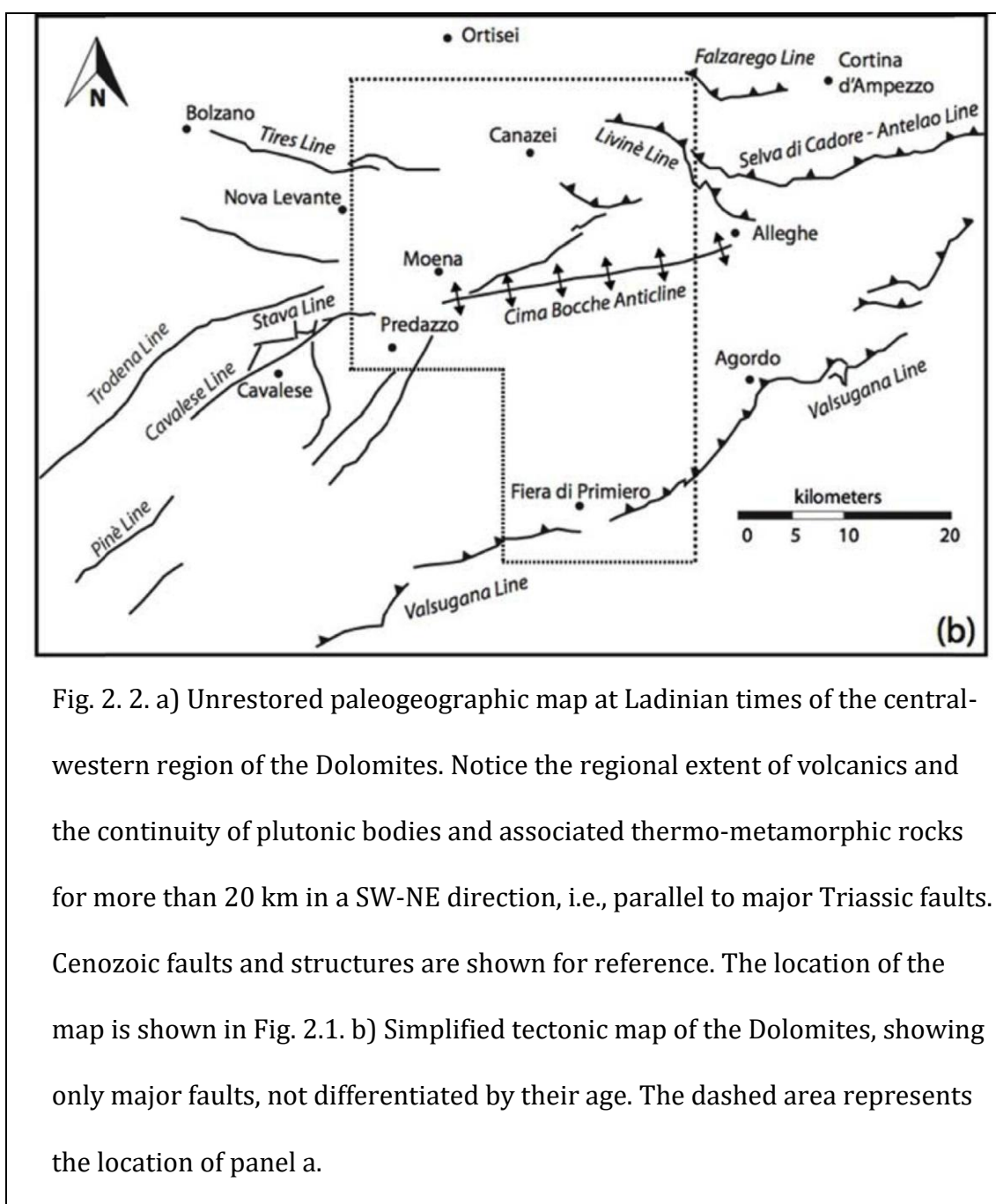


Fig. 2.1. Geographic (A) and geological (B) setting of the investigated area, with the distribution of volcanic products and possible extension of relative magmatic areas. Numbers in the circles indicate different regions of the Southern Alps: 1) Brescian Alps; 2) Non Valley and Western Adige Valley; 3) Vicentinian Alps; 4) Dolomites and Western Carnia; 5) Eastern Carnia and Western Julian Alps; 6) Eastern Julian Alps and Slovenian (Tolmin) Basin; 7) Southern Karawanken and Kamnik-Savinja Alps. PL: Periadriatic Line.





2.2. Permian and Middle Triassic stratigraphy of the Dolomites

During Carboniferous time, the agglutination of Gondwana and Laurussia led to the formation of the largest continental plate ever recorded, the Pangea. The collision of the two major continents resulted in a widespread complex suture zone known as Appalachian-Variscan Belt (e.g., Bell and Newman, 2006; Franke et al., 2017). The subduction of the Rheic Ocean, once separating northern Gondwana from southern Laurussia, led to the development of abundant Carboniferous-Permian ($\sim 300 \pm 5$ Ma) calcalkaline to high-K calcalkaline magmatism in the suture zone (e.g., Wilson et al., 2004). As commonly observed in all the orogens, the suture zones eventually evolved, probably as consequence of gravitational instability of the over-thickened lithosphere, into complex continental rifting systems.

The collapse of the Variscan Belt (also known as Hercynian Belt in central Europe) was accompanied by large subsidence and Early Permian bimodal (basic and acid) igneous activity (e.g., Schaltegger and Brack, 2007; Marocchi et al., 2008; Brandner et al., 2016). The Dolomites sedimentary succession unconformably overlies these Permian volcanics or directly older basement rocks (Bosellini et al., 2003; Gianolla et al., 2010; Brandner and Keim, 2011). The sedimentary rocks start with the Late Permian Val Gardena fluvial sandstones (red beds), followed by the deposition of evaporites and carbonates (Bellerophon Formation), driven by ephemeral marine incursions in coastal sabkha to shallow shelf environments (Bosellini and Hardie, 1973; Massari and Neri, 1997; Kustatscher et al., 2017). Stable marine conditions occurred since the Early Triassic, when the shallow-water carbonate and siliciclastic deposits of the

Werfen Formation were widely deposited in the region, eventually followed by the tidal flat carbonates of the Lower Serla Dolomite (Fig. 2.3).

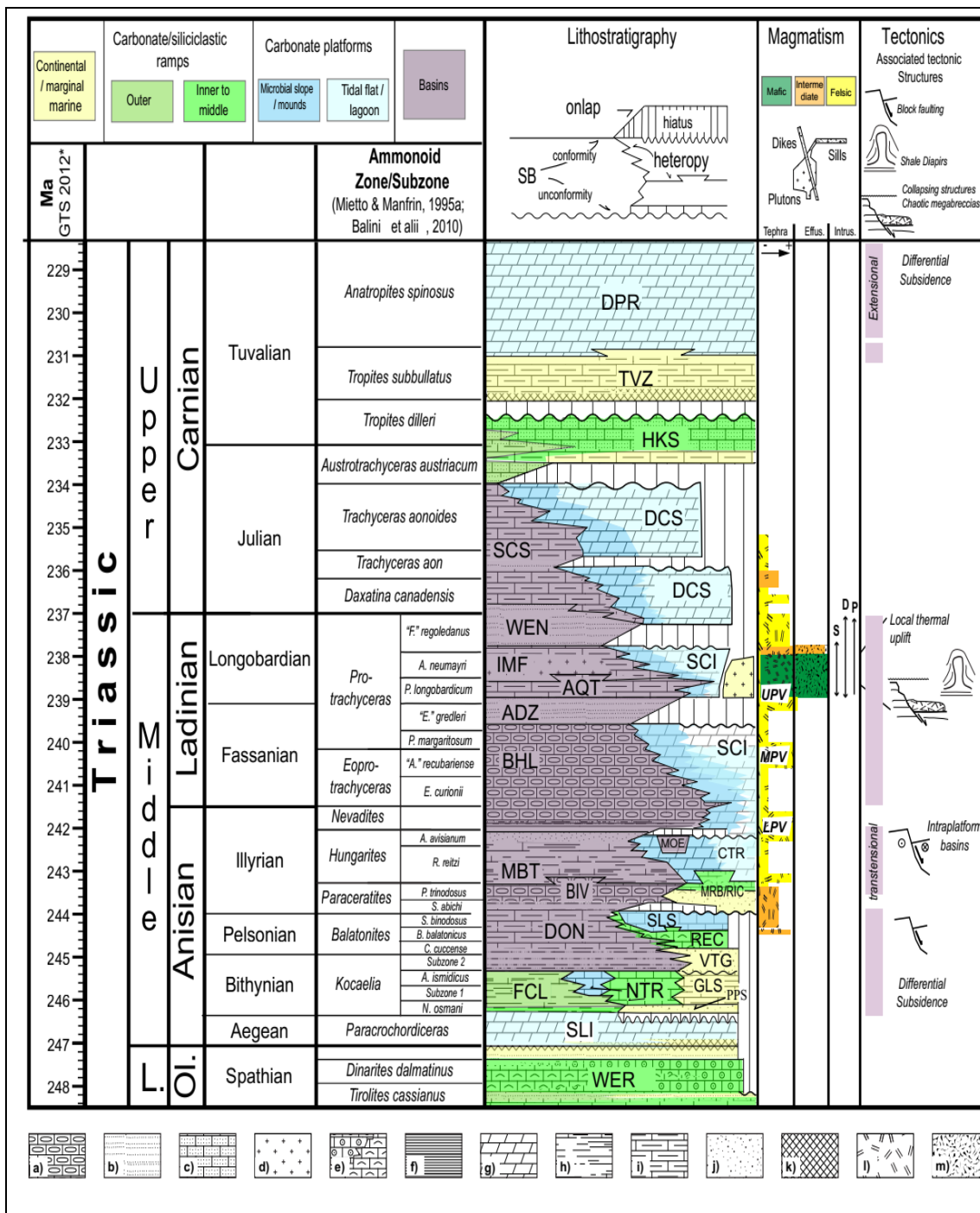
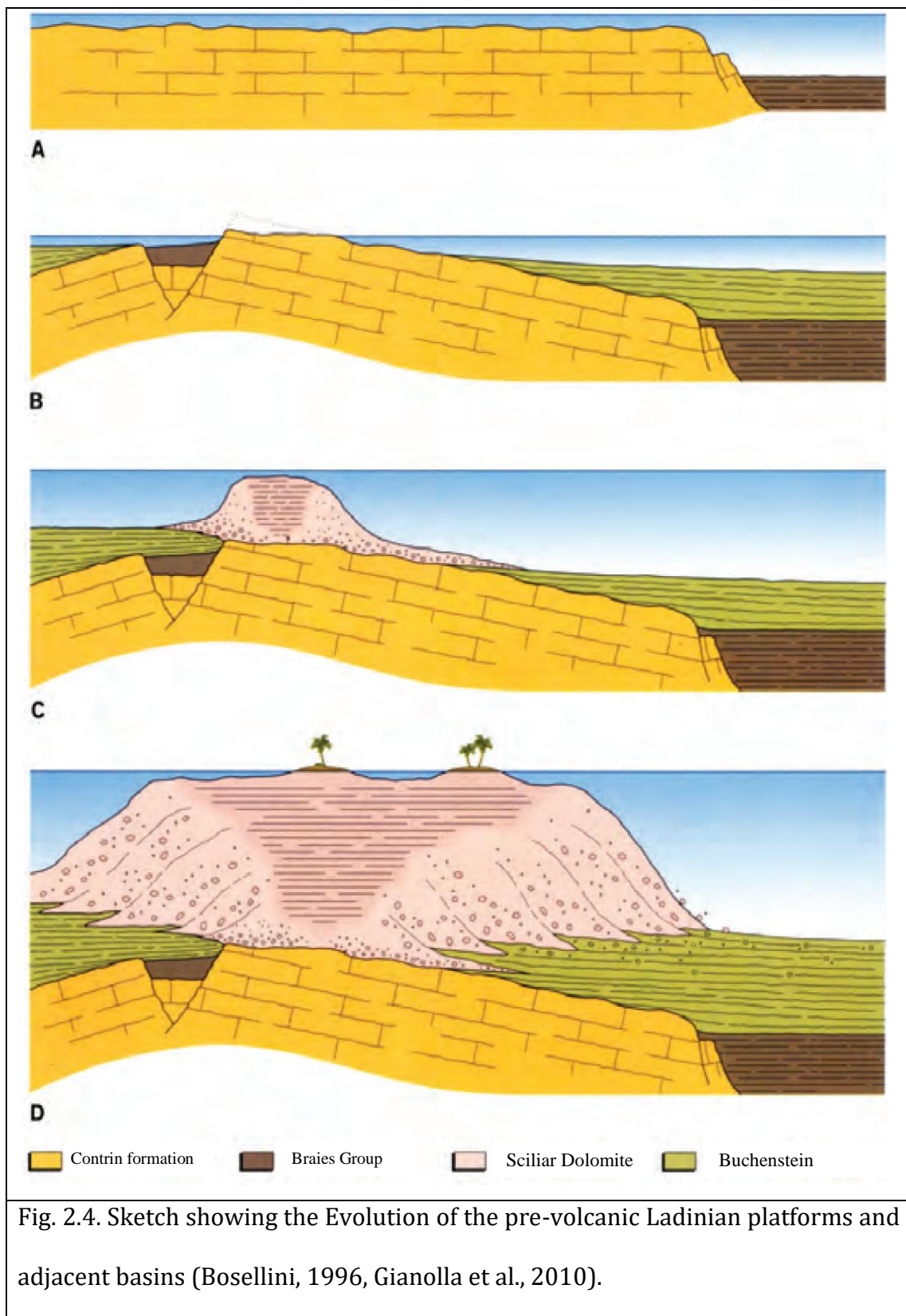


Fig. 2.3. Schematic bio-chrono-stratigraphic scheme of the Middle-Upper Triassic succession of the Dolomites with the most important magmatic pulse recorded as ash falls, tephtras or effusives. The position of the known possible

source volcanic areas from the Southern Alps is indicated. In the subsurface of Venetian Plain, a significant number of volcanic products (mainly effusive and intrusive) is known (e.g., Brusca et al., 1981). Igneous rock abbreviations: P: plutonic rocks; D: dyke; S: Sill. Lithostratigraphic abbreviations: WER: Werfen Formation; SLI: Lower Serla Dolomite; PPS: Piz da Peres Conglomerate; FCL: Collalto Formation; NTR: Monte Rite Formation; GLS: Gracilis Formation; VTG: Voltago Conglomerate; DON: Dont Formation; REC: Recoaro Limestone; SLS Upper Serla Dolomite/Formation; MRB/RIC: Richthofen Conglomerate and Morbiac dark Limestone; BIV: Bivera Formation; MBT: Ambata Formation; MNA: Moena Formation; CTR: Contrin Formation; BHL: Livinallongo Formation; SCI: Sciliar Formation; ADZ: Zoppè Sandstone; AQT: Aquatona Formation; IMF: Fernazza Volcanic Complex (Fernazza Formation); WEN: Wengen Formation; SCS: San Cassiano Formation; DCS: Cassian Dolomite; HKS: Heiligkreuz Formation; TVZ: Travenanzes Formation; DPR: Dolomia Principale. Lithologies: a) cherty limestone; b) sandstone; c) sandy limestone; d) volcanics and volcanoclastics; e) oolitic-bioclastic limestone; f) black platy limestone or dolostone, black shale; g) dolostone; h) marlstone, claystone and shale; i) marly limestone; j) conglomerate; k) evaporates; l) tuffs, pyroclastics; m) lava, pillow-lava, pillow breccia. LPV, MPV, UPV= Lower - Middle - Upper Pietra Verde. Ages from GTS 2012 modified after Wotzlaw et al. (2018).

In the early Middle Triassic (Anisian), local uplift and strong subsidence modified the flat topography of the area (Brandner, 1984; Doglioni, 1984, 1987; Masetti and Trombetta, 1998). Since the early Anisian, three carbonate platform generations (Fig. 2.4; Monte Rite, Upper Serla and Contrin Formations) developed in subsiding areas (eastern Dolomites) facing relatively deep basins (Neri et al., 2007; Gianolla et al., in press), whereas the western Dolomites experienced significant uplift and subaerial erosion (Rossi, 1973; Bosellini et al., 2003; Stefani et al., 2010). The last stage of local Anisian tectonics followed by a strong regional subsidence disrupted and drowned the Contrin carbonate platform. Isolated carbonate pinnacles nucleated and survived to the late Anisian sea-level rise (Sciliar Formation), prograding during the Ladinian onto coeval deep water basins (Fig. 2.4; Buchenstein Formation; Maurer and Schlager, 2000; Preto et al., 2005; Stefani et al., 2010).



Starting from the early Ladinian, but with a climax in late Ladinian, widespread magmatism occurred in the Southern Alps, now preserved as lava flows, pyroclastic rocks, plutonic rocks and epiclastic successions. Such magmatism locally perturbed the growth of the carbonate platforms. Ladinian volcanic rocks (mainly consisting of pillow lavas, pillow breccias and hyaloclastites) accumulated in basinal depressions and overlapped the carbonate platform slopes (e.g., Sacerdoti and Sommariva, 1962; Neri et al., 2007), with magmatic dykes intruding carbonate platform deposits (Fig. 2.5; Bosellini et al., 1982; Preto et al., 2011). In the Dolomites area, close to the magmatic centres (e.g., Latemar and Marmolada areas), carbonate platforms were buried beneath the volcanic products, whereas in other areas (e.g., Sciliar massif) carbonate production continued even close to the major magmatic centres (De Zanche et al., 1993; Brandner and Keim, 2011). The volcanic sequence is composed of alkali olivine basalt to latite association (Castellarin et al., 1982b; Visonà, 1997) and huge volumes of tuffs and volcanoclastics (Fernazza Formation). The rare quartz syenitic and the much more common shoshonitic dyke swarms cut the sedimentary cover and intrude the magmatic edifices (Vardabasso, 1930; Castellarin et al., 1982b; Doglioni, 1983). Local intrusions (Predazzo, Monzoni and Cima Pape; Bonadiman et al., 1994; Casetta et al., 2018a, 2018b; Abbas et al., 2018) occurred in the eastern Dolomites and were possibly related to subaerial volcanoes (De Zanche et al., 1993). At the end of volcanic activity, as a result of the erosion of the volcanics, coarse clastic material (e.g., Marmolada Conglomerate) was deposited in submarine fans, proximal to the magmatic eruptive centres, whereas in distal areas only finer turbiditic sediments

accumulated (Wengen Formation; Gianolla and Neri, 2007). The Ladinian volcano-tectonic event was associated with slope failures and deposition of mega-breccias on the basin floor (Fig. 2.5; Caotico eterogeneo, Fernazza Formation; De Zanche et al., 1993; Neri et al., 2007; Brandner and Keim, 2011). Volcanic activity is also associated with the formation of evaporitic diapirs (sourced in the Upper Permian evaporitic Bellerophon Formation) that deform sedimentary covers in areas adjacent to volcanic centers. The syn-volcanic age of these structures is documented by the fact that they are often cut by the magmatic dykes (Castellarin et al., 1998b). As widely discussed in the following, roughly coeval magmatism is recorded also in the Tarvisian western Julian Alps (e.g., Gianolla et al., 1992), Vicentinian Alps (e.g., De Vecchi and Sedeà, 1983) and Brescian Alps (e.g., Armienti et al., 2003; Cassinis et al., 2008).

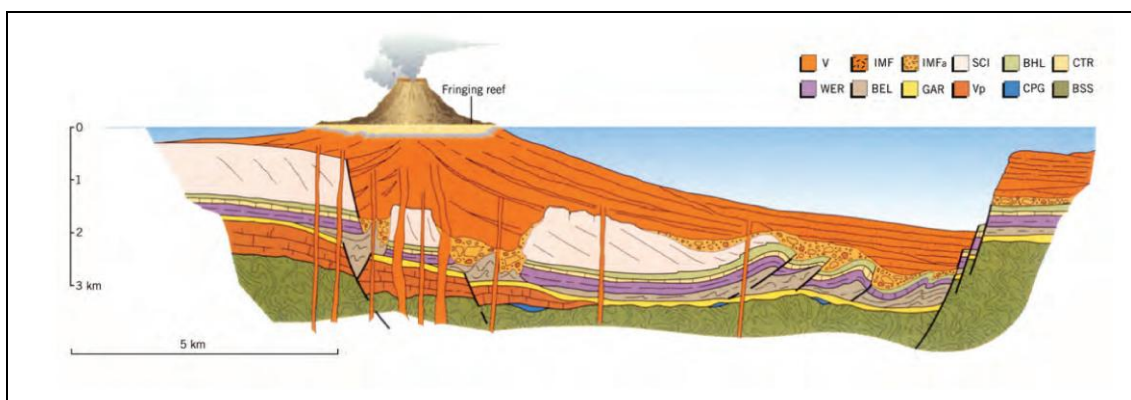
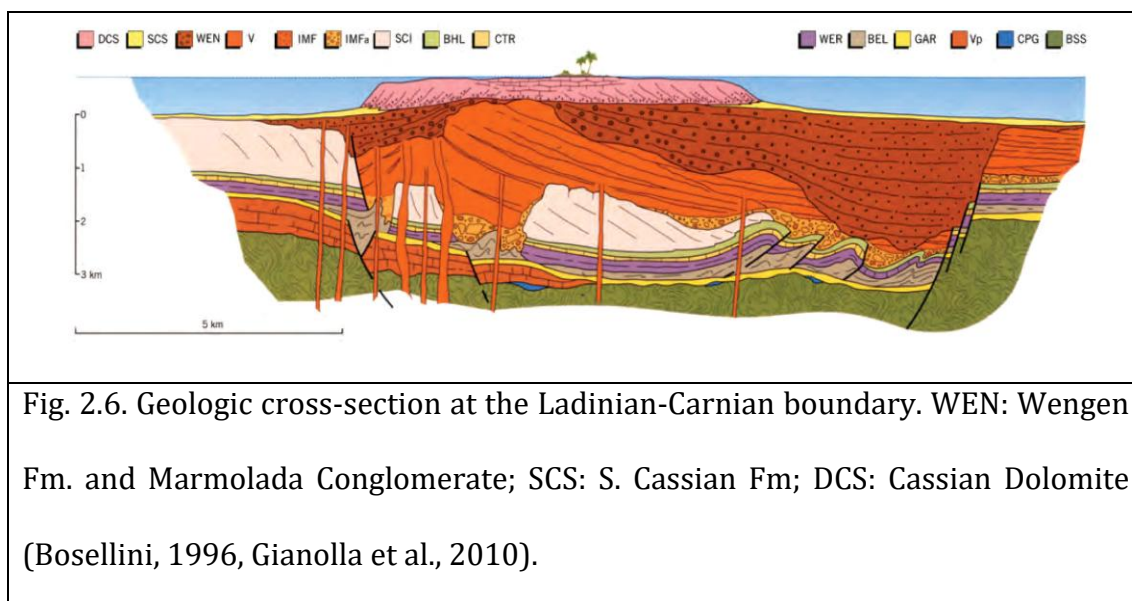


Fig. 2.5. Hypothetical geologic cross-section of the Western Dolomites during Upper Ladinian. BSS: metamorphic basement; CPG: Ponte Gardena Conglomerate; Vp: Bozen porphyries; GAR: Val Gardena Sandstone; BEL: Bellerophon Fm.; WER: Werfen Fm.; CTR: Contrin Fm.; BHL: Buchenstein Fm.; SCI: Sciliar Dolomite; IMFa: M. Fernazza Fm, chaotic megabreccias and polygenic breccias; IMF: M. Fernazza Fm, hyaloclastite; V: Volcanics in general (Bosellini, 1996, Gianolla et al., 2010).

At the end of the magmatic pulse, carbonate deposition re-established and several carbonate platforms (Cassian Dolomite) developed, and prograded onto coeval basinal deposits (Fig. 2.3, 2.6; San Cassiano Formation; Neri et al., 2007; Keim et al., 2001). The accommodation space in the western Dolomites inherited from the Pre-volcanic collapse, therefore, the platform extend laterally and prograding over the adjacent basins. Whereas, in the eastern Dolomites, the subsidence was still active and considerable. In the basinal areas, the high sedimentation rate, as a result of the enormous volcanoclastic input, produced a shallowing evolution of the basins (De Zanche et al., 1993, Bosellini et al., 2003, Stefani et al., 2010)..



2.3. Pre-Cenozoic magmatism in the Southern Alps and adjoining areas

2.3.1. Permian magmatism

In the central-eastern Southern Alps, the Permian medium to high-K calcalkaline magmatism consists of volcanic rock piles (Athesian volcanism) and plutons (Cima d'Asta, Bressanone, Ivigna, Monte Croce and Monte Sabion; e.g., Macera et al., 1994; Rottura et al., 1997, 1998; Marocchi et al., 2008; Bellieni et al., 2010). In the western and central Southern Alps, the Permian magmatism is represented by Ivrea Mafic Complex, the "Graniti dei Laghi" and the Lugano volcanics (e.g., Boriani et al., 1992; Pinarelli et al., 2002; Quick et al., 2009).

2.3.2. Triassic magmatism

Triassic magmatism occurred during the rifting processes and continental stretching related to the transcurrent movement between the European and African Plates (Abbate et al., 1986; Beccaluva et al., 2005). Triassic magmatic activity was located at the borders of the Adria plate (Fig. 2.7) and can be recognized in the following areas: Southern Alps, Sicily, Calabria, Sardinia, Tuscany and Liguria, Dinarides and Hellenides belts (Beccaluva et al., 2005).

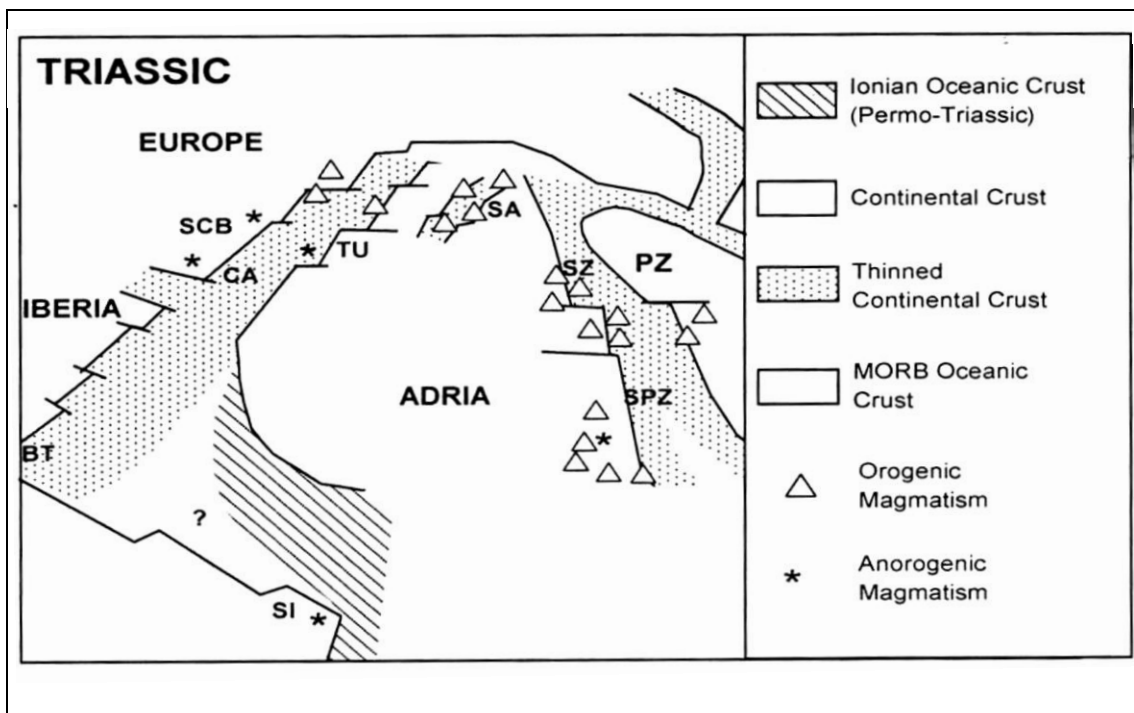


Fig. 2.7. Sketch showing the Triassic rift system in the Adria domain and showing the distribution of orogenic and anorogenic magmatic events. SI, Sicily; Ca, Calabria; SCB, Sardinia-Corsica block; TU, Tuscany; SA, Southern Alps; SZ, Serbian zone; SPZ, Sub-pelagonian zone; PZ, Pelagonian zone (Beccaluva et al., 2005).

The following discussion will be restricted to the Southern Alps, where the Middle Triassic magmatism is widely recorded (Fig. 2.1). Anisian acid volcanic rocks are restricted to small outcrops in eastern Carnia (Rio Turriea and Gartnerkofel; e.g., Obenholzner and Pfeiffer, 1991; Venturini, 2006) and in southern Karawanken (Loibl pass; Buser, 1980). Upper Anisian to lower Ladinian porphyrites are more common in the eastern Southern Alps, with an eastward volume increase from the western Julian Alps (Rio Freddo, Prisjonič; Gianolla, 1992; Celarc et al., 2013) to the southern Karawanken, Tolmin Basin and to the Kamnik-Savinja Alps (Western Slovenia; Buser, 1980, 1986; Pamič,

1984; Dozet and Buser, 2009). Acid pyroclastic successions are however frequent in the whole Southern Alps as “Pietra Verde” tuff layers or ash interbeds in basinal limestones of Buchenstein Fm. (Viel, 1979; Cros, 1980; Brack and Rieber, 1993; Maurer, 2003).

Upper Ladinian volcanic rocks are very common (both in basinal and shelf settings) in the western and central Dolomites (Figs. 2.1, 2.2; Pisa et al., 1980; Bosellini et al., 1982; Sloman, 1989), on the western side of the Adige Valley (Mendola massif and Non Valley; Avanzini et al., 2007; Rossi et al., 1980), and in the Vicentinian Alps (Recoaro-Schio-Posina; De_Vecchi et al., 1986). Small outcrops occur also in western Carnia (Forni di Sopra; Castellarin and Pisa, 1973) and in the Brescian Alps (Monte Guglielmo group; Cassinis et al., 2008). In addition, Middle Triassic (mainly Ladinian) magmatism has been recognised in boreholes drilled in the Po Plain and in the Adriatic Sea (Brusca et al., 1982; Castellarin et al., 1988).

The late Ladinian volcanic rocks could be age-constrained in the Dolomites by geochronological U-Pb-data: zircons from volcanic ash beds and accretionary lapilli interbedded in the underlying Buchenstein Fm., indicate an absolute age spanning from 242.8 ± 0.2 Ma to 238.0 ± 0.7 Ma (Seceda section, north-western Dolomites; Mundil et al., 1996; Brack et al., 2007; Wotzlav et al., 2017). Zircons from ash layers in the Frommer Mb. (Fernazza Fm.), lying at the top of volcanic rocks point to a 237.77 ± 0.05 Ma age (Alpe di Siusi; Mietto et al., 2012).

The intrusive rocks (Predazzo and Monzoni plutons) were dated by Rb/Sr and K/Ar methods at ~ 230 Ma (Borsi and Ferrara, 1967; Borsi et al., 1968). The Predazzo pluton was emplaced over a period of time 238-232 Ma ($^{40}\text{Ar}/^{39}\text{Ar}$;

Laurenzi et al., 1994; Laurenzi and Visonà 1996). The age of the Predazzo granite is 237.3 ± 1.0 Ma (mechanically abraded zircon dates; Brack et al., 1997; Brack et al., 2005).

Recently Bianchini et al (2018) reported data on basic dykes crosscutting the Valsugana crystalline basement (Trento province) with 260 to 227 Myr age (Rb-Sr and K-Ar methods), pointing to a transitional phase in between the Permian and Middle Triassic magmatic phase in Southern Alps.

Lower Carnian magmatism is recorded in the western Southern Alps (Brescian Alps), with both effusive and intrusive products (Cassinis et al., 2008). A possible occurrence of coeval volcanic edifices more to the south is suggested by the occurrence of very common Lower Carnian volcanoclastic sandstones (Val Sabbia Ss., Garzanti et al., 1985; Jadoul et al., 2004).

2.4. Tectonic evolution of the Southern Alps

2.4.1. Pre-Alpine evolution of the Southern Alps

The Variscan or Hercynian orogeny occurred as a result of at Late Paleozoic continental collision between Laurussia and Gondwana to form the supercontinent of Pangaea (Dal Piaz et al., 2003). The pre-Permian basement of the Southern Alps is affected by Variscan metamorphism. The metamorphism increases in grade from anchimetamorphism in the eastern, to greenschist-facies in the central to amphibolite facies in the western part (e.g., Serie dei Laghi) of the Southern Alps (Schaltegger and Brack 2007; Bernoulli, 2007).

After the end of the Variscan orogeny, the Southern Alps underwent three phases of extensional tectonics (Schaltegger and Brack 2007; Bernoulli, 2007) in the Permian and Mesozoic times.

1- In the Early Permian, the southern Alps crust experienced an extensional deformation (rifting) which produced sedimentary basins and massive magmatism.

2- Middle Triassic extension, which might be combined with transtension and transpression, and shoshonitic magmatism in the eastern Southern Alps.

3- Late Triassic to Middle Jurassic extension, which led to the opening of the Alpine Tethys to the west.

2.4.2. Alpine Orogeny in the Southern Alps

The Eurasian and African plates inverted their motion at the end of the early Cretaceous and the continental margin convergence controlled the subsequent evolution of the Southern Alps up to their present setting (Castellarin et al., 2006). The complex collision between Europe and Adria plate (African Promontory) generated the Alpine domain through three compressional phases: eoalpine phase, mesoalpine phase and neoalpine phase (Doglioni and Bosellini, 1987; Castellarin et al., 2006).

The eoalpine phase (late Cretaceous) producing a pure N-S compression. It deformed only the central and western parts of the Southern Alps and generated overthrust to the west and flower structure by sinistral transpression in the Giudicarie belt (Doglioni and Bosellini, 1987). The mesoalpine deformation phase or Dinaric compression (Eocene) was generated by ENE-WSW

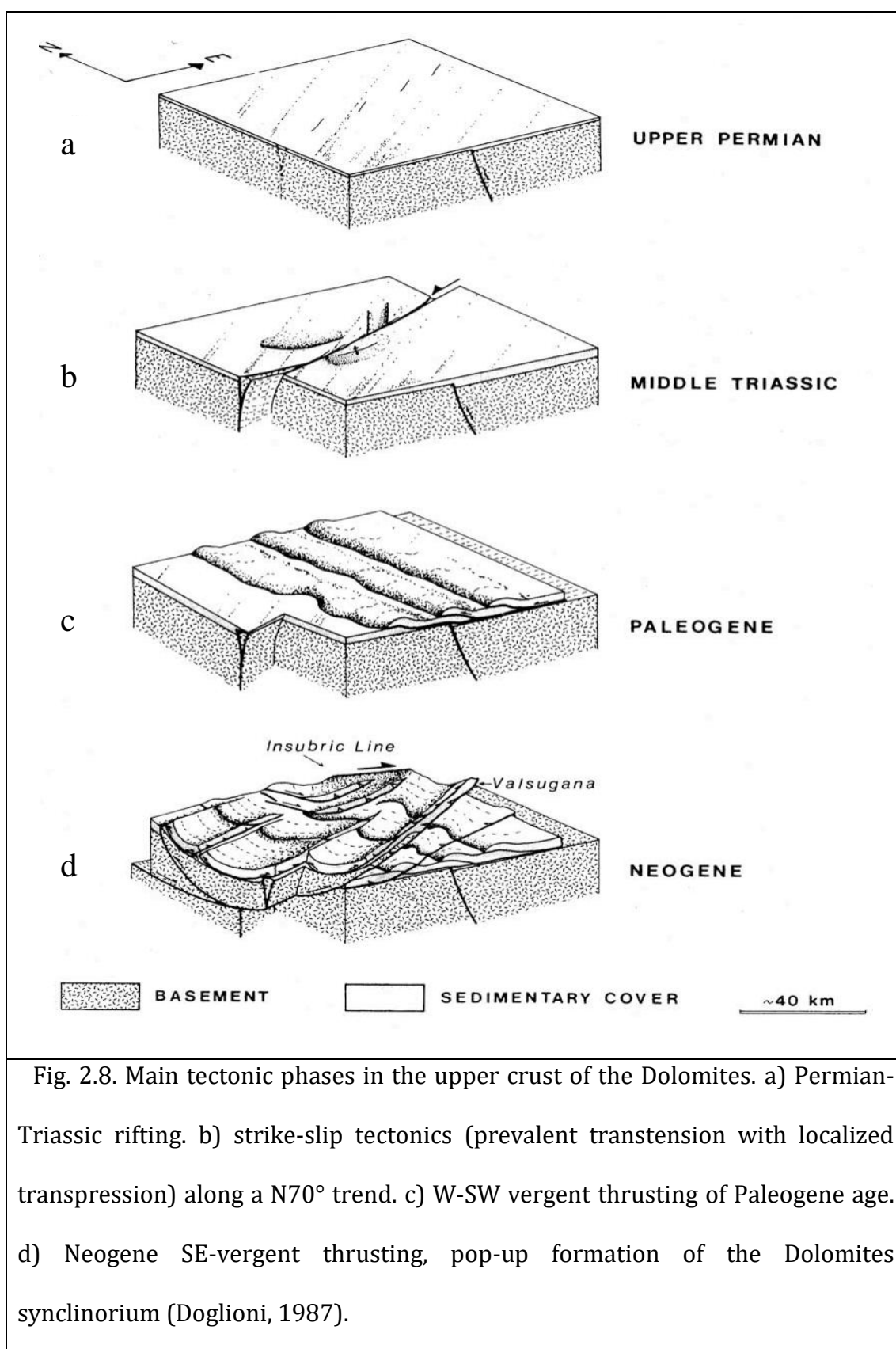
compression and produced NW–SE trending thrusts (overthrusts & folds) in the eastern Southern Alps and produced thin-skinned tectonics in the area of the Dolomites. The neoalpine phase (Late Miocene) deformed all the Southern Alps including the basement and inherited the eoalpine and mesoalpine structures. South-vergent thrusts (e.g., Val Tompia, Orobic, Valsugana) developed during this stage (Doglioni and Bosellini, 1987).

2.5. Tectonic evolution of the Dolomites

The main tectonic events recorded in the Dolomites area can be resumed as follows (Fig. 2.8): 1) Permian-Triassic strike-slip and rift-related extensional tectonics (Fig. 2.8.b). The WSW-ENE Valsugana “paleoline” and the E-W Funes Line (Selli, 1998) delimited the main basin where the Athesian Volcanic Group was emplaced. During the Anisian, a roughly N-S oriented fault system separated the Western Dolomites from the Cadore basin to the east. 2) Nearly a-magmatic Jurassic rifting associated with the opening of the Alpine Tethys Ocean. The Jurassic N-S trending extensional faults separated the Trento Horst to the west and the Belluno Graben to the east; 3) Compressional tectonics related to the Europe-Adria plates convergence developed outside of the Dolomites (e.g., Pre Adamello belt in Castellarin et al., 2006) since the Late Cretaceous. The Dolomites region was affected from the Paleogene by ENE-WSW thin-skinned shortening, which generated WSW-verging thrusts, N-S or NNW-SSE trending folds and conjugate strike-slip faults (Fig. 2.8.c). The shortening of the sedimentary cover, during this deformation phase, was about 10-15 km (Doglioni, 1987); 4) Late Oligocene to Recent NNW-SSE thick-skinned

shortening, which produced SSE-verging thrusting for a minimum 40-50 km shortening in the Dolomites and Venetian Alps. During this stage, the Dolomites developed as a ~60 km wide synclorium within the pop-up structure bounded by the Valsugana and Pusteria Lines (Fig. 2.8d). Mesozoic N-S inherited structures were re-sheared as strikes slip faults (Caputo et al., 2010).

Below more details on the Middle Triassic Tectonic evolution of the Dolomites are presented.



2.5.1. Middle Triassic Tectonics in the Dolomites

The Dolomites are cut by Middle Triassic sinistral strike-slip faults oriented N70-90E, defining the Stava, Trodena and Cavalase Lines (Abbas et al., 2018). These structures displace both basement and sedimentary successions up to lower-middle Ladinian ages (Doglioni 1984, 1987, 2007; Doglioni and Carminati, 2008). The Cima Bocche Anticline along the Stava Line is interpreted as a positive flower structure indicating transpressional sinistral motion (Doglioni, 1983).

Local Middle Triassic compression has been inferred in the Dolomites by several fold (Fig. 2.9) and reverse fault systems, also triggering N70E trending diapiric structures in Late Permian evaporites (Bellerophon Formation; Bechstadt et al., 1977; Pisa et al., 1980; Bosellini et al., 1982; Doglioni 1984, 1987, 2007; Castellarin et al., 1998; Doglioni and Carminati, 2008).

In the Triassic rocks of the Dolomites, extensional synsedimentary faults oriented N-S coexisting with above described strike slip tectonics can be also observed. These extensional tectonic features are consistent with the occurrence of 1-2 km thick carbonate platforms of Middle-Upper Triassic age that required a comparable subsidence for their deposition. The Middle Triassic sinistral transpressional structures and the coeval subsidence were ascribed to coeval sinistral movements between Adria and Europe (Doglioni 1984, 1987).

Well dated volcanic dykes and lava flows cross-cut the Triassic structures (thrusts, folds and diapirs) confirming their middle Triassic (late Ladinian) age (Doglioni 1984, 1987; Stefani and Caputo, 1998). Domal uplift associated with magmatism is reflected by the radial pattern of the Ladinian dykes in the

central-western part of the Dolomites (Doglioni, 1983). The orientation of the major axis of the dome (N70E, Stava Line, Cima Bocche anticline, Selle Line) was possibly controlled by a zone of weakness, inherited from previous sinistral transcurrent faults.

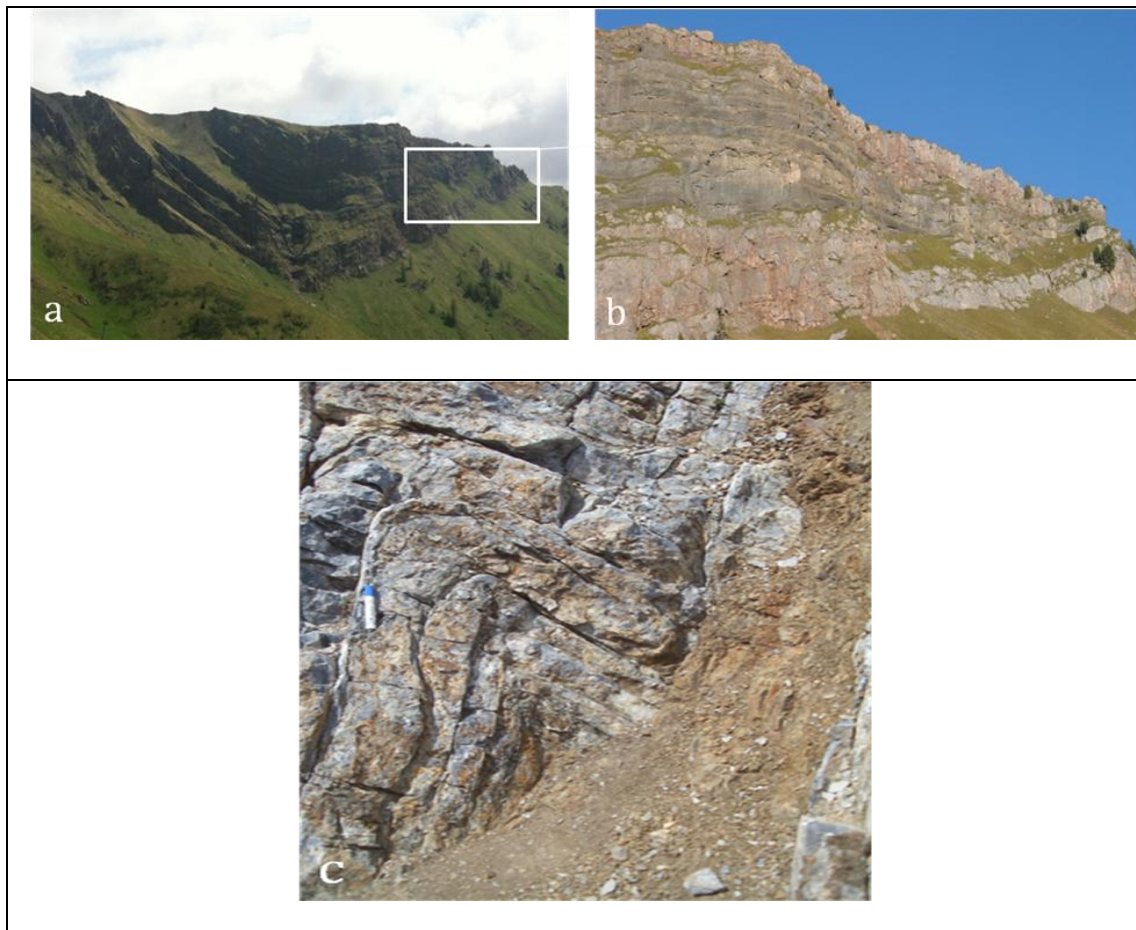


Fig. 2.9. a) The Crepe Rosse synsedimentary syncline (cropping out at Passo Fedaia) consists both of Ladinian volcanoclastic deposits and the interfingering carbonatic megabreccias. It developed to the south of a Triassic sinistral transpressional fault. Notice the onlaps, especially on the right flank of the syncline (closeup, Fig. 2.9b). c) A upper Ladinian latitic-basaltic dyke cuts both flanks of a chevron fault developed in the dark limestones of the Upper Anisian Moena Fm, constraining the age of deformation to be Middle Triassic.

2.3. The Predazzo intrusive complex

The Predazzo intrusive complex (Fig. 2.2) is ring-shaped, ~4 km in diameter and covers an area of ~13 km². It has been subdivided into four intrusive units on the basis of magma chemistry, geometry and relative geochronology (Menegazzo et al., 1995; Visonà 1997). Monzonitic unit M1 represents the first intruded unit and forms the outer part of the ring with mainly monzonitic composition associated with ultramafic rock types (pyroxenites). These ultramafic bodies are generally small, tabular and vertical with sinuous sharp contacts. Monzonitic unit M2 is intruded into the Middle Triassic volcanic rocks and into the Monzonitic unit M1 and cut them with short dykes. This unit crops out in the western part of the igneous complex and is mainly composed of quartz monzonite with subordinate leuco-quartz monzonite and quartz monzodiorite. In more recent studies, M1 and M2 units were merged into a single shoshonitic silica-saturated (SS) series (Casetta et al., 2017). Monzonitic unit M3 is mainly located in the eastern part of the pluton and intrudes both volcanic rocks and Monzonitic unit M1. It consists of monzodiorite to syenite, both quartz- or foid-bearing. The granite unit is located in the central part of the pluton and cuts both volcanic rocks and Monzonitic units M1 and M2. It consists of two separate lithotypes: a) biotite granite, b) tourmaline leuco-granite (Visonà, 1997). When exposed, the contact between lavas of the inner part of the volcanic-intrusive Predazzo body and the intrusive rocks is steep and outward-dipping (Fig. 2.10).

Mainly NNW-SSE oriented systems of basaltic to trachytic dykes that cut the entire intrusive complex together with the surrounding volcanic products, which in total cover an area of ~25 km² (Casetta et al., 2017).

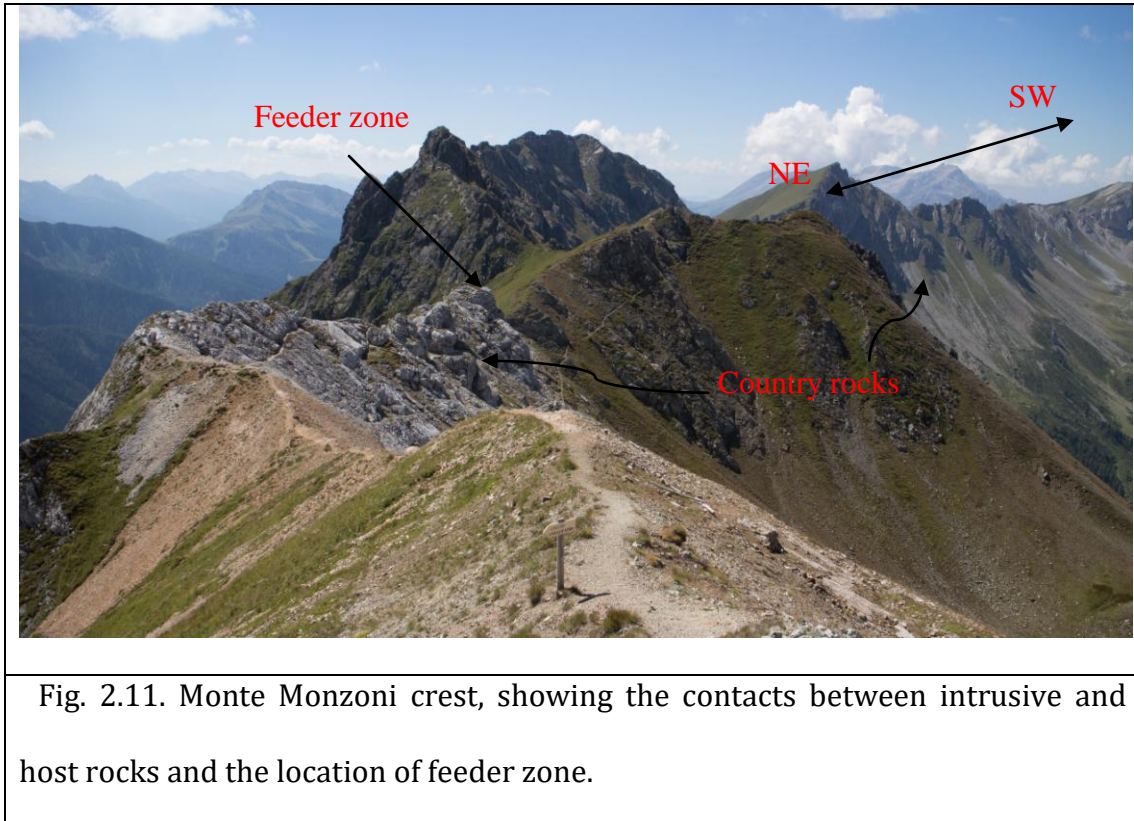


Fig. 2.10. Field photograph showing sharp intrusive contact between granite and volcanic rocks; the contact is steeply dipping outward.

2.4. The Monzoni intrusive complex

The Monzoni intrusive complex (Fig. 2.2), located 8 km to the NE of the Predazzo complex is a NE-SW elongated pluton with a length of <5 km covering an area of $\sim 8 \text{ km}^2$ (Fig. 2.2, 2.11). The Monzoni pluton played a central role not only for the study of the Middle Triassic magmatism but also in the development of petrography, being the type locality for monzonitic rocks (Brogger, 1895). The intrusion comprises a series of basic to intermediate plutonic rocks, which consist of gabbroic rocks (gabbro, olivine gabbro, monzogabbro), cropping out in the north-eastern part of the complex together with clinopyroxenite, while monzonites and monzodiorites constitute the western part of the intrusion (Del

Monte et al., 1967; Bonadiman et al., 1994; Gallien et al., 2007). The Monzoni complex and the thermo-metamorphosed Permian to Triassic host-rocks are cut by quartz syenitic and shoshonitic dyke swarms (Bonadiman et al., 1994).



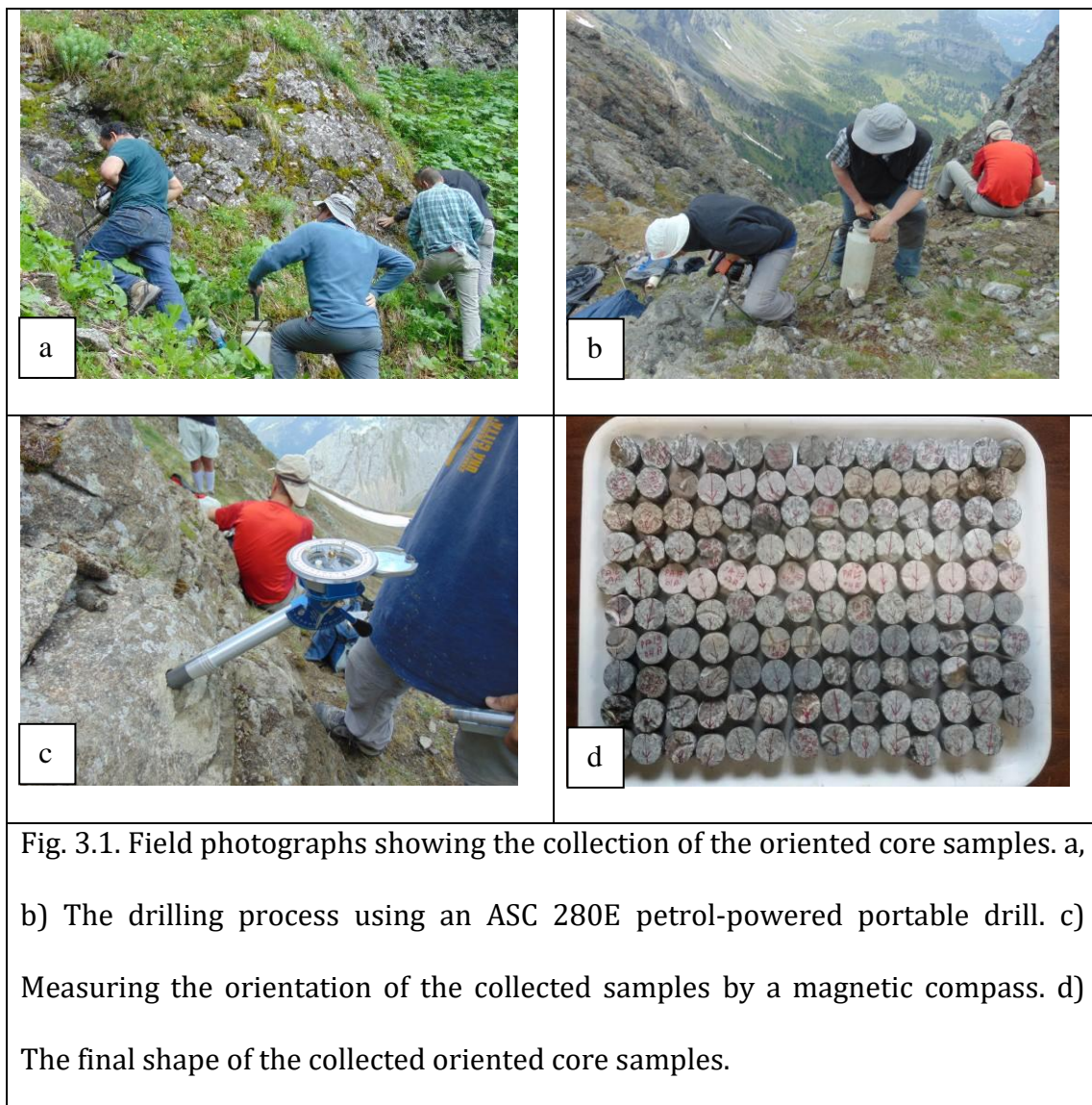
**CHAPTER THREE
SAMPLING AND METHODS****3.1. Sampling strategy**

105 Samples were collected (48 from Dolomites volcanic rocks, 22 from Predazzo, 11 from Monzoni and 22 samples from Vicentinian Alps) for petrological and geochemical analyses. The samples were collected in four fieldworks from 2015 to 2017. All the samples were cut to obtain thin sections and, after a detailed petrographic inspection, 62 representative samples were selected for whole-rock chemical analyses. The representative samples were cut with a diamond-disc saw to small chips to remove eventual weathered parts. These were first crushed in a steel mill to about mm-scale fragments, then washed with distilled water and dried at 110 °C for 12 hours. The dried and clean chips were powdered in a low-blank agate mortar to a size passing 200 mesh sieve.

Sampling for structural and AMS analyses was carried out both in the Predazzo and Monzoni plutons. In the Predazzo intrusive body, 14 sites were sampled and 107 cylindrical cores were collected for AMS analysis. In the Monzoni intrusive body, 10 sites were sampled for a total of 84 cylindrical cores. At each site, cores were drilled using an ASC 280E petrol-powered portable drill (Fig. 3.1a, b) and oriented in situ by a magnetic compass (Fig. 3.1c), corrected to account for a local $\sim 2^\circ$ magnetic declination according to the NOAA National Geophysical data

centre. Then, each core was cut into specimens of 2.5 cm diameter and 2.2 cm height (Fig. 3.1d).

The geographic distribution of the sampling was influenced by the difficulty to find accessible outcrops in many areas, preventing the possibility to make a homogeneously distributed sampling throughout the two intrusive bodies.



3.2. Methods

3.2.1. Petrographic descriptions

105 samples were prepared as thin-sections of 28-30 μm thickness at the laboratory of Dipartimento di Scienze della Terra of Sapienza University of Rome. The analysis of the thin sections was accomplished using an optical polarizing microscope.

3.2.2. Whole-rock major and trace element analyses

62 representative samples (31 from Dolomites volcanic rocks, 16 from Predazzo, 8 from Monzoni and 6 from Vicentinian Alps) have been analyzed for whole-rock chemistry. Whole-rock major and trace element analyses were performed at Actlabs laboratories (Ontario, Canada) using Code 4LITHO Major Elements Fusion ICPAES and trace Elements Fusion ICPMS. The detection limit ranges from 0.001 to 0.01 % for major elements, 0.1 to 30 ppm for trace element and 0.004 to 0.1 ppm for REE.

3.2.3. Mineral chemistry analyses

Microprobe analyses have been performed on 15 representative samples from the Dolomites lava only (the study of the Dolomites lava represents the main target in the present study). Mineral chemistry analyses were performed in the CNR-IGAG laboratory, Dipartimento di Scienze della Terra of Sapienza University of Rome, with a CAMECA SX 50 electron microprobe (Fig. 3.2). The analyses were carried out at 15 kV accelerating voltage, 15 nA beam current, 10 μm beam diameter for feldspar and 1 μm for pyroxene and opaque minerals. Counting

times were 20 s at the peak position and 10 s for background for all elements.

Calibration was made on synthetic and natural minerals.



Fig. 3.2. CAMECA SX 50 electron microprobe, at the CNR-IGAG laboratory, Dipartimento di Scienze della Terra of Sapienza University of Rome.

3.2.4. Isotope analyses

Seven representative samples from the Dolomites lava have been analysed for Sr-Nd-Pb isotope ratios at the Istituto di Geoscienze e Georisorse, at the CNR-ICG of Pisa. The powder of the rocks were dissolved in HF+HNO₃ and then completely dried. Sr and Nd were extracted by Ion Exchange Chromatography (IEC). By using of ion-exchange chromatography columns, Sr and REE were purified in an HCl solution and then isolate the Nd from REE. Lead was extracted from the matrix after eluting with HBr and HCl. The separated Sr-Nd and Pb were

loaded on rhenium filaments and then loaded into a Finnigan Mat 262 multi-collector Thermal Ionization Mass Spectrometer (TIMS; Fig. 3.3).

Sr and Nd isotopic compositions were corrected for mass fractionation using $^{86}\text{Sr}/^{88}\text{Sr} = 0.1194$ and $^{146}\text{Nd}/^{144}\text{Nd} = 0.7219$. During the analytical process, the Sr standard NIST SRM 987 and the Nd standard J-Ndi1 yielded average values, respectively, of $^{86}\text{Sr}/^{88}\text{Sr} = 0.710212 \pm 0.000018$ (2SD; $n = 26$) and $^{146}\text{Nd}/^{144}\text{Nd} = 0.512107 \pm 0.000012$ (2SD; $n = 16$); measured values were adjusted to 0.710250 for $^{86}\text{Sr}/^{88}\text{Sr}$, whereas no Nd isotope adjustment was necessary. The Sr and Nd blanks were respectively about 2.3 ng and 1.0 during chemical analyses, which are insignificant for the analyzed samples. The analyses of Lead isotope were carried out using a Finnigan MAT 262 multi-collector mass spectrometer operating in static mode. Replicate analyses of Pb isotope ratios are accurate within 0.25 ‰ (2SD) per mass unit after applying mass discrimination corrections of 0.15 ‰ per mass unit relative to the NIST SRM 981 reference composition of Todt et al. (1993). Pb blanks were of the order of 0.2-0.4 ng, and no blank correction was made.

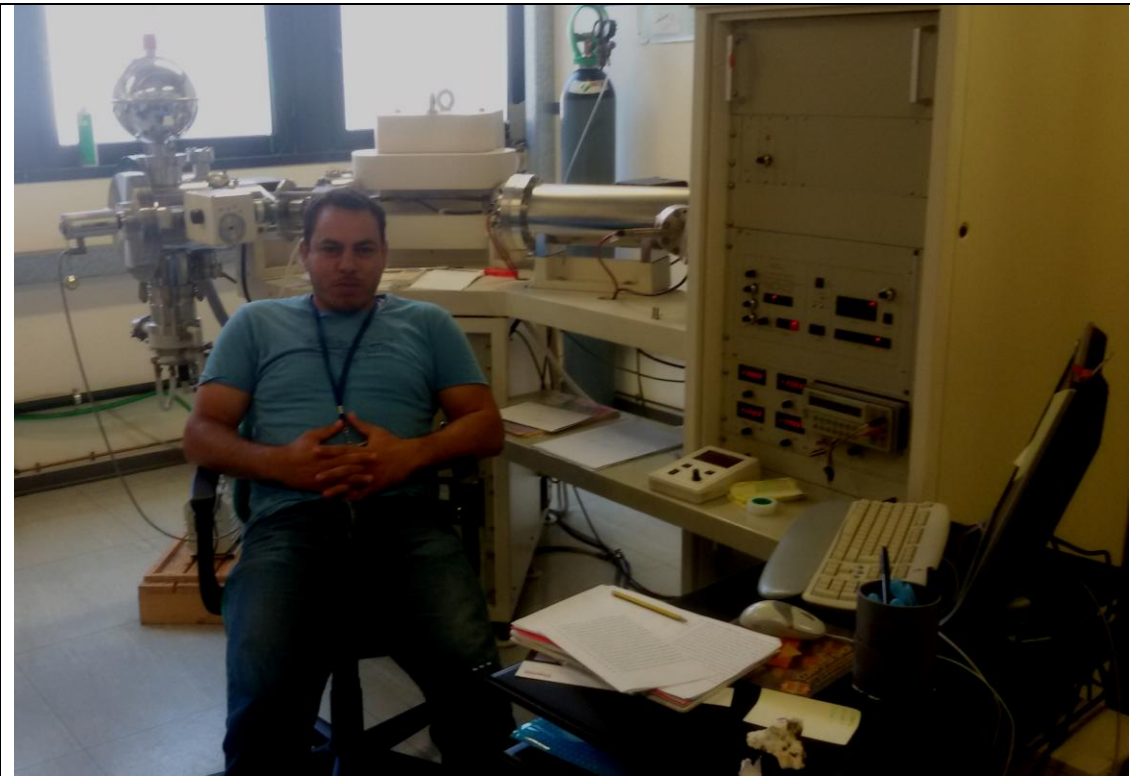


Fig. 3.3. Finnigan Mat 262 multi-collector Thermal Ionization Mass Spectrometer (TIMS), at CNR-IGG Laboratories, Pisa.

3.2.5. Microstructural analysis

29 thin sections from Predazzo and Monzoni were studied for Microstructural analysis. The analysis of the thin sections was accomplished using an optical polarizing microscope at Dipartimento di Scienze della Terra of Sapienza University of Rome.

3.2.6. Magnetic mineralogy

The AMS technique provides a quick and accurate determination of igneous rock fabric. The magnetic fabric (lineation and foliation) data obtained from AMS measurement can record the primary magma flow in magmatic sheet intrusions (Polteau et al., 2008; Petronis et al., 2013, Andersson et al., 2016; Magee et al., 2016), although magnetic fabric data are sometimes complex and in some cases subject of controversy.

The precise knowledge of the magnetic mineralogy is an important aspect to use AMS for tectonic purposes because the preferred orientation of different magnetic minerals reflects the deformation history of the rock (e.g., Rochette et al. 1992; Hrouda et al. 1997). Magnetic mineralogy analyses were carried out in order to characterize which are the main magnetic minerals in the sampled sites. The variation of magnetic susceptibility with temperature was measured on powders from 24 representative samples one for each site, by means of the same Agico KLY-3 Kappabridge use for LF-AMS measurements, equipped with a CS-2 furnace (Fig. 3.4), at the paleomagnetic laboratory of the Department of Sciences of Roma Tre University. Samples were heated up to 700 °C and cooled back to 40 °C to estimate the Curie/Néel range of temperatures, according to the inverse susceptibility method proposed by Petrovský and Kapička (2006), and to examine any possible mineralogical changes associated to the heating process in air. Moreover, the hysteresis properties of powders from 21 representative samples were measured on a Princeton Measurements Corporation 3900 vibrating sample magnetometer (VSM; Fig. 3.5), in field up to 1 T. The powders have been placed in pharmaceutical gel caps suitable for vibrating in the VSM, in

order to determine, after subtracting the high field linear trend, the coercive force (B_c), the saturation remanent magnetization (M_{rs}), as well as the saturation magnetization (M_s). The coercivity of remanence (B_{cr}) values have been extrapolated from backfield remagnetization curves up to -1 T, following forward magnetization in a +1 T field. These measurements were carried out in the Istituto Nazionale di Geofisica e Vulcanologia (INGV, Rome).



Fig. 3.4. Agico KLY-3 Kappabridge use for LF-AMS measurements, equipped with a CS-2 furnace, at the paleomagnetic laboratory of the Department of Sciences of Roma Tre University.



Fig. 3.5. Princeton Measurements Corporation 3900 vibrating sample magnetometer (VSM), at the Istituto Nazionale di Geofisica e Vulcanologia (INGV, Rome).

3.2.7. Anisotropy of low-field magnetic susceptibility (LF-AMS)

AMS is defined by a second rank tensor and represented geometrically by an ellipsoid in which the greatest intensity of magnetization is induced along the long axis k_1 and the weakest intensity along the short axis k_3 (with the principal axes $k_1 > k_2 > k_3$). Since the pioneering work of Graham (1954), a close correlation between the directions of the main axes of AMS ellipsoid (k_1, k_2, k_3) and the petrofabric strain axes (η_1, η_2, η_3) has been widely demonstrated. Several parameters have been defined both for the quantification of the magnitude of anisotropy and for defining the shape of the ellipsoid (Jelinek, 1981; Hrouda, 1982). The mean susceptibility values k_m have been computed as $k_m = (k_1 + k_2 + k_3)/3$. The magnetic lineation is computed by $L (k_1/k_3)$ and has an orientation defined by the orientation of k_1 , while the magnetic foliation is computed by $F (k_2/k_3)$ and it is defined as the plane perpendicular to k_3 . T is the shape parameter and range from -1 (perfectly prolate ellipsoid with $L \gg F$) to +1 (perfectly oblate ellipsoid with $F \gg L$) with zero values corresponding to a triaxial shape ($F \sim L$). The anisotropy degree is computed by the parameter P_j (Jelinek, 1981), which is obtained considering all the three principal susceptibility values.

Measurement of the anisotropy of low-field magnetic susceptibility (LF-AMS) represents a rapid and non-destructive technique for the characterisation of the mineral fabric in rocks (Hrouda, 1982). In this study, the LF-AMS was measured on about 200 samples, with an Agico KLY-3S susceptibility bridge (Jelínek and Pokorný, 1997) in the paleomagnetic laboratory of the Department of Sciences of

Roma Tre University. The anisotropy measurements at both the sample and the site scale were evaluated using Jelínek's statistics (Jelinek, 1977).

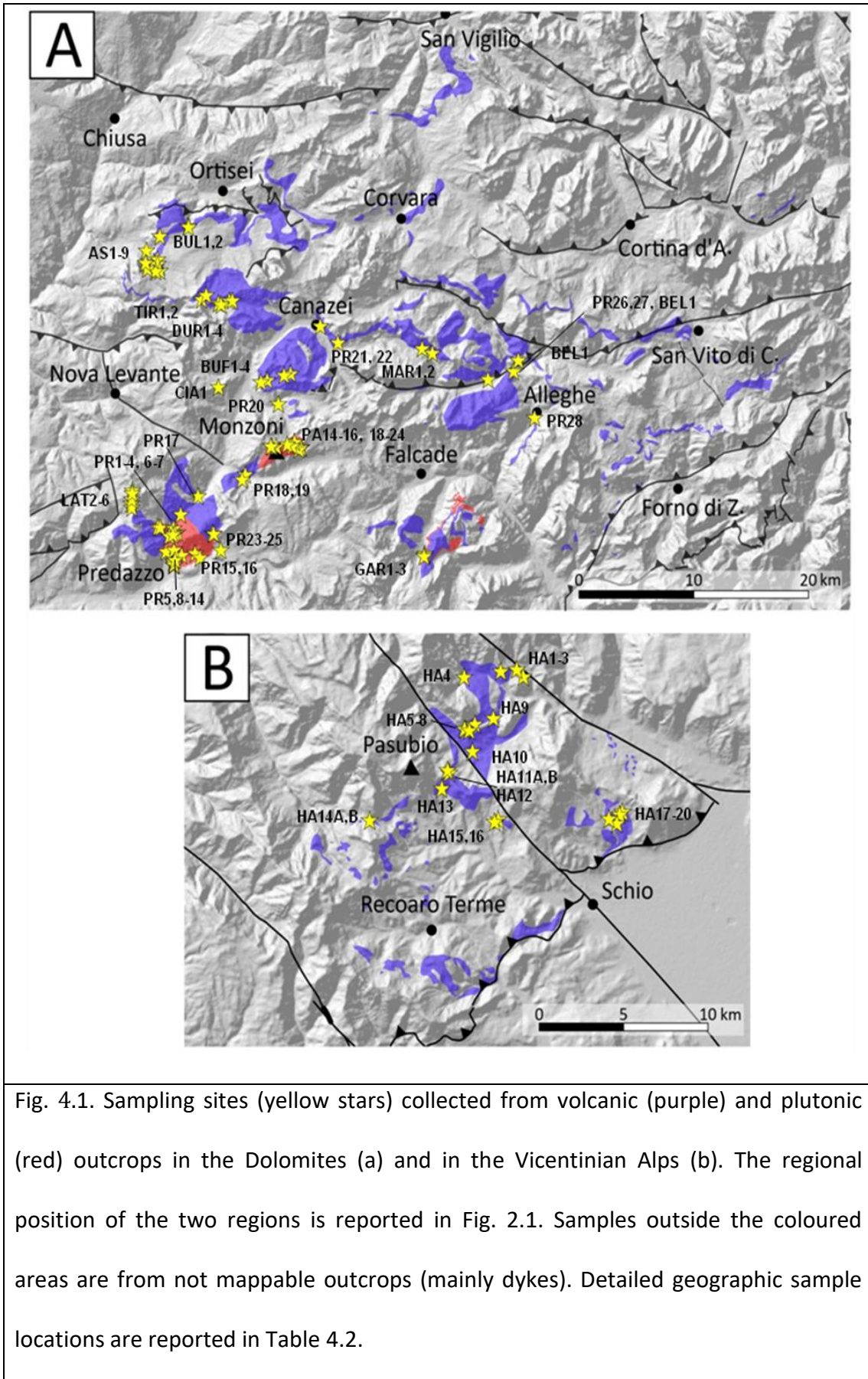
3.2.8. Anisotropy of high-field magnetic susceptibility (HF-AMS)

As the LF-AMS is the sum of the contribution from all minerals, which include ferromagnetic, paramagnetic and diamagnetic phases (Rochette et al., 1983), we measured high-field AMS (HF-AMS) on 13 selected samples from Predazzo and Monzoni plutons in order to discriminate the relative contribution of ferromagnetic and paramagnetic minerals to the magnetic anisotropy (e.g., Martin Hernandez and Hirt, 2001). HF-AMS measurements were carried out, using magnetic fields up to 1500 mT. These fields are strong enough to saturate all ferromagnetic minerals except hematite (not present in the analyzed samples), and allow the separation of paramagnetic and ferromagnetic contribution to the magnetic anisotropy (e.g., Hrouda and Jelínek, 1990). Measurements were made with a high-field torque magnetometer (Bergmüller et al., 1994) in the Laboratory of Natural Magnetism of the Institute of Geophysics ETH in Zürich.

CHAPTER FOUR
PETROLOGICAL AND GEOCHEMICAL STUDIES

4.1. Petrographic description

The investigated samples are essentially massive volcanic rocks (44 samples; dykes, sills and lava flows) plus rarer pyroclastic facies rocks (4 samples) from the Dolomites. Seven volcanic rocks from Vicentinian Alps (hereafter referred to Recoaro), 8 plutonic rocks from Monzoni and 16 plutonic rocks from Predazzo complete the analyzed dataset presented here (fig. 4.1; see whole-rock chemistry section). The main topic of this research are the massive volcanic rocks of the Dolomites and consequentially only minor comments will be devoted to the other volcanic and plutonic rocks presented here, the readers being referred to the recent articles of Casetta et al. (2018a, 2018b) and to Bonadiman et al. (1994) for Predazzo and Monzoni plutonic rocks . Below a petrographic description of the two types of Dolomite volcanic rocks is reported.



4.1.1. Dolomites massive volcanic rocks

The rocks are generally porphyritic to glomeroporphyritic (Fig. 4.2a, b) with porphyritic index (P.I.) ranging from ~10 to ~40% (Table 4.1). The main phenocryst assemblage is dominated by plagioclase (~6-36%) and clinopyroxene (~1-14%), with subordinate olivine (~1-9%). The groundmass of the lavas is either very fine grained, intersertal hypohyaline to hypocrySTALLINE or fine grained, intergranular to subophitic hypocrySTALLINE to holocrySTALLINE. The groundmass is generally pilotaxitic, but in a few cases a moderate preferred orientation of plagioclase microlites is observed.

Plagioclase is always the most abundant phenocryst phase, occurring as euhedral to subhedral (~1-4 mm) and usually zoned crystals, in many cases showing slight to moderate sericite pseudomorphosis, with cores more altered than rims. In many cases plagioclase phenocrysts exhibit a sieve structure and contain glass shreds and iron oxides (Fig. 4.2c). Clinopyroxene phenocrysts are generally euhedral to subhedral and range in size from 2 to 4 mm. They are well preserved, sometimes zoned and in many cases fractured. Clinopyroxene crystals usually include plagioclase microphenocrysts, iddingsite pseudomorphs on olivine crystals and iron oxides. In a few cases, clinopyroxene phenocrysts exhibit sieved structure. Olivine phenocrysts are euhedral to subhedral (~1-2 mm) and are usually completely transformed mainly to iddingsite and, in a few cases, to serpentine (Fig. 4.2d, e) or chlorite. Sometimes olivine is completely replaced by quartz or calcite in the most altered samples. Relics of the original olivine are commonly preserved.

Groundmass is generally composed of feldspar microlites (plagioclase and rare sanidine) with clinopyroxene, iddingsite pseudomorphs after olivine and

opaques, with or without variably transformed glass. Cavities or vesicles (amygdaloidal texture) with irregular shape are seldom recorded and filled with secondary minerals such as chlorite, zeolites, and calcite. The dykes and sills show the same composition and textures of the lava flows and are characterized by higher degree of crystallinity (Fig. 4.2f). Rare quartz xenocrysts (~1.5 mm) with oval shape surrounded by fine clinopyroxene aggregates have been recorded (Fig. 4.2g). Also, few clinopyroxenite xenoliths ranging in size from ~2 mm to ~3 mm have been recorded in few samples (Fig. 4.2h, i).

Sample(s)	Phenocryst phase (modal %)			P.I.	Mode of occurrence
	Plagioclase	Clinopyroxene	Olivine		
DUR4,3	12	7	4	23	Basaltic Lava
TIR1,2	14	11	3	28	Basaltic Lava
GAR3	16	14	4	34	Sill
BUF1	6	3	3	12	Basaltic Lava
BUF2	15	8	5	28	Basaltic Lava
BUF3	10	2	3	15	Basaltic Lava
BUF4	16	2	3	21	Basaltic Lava
Mar(1)	19	3	2	24	Basaltic Lava
Mar(2)	18	6	3	27	Basaltic Lava
AS1	11	8	3	22	Basaltic Lava
AS2	16	14	6	36	Basaltic Lava
AS3	15	13	9	37	Basaltic Lava
AS4	12	3	3	18	Basaltic Lava
AS7	12	7	3	22	Basaltic Lava
AS8	14	9	5	28	Basaltic Lava
AS9	12	8	5	25	Basaltic Lava
DUR1,2	10	5	3	18	Basaltic Lava
BUL1,2	13	6	4	23	Basaltic Lava
PR1	11	4	2	17	Basaltic Lava
PR17	23	3	2	28	Basaltic Lava
PR20	27	6	4	27	Basaltic Lava
BEL1	35	6	5	46	Basaltic Lava
LAT2	33	5	3	41	Dyke
LAT3	22	3	2	27	Dyke
LAT5	27	7	5	39	Dyke
CAI1	12	10	2	25	Dyke
PR3	18	1	1	20	Basaltic Lava

Table 4.1. The percentage of the phenocryst phases and the porphyritic index (P.I.) in the studied Dolomites massive volcanic rocks.

4.1.2. Dolomites pyroclastic rocks

The rare pyroclastic rocks investigated in this study can be subdivided into three sub-types: lithic-crystal-vitric hyaloclastite tuff (sample AS6), lithic-vitric-crystal tuff (samples PR26, PR28) and crystal tuff (sample PR27).

Lithic-crystal-vitric hyaloclastite tuff (sample AS6). The sample is isotropic and dominated by glassy shards (~45%), crystal fragments (~35%) and lithic fragments (~20%). Two types of glassy fragments are recorded, with a similar maximum size (~0.5 mm), brown and dark (Fig. 4.2j, k). The state of the glass fragments is generally good with slight alteration to palagonite, mostly confined to the outermost sectors. Crystal fragments (<0.5 mm) are mainly represented by feldspars (fresh plagioclase), mafic minerals – completely altered and transformed to secondary minerals – and minor opaque minerals. The lithic fragments (<1 mm) are composed of plagioclase, altered mafic minerals, opaque minerals and glass. The groundmass is fine-grained and composed mainly by secondary calcite and subordinate opaque minerals.

Lithic-vitric-crystal tuff (samples PR26, PR28). The samples are fine-grained, isotropic and composed of crystal fragments (~45-50%), glass fragments (~35-40%) and lithic fragments (~8-10%). Crystals fragments (<0.5 mm) are mainly feldspars with subordinate moderately altered clinopyroxene and minor completely altered unidentified mafic minerals. Glass fragments (<0.5 mm) are found in good state and mainly in black colour with minor brown glass. Lithic fragments (<0.5 mm) are composed of feldspar, mafic minerals, and glass. The matrix of sample PR26 is fine-grained and dominant by secondary calcite, whereas sample PR28 characterized by a very fine-grained matrix and moderately to highly altered.

Crystal tuff (sample PR27). The sample is fine-grained, isotropic and dominated by feldspars (~85%) and subordinate opaque minerals (~15%) with the absence of pyroxene and olivine (Fig. 4.21). Plagioclase and opaque fragments were found in different grain size (up to 1 mm and 0.5 mm, respectively). Plagioclase crystals are generally fresh, except a few completely altered cases where this phase is completely replaced by calcite. Plagioclase and opaque fragments are cemented together by very fine-grained groundmass.

4.1.3. Vicentinian Alps rocks

The rocks collected in the Recoaro-Schio area are generally highly altered. They are porphyritic, fine grained with hypocrySTALLINE groundmass. Three main mineral assemblages are indicated by rocks with phenocrysts mainly of plagioclase (~0.5-2 mm) with subordinate clinopyroxene (~1-2 mm; samples HA1 & HA7), rocks with phenocrysts of plagioclase (~1-2.5 mm), amphibole (~1-2 mm), biotite (~0.5-2 mm), and clinopyroxene (~0.5-2 mm; sample HA17), and rocks with phenocrysts of sieved and zoned plagioclase (~1-2.5 mm), clinopyroxene partially to completely altered to amphibole (~1-3 mm) and rare olivine (sample HA19).

4.1.4. Predazzo plutonic rocks

The samples collected from Predazzo pluton show a wide compositional spectrum with compositions ranging from clinopyroxenites and gabbros to granites.

Clinopyroxenites (PA12, PR11a,b,c) and cumulitic gabbros (PR 10) show a hypidiomorphic inequigranular medium- to coarse-grained cumulitic texture. In

the clinopyroxenite rocks, clinopyroxene is the only cumulus phase, while the intercumulus phases consist of opaque, biotite and plagioclase. In the the cumulitic gabbro rocks, the cumulus phases are plagioclase and clinopyroxene, whereas the intercumulus phases consist of biotite, opaques and plagioclase.

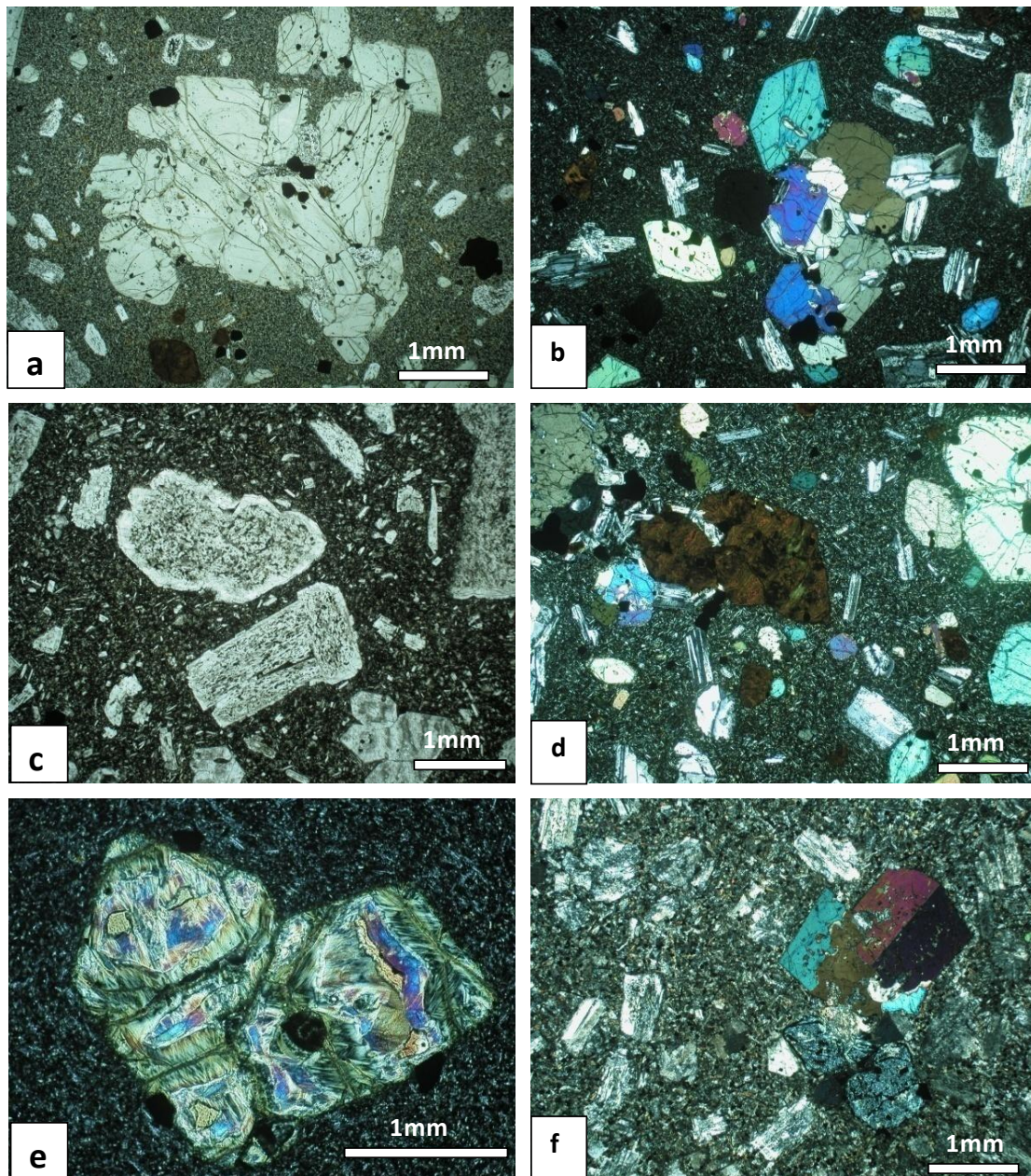
Monzonites (PR4, PR16), monzodiorites (PR13, PR14c, PR15), monzogabbros (PR12) and diorites (PR8) generally have the same petrographic characteristics, with different alkali feldspar/plagioclase ratios. Monzonite and monzogabbros are medium-grained, while monzodiorites and diorites are medium- to fine-grained. The amount of mafic minerals increases from monzonites to monzodiorites to monzogabbros and diorites. This rock group shows hypidiomorphic inequigranular texture with poikilitic texture (anhedral alkali feldspars including other minerals). The rocks are generally composed, in order of decreasing abundance, of plagioclase, alkali feldspar, clinopyroxene, amphibole, biotite, quartz, opaques, orthopyroxene and accessory minerals.

Granites are subdivided into two main groups: albitized granite (LAT1, PR7, PA05, PA17) and biotite granite (PR9, PR5, PA13). The samples show hypidiomorphic inequigranular texture. In few cases, granophyric texture is also recorded. The rocks are composed of, in order of decreasing abundance, alkali feldspar, quartz and plagioclase with minor biotite, muscovite, chlorite and rare amphibole.

4.1.5. Monzoni plutonic rocks

The samples collected from the Monzoni pluton can be subdivided into gabbroic rocks, located at the north-eastern part of the pluton, and monzonites, concentrated in the south-western sector of the massif.

The gabbroic rocks have been classified as olivine-gabbros (PA20, PA18), gabbros (PA15 and PA16), and monzogabbros (PA21). These rocks are generally medium- to coarse-grained with hypidiomorphic inequigranular texture. In several cases, cumulitic textures are recorded. The rocks are generally composed of plagioclase, clinopyroxene, K-feldspar, opaques, olivine, biotite and accessory minerals. The monzonites (PA22, 22A, 23, 24) are medium- to fine-grained and show hypidiomorphic inequigranular texture. The rocks are composed, in order of decreasing abundance, of plagioclase, alkali feldspar, biotite, clinopyroxene, amphibole, opaques, quartz and accessory minerals.



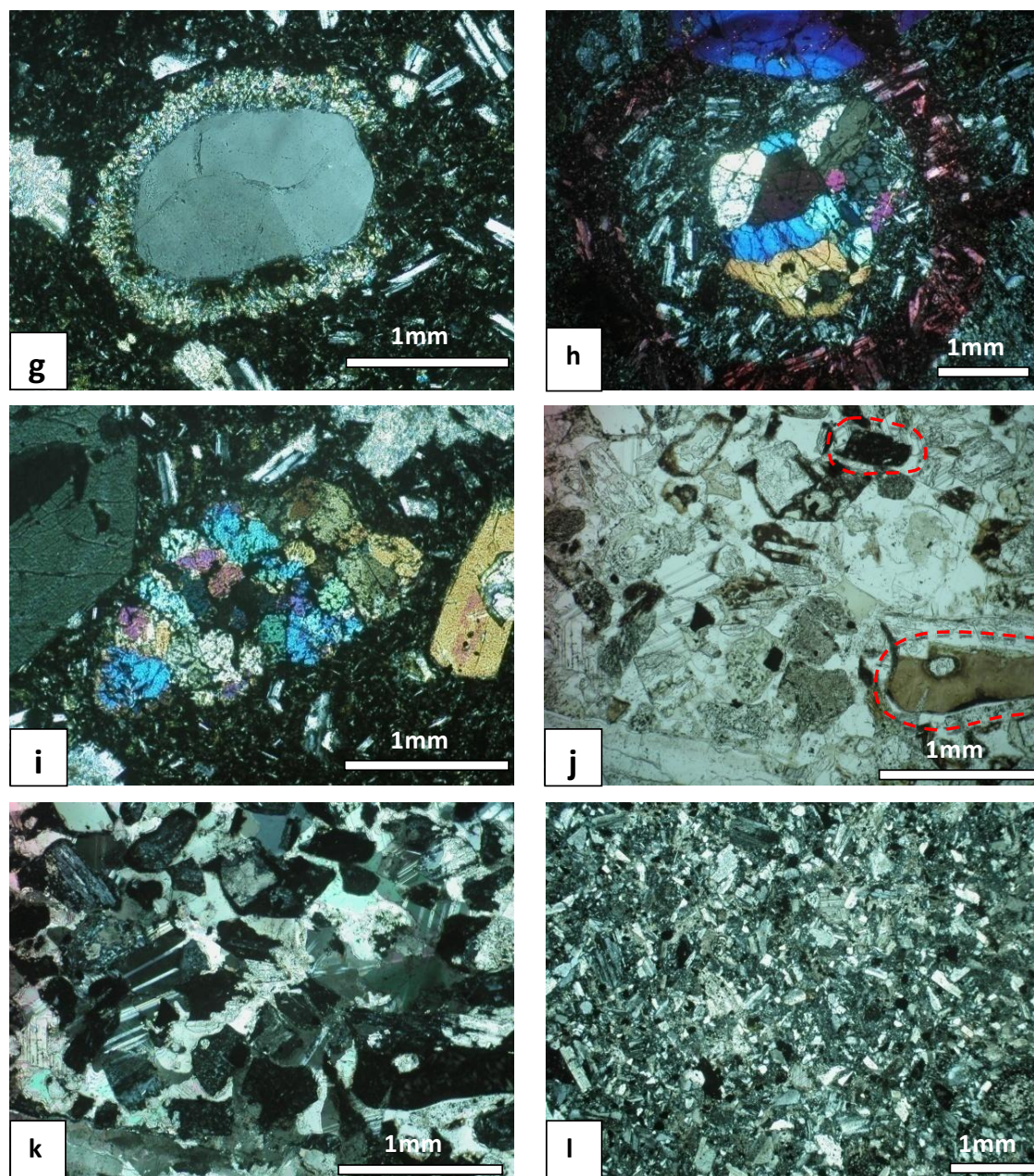


Fig. 4.2. Representative photomicrographs of the investigated Dolomite rock samples. a,b) Photomicrograph showing porphyritic to glomeroporphyritic texture consisting of plagioclase, clinopyroxene and olivine (completely altered to iddingsite) phenocrysts with iron oxide microphenocrysts (sample DUR4). c) Photomicrograph showing sieve texture in plagioclase phenocrysts (sample MAR2). d) Photomicrograph showing a completely altered olivine to iddingsite pseudomorph (sample TAR2). e) Photomicrograph showing pseudomorphs

(serpentine) after olivine with small relics of olivine preserved (sample BUF4). f) Photomicrograph showing porphyritic texture in dyke (sample LAT3). g) Photomicrograph showing a quartz xenocryst with oval shape surrounded by fine clinopyroxene crystals aggregates (sample GAR3). e) Photomicrographs showing a clinopyroxenite xenoliths (sample GAR3). j,h) Photomicrographs showing brown and dark glass fragments in hyaloclastites (sample AS6). l) Photomicrograph showing a crystal tuff sample consist of crystal fragments from plagioclase and subordinate opaque (sample PR27). Photomicrographs a, c and j were taken in plane-polarized light, whereas the other photos were taken in cross-polarized light.

4.2. Mineral chemistry

Electron microprobe analyses were performed on 15 representative samples from the Dolomites area only. A total of 364 points (123 plagioclases, 24 K-feldspars, 158 clinopyroxenes, 61 opaques, 8 olivines and 17 glass shards) were analysed and are reported in appendix 1.

Feldspars – The composition of plagioclase ranges from rare andesine to more common labradorite and bytownite (Fig. 4.3a; $Ab_{12-60}An_{36-87}Or_{1-8}$). Plagioclase shows both normal zoning with anorthite-rich cores and anorthite-poor rims and inverse zoning, with increase of anorthite content from the core to the rim. In the Si+Na vs. Al+Ca diagram the plagioclase data define good negative correlation and the samples plot exactly on the theoretical trend (Fig. 4.3a). Sr and Ba contents are always low (<0.025 and <0.019 apfu, respectively). Alkali feldspar is less abundant than plagioclase and is confined to the groundmass of the most evolved samples only. It is represented by Na-rich sanidine (Fig. 4.3a; $Ab_{26-46}An_{2-}$

$_{13}\text{Or}_{44-69}$), with much rarer nearly pure sanidine ($\text{Ab}_{2-4}\text{An}_{0-0}\text{Or}_{96-98}$), likely resulting from secondary alkali mobilization producing a significant Na loss. Ca and Ba contents are always low (0.004-0.494 and 0-0.093 apfu, respectively).

Clinopyroxene – This is a common phase in all the samples, with compositions straddling the diopside and augite fields (Fig. 4.3c; $\text{Wo}_{38-47}\text{En}_{35-47}\text{Fs}_{7-22}$). $^{\text{IV}}\text{Al}$ is always in excess to fill the tetrahedral site, with the remaining Al allocated in the M1 site. Both diopside ($\text{Wo}_{45-47}\text{En}_{39-46}\text{Fs}_{7-15}$) and aluminian diopside ($\text{Wo}_{45-47}\text{En}_{37-42}\text{Fs}_{11-17}$) are present with the first being characterized by lower Al (0.002-0.037 apfu) with respect to the second (Al = 0.103-0.925 apfu). Diopside shows generally higher Mg (0.774-0.908 apfu) than aluminian diopside (Mg = 0.697-0.825 apfu). A rare subset of crystals from BUF2 and BUF4 samples can be defined chromian diopside ($\text{Wo}_{46-47}\text{En}_7\text{Fs}_{46-47}$; Cr = 0.011-0.013 apfu) and aluminian ferrian diopside ($\text{Wo}_{45-47}\text{En}_{12-16}\text{Fs}_{39-42}$), marked by high Al (0.148-0.244 apfu) and Fe^{3+} (0.102-0.177 apfu). Augite ($\text{Wo}_{38-43}\text{En}_{38-46}\text{Fs}_{13-21}$) is characterized by lower Al (0.007-0.098 apfu) and slight higher Mg (0.747-0.889 apfu) with respect to the other types. A subset of clinopyroxene crystals has aluminian augite composition ($\text{Wo}_{40-45}\text{En}_{35-43}\text{Fs}_{13-22}$), with higher Al content (0.103-0.230 apfu) and aluminian ferrian augite ($\text{Wo}_{42-45}\text{En}_{38-42}\text{Fs}_{14-19}$) with relatively high Al (0.132-0.238 apfu) and Fe^{3+} (0.1-0.127 apfu). Ti and Na contents are always low (respectively 0.001-0.035 apfu in all but three crystals and 0.013-0.035 in all but two samples). Mg# [$\text{Mg}/(\text{Mg}+\text{Fe}^{2+})\cdot 100$] spreads over a large range from 67.1 to 87.2, with two outliers around 90.3-91.

Olivine – This phase is commonly replaced by iddingsite, except in the sample BUF4, where few relics of olivine phenocryst have been analysed. Here, forsterite [Fo; Fo = $\text{Mg}/(\text{Mg}+\text{Fe})\cdot 100$] contents indicate lower Mg enrichment compared

with clinopyroxene and a lower variability, ranging from 72.0 to 73.9. Minor elements such as Ca (0.008-0.0094 apfu), Ni (0.0003-0.0018 apfu), and Mn (0.010-0.013 apfu) are very low, with Ca showing a scattered negative correlation with Fo and Ni a scattered positive correlation (Fig. 4.3d, e).

Opagues – The analyzed opaque minerals are Fe-Ti oxides belonging to the spinel solid solution (Fig. 4.3f) with ulvöspinel molecule ranging from 10 to 69%. They show a variable content of Ti (0.064-0.678 apfu), Mg (0.004-0.308 apfu), Al (0.106- 0.879 apfu), Mn (0.008-0.177 apfu) and a low Cr content (0-0.1 apfu).

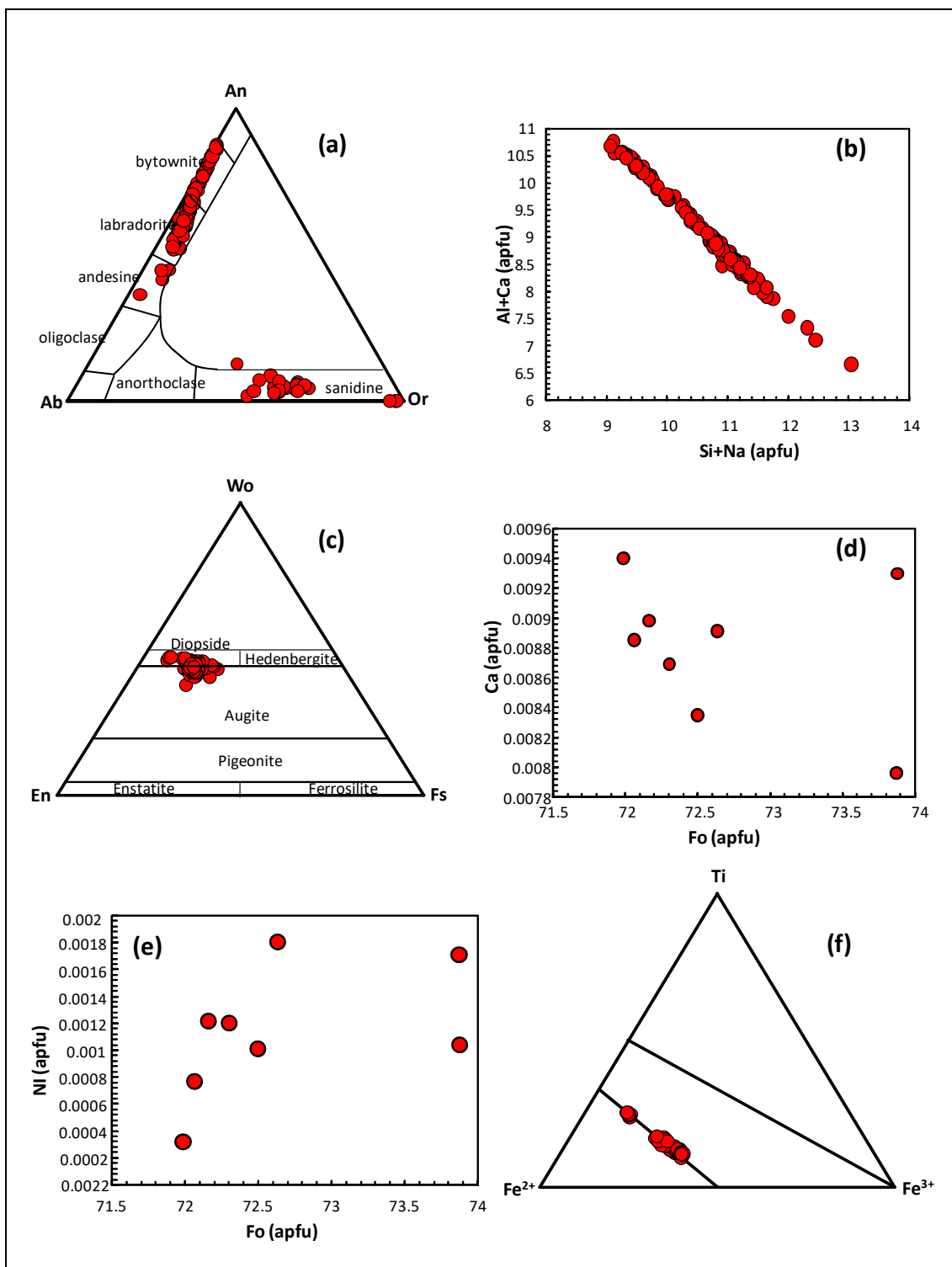


Fig. 4.3. Composition of the main mineral phases of the investigated Dolomite rock samples. a) Ternary diagram for plagioclase and alkali feldspar classification. b) Si+Na (apfu) vs. Al+Ca (apfu) diagram for plagioclase analyses. c) Ternary diagram for clinopyroxene and orthopyroxene classification. d) Ca (apfu) vs. Fo (apfu) diagram for olivine analyses. e) Ni (apfu) vs. Fo (apfu) diagram for olivine analyses. f) Ti₂O-FeO-Fe₂O₃ diagram for opaque minerals. The two tie-lines indicate spinel (lower) and rhombohedral (upper) phase solid solutions.

4.3. Whole-rock chemistry

Thirty-one representative samples of Dolomites volcanic rocks were analyzed for whole-rock chemistry. The results of these chemical analyses and CIPW normative minerals are reported in Table 4.2. In the same table, new whole-rock analyses of Recoaro (Vicentinian Alps) volcanic rocks (7 samples) and of the Monzoni (8 samples) and Predazzo (16) plutonic rocks are reported too. Major oxides and trace elements of the present and literature SATIR data (Southern Alps Triassic Igneous Rocks, a total of 1066 whole-rock analyses) is reported in Fig. 4.5 and 4.6. For sake of clarity, the same diagrams, with each single district at one time, are reported in Appendix 2.

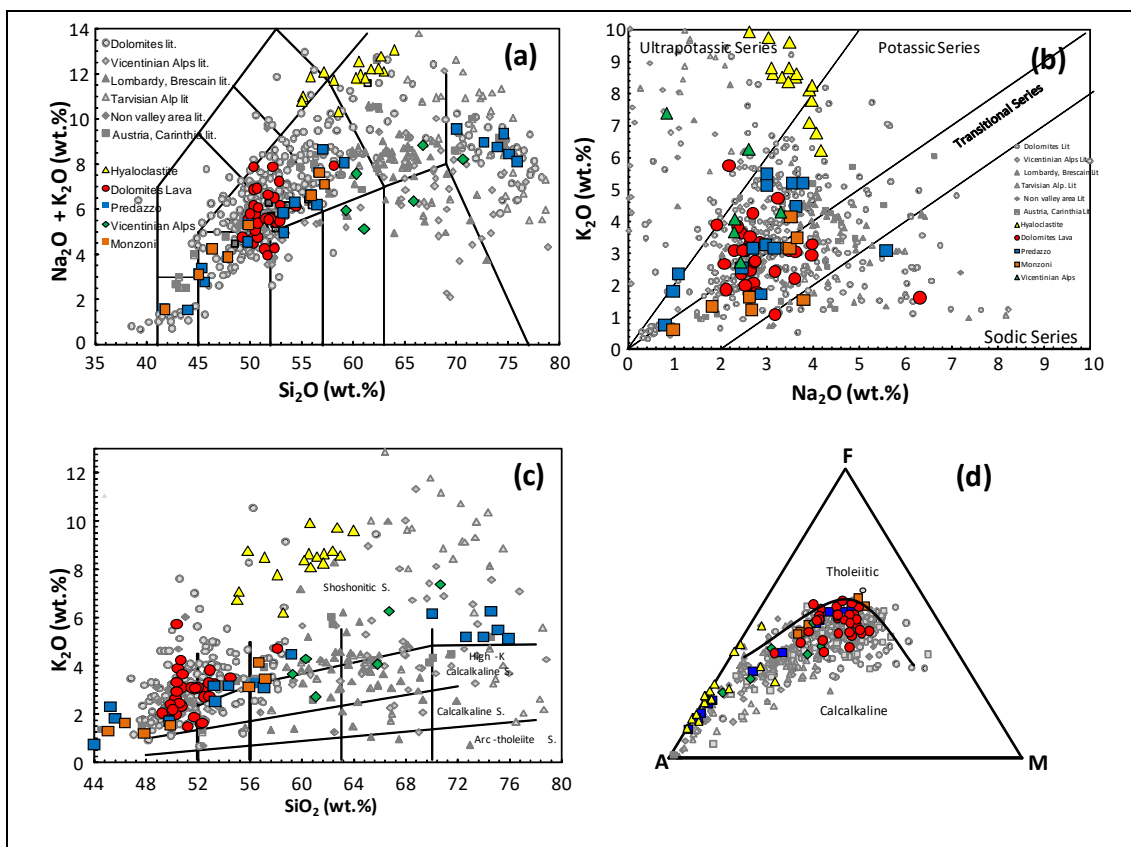


Fig. 4.4. Plots of whole-rock chemical data for the studied Dolomites volcanic rocks, Predazzo, Monzoni and Vicentian Alps, with literature SATIR (Southern Alps Triassic Igneous Rocks) and Carinthia rock samples reported for comparison. a) Total alkali vs. SiO_2 (TAS) diagram (Le Maitre, 2002). b) K_2O vs. Na_2O diagram defining the limit between the sodic series and the potassic series among the alkaline rocks. c) K_2O vs. SiO_2 classification (Peccerillo and Taylor, 1976) d) AFM (A = $\text{Na}_2\text{O} + \text{K}_2\text{O}$; F = FeO_{tot} ; M = MgO) ternary diagram with boundary curves dividing calc-alkaline and tholeiitic fields (Kuno, 1968). Data sources are as follows: Dolomites (Sacerdoti and Somavilla, 1962; Emiliani and Vespignani-Balzani, 1964; Paganelli and Tiburtini 1964; Bonarelli-Marzocchi et al., 1965; Del monte and Paganelli 1965; Simboli, 1966; Bonarelli-Marzocchi et al., 1967; Del Monte et al., 1967; Borsi and Ferrara, 1967; Paganelli, 1967; Emiliani and Vespignani-Balzani, 1968; Borsi et al., 1968; Lucchini et al 1969; Emiliani et al., 1970; Rossi, 1970; Lucchini and Simboli 1970; 1972; Fabbri and Paganelli, 1973, 1976; Ferrara et al., 1974; Rossi et al., 1974; Rossi et al., 1976; Castellarin et al., 1977; Lucchini and Morten, 1977, 1978; Calanchi et al., 1978; Petersen et al., 1980; Morandi et al., 1981; Lucchini et al., 1982; Sloman, 1989; Gasparotto and Simboli, 1991; Bonadiman et al., 1994; Nimis et al., 2012; Bianchini et al., 2018; Casetta et al., 2018a, 2018b), Vicentian Alps (De Vecchi et al., 1974; De Vecchi and De Zanche, 1982; De Vecchi and Sedea 1983), Lombardy (Cassinis and Zezza., 1982; Crisci et al., 1984; Armienti et al., 2003; Cassiniset al., 2008), Tarvisian Alps (Spadea, 1970; Lucchini et al., 1980; Gianolla, 1992), Non valley (Rossi et al., 1980), Austria, Carinthia (Visonà and Zanferrari, 2000; Miller et al., 2011), Dinarides (Bebien et al., 1978; Trubelja et al., 2004).

Sample	BEL 1	GAR 3	BUF2	AS2	PR20	LAT2	LAT5
Area	Dolomites	Dolomites	Dolomites	Dolomites	Dolomites	Dolomites	Dolomites
Locality	Belvedere	Cima Pape, Val di Gares	Val Giumela, Buffaure	Alpe di Siusi	Val di S. Nicolo	Latemar	Latemar
Latitude	46°26'38.00"N	46°18'16.00"N	46°26'23.00"N	46°31'38.00"N	46°25'8.20"N	46°21'2.00"N	46°21'36.00"N
Longitude	12° 0'4.00"E	11°53'9.10"E	11°44'5.90"E	11°35'44.00"E	11°43'38.90"E	11°33'27.00"E	11°33'33.00"E
Rock Type	Subalkali Basalt	Subalkali Basalt	Subalkali Basalt	K-Alkali Basalt	K-Alkali Basalt	K-Alkali Basalt	K-Alkali Basalt
SiO ₂	47.66	50.18	50.36	49.44	48.66	48.83	48.33
TiO ₂	1.34	0.87	0.93	0.91	1.14	1.31	1.17
Al ₂ O ₃	17.81	14.18	14.60	14.04	16.44	17.78	16.65
Fe ₂ O ₃	9.98	9.48	11.09	12.85	10.55	10.32	9.13
MnO	0.19	0.21	0.17	0.20	0.19	0.20	0.13
MgO	5.78	6.74	5.26	5.44	5.27	5.68	6.30
CaO	9.02	11.51	10.78	10.42	9.77	9.13	8.61
Na ₂ O	2.62	3.10	2.06	2.05	2.44	2.73	2.33
K ₂ O	1.98	1.06	1.81	2.61	1.93	1.75	2.23
P ₂ O ₅	0.40	0.32	0.34	0.36	0.34	0.37	0.37
L.O.I.	2.90	2.30	1.80	2.15	2.60	2.34	3.73
Total	99.68	99.95	99.20	100.47	99.32	100.44	98.98
Mg#	0.57	0.62	0.52	0.49	0.53	0.55	0.61
Rb	50	18	34	74	51	50	53
Sr	699	596	794	758	657	830	674
Ba	376	222	466	448	351	432	443
Cs	0.9		1.3	0.6		3.7	
Sc	25	35	30	36	29	25	27
V	251	248	252	302	286	258	264
Cr	110	330	100	90	90	100	180
Co	33	39	38	42	35	30	29
Ni	50	70	30	30	50	60	80
Cu	90	90	120	120	100	90	90
Zn	100	110	100	120	110	90	90
Y	22	19	21	20	18	21	19
Zr	153	110	130	118	113	148	136
Nb	8	6	9	7	7	9	9
Hf	3.2	2.6	2.9	3	2.7	3.2	3.1
Ta	1	0.9	0.6	0.5	0.6	0.5	0.5
La	24.4	24.3	26.9	25.7	21.1	22.4	22.7
Ce	52.9	50.4	54.6	53.1	44.4	46.8	46.8
Pr	6.65	5.99	6.69	6.63	5.69	5.89	5.88
Nd	27.7	25.4	27.2	27.3	24.4	24.8	23.8
Sm	6	5.6	6.1	6	5.7	5.3	5.1
Eu	1.79	1.43	1.6	1.67	1.62	1.67	1.54
Gd	5.3	5	5.1	5.3	5	4.8	4.5
Tb	0.8	0.8	0.7	0.8	0.7	0.7	0.6
Dy	4.4	4.4	4.3	4.2	4.1	4	3.8
Ho	0.8	0.8	0.8	0.8	0.8	0.8	0.7
Er	2.4	2.3	2.3	2.4	2.3	2.4	2.1
Tm	0.32	0.34	0.34	0.32	0.29	0.32	0.3
Yb	2.2	2	2.1	2.1	2.1	2.1	1.8
Lu	0.33	0.31	0.35	0.33	0.31	0.33	0.28
Pb	11	8	12	15	8	7	6
Th	4.2	6.4	6.2	6.5	3.8	3.5	4.4
U	1	1.5	1.5	1.8	1.1	1	1.2
Q	0.00	0.00	0.81	0.00	0.00	0.00	0.00
C	0.00	0.00	0.00	0.00	0.00	0.00	0.00
or	12.09	6.41	10.98	15.69	11.79	10.54	13.84
ab	22.91	26.86	17.89	17.64	21.34	23.55	20.70
an	32.02	22.17	25.92	21.76	29.16	31.69	29.80
ne	0.00	0.00	0.00	0.00	0.00	0.00	0.00
-wo	4.81	14.27	11.15	11.87	7.79	5.02	5.22
-en	2.57	8.03	5.34	5.35	3.86	2.62	2.97
-fs	2.09	5.65	5.65	6.45	3.77	2.26	2.03
di	9.47	27.95	22.14	23.66	15.42	9.89	10.22
-en	1.88	0.50	8.11	2.59	4.39	4.10	6.91
-fs	1.53	0.35	8.57	3.13	4.28	3.54	4.72
hy	3.40	0.85	16.68	5.72	8.68	7.64	11.63
-fo	7.31	6.07	0.00	4.09	3.72	5.40	4.62
-fa	6.54	4.71	0.00	5.43	4.00	5.14	3.48
ol	13.85	10.78	0.00	9.52	7.72	10.53	8.10
mt	1.78	1.67	1.96	2.25	1.88	1.81	1.65
il	2.63	1.69	1.81	1.75	2.23	2.54	2.33
ap	0.98	0.78	0.83	0.87	0.83	0.89	0.92

Table 4.2. XRF major- and trace element concentrations (respectively in wt.% and in ppm) for a representative studied samples from Dolomites volcanic rocks,

Predazzo, Monzoni and Vicentinian Alps. LOI = loss on ignition (wt.%); Mg# = molar Mg/(Fetot + Mg + Mn).

Sample	BUF4	AS7	AS8	MAR1	BUL 2	GAR 1	PR 28
Area	Dolomites	Dolomites	Dolomites	Dolomites	Dolomites	Dolomites	Dolomites
Locality	Val Giumela, Buffaure	Alpe di Siusi	Alpe di Siusi	Marmolada	Bulla	Cima Pape, Val di Gares	Lago di Alleghe
Latitude	46°26'7.00"N	46°32'2.00"N	46°31'30.00"N	46°27'19.00"N	46°32'58.80"N	46°18'16.00"N	46°24'6.00"N
Longitude	11°42'30.80"E	11°34'60.00"E	11°34'55.00"E	11°53'33.00"E	11°37'55.20"E	11°53'9.10"E	12° 1'1.60"E
Rock Type	Potassic Trachybasalt	Potassic Trachybasalt	Potassic Trachybasalt	Potassic Trachybasalt	Potassic Trachybasalt	Potassic Trachybasalt	Mugearitec (Tuff)
SiO ₂	50.03	48.61	49.32	48.05	48.86	47.97	49.10
TiO ₂	1.12	0.90	0.89	1.12	0.87	1.26	1.17
Al ₂ O ₃	17.44	15.06	15.20	18.74	14.69	17.09	16.79
Fe ₂ O ₃	11.16	11.47	11.86	10.33	12.00	9.63	9.38
MnO	0.16	0.16	0.13	0.14	0.19	0.14	0.17
MgO	4.08	7.46	5.69	4.50	5.83	6.30	4.79
CaO	9.55	6.69	8.43	7.69	8.27	7.57	4.95
Na ₂ O	2.61	1.85	2.23	3.06	2.77	3.46	5.94
K ₂ O	2.43	3.75	3.00	2.33	3.22	2.11	1.51
P ₂ O ₅	0.41	0.38	0.40	0.46	0.38	0.37	0.45
L.O.I.	1.44	4.41	2.98	2.79	2.90	3.80	5.76
Total	100.44	100.75	100.13	99.21	99.99	99.70	99.99
Mg#	0.45	0.59	0.52	0.49	0.52	0.60	0.53
Rb	58	51	73	31	65	41	28
Sr	781	537	752	904	1091	510	398
Ba	501	726	509	598	534	377	470
Cs	0.5			0.8		2.2	7
Sc	21	30	29	18	31	26	19
V	261	283	273	249	272	243	189
Cr	80	70	60	100	80	80	30
Co	32	41	37	36	41	30	27
Ni	30	20		40	30	40	
Cu	130	120	140	80	130	70	50
Zn	110	110	110	130	120	90	100
Y	22	23	21	24	22	22	24
Zr	150	125	127	165	120	154	166
Nb	9	8	8	11	6	8	11
Hf	3.4	3	3	3.6	2.8	3.4	3.8
Ta	0.6	0.5	0.5	0.6	0.9	0.9	0.9
La	28.6	26.7	27.6	30.1	26.4	21.5	31
Ce	59	56	57.5	62.9	55.9	46.7	63.4
Pr	7.26	6.99	7.04	7.67	6.81	5.81	7.5
Nd	30.2	28.8	29.1	30.6	28.1	25.6	31.2
Sm	6.5	6.3	6.3	6.5	6.2	5.2	6.2
Eu	1.79	1.65	1.68	1.9	1.59	1.63	1.82
Gd	5.8	5.5	5.6	5.6	5.5	5.1	5.9
Tb	0.8	0.8	0.8	0.8	0.8	0.7	0.8
Dy	4.6	4.7	4.4	4.5	4.5	4.4	4.8
Ho	0.9	0.9	0.8	0.9	0.9	0.9	0.9
Er	2.5	2.4	2.3	2.4	2.3	2.3	2.4
Tm	0.35	0.34	0.35	0.35	0.32	0.35	0.36
Yb	2.4	2.1	2	2.2	2.2	2.1	2.4
Lu	0.34	0.33	0.34	0.34	0.33	0.31	0.37
Pb	12	8	8	10	29	21	
Th	5.9	6.9	7.3	8.3	6.6	3.2	5
U	1.5	2.1	2.2	2	1.7	0.9	1.2
Q	0.00	0.00	0.00	0.00	0.00	0.00	0.00
C	0.00	0.00	0.00	0.00	0.00	0.00	0.00
or	14.50	23.00	18.25	14.28	19.60	13.00	9.47
ab	22.31	16.25	19.42	26.85	20.04	26.99	39.63
an	28.98	22.54	23.27	31.65	18.68	25.93	15.59
ne	0.00	0.00	0.00	0.00	2.22	1.92	7.42
-wo	6.75	3.90	7.14	2.00	8.78	4.47	3.07
-en	2.89	2.12	3.43	0.94	4.22	2.50	1.55
-fs	3.87	1.64	3.60	1.04	4.42	1.79	1.45
di	13.51	7.66	14.17	3.99	17.42	8.76	6.07
-en	3.07	5.18	4.02	0.88	0.00	0.00	0.00
-fs	4.11	4.01	4.22	0.98	0.00	0.00	0.00
hy	7.17	9.19	8.23	1.86	0.00	0.00	0.00
-fo	3.02	8.40	5.01	6.87	7.52	9.71	7.78
-fa	4.45	7.17	5.79	8.41	8.68	7.68	7.99
ol	7.47	15.56	10.80	15.28	16.20	17.40	15.77
mt	1.94	2.05	2.11	1.85	2.13	1.73	1.72
il	2.15	1.78	1.73	2.20	1.71	2.50	2.36
ap	0.98	0.93	0.98	1.13	0.93	0.91	1.13

Table 4.2 (continued)

Sample	MAR2	BUF1	BUF3	PR17	AS 1	AS3	AS 9	DUR 2
Area	Dolomites	Dolomites	Dolomites	Dolomites	Dolomites	Dolomites	Dolomites	Dolomites
Locality	Marmolada	Val Giumela, Buffaure	Val Giumela, Buffaure	Forno, Fiemme valley	Alpe di Siusi	Alpe di Siusi	Alpe di Siusi	Val di Duron
Latitude	46°27'6.00"N	46°26'26.20"N	46°26'11.30"N	46°21'15.00"N	46°31'30.00"N	46°31'26.00"N	46°32'27.50"N	46°29'33.54"N
Longitude	11°54'14.00"E	11°44'32.70"E	11°42'57.00"E	11°37'59.70"E	11°35'29.00"E	11°35'44.00"E	11°36'13.50"E	11°39'58.28"E
Rock Type	Shoshonite	Shoshonite	Shoshonite	Shoshonite	Shoshonite	Shoshonite	Shoshonite	Shoshonite
SiO ₂	51.06	52.18	51.12	51.48	47.50	49.74	48.42	49.55
TiO ₂	1.08	0.83	1.06	1.02	0.82	0.88	0.93	0.81
Al ₂ O ₃	19.28	16.52	17.75	18.37	15.30	14.51	14.94	15.26
Fe ₂ O ₃	8.03	10.57	9.60	8.88	10.64	12.25	11.83	10.06
MnO	0.11	0.17	0.16	0.14	0.10	0.24	0.16	0.11
MgO	2.93	3.17	2.33	2.94	7.97	6.60	7.11	5.51
CaO	8.19	8.41	9.64	8.75	4.21	7.37	5.77	7.67
Na ₂ O	3.39	2.58	2.65	2.67	2.06	2.40	3.82	3.46
K ₂ O	2.99	3.19	2.64	2.68	5.41	3.57	2.83	2.92
P ₂ O ₅	0.42	0.45	0.48	0.44	0.37	0.37	0.38	0.38
L.O.I.	2.60	1.45	2.03	2.63	6.18	2.83	4.40	3.31
Total	100.08	99.52	99.46	100.00	100.60	100.76	100.60	99.04
Mg#	0.45	0.40	0.35	0.43	0.63	0.55	0.57	0.55
Rb	69	80	59	64	112	82	40	41
Sr	923	961	883	885	371	609	460	555
Ba	554	589	541	537	586	637	634	565
Cs		0.9		0.8	1.4	0.6		0.7
Sc	15	17	18	15	26	32	32	27
V	219	185	228	195	239	276	297	229
Cr	70		30		60	70	90	110
Co	22	32	28	22	36	39	44	33
Ni	80		30		20	20	30	30
Cu	180	140	140	140	170	130	110	120
Zn	240	120	110	100	120	110	140	110
Y	24	23	24	21	21	20	21	20
Zr	147	153	163	154	151	123	122	128
Nb	10	9	10	11	10	8	7	7
Hf	3.6	3.4	3.5	3.6	3.4	2.8	3.1	3.1
Ta	0.6	0.7	0.7	0.8	0.9	0.5	0.9	0.9
La	32.7	34.1	31.7	31.8	31.1	26.1	25.6	28.6
Ce	64.9	68.3	64.4	64.8	64.3	53.9	55.2	59.1
Pr	7.74	8.35	7.9	8.01	7.59	6.71	6.75	7.16
Nd	30	33.4	32.4	31.9	30.7	27.6	29.6	28.9
Sm	6	7.1	6.9	6.7	6.7	5.9	6.7	6.1
Eu	1.78	1.81	1.87	1.88	1.75	1.53	1.65	1.61
Gd	5.2	6	6	5.6	6.3	5.2	5.8	5.3
Tb	0.7	0.8	0.8	0.8	0.8	0.7	0.8	0.8
Dy	4.4	4.6	4.6	4.8	4.5	4.1	4.5	4.5
Ho	0.9	0.9	0.9	0.9	0.9	0.8	0.8	0.8
Er	2.5	2.5	2.5	2.5	2.5	2.3	2.4	2.4
Tm	0.35	0.36	0.37	0.34	0.34	0.31	0.34	0.33
Yb	2.2	2.4	2.4	2.3	2.1	2.1	2.1	2.2
Lu	0.35	0.37	0.36	0.37	0.34	0.32	0.31	0.33
Pb	18	37	13	11	12	12	11	17
Th	7.6	8.5	6.5	6.9	7.6	6.7	6.7	7.6
U	2.2	2.3	1.7	1.7	1.9	1.9	1.9	2
Q	0.00	0.62	1.03	1.22	0.00	0.00	0.00	0.00
C	0.00	0.00	0.00	0.00	0.00	0.00	0.00	0.00
or	18.13	19.22	16.01	16.26	33.87	21.54	17.39	18.02
ab	29.42	22.26	23.01	23.20	14.05	20.74	25.85	25.75
an	29.30	24.55	29.50	31.04	17.51	18.66	15.86	18.26
ne	0.00	0.00	0.00	0.00	2.39	0.00	4.20	2.61
-wo	4.00	6.26	6.84	4.42	0.86	6.77	4.72	7.89
-en	1.75	2.37	2.35	1.81	0.49	3.39	2.49	4.02
-fs	2.24	4.00	4.68	2.64	0.33	3.23	2.09	3.67
di	7.98	12.63	13.86	8.87	1.68	13.39	9.31	15.58
-en	0.41	5.68	3.61	5.71	0.00	1.21	0.00	0.00
-fs	0.52	9.57	7.19	8.29	0.00	1.15	0.00	0.00
hy	0.93	15.24	10.80	14.00	0.00	2.35	0.00	0.00
-fo	3.73	0.00	0.00	0.00	14.39	8.54	11.15	7.23
-fa	5.27	0.00	0.00	0.00	10.60	8.94	10.28	7.27
ol	9.00	0.00	0.00	0.00	25.00	17.48	21.43	14.50
mt	1.42	1.86	1.70	1.57	1.94	2.16	2.12	1.81
il	2.09	1.61	2.07	1.98	1.66	1.71	1.84	1.61
ap	1.02	1.09	1.17	1.07	0.93	0.89	0.94	0.94

Table 4.2 (continued)

Sample	DUR 3	DUR 4	TIR 1	TIR 2	LAT 3	CIA 1	PR 1	PR23
Area	Dolomites	Dolomites	Dolomites	Dolomites	Dolomites	Dolomites	Dolomites	Dolomites
Locality	Val di Duron	Val di Duron	Alpe di Tires	Alpe di Tires	Latemar	Ciampedie	Mezzavalle, Predazzo	Val di Viezzena, Predazzo
Latitude	46°29'38.30"N	46°29'38.93"N	46°29'48.70"N	46°29'59.60"N	46°20'51.00"N	46°25'58.10"N	46°20'28.80"N	46°19'36.00"N
Longitude	11°40'33.90"E	11°40'41.44"E	11°38'39.70"E	11°38'58.70"E	11°33'28.00"E	11°39'36.50"E	11°36'47.00"E	11°38'55.00"E
Rock Type	Shoshonite	Shoshonite	Shoshonite	Shoshonite	Shoshonite	Shoshonite	Shoshonite	Basaltic andesite
SiO₂	51.13	50.93	52.43	51.48	51.78	49.33	49.77	52.05
TiO₂	0.81	0.83	0.82	0.82	1.14	0.85	1.07	1.20
Al₂O₃	15.22	15.51	15.97	15.50	19.47	14.73	17.86	18.07
Fe₂O₃	10.92	11.21	6.34	11.09	7.35	9.23	10.49	10.97
MnO	0.19	0.19	0.13	0.16	0.11	0.16	0.16	0.13
MgO	4.59	4.60	4.03	4.64	2.88	3.25	3.59	3.99
CaO	9.62	9.72	10.16	9.76	7.78	9.58	7.99	8.37
Na₂O	2.48	2.51	2.54	2.46	3.91	2.21	2.65	2.63
K₂O	3.05	3.06	3.38	3.05	3.22	3.57	4.16	1.63
P₂O₅	0.40	0.41	0.49	0.41	0.40	0.33	0.44	0.38
L.O.I.	1.30	1.21	3.27	1.32	2.49	7.28	2.32	1.26
Total	99.72	100.20	99.56	100.70	100.50	100.50	100.50	100.68
Mg#	0.49	0.48	0.59	0.48	0.47	0.44	0.43	0.45
Rb	67	70	68	68	77	88	139	64
Sr	872	891	911	872	1087	599	825	652
Ba	529	526	657	520	490	487	723	197
Cs		0.6		0.6	5.3	1.7	3.3	5.9
Sc	28	28	29	29	17	34	19	26
V	230	234	237	232	219	252	246	269
Cr	80	80	90	90	30	180	30	
Co	39	39	27	39	17	28	32	23
Ni	20	20		20	20	30	20	20
Cu	120	120	120	120	50	110	150	
Zn	120	120	90	120	50	100	110	80
Y	21	21	22	21	24	25	23	16
Zr	130	126	134	129	201	125	162	120
Nb	7	6	7	7	11	8	12	6
Hf	2.9	2.9	3.2	2.9	3.8	3.3	3.8	2.6
Ta	0.9	0.9	1	0.9	0.9	0.8	0.9	0.4
La	28.8	28.7	33.6	28.5	29.3	31.1	34.5	17.7
Ce	60.7	59.9	67.6	59.4	62.2	64.4	69.5	33.8
Pr	7.34	7.39	7.93	7.31	7.35	7.6	8.04	4.13
Nd	30.1	29.4	32.8	29.9	30.2	31.4	31.7	17.6
Sm	6.4	6.4	6.7	6.2	6.6	7.3	7.2	4.1
Eu	1.61	1.64	1.7	1.59	1.64	1.79	1.89	1.28
Gd	5.6	5.6	5.7	5.6	6.2	6.5	6.4	3.9
Tb	0.8	0.8	0.8	0.8	0.8	0.9	0.9	0.6
Dy	4.4	4.7	4.7	4.5	4.7	4.9	4.6	3.6
Ho	0.9	0.9	0.9	0.9	0.9	0.9	0.9	0.7
Er	2.4	2.5	2.3	2.5	2.6	2.6	2.6	1.9
Tm	0.34	0.36	0.35	0.34	0.37	0.38	0.36	0.29
Yb	2.3	2.2	2.3	2.1	2.4	2.4	2.2	1.8
Lu	0.32	0.32	0.33	0.35	0.35	0.34	0.34	0.29
Pb	19	20	13	17	6	17	16	
Th	7.6	7.5	7.9	7.3	5.3	7.5	7.1	2.4
U	2	2	2.2	2	1.3	1.9	1.6	0.7
Q	0.00	0.00	0.33	0.00	0.00	0.00	0.00	3.10
C	0.00	0.00	0.00	0.00	0.00	0.00	0.00	0.00
or	18.31	18.27	20.74	18.14	19.41	22.62	25.04	9.69
ab	21.32	21.46	22.32	20.95	29.75	20.05	19.04	22.38
an	21.74	22.25	23.05	22.38	26.59	21.16	25.01	32.88
ne	0.00	0.00	0.00	0.00	2.16	0.00	2.06	0.00
-wo	10.07	9.93	10.85	9.87	4.22	11.48	5.19	2.67
-en	4.53	4.41	5.98	4.44	1.94	4.78	2.15	1.15
-fs	5.48	5.47	4.47	5.38	2.25	6.75	3.07	1.52
di	20.08	19.81	21.29	19.69	8.41	23.02	10.42	5.34
-en	2.72	1.44	4.45	2.86	0.00	1.67	0.00	8.85
-fs	3.29	1.79	3.32	3.46	0.00	2.35	0.00	11.72
hy	6.01	3.23	7.77	6.32	0.00	4.02	0.00	20.57
-fo	3.06	4.01	0.00	3.04	3.77	1.56	4.87	0.00
-fa	4.09	5.48	0.00	4.06	4.81	2.43	7.68	0.00
ol	7.15	9.48	0.00	7.10	8.58	4.00	12.55	0.00
mt	1.91	1.95	1.14	1.92	1.29	1.71	1.84	1.90
il	1.56	1.59	1.61	1.56	2.20	1.73	2.07	2.28
ap	0.96	0.98	1.21	0.98	0.97	0.84	1.06	0.91

Table 4.2 (continued)

CHAPTER FOUR

PETROLOGICAL AND GEOCHEMICAL STUDIES

Sample	PR11A	PA12	PR10	PR12	PR8	PR15	PR13	PR4
Area	Dolomites	Dolomites	Dolomites	Dolomites	Dolomites	Dolomites	Dolomites	Dolomites
Locality	Malgola, Predazzo	Predazzo	Malgola, Predazzo	Malgola, Predazzo	Predazzo	Val Deserta, Predazzo	Predazzo	Predazzo
Latitude	46°18'16.30"N	46°18'16.30"N	46°18'16.30"N	46°18'16.30"N	46°18'52.70"N	46°18'46.00"N	46°18'23.60"N	46°19'53.00"N
Longitude	11°36'11.40"E	11°36'11.26"E	11°36'11.40"E	11°36'11.40"E	11°35'44.50"E	11°37'40.90"E	11°36'9.10"E	11°36'15.10"E
Rock Type	Clinpyroxenite	Clinpyroxenite	Cumilitic Gabbro	Monzogabbro	Diorite	Monzodiorite	Monzodiorite	Monzonite
SiO₂	43.96	44.80	45.44	53.16	48.04	56.09	58.32	52.91
TiO₂	1.50	0.80	0.80	0.86	1.11	0.97	0.76	0.89
Al₂O₃	5.19	17.11	16.29	14.95	17.24	16.70	17.91	15.75
Fe₂O₃	20.86	13.90	14.26	11.15	11.45	9.08	6.49	11.16
MnO	0.26	0.19	0.19	0.20	0.19	0.17	0.15	0.19
MgO	10.98	7.11	7.53	4.84	5.10	3.28	2.21	3.96
CaO	15.56	11.63	12.33	9.26	8.55	6.47	4.50	8.31
Na₂O	0.80	1.07	0.97	2.45	2.78	2.95	3.57	2.68
K₂O	0.74	2.31	1.81	2.52	1.65	3.24	4.41	3.14
P₂O₅	0.04	0.03	0.04	0.35	0.47	0.38	0.26	0.38
L.O.I.	0.47	1.30	1.09	0.87	2.46	0.96	1.44	0.73
Total	100.36	100.20	100.75	100.62	99.04	100.29	100.00	100.10
Mg#	0.54	0.53	0.54	0.49	0.50	0.45	0.43	0.44
Rb	30	117	92	87	86	124	155	105
Sr	217	620	628	793	906	756	741	712
Ba	126	273	213	461	282	594	670	462
Cs	3.1	10.5	9.7	4.3	13.2	7.7	8.2	3.7
Sc	75	38	38	27	22	17	12	24
V	738	425	414	238	259	175	118	219
Cr	210	100	90	70	40		30	30
Co	79	57	62	37	32	22	15	34
Ni	60	60	60	20	30			
Cu	160		20	110	70	40	40	90
Zn	120	100	110	120	90	110	100	110
Y	8	12	8	20	18	25	24	23
Zr	64	46	45	111	108	195	240	141
Nb	3	3	3	9	8	12	16	11
Hf	1.8	1.5	1.3	2.8	2.7	4.8	5.7	3.3
Ta	0.3	0.3	0.2	0.7	0.6	1	1.2	0.8
La	10.7	10.6	10.5	29.6	29.2	38.7	40.8	35.6
Ce	28.8	23.8	23.8	60.4	60.2	77.6	82.3	72.1
Pr	4.1	3.16	3.24	7.5	7.47	9.32	9.34	8.88
Nd	18.5	14.3	14.3	30.5	31.1	37	35.7	35
Sm	4.8	3.8	3.7	6.5	6.7	7.5	7	7.4
Eu	1.05	1.07	1.06	1.62	1.88	1.75	1.73	1.72
Gd	4.5	3.3	3.3	5.9	5.6	6.4	5.7	6.3
Tb	0.7	0.5	0.5	0.8	0.8	1	0.8	0.9
Dy	4	2.8	2.8	4.6	4.5	5.2	4.7	4.9
Ho	0.8	0.6	0.6	0.9	0.9	1.1	0.9	1
Er	2.1	1.5	1.5	2.5	2.4	2.9	2.5	2.7
Tm	0.3	0.22	0.21	0.33	0.34	0.43	0.4	0.38
Yb	1.9	1.4	1.4	2.2	2	2.8	2.7	2.4
Lu	0.28	0.22	0.2	0.36	0.34	0.46	0.4	0.38
Pb	8	6	6	23	19	22	29	18
Th	2.2	1.8	1.7	8.1	5.3	9.8	12.2	8.7
U	0.6	0.4	0.5	1.9	1.2	2.4	2.8	1.9
Q	0.00	0.00	0.00	1.39	0.00	5.34	5.15	0.00
C	0.00	0.00	0.00	0.00	0.00	0.00	0.00	0.00
or	2.41	13.80	10.73	14.93	10.10	19.28	26.44	18.67
ab	0.00	4.63	7.34	20.78	24.35	25.13	30.64	22.82
an	8.39	35.43	34.87	22.41	30.74	22.91	20.11	21.81
ne	3.67	2.45	0.49	0.00	0.00	0.00	0.00	0.00
-wo	28.65	9.47	10.96	8.92	4.18	2.88	0.34	7.17
-en	14.29	4.63	5.42	4.08	1.96	1.23	0.14	2.98
-fs	13.76	4.68	5.32	4.77	2.17	1.66	0.20	4.23
di	56.70	18.77	21.70	17.76	8.30	5.77	0.69	14.39
-en	0.00	0.00	0.00	8.01	4.88	7.00	5.44	6.90
-fs	0.00	0.00	0.00	9.36	5.41	9.46	7.76	9.81
hy	0.00	0.00	0.00	17.36	10.28	16.45	13.20	16.71
-fo	9.17	9.30	9.39	0.00	4.43	0.00	0.00	0.03
-fa	9.73	10.36	10.15	0.00	5.41	0.00	0.00	0.05
ol	18.89	19.66	19.53	0.00	9.83	0.00	0.00	0.08
mt	3.60	2.42	2.47	1.93	2.04	1.58	1.14	1.94
il	2.85	1.53	1.52	1.65	2.17	1.85	1.45	1.71
ap	0.09	0.07	0.10	0.83	1.15	0.91	0.62	0.91

Table 4.2 (continued)

Sample	PA15	PA16	PA18	PA20	PA21	PA22A	PA23	PA24
Area	Dolomites	Dolomites	Dolomites	Dolomites	Dolomites	Dolomites	Dolomites	Dolomites
Locality	Monzoni	Monzoni	Monzoni	Monzoni	Monzoni	Monzoni	Monzoni	Monzoni
Latitude	46°23'25.14"N	46°23'20.53"N	46°23'41.81"N	46°23'30.21"N	46°23'34.71"N	46°23'32.43"N	46°23'30.04"N	46°23'31.48"N
Longitude	11°45'4.00"E	11°44'57.47"E	11°44'39.81"E	11°44'30.07"E	11°44'10.35"E	11°43'34.29"E	11°43'8.40"E	11°43'3.48"E
Rock Type	Gabbro	Gabbro (cumulate)	Olivine gabbros	Olivine gabbros	Monzogabbros	Monzonites	Monzonites	Monzonites
SiO ₂	44.51	40.94	48.85	48.21	46.43	55.51	56.39	56.08
TiO ₂	1.32	1.23	1.26	1.37	1.60	0.90	0.87	0.86
Al ₂ O ₃	12.22	18.19	17.40	16.85	16.85	17.19	17.34	17.43
Fe ₂ O ₃	15.62	14.42	10.83	12.52	13.94	9.06	8.24	8.51
MnO	0.24	0.14	0.17	0.20	0.21	0.19	0.15	0.16
MgO	9.81	5.63	5.32	6.30	5.89	2.89	2.61	2.70
CaO	11.91	15.91	8.55	11.03	10.46	6.56	5.64	5.25
Na ₂ O	1.79	0.95	3.72	2.69	2.64	3.47	3.60	3.47
K ₂ O	1.30	0.60	1.50	1.22	1.62	3.12	3.43	4.09
P ₂ O ₅	0.11	0.06	0.39	0.34	0.69	0.36	0.33	0.37
L.O.I.	0.84	1.35	2.14	0.10	0.33	1.05	1.28	1.65
Total	99.68	99.42	100.10	100.80	100.70	100.30	99.88	100.60
Mg#	0.59	0.47	0.52	0.53	0.49	0.42	0.42	0.42
Rb	38	26	39	25	38	127	138	180
Sr	620	1008	1108	891	1079	819	810	821
Ba	239	85	463	343	425	557	578	582
Cs	2.8	2.9	2.6	0.9	1.5	3.4	5.7	6.3
Sc	47	40	24	35	26	15	14	13
V	483	527	283	277	367	159	146	157
Cr	150	30	70	80	90	20	20	20
Co	60	49	30	41	42	22	18	19
Ni	70	60	30	40	40			
Cu	40	630	40	20	70	50	50	60
Zn	110	80	100	110	120	100	90	60
Y	15	9	17	18	19	27	26	26
Zr	82	44	96	64	93	167	188	190
Nb	5	2	7	6	8	12	12	13
Hf	2.4	1.7	2.3	2	2.6	3.9	4.8	4.7
Ta	0.4	0.2	0.5	0.5	0.5	1.1	1	1
La	13.2	8.2	23.7	21.7	26.3	36.7	35	36.2
Ce	28.9	19	49.5	45.6	55.9	77	73	74.7
Pr	3.77	2.57	5.99	5.9	6.93	9.14	8.73	8.89
Nd	17.2	12.6	25.8	25.7	29.6	37.6	34.6	36
Sm	4.4	3.1	5.8	5.7	6.4	7.4	6.7	7.1
Eu	1.28	0.99	1.91	1.83	1.95	1.79	1.8	1.65
Gd	4.5	3	5	5.3	5.3	6.6	6.2	6.2
Tb	0.7	0.4	0.7	0.7	0.8	1	0.9	1
Dy	3.6	2.4	3.8	4	4.3	5.5	5.1	5.4
Ho	0.7	0.5	0.7	0.7	0.8	1	1	1
Er	1.9	1.2	1.9	2.1	2.1	3	2.7	2.8
Tm	0.27	0.17	0.27	0.3	0.31	0.44	0.39	0.41
Yb	1.7	1	1.8	1.8	1.8	2.8	2.5	2.7
Lu	0.25	0.17	0.27	0.26	0.28	0.46	0.43	0.43
Pb	12	11	18	6	8	12	17	12
Th	2.5	1.7	3	1.3	3.3	9.6	9.1	8.6
U	0.6	0.5	0.7	0.3	0.8	2.6	2.6	1.9
Q	0.00	0.00	0.00	0.00	0.00	2.72	3.81	2.10
C	0.00	0.00	0.00	0.00	0.00	0.00	0.00	0.00
or	7.77	0.00	9.05	7.16	9.54	18.57	20.56	24.43
ab	6.83	0.00	29.45	21.47	18.29	29.58	30.89	29.68
an	21.72	44.45	26.89	30.08	29.24	22.28	21.32	20.12
ne	4.60	4.44	1.45	0.61	2.15	0.00	0.00	0.00
-wo	15.59	13.24	5.76	9.20	7.51	3.40	2.03	1.57
-en	8.39	5.82	2.85	4.59	3.48	1.35	0.81	0.62
-fs	6.69	7.39	2.79	4.42	3.96	2.09	1.25	0.97
di	30.66	26.45	11.41	18.21	14.95	6.84	4.09	3.16
-en	0.00	0.00	0.00	0.00	0.00	5.90	5.78	6.17
-fs	0.00	0.00	0.00	0.00	0.00	9.16	8.92	9.57
hy	0.00	0.00	0.00	0.00	0.00	15.07	14.70	15.75
-fo	11.45	5.94	7.47	7.70	7.81	0.00	0.00	0.00
-fa	10.06	8.31	8.06	8.17	9.78	0.00	0.00	0.00
ol	21.51	14.25	15.53	15.87	17.59	0.00	0.00	0.00
mt	2.73	2.54	1.91	2.14	2.40	1.57	1.44	1.48
il	2.53	2.38	2.43	2.59	3.03	1.73	1.68	1.65
ap	0.26	0.14	0.94	0.80	1.63	0.86	0.79	0.89

Table 4.2 (continued)

Sample	HA 7	HA 1	HA 19	HA 17	HA 13	HA 9
Area	Vicentinian Alps	Vicentinian Alps	Vicentinian Alps	Vicentinian Alps	Vicentinian Alps	Vicentinian Alps
Locality	Val di Leder, Posina	Collegio, Laghi	Trail to Busi, Schio	Contrà Lovati, Schio	1 Km from Passo Xomo toward the South, Posina	Bragioli, Posina
Latitude	45°48'4.00"N	45°49'46.12"N	45°45'9.52"N	45°45'29.57"N	45°46'21.30"N	45°48'23.09"N
Longitude	11°14'58.00"E	11°16'43.40"E	11°21'50.43"E	11°22'6.45"E	11°13'53.41"E	11°16'19.88"E
Rock Type	Andesite	Andesite	Latite	Dacite	Trachydacite	Rhyolite
SiO₂	58.93	58.07	58.04	63.81	64.64	68.07
TiO₂	0.95	0.99	0.83	0.55	0.49	0.36
Al₂O₃	16.13	16.34	15.87	15.66	15.64	15.87
Fe₂O₃	7.26	6.64	6.78	4.95	4.15	2.72
MnO	0.14	0.09	0.10	0.09	0.07	0.02
MgO	2.44	3.66	3.63	1.24	1.31	0.41
CaO	5.47	6.03	3.41	4.27	1.88	0.89
Na₂O	2.35	2.24	3.17	2.23	2.53	0.81
K₂O	2.63	3.59	4.13	3.93	6.05	7.11
P₂O₅	0.22	0.30	0.22	0.21	0.14	0.09
L.O.I.	4.13	2.77	3.26	3.15	3.41	4.19
Total	100.70	100.70	99.45	100.10	100.30	100.50
Mg#	0.43	0.55	0.55	0.36	0.42	0.25
Rb	81	117	153	159	252	209
Sr	409	471	283	402	222	65
Ba	541	635	636	825	749	603
Cs	4.9	2.8	3.1	5.7	18.5	6.5
Sc	19	19	19	12	8	9
V	165	161	163	70	45	56
Cr	20	120	60			20
Co	14	18	16	8	5	4
Ni		20				
Cu	10	20	40			
Zn	90	90	80	80	50	30
Y	29	31	35	32	37	63
Zr	180	211	198	200	206	175
Nb	12	16	14	13	14	8
Hf	4.6	4.2	5.1	5	4.8	4.6
Ta	1.2	1.3	1.2	1.4	1.5	1.1
La	38.9	45.6	47.5	50.8	55.2	60.5
Ce	76	91.6	83.3	98.2	90.1	77.4
Pr	8.49	10.3	10.1	10.6	10.9	13.3
Nd	32.1	39.7	40.3	38.9	40.2	51.3
Sm	6.9	8	8.3	7.9	7.6	10.2
Eu	1.72	1.85	2.04	1.76	1.72	1.98
Gd	6.3	6.2	7.9	6.9	7	10.8
Tb	0.9	1	1.1	1	1	1.5
Dy	5.6	6	5.9	5.9	5.6	8.3
Ho	1.1	1.1	1.2	1.1	1.1	1.7
Er	3.2	3.2	3.2	3.5	3.1	4.8
Tm	0.49	0.45	0.44	0.51	0.49	0.65
Yb	3.1	3	2.8	3.4	3.2	3.9
Lu	0.44	0.49	0.42	0.5	0.48	0.59
Pb	19	20	15	25	26	21
Th	11.6	12.2	13.2	14.9	16.3	16.1
U	2.8	3.3	3.2	3.6	4.7	2.8
Q	17.17	11.44	8.37	23.39	19.54	33.69
C	0.00	0.00	0.53	0.49	1.91	5.65
or	16.10	21.66	25.38	23.96	36.90	43.61
ab	20.60	19.35	27.89	19.47	22.09	7.11
an	26.62	24.43	16.10	20.44	8.68	3.97
ne	0.00	0.00	0.00	0.00	0.00	0.00
-wo	0.00	1.72	0.00	0.00	0.00	0.00
-en	0.00	0.91	0.00	0.00	0.00	0.00
-fs	0.00	0.75	0.00	0.00	0.00	0.00
di	0.00	3.38	0.00	0.00	0.00	0.00
-en	6.30	8.40	9.40	3.19	3.37	1.06
-fs	8.85	6.97	8.34	6.17	5.12	3.25
hy	15.15	15.36	17.74	9.35	8.48	4.31
-fo	0.00	0.00	0.00	0.00	0.00	0.00
-fa	0.00	0.00	0.00	0.00	0.00	0.00
ol	0.00	0.00	0.00	0.00	0.00	0.00
mt	1.30	1.17	1.22	0.88	0.74	0.49
il	1.86	1.91	1.63	1.07	0.95	0.71
ap	0.54	0.73	0.54	0.51	0.34	0.22

Table 4.2 (continued)

The massive volcanic rocks of the Dolomites are basic to intermediate in terms of silica content ($\text{SiO}_2 = 49.2\text{-}58.1$ wt%, LOI-free basis) with total alkali content ($\text{Na}_2\text{O}+\text{K}_2\text{O}$) ranging from 4.0 to 7.9 wt%. The Loss-on-ignition (LOI) content is generally <3 wt%, except for few samples recording higher values up to 7.28 wt%. On the basis of TAS classification scheme (Le Maitre, 2002), the analyzed samples are classified mostly as trachybasalts and basaltic trachyandesites, with minor alkali basalts, basaltic andesites and one trachyandesite (Fig. 5a). The Alpe di Siusi hyaloclastites tuff (sample AS6) is characterized by fresh glassy shards that have been analyzed with EMP. These latter show very different compositions, being characterized by higher SiO_2 (55.1-64.0 wt%) and alkalis ($\text{Na}_2\text{O}+\text{K}_2\text{O} = 10.4\text{-}13.1$ wt%) than the massive volcanic rocks, mostly falling in the trachyte field with rarer tephri-phonolite and one trachyandesite (Fig. 4.4a). Only the altered tuff sample shows a sodic alkaline affinity, falling in the mugearite field, possibly suggesting K_2O depletion.

The Monzoni plutonic rocks range from ultrabasic to intermediate compositions ($\text{SiO}_2 = 41.7\text{-}57.2$ wt%), aligned along a rather sharp trend with medium enriched alkali content compared to the massive volcanic rocks of the Dolomites ($\text{Na}_2\text{O} + \text{K}_2\text{O} = 1.6\text{-}7.6$ wt%). The Predazzo plutonic rocks spread over a much larger range of SiO_2 (44.0-75.9 wt%) and alkalis ($\text{Na}_2\text{O} + \text{K}_2\text{O} = 1.5\text{-}9.6$ wt%), completely overlapping the Monzoni rocks, straddling the subalkaline-alkaline division in the TAS diagram, reaching rhyolitic composition, with a gap in the trachyte field. The Recoaro volcanic rocks mostly fill the Predazzo rock gap, plotting in the 59.3-69.6 wt% SiO_2 range. As already described in the literature, and confirmed in this study, the Recoaro rocks are characterized by

strong mobility of the alkalis (De Vecchi and Seda, 1983), thus making the handling of these geochemical data at least dubious (see the discussion section).

According to K_2O vs. Na_2O diagram (Fig. 4.4b), with the exception of two outliers characterized by high LOI, all the Dolomites samples fall into the field of the transitional and potassic series. The two outliers are the Lago di Alleghe mugearitic tuff (LOI = 5.8 wt%), characterized by anomalously high Na_2O (6.3 wt% on LOI-free basis) and very high Na_2O/K_2O (3.93), and the Alpe di Siusi shoshonite (LOI = 6.2 wt), characterized by high K_2O (5.7 wt%) and low Na_2O/K_2O (0.38). Also in this case, the EMP compositions of sample AS6 glassy shards fall into the potassic and ultrapotassic series fields (Fig. 4.4b). The new samples from Predazzo, Monzoni and Recoaro districts completely overlap the Dolomites rocks.

According to the K_2O vs. SiO_2 diagram (Peccerillo and Taylor, 1976), all the investigated rocks mainly belong to the high-K calcalkaline and shoshonitic series, (Fig. 4.4c), as most of the samples reported in literature. Only moderately to strongly altered SiO_2 -rich samples from Vicentinian and Brescian areas tend to plot in the calcalkaline or arc-tholeiite fields, due to K_2O depletion. On the AFM Diagram (Kuno, 1968), all the studied samples and the literature analyses plot in the calcalkaline field, lacking substantial iron enrichment during the evolutionary trend (Fig. 4.4d).

The CIPW normative mineralogy is reported in Table 4.2. More than half of the Dolomites samples are SiO_2 -critically saturated with normative orthopyroxene and olivine. Six are characterized by small normative quartz contents (0.62-4.98%), and eight of them are SiO_2 -undersaturated with normative nepheline ranging from 1.92 to 7.42%. The glassy shards in the hyaloclastite sample range

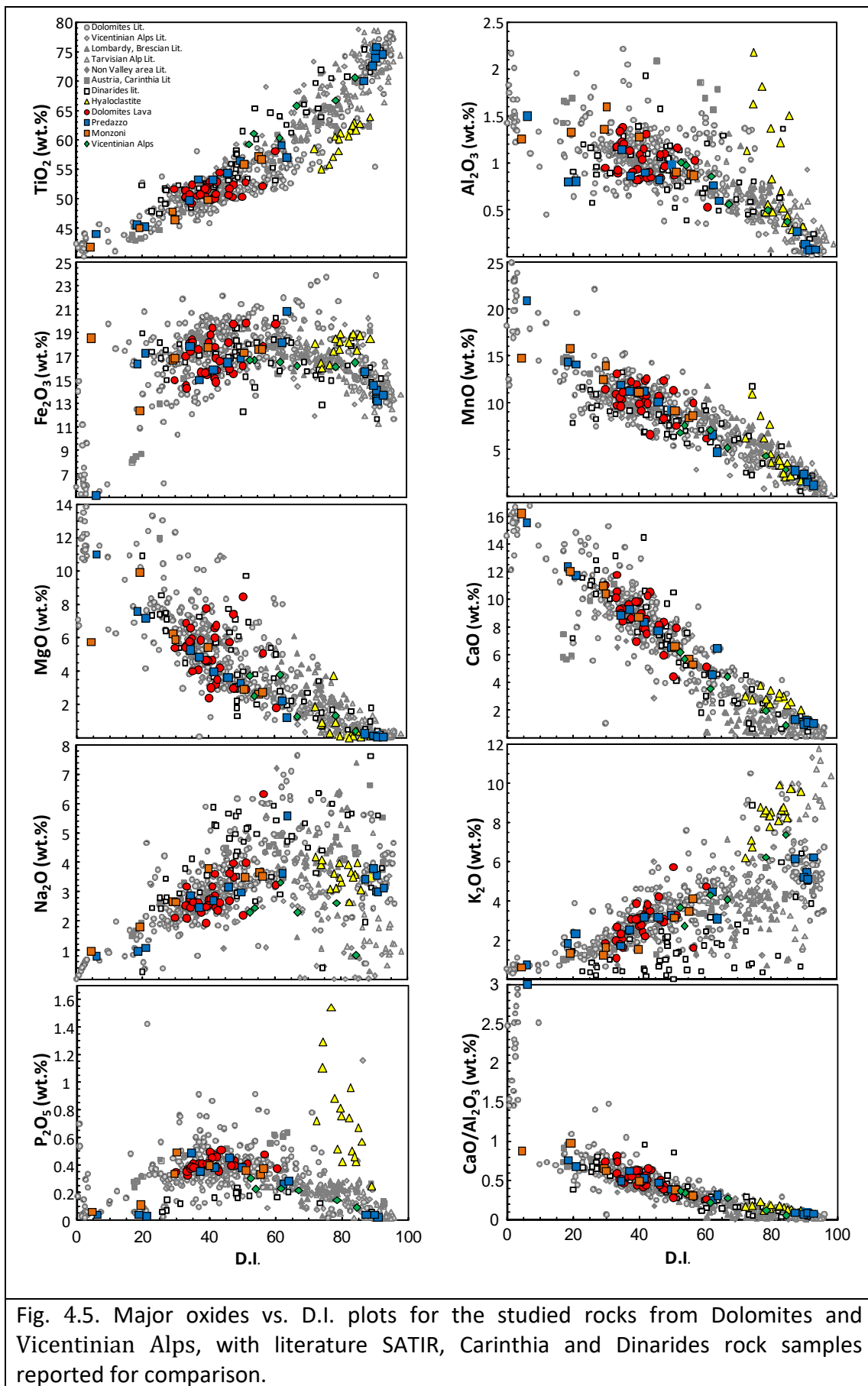
from slightly SiO₂-oversaturated (with CIPW normative quartz = 1.7-3.3%) to slightly SiO₂-undersaturated (CIPW normative nepheline = 1.1-3.4%). More than 37% of Monzoni samples, more than 60% of the Predazzo samples and all the Recoaro rocks are CIPW quartz-normative.

The major oxides of the analysed samples have been plotted against Differentiation Index (D.I.= sum of CIPW normative Q, Or, Ab, Ne, Lc and Kp; Thornton and Tuttle, 1960) in Fig. 4.5. In the same figure the literature data of Triassic volcanic and plutonic rocks from the Southern Alps (Dolomites, 762 samples; Vicentinian Alps, 62 samples; Brescian Alps, 104 samples; Tarvisian Alps, 25 samples; Non Valley, 20 samples; Valsugana, 12 samples), Carinthia (Austria, 20 samples) and Dinarides (53 samples) are reported for comparison. When considering the entire dataset (present and literature data), MgO, TiO₂, Fe₂O_{3tot} and CaO exhibit well defined negative correlation with D.I (Fig. 4.5). Al₂O₃ and P₂O₅ define bell-shaped patterns, with maximum values at ~60 and ~40, respectively, whereas a positive correlation is observed for SiO₂, K₂O (well-defined) and Na₂O (more scattered) vs. D.I.. The glassy shards usually overlap whole-rock data of the other Triassic igneous rocks from the Alps and Dinarides.

The Dolomites lava samples plot within the literature data of Dolomites Carnian volcanic rocks and, with one exception, span in a rather limited SiO₂ range, from 49.4 to 54.3 wt%. Similar values are found in the glass shards of pyroclastite sample AS6, showing a relatively narrow SiO₂ variation (55.2-54.0 wt%). In this restricted SiO₂ and D.I. range, the trends depicted by Dolomite lavas are quite scattered, except for a negative linear correlation between Fe₂O_{3tot} and CaO vs. D.I. and correlation between K₂O and D.I..

Predazzo plutonic rocks define a large and quite continuous spread of major oxides, showing always a good correlation with D.I., in nearly all the cases with $R^2 > 0.85$ (up to > 0.96 for CaO and Fe_2O_{3tot}). Also Monzoni and Recoaro rocks exhibit straight correlations with D.I., overlapping the trends depicted by the previous two districts.

The trace element content of the analysed samples has been plotted against D.I. in Fig. 4.6. Both compatible (e.g., transition elements TE; Sc, V, Cr, Co, Ni, Cu, Zn) and incompatible elements [e.g., large ion lithophile elements (LILE; Rb, Sr, Cs, Ba) and high field strength elements (HFSE; Y, Zr, Nb, Hf, Ta)] of Dolomites rocks do not show appreciable correlations with D.I., similarly to what observed for literature samples. Light-REE (LREE; La, Ce, Pr, Nd and Sm) display a rough correlation with SiO_2 , except sample PR23 (highly altered basaltic andesite lava), which usually plots out of the main trend for nearly all the trace elements. Middle-REE (MREE: Eu, Gd, Tb, Dy, and Ho) and heavy-REE (HREE; Er, Tm, Yb and Lu) do not show any correlation with D.I..



The other three Southern Alps districts (Predazzo, Monzoni and Vicentinian Alps) show recognizable and rather coherent trends. Among LILE, only Rb behaves continuously as incompatible element, showing enrichment with increasing D.I. (Fig. 4.6). Strontium and Ba reach a peak around D.I. 50, then decrease. Transition elements show defined negative trends with D.I., particularly evident for Sc, V and Co (Fig. 4.6). HFSE + Y behave as a coherent group, aligning along straight correlation with D.I., with the only exception of the most differentiated compositions of Predazzo (D.I. >87). What seen for HFSE is mimicked by REE, with the exception of Eu, which is strongly depleted in the most differentiated Predazzo samples (Fig. 4.6). Thorium and U behave as strongly incompatible elements, with the most differentiated Predazzo samples characterized by high Th (up to 70 ppm) and U (up to 14 ppm). Lead distribution is less defined for all the districts.

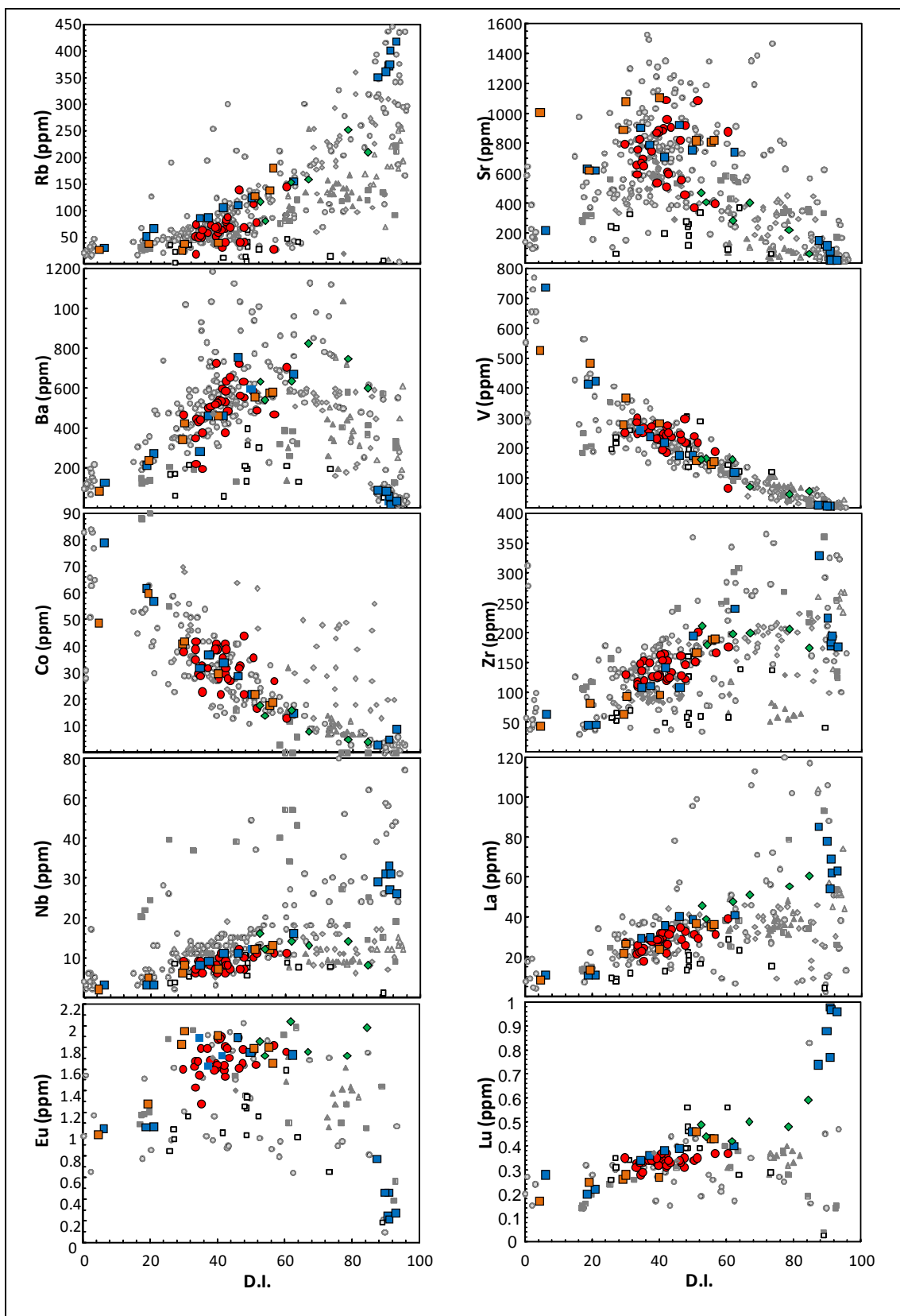
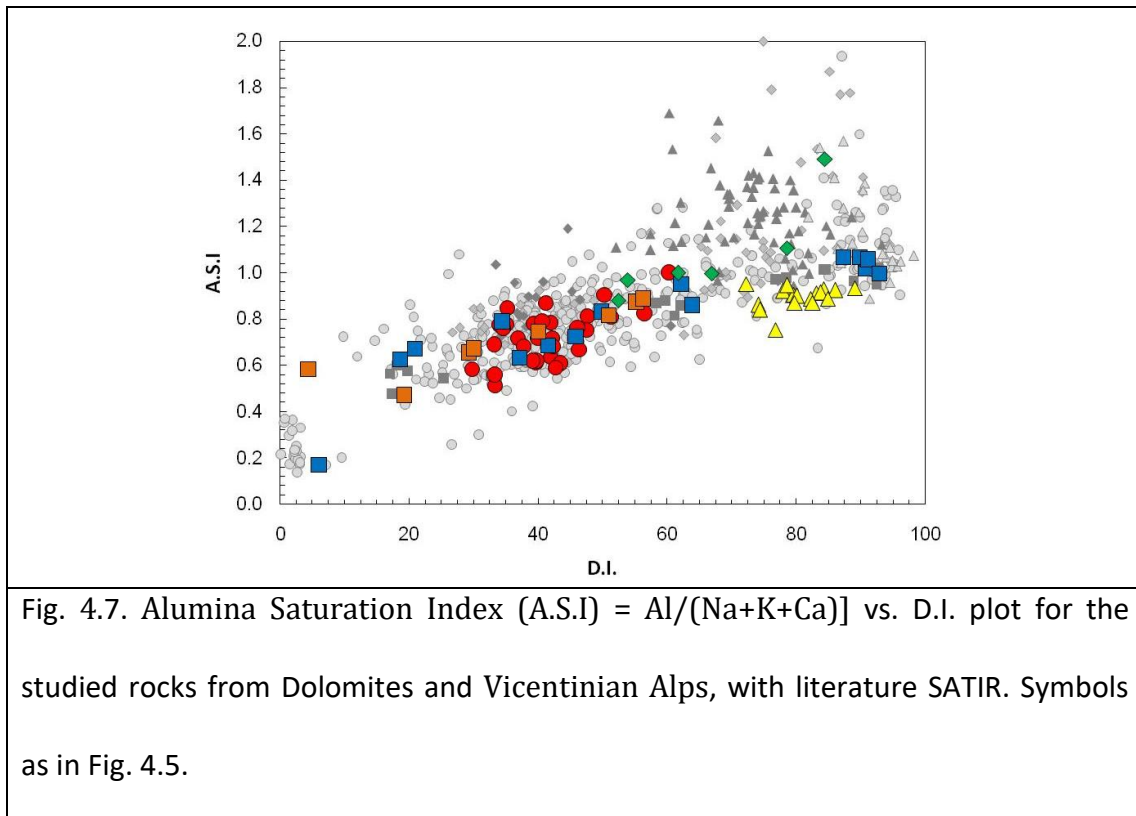


Fig. 4.6. Selected trace elements vs. D.I. plots for the studied rocks from Dolomites and Vicentinian Alps, with literature SATIR, Carinthia and Dinarides rock samples reported for comparison. Symbols as in Fig. 4.5.

All the Dolomites samples are metaluminous with ASI [ASI = Alumina Saturation Index = $Al/(Na+K+Ca)$] ranging from 0.52 to 1.00, similarly to what observed for the glassy shards (ASI = 0.75-0.95) and the other investigated Southern Alps igneous rocks. A good correlation between ASI and D.I. (Differentiation Index; Thornton and Tuttle, 1960) can be observed, with ASI values increasing from 0.47 to 1.00 in the 19.2-66.8 D.I. range. Only the most evolved compositions (D.I. >78; SiO_2 >66.5 wt%) have peraluminous compositions with ASI as high as 1.49 (Fig. 4.7).



Mg number [$Mg\# = 100 \cdot Mg / (Mg + Fe^{2+})$] of the Dolomites volcanic rocks ranges from 35 to 63, with no correlation with D.I. and a poor correlation with SiO_2 ($R^2 = 0.39$, excluding the two SiO_2 -richest samples). On the other hand, the Predazzo and Recoaro rocks show good negative correlations of Mg# with SiO_2 ($R^2 = 0.96$ and 0.86 , respectively). The low Mg# value, coupled with relatively low Cr (30-330 ppm) and Ni (20-80 ppm) indicate that the investigated rocks cannot be considered primary melts in equilibrium with mantle rocks and that they experienced fractionation during the ascent to the surface (see below).

Primitive mantle (PM)-normalized multi-elemental patterns (Fig. 4.8) are homogeneous with nearly inexistent inter-elemental fractionation for the different analysed rock types. The key features are medium to high enrichment of LILE (Rb \sim 39-315, Ba \sim 39-143, Th \sim 38-181, U \sim 40-168, K \sim 46-235 and Pb \sim 42-257 times PM), deep Nb-Ta troughs (\sim 13-26 times PM), strong trough at Ti (\sim 3-8 times PM) and very flat HREE ($H_{ON}/L_{UN} = 1.02-1.29$). The Dolomites volcanic rocks define a pattern which, with the only exception of P, perfectly overlaps the Global Subducting Sediment (GloSS) composition (Plank, 2014). When compared to a classical within-plate oceanic locality such as the St. Helena basalts in central Atlantic Ocean (the type locality of HiMu-OIB, Kawabata et al., 2011), the Dolomite rocks show remarkable differences, in particular much higher LILE, troughs at Nb-Ta-Ti and marked peaks at K and Pb (Fig. 4.8a).

The rocks from the other three investigated districts (Predazzo and Monzoni plutons and Vicentinian Alps) show inter-elemental fractionation patterns similar to those of Dolomites volcanic rocks. The Predazzo plutonic rocks nearly overlap the incompatible elements of Dolomites volcanic rocks, showing slightly

higher Rb, peaking at U-Th. Predazzo cumulitic clinopyroxenites show the lowest incompatible element contents, but on the whole they show a similar pattern with respect to the plutonic rocks. The only syenitic sample (PR25) is characterized by the highest enrichment in nearly all the elements (Fig. 4.8b). Predazzo granites display even more spiked patterns, with deep troughs at Ba, Sr, P, Eu and Ti and the highest concentrations for the other elements, as well as flat HREE clustering around 13-16 PM times (Fig. 4.8c). Also Monzoni plutonic rocks closely resemble the Dolomites lava patterns, sharing strong similarities with the GloSS composition too, although incompatible element contents are generally displaced towards lower abundances (Fig. 4.8d). Also in this case the cumulitic rocks (gabbros) show very low elemental content, overlapping the Predazzo clinopyroxenites.

The Vicentinian Alps samples are usually displaced towards higher incompatible element contents, with the exceptions of deeper troughs at Sr, P and Ti. The sample with the highest LOI (HA9; LOI = 4.19 wt%) slightly departs from the main pattern, the most peculiarity being the lowest Sr and P and high MREE-HREE contents (Fig. 4.8e).

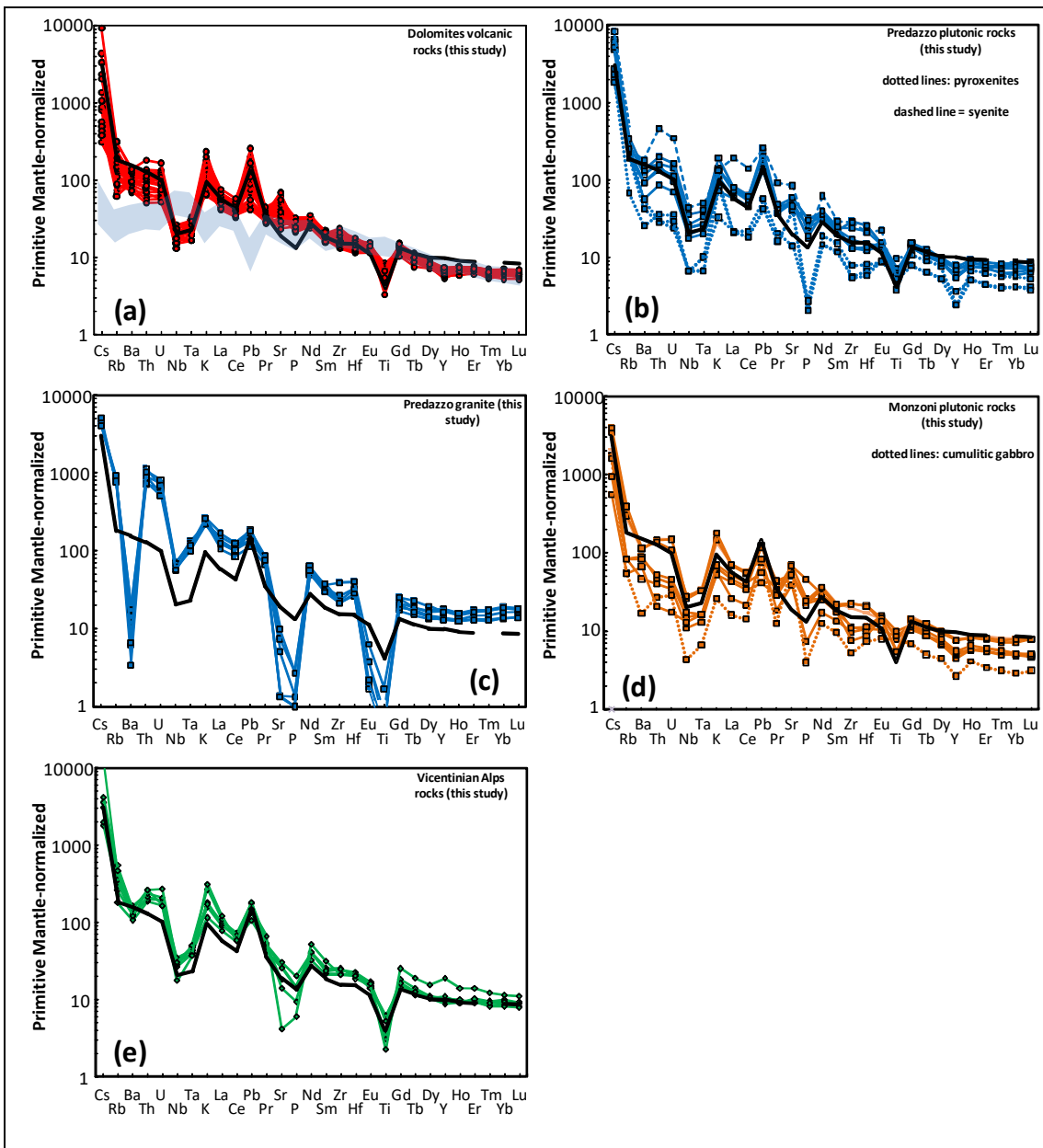


Fig. 4.8. Primitive mantle-normalized diagrams (normalizing factors after Lyubetskaya and Korenaga, 2007) for the studied Dolomite rock samples. (a) = Dolomites lava; (b) = Predazzo; (c) = Predazzo granite; (d) = Monzoni; (e) = Vicentinian Alps. Light blue field = St. Helena Island basalts (Southern Atlantic Ocean), considered the classical HiMu-OIB composition (Kawabata et al., 2011). Black line = GloSS composition (Global Subducting Sediments; Plank 2014).

4.4. Sr-Nd-Pb isotopic ratios

On the basis of petrographic characteristics and geochemical signatures, seven Southern Alps volcanic samples were selected for Sr-Nd-Pb isotopic determination, a novelty for the rocks from this domain. The results of these analyses are reported in table 4.3 and shown in Fig. 4.9, with the isotopic ratios age-corrected to 230 Ma. The Dolomites lava samples have relatively high $^{87}\text{Sr}/^{86}\text{Sr}_{(i)}$ (0.7043-0.7051) with $\epsilon\text{Sr}_{(i)}$ ranging from 1.8 to 12.7, with the exception a Latemar basaltic dyke (LAT2) showing slightly more radiogenic $^{87}\text{Sr}/^{86}\text{Sr}$ (0.7058) with $\epsilon\text{Sr}_{(i)}$ 22.5. The $^{143}\text{Nd}/^{144}\text{Nd}_{(i)}$ ranges from 0.51227 to 0.51237, with $\epsilon\text{Nd}_{(i)}$ values slightly lower to slightly higher than $\text{ChUR}_{(230\text{ Ma})}$ (from -1.4 to +0.5). The Pb isotopic compositions are homogeneous, with $^{206}\text{Pb}/^{204}\text{Pb}$ clustered around 18.26 and 18.41, $^{207}\text{Pb}/^{204}\text{Pb}$ from 15.62 to 15.67 and $^{208}\text{Pb}/^{204}\text{Pb}$ from 38.36 to 38.48, with the exception of sample LAT2 showing slightly higher $^{208}\text{Pb}/^{204}\text{Pb}$ 38.89 compared to the other samples.

The Dolomites lavas mostly plot in the enriched Sr-Nd isotopic quadrant (Fig. 4.9a), partially overlapping the compositions of Predazzo plutonic rocks (Casetta et al., 2018b), but being displaced towards slightly more radiogenic Nd compared to Monzoni plutonic rocks (Bonadiman et al., 1994) at a given $^{87}\text{Sr}/^{86}\text{Sr}$. The recent data of Valsugana dykes (227-260 Ma; Bianchini et al., 2018), located in between Dolomites and Vicentinian Alps, ~10-15 km E of Trento city, are characterized by much more radiogenic Sr ($^{87}\text{Sr}/^{86}\text{Sr} = 0.7082\text{-}0.7172$) and much less radiogenic Nd ($^{143}\text{Nd}/^{144}\text{Nd} = 0.51197\text{-}0.51209$; Fig. 4.9a).

To the best of the author's knowledge, the only Pb isotopic data on Triassic igneous rocks from Dolomites and neighbouring districts are those reported in Nimis et al. (2012) and Bianchini et al (2018). The new data presented here show a partial overlap with the sulphides in Triassic igneous rocks of Southalpine region only (Nimis et al., 2012), being the Valsugana dykes characterized by more radiogenic $^{206}\text{Pb}/^{204}\text{Pb}$ (18.57-19.12) and $^{207}\text{Pb}/^{204}\text{Pb}$ (15.68-15.72; Fig. 4.9b, c). No direct comparison with $^{208}\text{Pb}/^{204}\text{Pb}$ can be made, because Th elemental content to recalculate the initial values is missing in Bianchini et al. (2018). Assuming a reasonable Th/Pb ratio ~ 0.5 for the Valsugana dykes, the $^{208}\text{Pb}/^{204}\text{Pb}_{(238 \text{ Ma})}$ ratios of these samples ranges from 38.87 to 40.19, values much more radiogenic than the Dolomites massive volcanic rocks presented here.

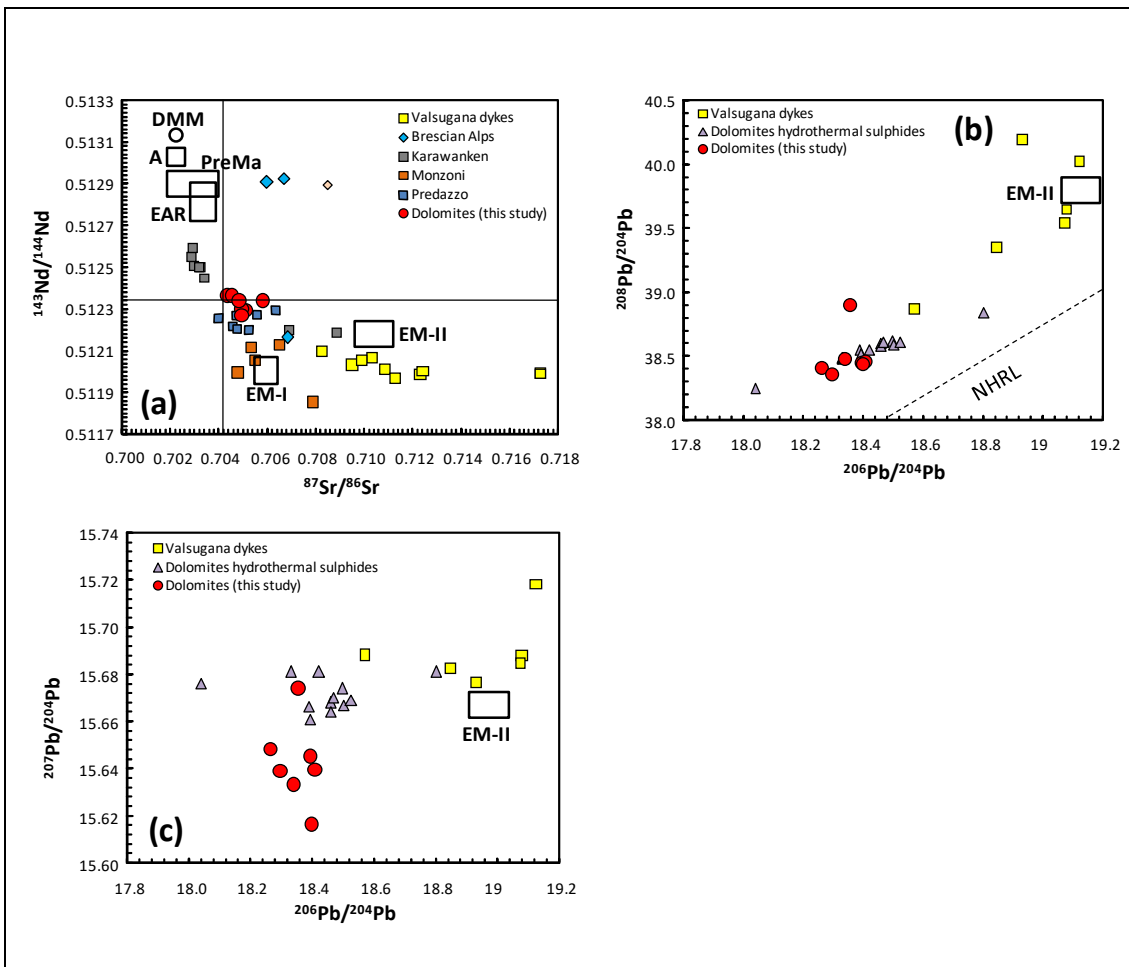


Fig. 4.9. Sr-Nd-Pb isotope plots for the studied Dolomite rock samples, with literature data for Valsugana dykes, and rocks from the Brescian Alps, Karawanken, Monzoni, and Predazzo, as well as Dolomites hydrothermal sulphides, reported for comparison (see text for data sources). a) $^{143}\text{Nd}/^{144}\text{Nd}$ vs. $^{87}\text{Sr}/^{86}\text{Sr}$ diagram. b) $^{208}\text{Pb}/^{204}\text{Pb}$ vs. $^{206}\text{Pb}/^{204}\text{Pb}$ diagram. c) $^{207}\text{Pb}/^{204}\text{Pb}$ vs. $^{206}\text{Pb}/^{204}\text{Pb}$ diagram. BSE = Bulk Silicate Earth at 230 Ma; ChUR = Chondritic Uniform Reservoir at 230 Ma. Empty circles and rectangles indicate the isotopic signatures of the principal mantle sources. DMM, Depleted MORB Mantle; EM-I, Enriched Mantle I; EM-II, Enriched Mantle II; EAR, European Asthenospheric Reservoir; PreMa, Prevalent Mantle. NHRL = Northern Hemisphere Reference Line.

The Dolomites lavas samples analyzed completely overlap the Predazzo and Monzoni plutonic rocks in terms of $^{87}\text{Sr}/^{86}\text{Sr}$ and do not show any appreciable variation with SiO_2 or MgO , as recorded by Predazzo and Monzoni plutonic samples (Fig. 4.10a,b). The Valsugana dykes are displaced towards very radiogenic values, but again without any correlation with differentiation parameters. On the other hand, the Karawanken (Austria) Triassic igneous rocks mimic increase of $^{87}\text{Sr}/^{86}\text{Sr}$ with increase of magma evolution. With the exception of the most evolved sample analyzed here, also $^{143}\text{Nd}/^{144}\text{Nd}$, do not show any correlation with SiO_2 or MgO (Fig. 4.10c,d). The samples analyzed here are the most radiogenic of the entire Southalpine area in terms of $^{143}\text{Nd}/^{144}\text{Nd}$, with higher values recorded in the Karawanken pluton only (Miller et al., 2011). As concerns the Pb isotopes, the bulk of the Dolomites samples do not show any correlation with SiO_2 or MgO , even if the most evolved sample (PR3 latite; 1.8 wt% MgO) is characterized by the lowest $^{207}\text{Pb}/^{204}\text{Pb}$ (Fig. 4.10e, f).

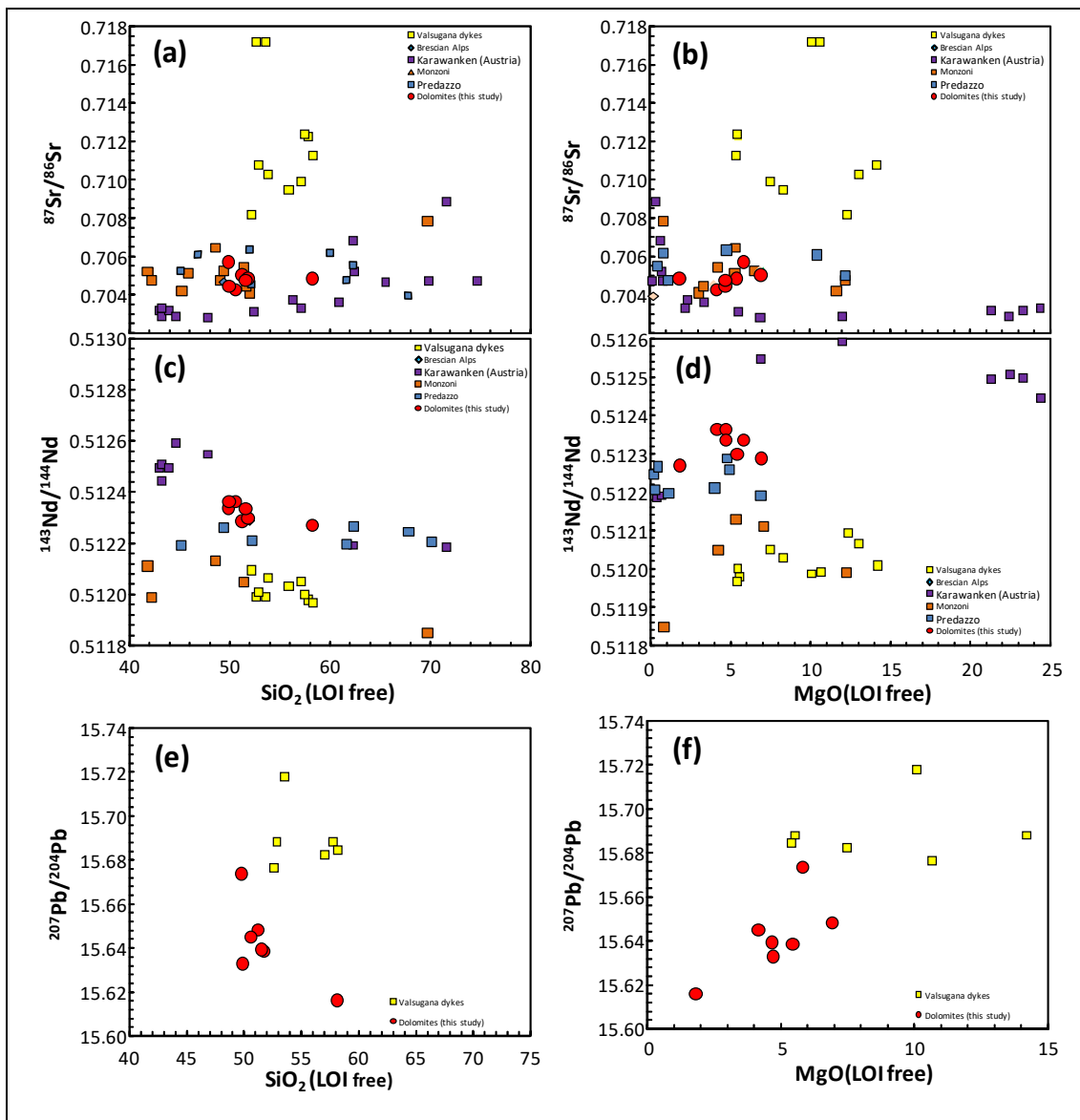


Fig. 4.10. Sr-Nd-Pb isotope ratios vs. SiO_2 and MgO for the studied Dolomite rock samples, with literature sata for Valsugana dykes, and rocks from the Brescian Alps, Karawanken, Monzoni, and Predazzo reported for comparison (see text for data sources). a) $^{87}\text{Sr}/^{86}\text{Sr}$ vs. SiO_2 . b) $^{87}\text{Sr}/^{86}\text{Sr}$ vs. MgO . c) $^{143}\text{Nd}/^{144}\text{Nd}$ vs. SiO_2 . d) $^{143}\text{Nd}/^{144}\text{Nd}$ vs. MgO . e) $^{207}\text{Pb}/^{204}\text{Pb}$ vs. SiO_2 . f) $^{207}\text{Pb}/^{204}\text{Pb}$ vs. MgO .

Sample	Rock Type	Age-corrected (230 Ma) values				
		$^{87}\text{Sr}/^{86}\text{Sr}$	$^{143}\text{Nd}/^{144}\text{Nd}$	$^{206}\text{Pb}/^{204}\text{Pb}$	$^{207}\text{Pb}/^{204}\text{Pb}$	$^{208}\text{Pb}/^{204}\text{Pb}$
GAR 3	Subalkali Basalt	0.70508	0.512289	18.263	15.648	38.406
BUF2	Subalkali Basalt	0.70492	0.512301	18.296	15.639	38.356
LAT2	K-Alkali Basalt	0.70577	0.512339	18.353	15.674	38.894
BUF4	Potassic Trachybasalt	0.70432	0.512365	18.393	15.645	38.450
MAR1	Potassic Trachybasalt	0.70451	0.512365	18.337	15.633	38.483
DUR 4	Shoshonite	0.70480	0.512337	18.406	15.640	38.455
PR3	Latite	0.70491	0.512271	18.398	15.616	38.434

Table 4.3. Sr-Nd-Pb radiogenic isotope ratios for selected representative samples of the investigated Dolomites lavas rocks.

**CHAPTER FIVE
STRUCTURAL AND AMS STUDIES**

5.1. Microstructural and petrographic description

In the Predazzo pluton, lithologies vary from cumulitic clinopyroxenite (samples PA12, PA11a, b, c) to cumulitic gabbro (PR 10), diorites (PA06), monzonite (PA02, PA10), monzodiorite (PA08, PA14c, PA09), monzogabbro (PA12) albitized granite (PA01, PA04, PA05, PA17) and biotite granite (PA07, PA03, PA13). We found evidence of hydrothermal alteration in samples from the northern part of the granite body of the Predazzo pluton (PA01, PA04, PA05, and PA17; Fig. 5.1).

The samples from Monzoni pluton are classified into two main groups: gabbroic rocks and monzonites. Gabbroic rocks are mainly located in the north-eastern sector of the pluton and consist of monzogabbros (PA21), gabbros (PA16) cumulitic gabbros (PA15) and olivine gabbros (PA20, PA18). Monzonites (PA22, PA22a, PA23, PA24) are mainly located in the south-western sector of the pluton and represent the most widespread rock type (Fig. 5.2).

The samples from both plutons show purely magmatic structures with feldspar, clinopyroxene, and amphibole devoid of any deformation. In few cases, kinked biotite occurs. Quartz does not show any or very limited undulatory extinction, and no or rare subgrains. Magmatic foliation has been observed in the studied rocks both at the meso- and micro-scale. The magmatic foliation is evidenced by orientation of minerals such as clinopyroxene, plagioclase, and biotite (Figs. 5.3a-j).

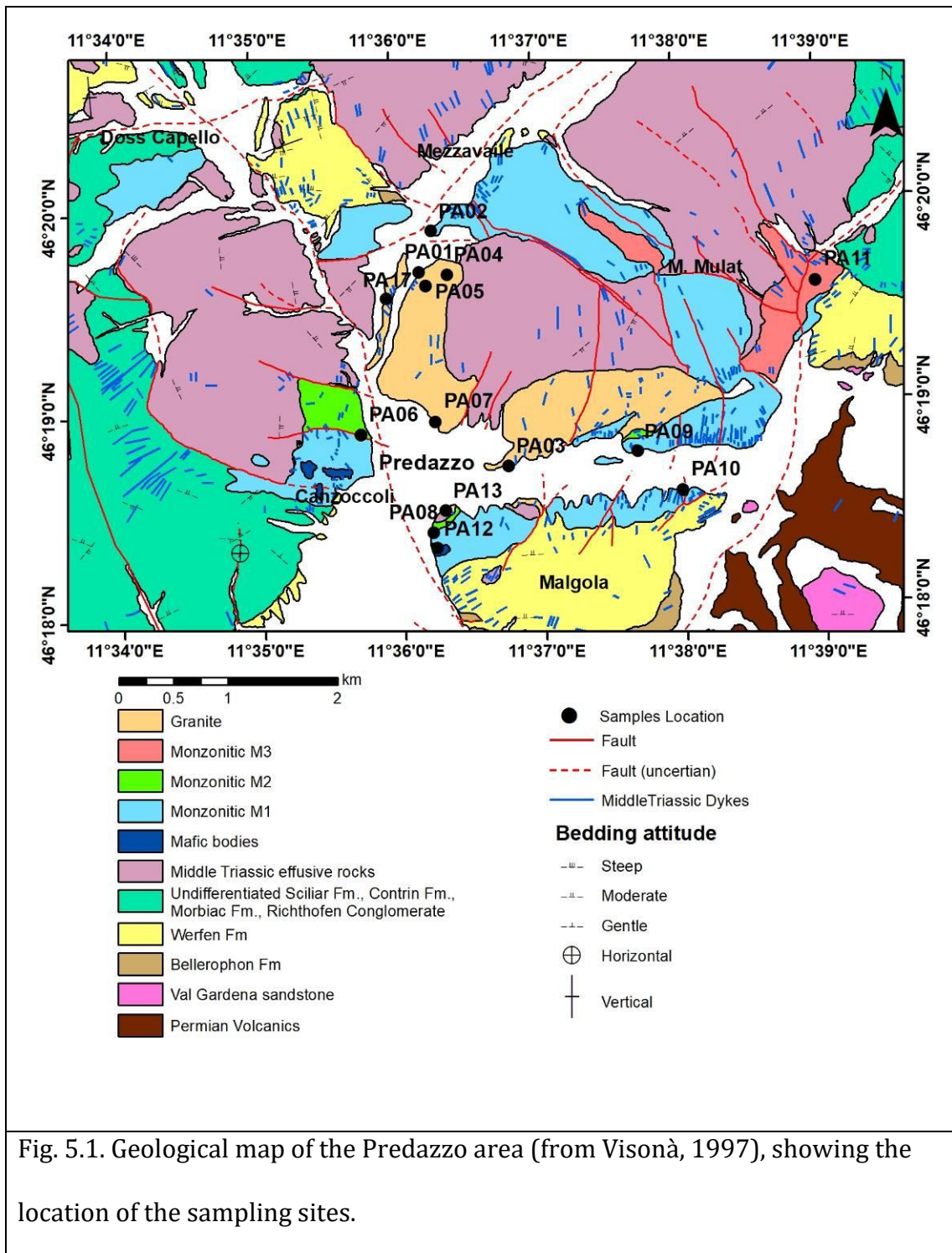


Fig. 5.1. Geological map of the Predazzo area (from Visonà, 1997), showing the location of the sampling sites.

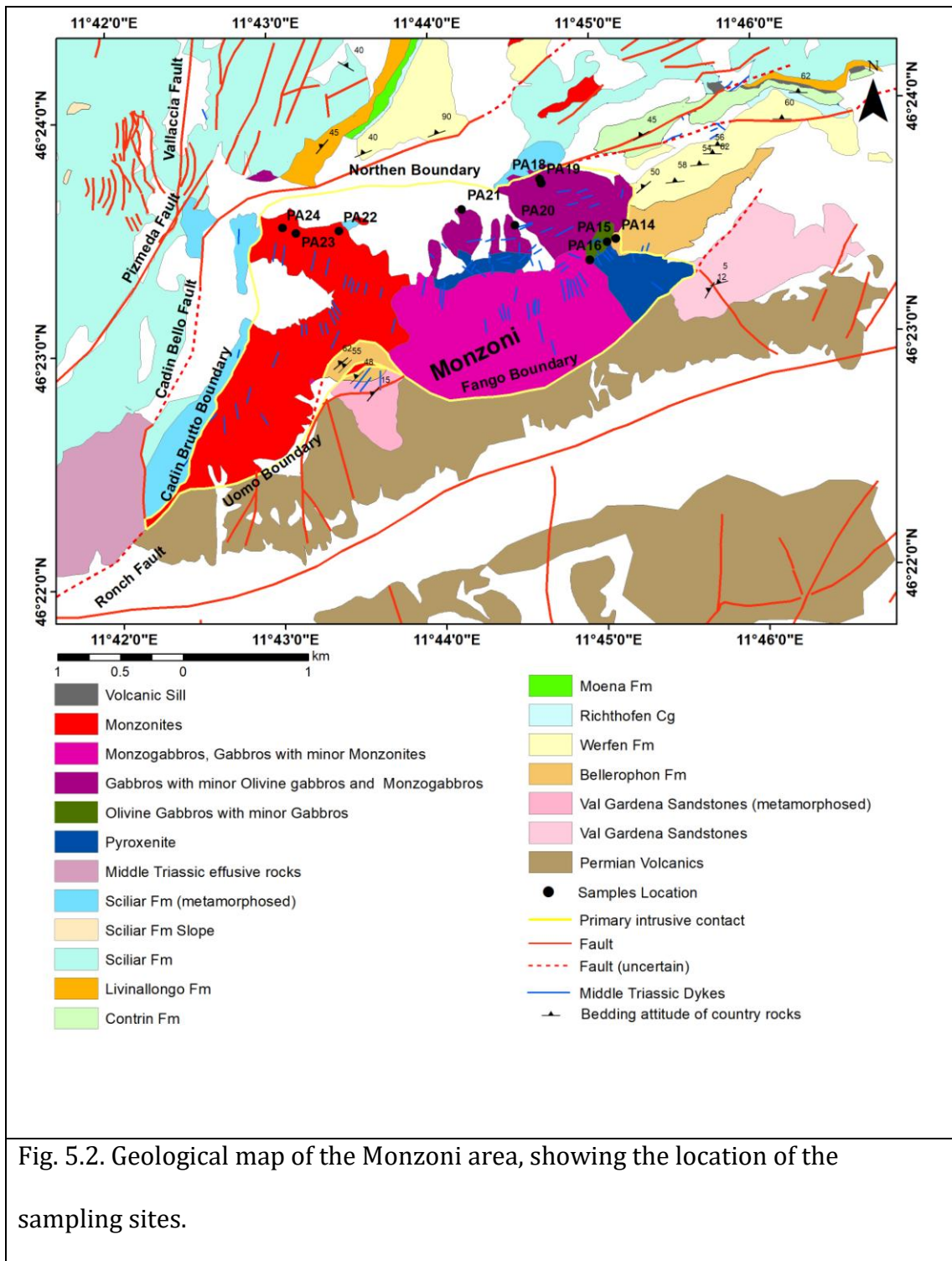
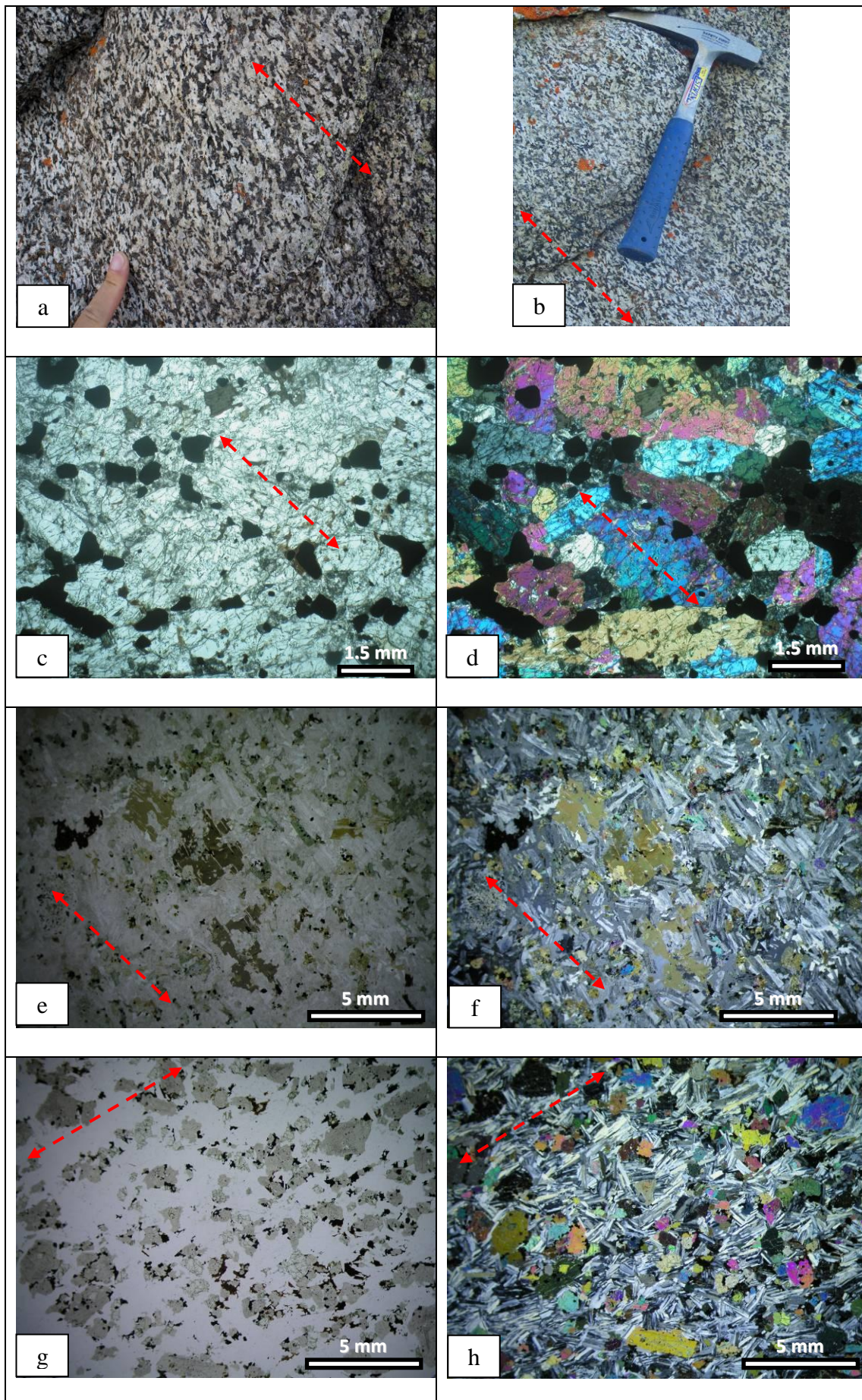


Fig. 5.2. Geological map of the Monzoni area, showing the location of the sampling sites.



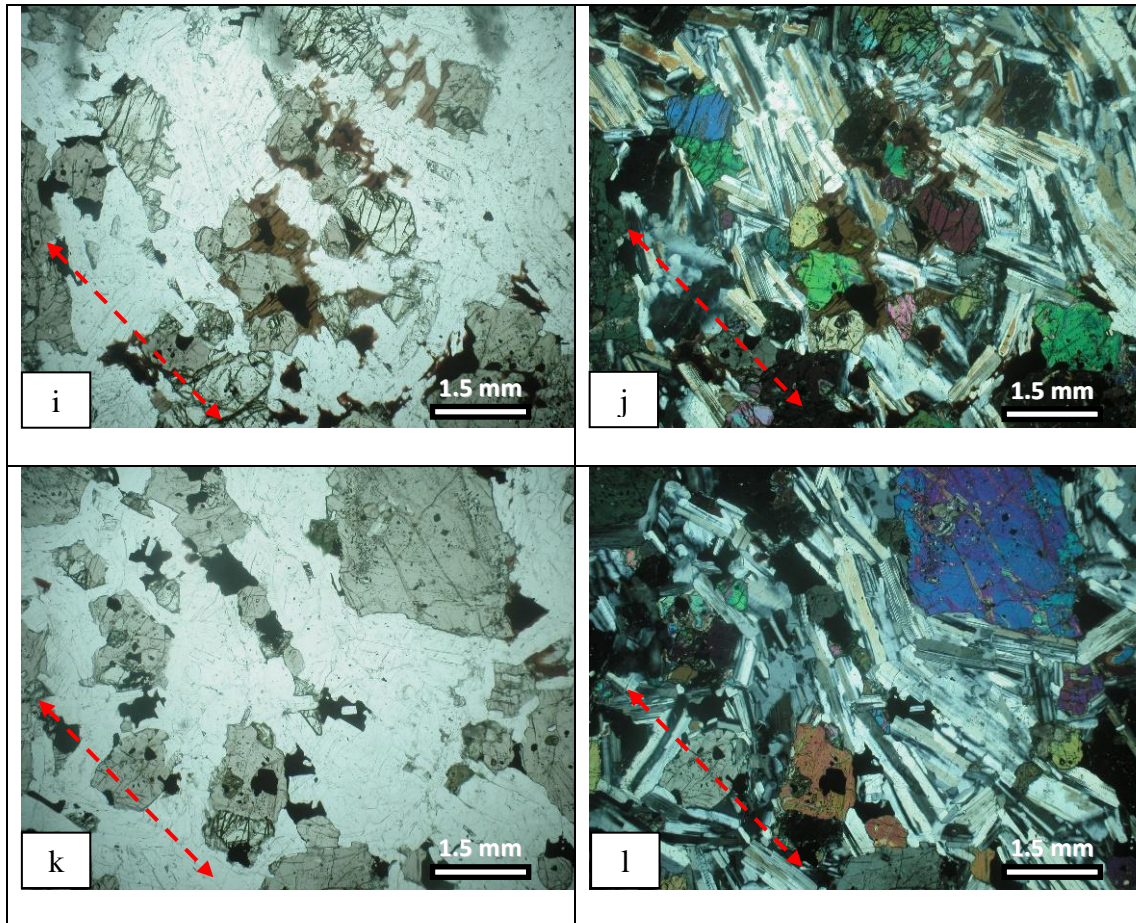


Fig. 5.3. Representative field photographs and thin section microphotographs for the investigated rock samples from the Predazzo and Monzoni plutons. a,b) Monzogabbro from the Monzoni body showing a well defined magmatic foliation. c,d) Clinopyroxenite showing preferred orientation of clinopyroxene and iron oxide minerals. (sample PA12) e,f) Monzonite showing preferred orientation of plagioclase and biotite crystals (sample PA22a, same location of sample 22), plane-polarized and cross-polarized light respectively; and g,h,i,j,k,l) Olivine gabbro showing preferred orientation of plagioclase and pyroxene crystals (sample PA20), plane-polarized and cross-polarized light respectively.

5.1.1. Predazzo pluton

Clinopyroxenites (PA12, PR11a, b, c)

Clinopyroxenites show a typical hypidiomorphic inequigranular medium- to coarse grained mesocumultic texture (Fig. 5.4a, b). The cumulus phase (clinopyroxene) accounts for more than ~65% of the rock with usually subhedral, fresh and rarely twinned crystals. Clinopyroxene is mainly medium grained (~3 mm) but a few reach larger dimensions, up to ~6 mm. The intercumulus phases consist of subhedral fine- to medium-grained opaques (~0.3-1.3 mm; ~15%), sometimes included in larger biotite crystals (Fig. 5.4c, d), anhedral to subhedral biotite (~13%) with an average size of ~4 mm and anhedral to subhedral small (~1 mm) plagioclase (~7%). In few cases biotites are partly chloritized, while plagioclases are usually partially sericitized. Fine-grained opaques, biotite and plagioclase are also found included in the clinopyroxene oikocrysts (poikilitic). Apatite and zircon are the common accessory minerals usually found as tiny grains included in clinopyroxene and biotite.

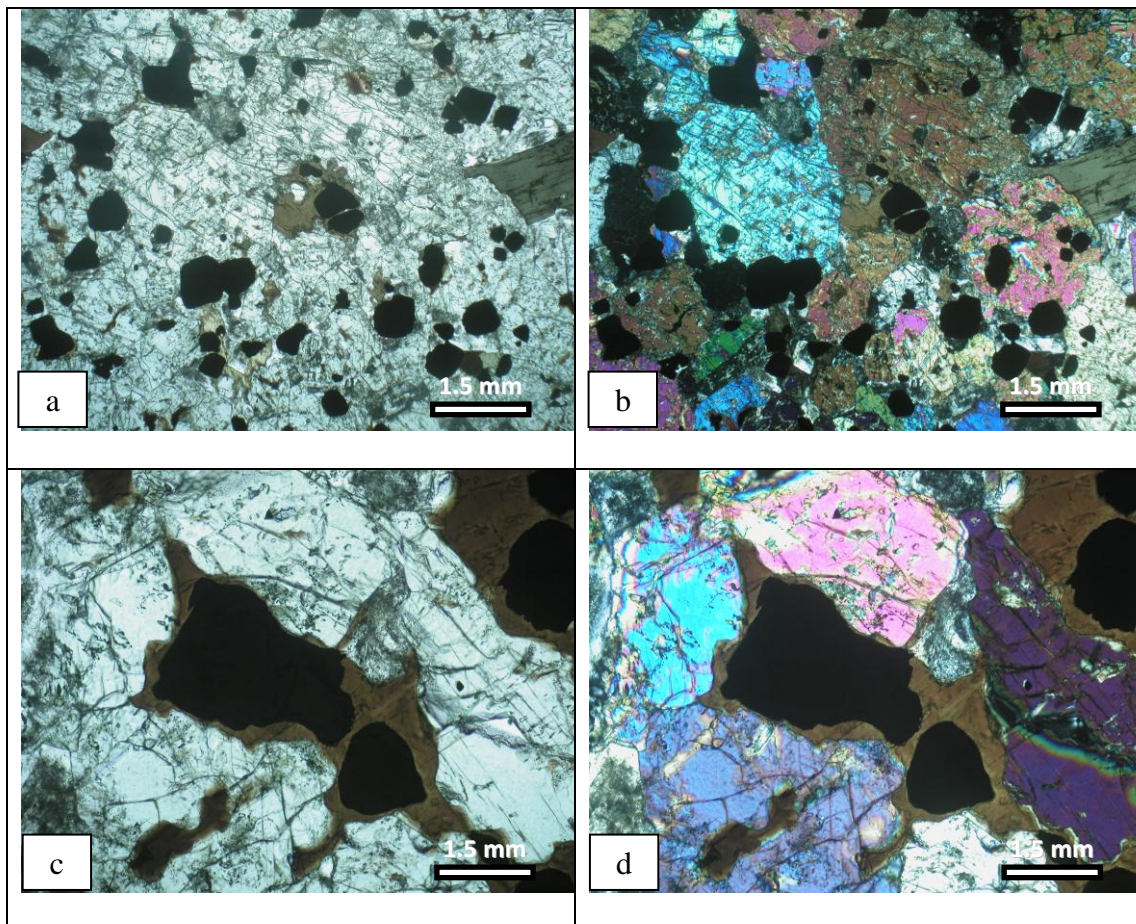


Fig. 5.4. Representative photomicrographs of the investigated Predazzo pluton rock samples. a, b) Photomicrographs showing hypidiomorphic inequigranular medium- to coarse grained mesocumultic texture in clinopyroxenite (sample Pa12). c, d) Photomicrograph showing subhedral opaques included in larger biotite crystals (sample Pa12). Photomicrographs a and c were taken in plane-polarized light, whereas b and d were taken in crossed-polarized light.

Cumulitic gabbro (PR 10)

The cumulitic gabbro is medium-grained with hypidiomorphic inequigranular texture. The cumulitic phases are plagioclase (~50%), clinopyroxene (~36%) and opaques (~10%). Subhedral to euhedral medium-grained (~3 mm) plagioclase is strongly altered to sericite with cores more altered than rims.

Clinopyroxene is subhedral medium grained (~2 mm), highly fractured, slightly altered and usually twinned. Opaques occur as subhedral to anhedral fine grained (<1 mm) and usually found in clusters with clinopyroxene or included in clinopyroxene and biotite. The intercumulus phases (~4%) consist of anhedral to subhedral fine grained (<1 mm) biotite and plagioclase. Biotite and plagioclase also occur as anhedral small grains included in the clinopyroxenes. Apatite is a common accessory mineral occurring as minute inclusion in clinopyroxene and biotite.

Diorite (PA06)

The diorite is characterized by hypidiomorphic inequigranular medium- to fine-grained texture (Fig. 5.5a, b). The rock is composed of plagioclase (~60%), amphibole (~15%), biotite (~10%), clinopyroxene (~10%), plus smaller amounts of alkali feldspar, opaques, quartz and accessory minerals. Plagioclase occurs as slightly sericitized tabular to equant subhedral crystals with an average size of ~1.5 mm. Anhedral to subhedral amphibole, biotite and clinopyroxene occur as small (~1 mm) interstitial clusters, together with subhedral fine-grained opaques, usually found as inclusion in these minerals (amphibole, biotite and clinopyroxene). Clinopyroxene is variably replaced by amphibole. Most of the biotite crystals are slightly to moderately altered to chlorite. Alkali feldspar and quartz (<1 mm) occur as anhedral intergranular crystals in between plagioclase laths. Apatite and rare zircon are present as small inclusions mainly within plagioclase and clinopyroxene.

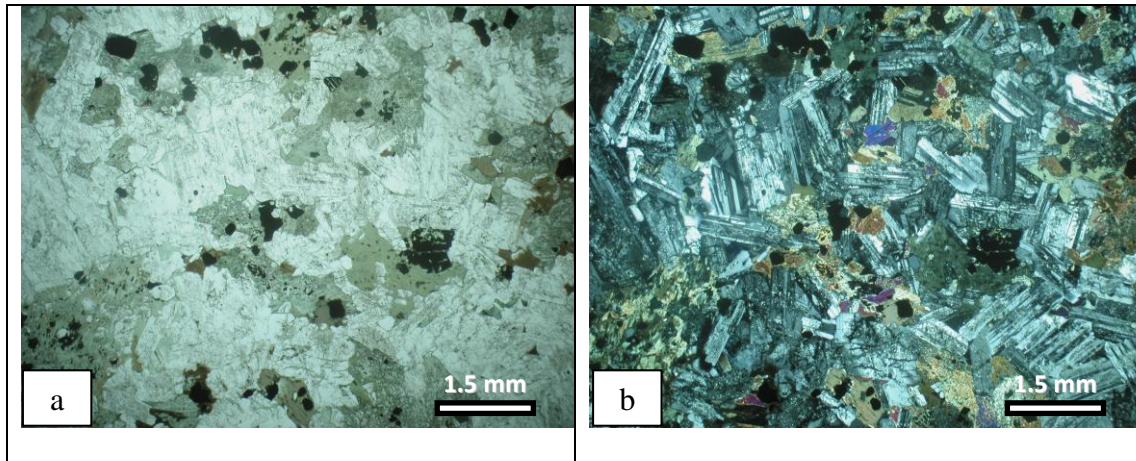


Fig. 5.5. Representative photomicrographs of the investigated Predazzo pluton rock samples. a, b) Photomicrographs showing hypidiomorphic inequigranular with medium- to fine-grained texture in Diorite (sample PA06), plane-polarized and cross-polarized light respectively.

Monzonites (PA02, PA10), monzodiorites (PA08, PR14c, PA09) and monzogabbro (PR12)

These three types of rocks generally share the same petrographic features, being different only for the relative alkali feldspar/plagioclase ratio. The amount of mafic minerals increases from monzonites to monzodiorites and monzogabbros. This rock group shows hypidiomorphic inequigranular texture. Monzonite and monzogabbros are medium-grained, while monzodiorites are medium- to fine-grained. The rocks are poikilitic, with big anhedral alkali feldspars including other minerals (Fig. 5.6a).

The rocks are generally composed, in order of decreasing abundance, of plagioclase, alkali feldspar, clinopyroxene, amphibole, biotite, quartz, opaques, orthopyroxene and accessory minerals. Plagioclase is usually euhedral with variable grain size (~0.5-3 mm) and sometimes zoned, with cores always more altered than the rims (i.e., sericitized and saussuritized). Few crystals show

combined pericline and albite twinning. Alkali feldspar (~1-4 mm) occurs as anhedral irregular grains characterized by perthitic exsolution. Clinopyroxene is subhedral with medium size (~1-2 mm), sometimes twined and in most cases found in clusters. The clinopyroxene crystals are partially to completely altered to amphibole (uralitization; Fig. b, c). Amphibole is anhedral to subhedral (~0.5-1.5 mm) and mostly found along the margin of clinopyroxene. Biotite occurs as subhedral to anhedral crystals with different grain size (~2-0.5mm) and often found in clusters. In some cases large biotite crystals are poikilitic for the presence of opaque mineral inclusions. Biotite is generally fresh, but in some cases it is partly altered into chlorite. In few cases, kinked biotite has been observed (Fig. d). Anhedral quartz is fine- to medium-grained (~1.5-0.3 mm) and occurs as interstitial phase. Orthopyroxene is subhedral to anhedral and is usually found in accessory abundances and recorded not in all the thin sections. Also orthopyroxenes are variably altered to amphibole. Opaques are small subhedral grains usually included in the mafic minerals or occupying interstitial positions. The accessory minerals are apatite, zircon and sphene, observed as inclusions or along mineral boundaries.

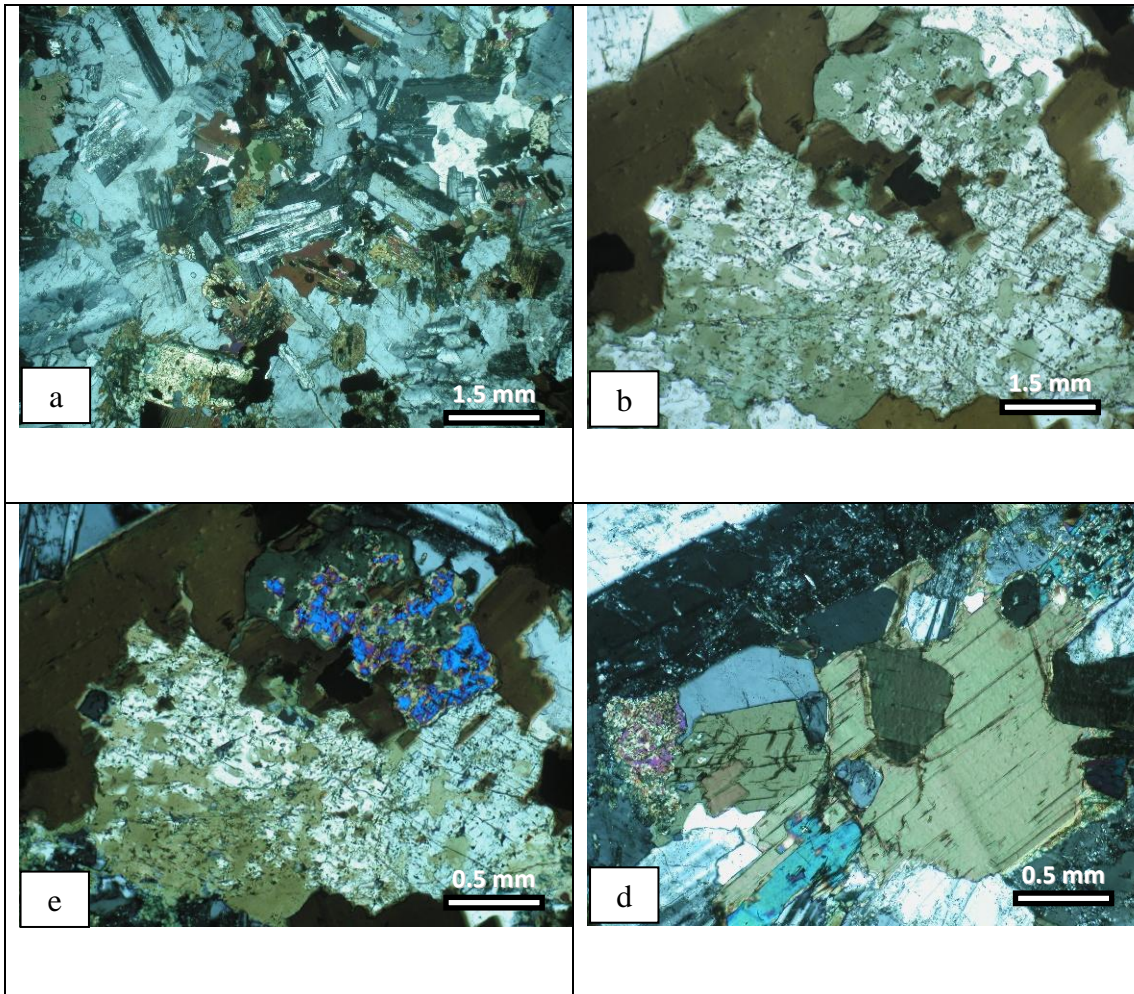


Fig. 5.6. Representative photomicrographs of the investigated Predazzo pluton rock samples. a) Photomicrographs showing primary magmatic structures (e.g., poikilitic texture; Monzonites sample PA10). b, c) Photomicrographs showing clinopyroxene crystals are partially altered to amphibole (sample PR12). d) Photomicrograph showing kinked biotite in monzodiorites (sample PA09). Photomicrographs a, c and d were taken in crossed-polarized light, whereas b was taken in plane-polarized light.

Granite group (PA01, PA03, PA04, PA05, PA07, PA13, PA17)

The samples exhibit hypidiomorphic inequigranular texture. Granophyric and perthitic textures are also recorded (Fig. 5.7a, b). The granite rocks are classified into two main groups: albitized granite (affected by hydrothermal alteration) and biotite granite.

In the first group biotite is completely transformed mainly to sericite and subordinately to chlorite (PA01, PA04, PA05, PA17), while in the second group biotite is generally found in a good state of preservation (PA07, PA03, PA13). The biotite granite group is characterized by the presence of microgranular quartz usually forming aggregates around feldspar crystals.

The rocks are made up, in order of decreasing abundance, of alkali feldspar, quartz and plagioclase with minor biotite, muscovite, chlorite and rare amphibole.

Alkali feldspar occurs as subhedral medium grained (~2-4 mm) crystals characterized by perthitic exsolution lamellae. Carlsbad twinning is common and the crystals usually show minor alteration. Quartz mainly occurs in anhedral grains (~1-3 mm) but is also sometimes found in the interstitial spaces (<0.5 mm) or forming aggregates around feldspar crystals. Quartz crystals show no or incipient undulatory extinction. Plagioclase is subhedral and medium grained (~1-3 mm), sometimes zoned and usually shows albite twinning. In biotite granite, Most of the plagioclase crystals are slightly to moderately altered (sericitized and saussuritized), with the cores more altered than the rims. On the other hand, in albitized granite plagioclase is completely transformed to pure albite. Biotite is present as subhedral platy crystals (~0.5-2 mm) and usually forms clusters of numerous crystals. Biotite is partially (Fig. 5.7c) to completely

altered to chlorite and sericite (Fig. 5.7d). Sericite occurs as anhedral to subhedral (~1-2 mm) forming pseudomorphs after biotite and is commonly associated with chlorite. Chlorite is subhedral to anhedral (~0.5-2 mm) and grows as pseudomorphs after biotite. Rare amphibole crystals have been recorded in the second group. Accessory minerals are zircon, apatite, fluorite, iron oxide and monazite.

Monzonite/Syenite? (PA11)

This sample is strongly affected by hydrothermal alteration and a precise classification cannot be conducted.

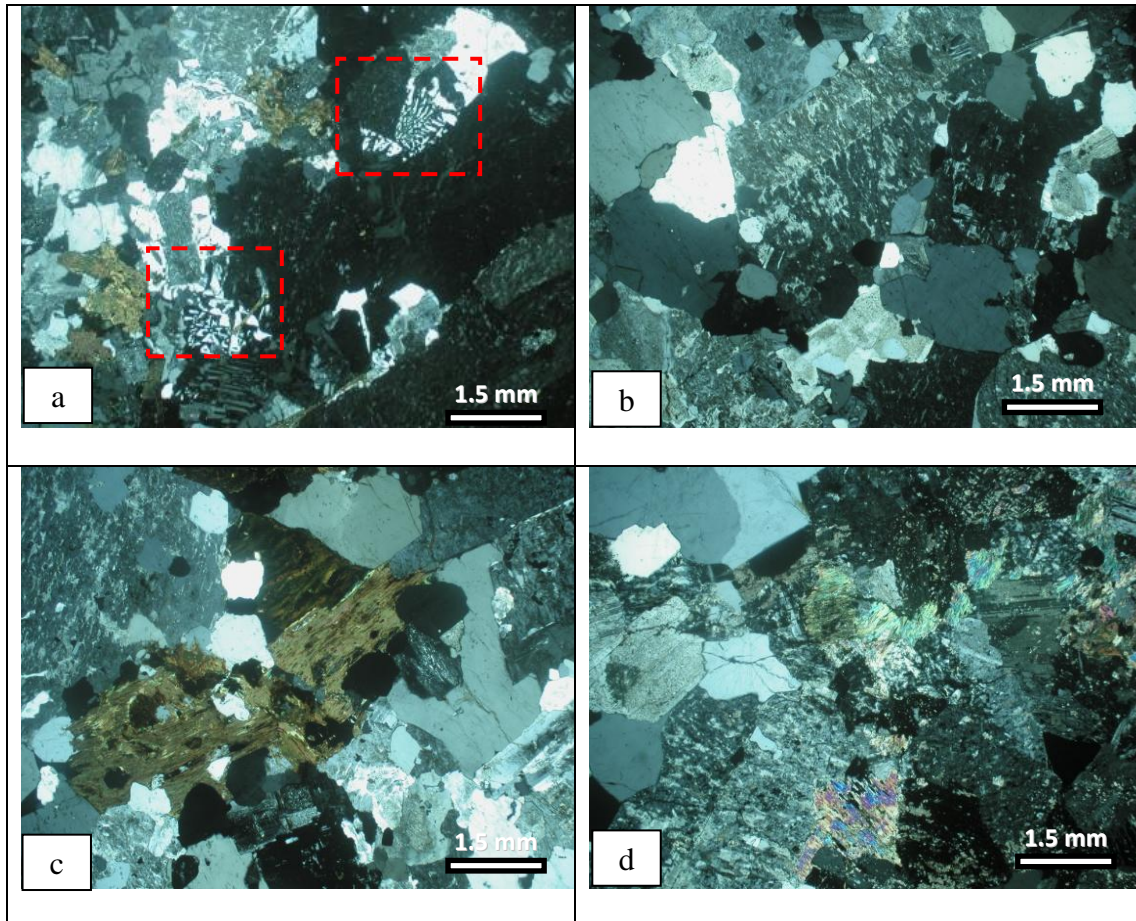


Fig. 5.7. Representative photomicrographs of the investigated Predazzo pluton rock samples. a, b) Photomicrograph showing granophyric (the two red dashed boxes) and perthitic textures which formed in subsolidus stage in biotite-granite (samples PR13, PR9). c) Photomicrograph showing chloritized biotite in biotite granite (sample PR9). d) Photomicrograph showing completely altered biotite to chlorite and sericite in Albitized granite (sample PR7). All the Photomicrographs were taken in crossed-polarized light.

5.1.2. Monzoni pluton

Monzogabbros (PA21).

These rocks are medium- to coarse-grained with hypidiomorphic inequigranular texture. The rocks are composed, in order of decreasing abundance, of plagioclase, clinopyroxene, alkali feldspar, opaques, olivine, biotite and accessory minerals (Fig. 5.8a, b).

Plagioclase is the most abundant phase. It is euhedral to subhedral medium-grained (~1-4 mm), always twinned, rarely zoned and mostly unaltered. Clinopyroxene is represented by subhedral medium- to coarse-grained (~1-5 mm) unaltered crystals. Alkali feldspar is anhedral to subhedral medium- to fine-grained (~0.5-4 mm), unaltered, untwined, usually interstitial and in some cases occurs as oikocryst, including the other minerals (poikilitic texture). Opaques are subhedral fine- to medium-grained (~0.2-1.3 mm), mainly included within other minerals (biotite, clinopyroxene and olivine) or occupying interstitial spaces. Olivine is subhedral medium-grained (~1-5 mm), usually unaltered and fractured. Biotite is anhedral to subhedral fine- to medium-grained and unaltered, occupying the interstitial spaces.

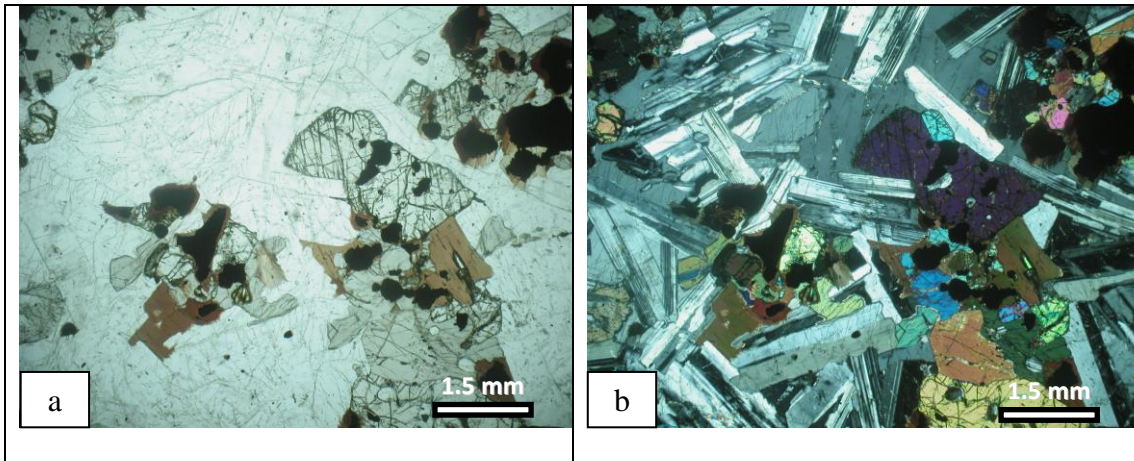


Fig. 5.8. Representative photomicrographs of the investigated Monzoni pluton rock samples. a, b) Photomicrographs showing medium- to coarse-grained with hypidiomorphic inequigranular texture in monzogabbro (sample PA21), plane-polarized and cross-polarized light respectively.

Gabbro PA 16.

This rock exhibits coarse-grained with hypidiomorphic inequigranular texture. It is made up with plagioclase, clinopyroxene, opaque, biotite and accessory minerals (in order of decreasing occurrence). Plagioclase is euhedral medium- to coarse-grained (~2-5 mm), usually unaltered or showing slight alteration to sericite and is usually twinned. Clinopyroxene is subhedral medium- to coarse-grained (~2-6 mm), unaltered, rarely twinned, with ophitic and subophitic texture (plagioclase partially or completely enclosed by clinopyroxene). Opaques are subhedral fine- to medium-grained (~0.3-1.3 mm), occupying the interstitial spaces or included within the biotite and clinopyroxene crystals. Biotite is anhedral to subhedral, fine- to medium-grained (~0.5-2.5 mm), unaltered, and interstitial.

Cumulitic gabbro PA15.

This rock is coarse-grained with orthocumulitic texture. Cumulus phases are mainly clinopyroxene with minor olivine. Intercumulus phases are primarily plagioclase and biotite with minor opaque oxides. Clinopyroxene is euhedral to subhedral coarse- to medium-grained (~2-8 mm), rarely twinned and sometimes slightly zoned. Olivine is subhedral medium-grained (~1-3 mm) and usually found fresh and only slightly altered to iddingsite along the fractures. Plagioclase is euhedral to subhedral medium-grained (~1-2 mm), slightly altered to sericite and always twinned. Biotite is subhedral to anhedral medium- to fine-grained (~0.5-2 mm) and in a few cases is slightly chloritized. Opaques are subhedral fine- to medium-grained (~0.1-1.5 mm). They occur both as interstitial phases or included within clinopyroxene and biotite.

Cumulitic olivine gabbro (PA20, PA18).

These rocks are medium- to coarse-grained. Cumulus phases are represented by clinopyroxene, plagioclase, and olivine (Fig. 5.9a, b). Clinopyroxene occurs as subhedral medium- to coarse-grained (~ 2-6 mm), unaltered and usually untwinned. Clinopyroxene oikocrysts usually include small crystals of opaques, plagioclase, olivine and biotite. Olivine crystals are subhedral medium-grained (~ 1-2.5 mm). Olivine in sample PA20 is fresh and fractured, whereas in sample PA18, it is completely altered to secondary minerals (iddingsite, bowlingite and celadonite). Plagioclase is euhedral to subhedral medium-grained (~ 1-2.5 mm), rarely zoned, and always showing twinning. Plagioclase is fresh in sample PA20 and slightly altered in PA18. Intercumulus phases are composed of plagioclase, biotite, opaques, and alkali feldspar. Plagioclase occurs as fresh subhedral fine-grained (~ 1 mm). Biotite is fresh medium-grained (~ 1-3 mm), subhedral or

sometimes anhedral, when occupying interstitial positions. Opaques occur as subhedral fine- to medium-grained ($\sim 0.5\text{-}1.3\text{ mm}$), and commonly are interstitial phases or are included in clinopyroxene, biotite and olivine. Alkali feldspar is fresh anhedral fine- to medium-grained ($\sim 0.5\text{-}1.5\text{ mm}$) and is usually found as interstitial crystals.

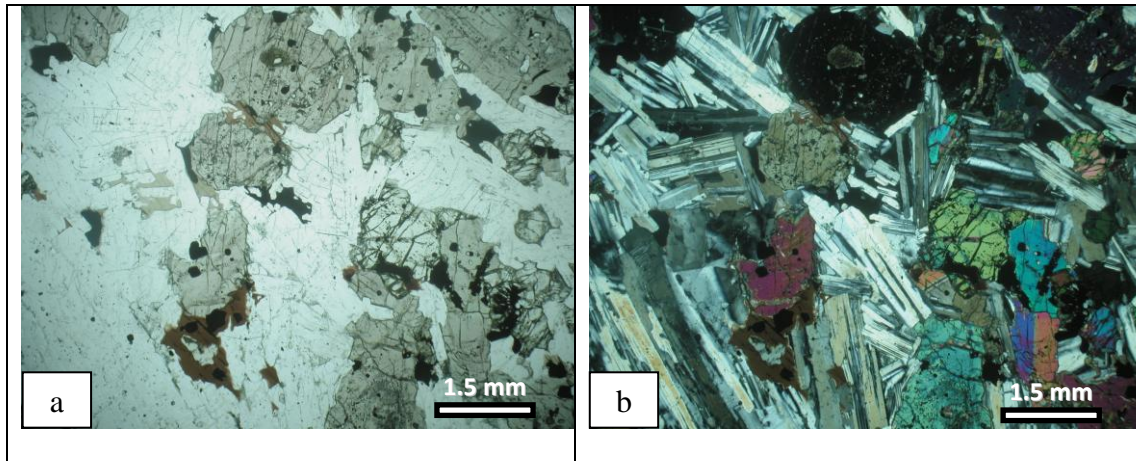


Fig. 5.9. Representative photomicrographs of the investigated Monzoni pluton rock samples. a, b) Photomicrographs showing orthocumulitic texture in Olivine gabbro (sample PA20) , plane-polarized and cross-polarized light respectively.

Monzonites (PA22, 22A, 23, 24).

These rocks are mainly located in the south-western sector of Monzoni pluton and represent the most widespread rock type. Monzonites are medium- to fine-grained and exhibit hypidiomorphic inequigranular texture. The rocks are composed, in order of decreasing abundance, of plagioclase, alkali feldspar, biotite, clinopyroxene, amphibole, opaques, quartz and accessory minerals.

Plagioclase represents the most abundant phase, with euhedral to subhedral tabular laths with variable grain size (up to 4 mm), usually twinned. Plagioclase crystals generally show slight to moderate degrees of alteration (sericitization). Alkali feldspar occurs as anhedral to subhedral crystals, rarely perthitic,

untwined with variable size (up to 5 mm) and is usually found fresh or in some cases slightly sericitized. Alkali feldspar oikocrysts usually include other minerals (plagioclase, clinopyroxene and amphibole) in a poikilitic relation (Fig. 5.10a, b). Clinopyroxene is subhedral to anhedral fine- to medium-grained (up to 2 mm), usually showing different degrees of alteration to amphibole (uralitization). Biotite is subhedral to anhedral fine- to medium-grained (up to 3 mm), generally found in a good state of preservation or sometimes showing slight to moderate alteration to chlorite. Quartz occurs as fine interstitial grains. Opaques are subhedral to anhedral fine-grained (~0.2-1 mm), and occupy the irregular interstices in between the other minerals or are included within alkali feldspar. Orthopyroxene is rarely found and is anhedral to subhedral medium-grained. Sample PA24 is more altered than the other Monzonite samples.

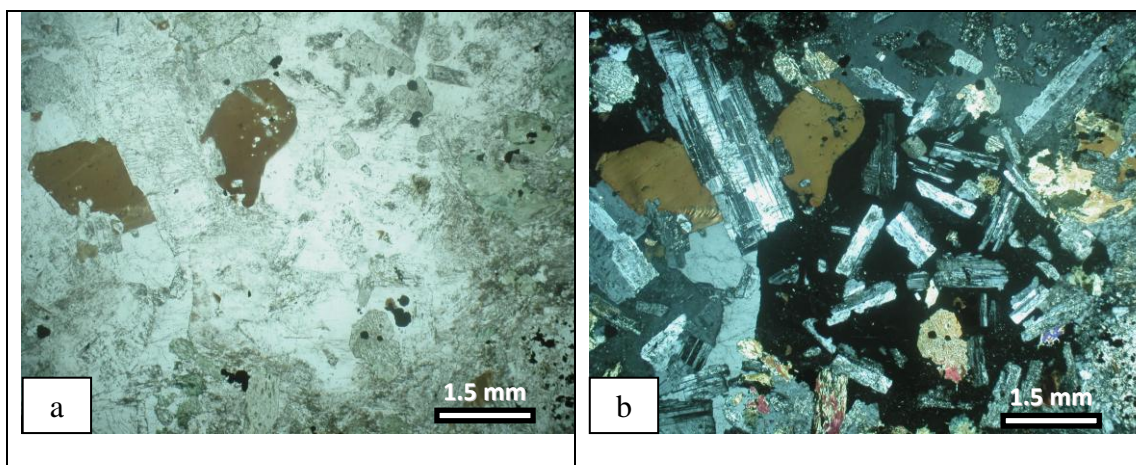


Fig. 5.10. Representative photomicrographs of the investigated Monzoni pluton rock samples. a, b) Photomicrographs showing poikilitic texture in monzonites (PA22A), plane-polarized and cross-polarized light respectively.

5.2. Magnetic susceptibility

The magnetic susceptibility and main anisotropy parameters of the analysed sites are listed in Table 5.1 and Appendix 3. In the Predazzo pluton, a bimodal distribution of k_m values is observed, which reflects the lithological differences of the analysed samples (Table 5.1). Samples taken from granites show low values, in the range of E^{-03} - E^{-05} SI, whereas samples from clinopyroxenites, gabbros and diorites show higher values (up to $1.63 E^{-01}$ SI), qualitatively suggesting a major contribution of ferromagnetic minerals to the magnetic susceptibility in the latter (Fig. 5.11). In the Monzoni pluton, monzonites and gabbroic rocks show similar values of k_m , in the range of E^{-02} SI (Fig. 5.12), suggesting a strong contribution of ferromagnetic minerals.

5.3. Magnetic Properties

The susceptibility vs. temperature heating-cooling curves reported in Figs. 5.13a-d and Appendix 4 indicate that low-Ti content titanomagnetite (TMag) and magnetite (Mag) are the main ferromagnetic minerals both in the Predazzo and Monzoni intrusive bodies, as an abrupt decrease in the susceptibility values were observed at ~ 500 - 560 °C. Another drop was noted at around 350 °C pointing to the presence of a small amount of maghemite. It was observed that the heating-cooling are not reversible, with a slight to moderate decrease in the susceptibility values of the cooling curves indicating, most likely, oxidation of the enclosed magnetic minerals. Also, a well-defined Hopkinson peak has been recorded in few samples, before a sudden drop in susceptibility which might corresponds to a partially oxidized titanomagnetite (Fig. 5.13 c, d). Hysteresis loop analyses (Fig. 5.13 e-h; Appendix 5) show that saturation magnetization

(M_s) in the investigated samples were reached at 200-300 mT indicating the predominance of soft magnetic mineral (s). Isothermal remanent magnetization (IRM) acquisition curves (Fig. 5.13 i-l; Appendix 5) indicate that the coercivity of remanence (H_{cr}) are generally less than 40 mT which, in line with the hysteresis analyses, confirm that TMag and/or Mag are the main magnetic minerals. The grain size of the magnetic minerals was deduced from the hysteresis parameters, M_s , M_{rs} , H_{cr} , and H_c , with plotting them in the Day plot (Day et al., 1977). The samples are mainly located within the pseudo-single domain (PSD) field. However, the trend of the plotted values suggesting a mixture of SD, MD is present (Fig. 5.14).

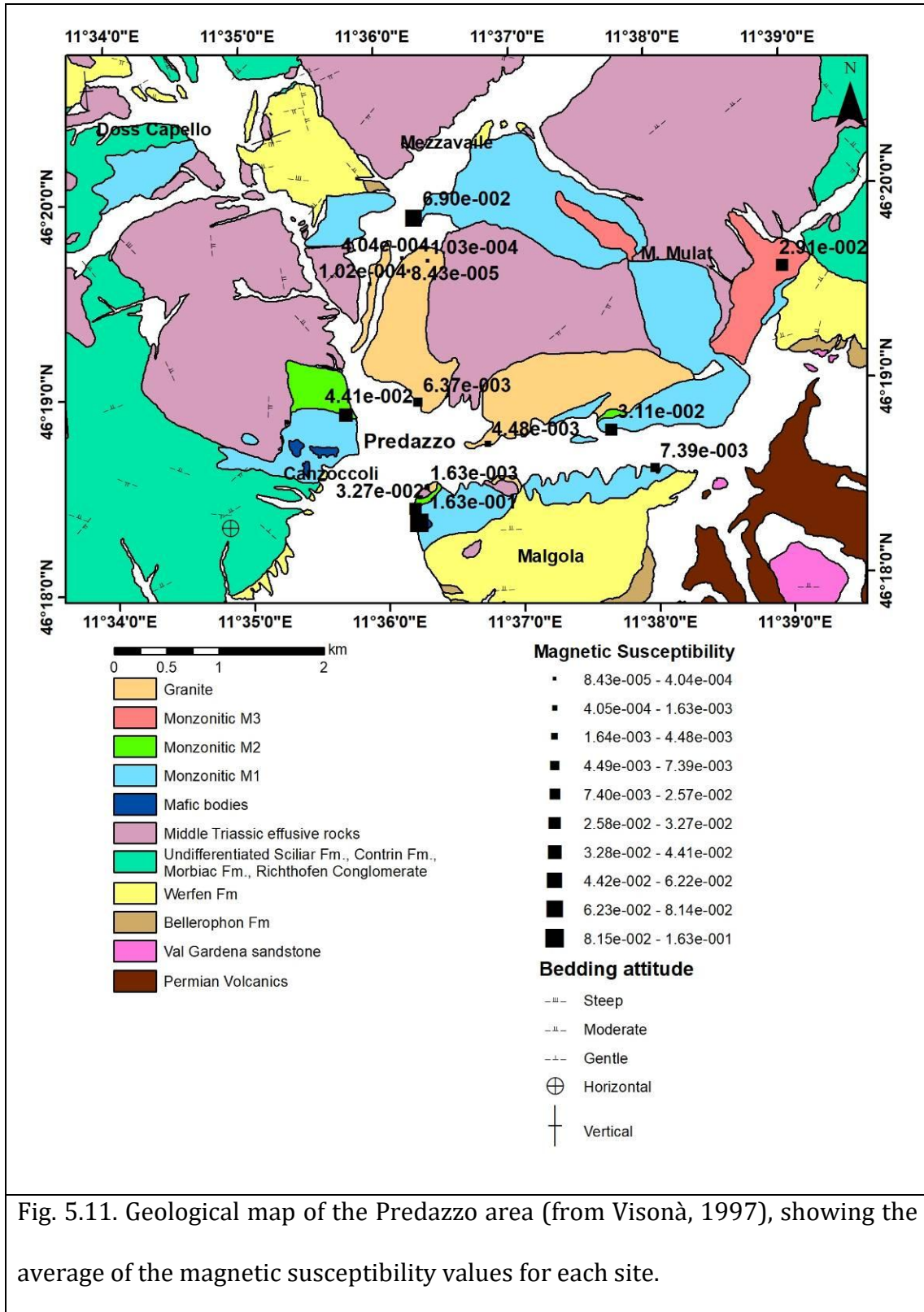


Fig. 5.11. Geological map of the Predazzo area (from Visonà, 1997), showing the average of the magnetic susceptibility values for each site.

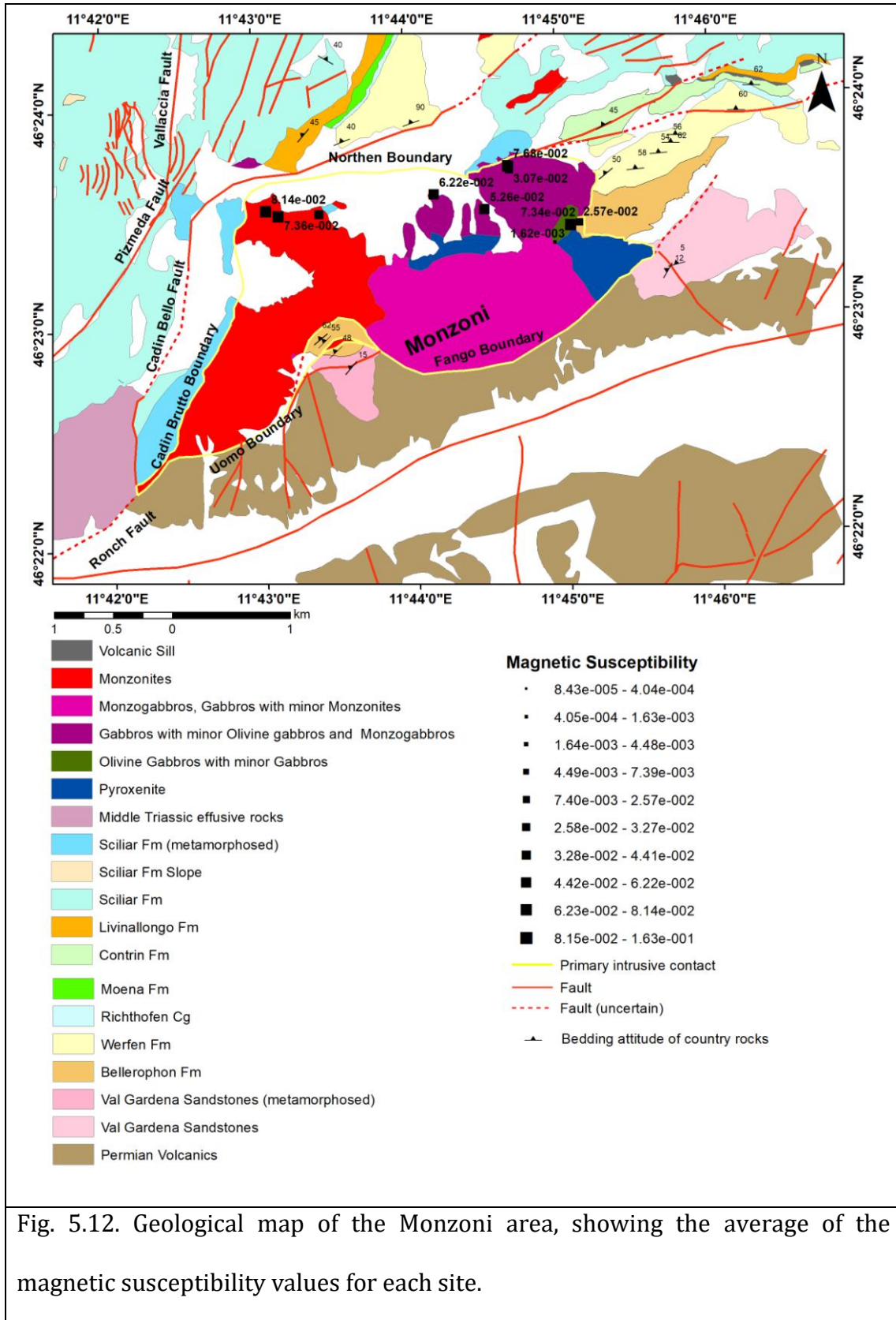


Fig. 5.12. Geological map of the Monzoni area, showing the average of the magnetic susceptibility values for each site.

CHAPTER FIVE

STRUCTURAL AND AMS STUDIES

Site	Lithology	Area	Lat	Long	N	Km	L	std	F	std	Pj	std	T	std	D,I (k ₁)	α ₉₅	D,I (k ₃)	α ₉₅
PA01	Albitized granite	Predazzo	46°19'41"N	11°36'09"E	10	4.04E-04	1.002	0.01	1.010	0.011	1.013	0.018	0.667	0.461	246,68	74.7/36.4	342.2	40.9/21.3
PA02	Monzonites	Predazzo	46°19'53"N	11°36'15"E	8	6.90E-02	1.016	0.006	1.032	0.006	1.049	0.006	0.318	0.217	351,73	11.3/7.8	83,7	9.7/5.4
PA03	Biotite granite	Predazzo	46°18'42"N	11°36'45"E	8	4.48E-03	1.011	0.009	1.018	0.013	1.030	0.01	0.256	0.443	264,11	23.8/20.5	4,40	24.1/18.5
PA04	Albitized granite	Predazzo	46°19'39"N	11°36'21"E	6	1.03E-04	1.008	0.002	1.018	0.005	1.026	0.006	0.394	0.188	177,67	23.5/3.6	286,8	11.2/5.6
PA05	Albitized granite	Predazzo	46°19'36"N	11°36'13"E	7	8.43E-05	1.009	0.01	1.025	0.015	1.035	0.02	0.483	0.329	299,71	35.9/8.2	142,17	18.1/5.9
PA06	Diorite	Predazzo	46°18'52"N	11°35'44"E	9	4.41E-02	1.004	0.006	1.034	0.008	1.042	0.008	0.809	0.284	108,10	37.2/4.7	205,32	6.3/4.1
PA07	Biotite granite	Predazzo	46°18'56"N	11°36'14"E	5	6.37E-03	1.007	0.008	1.027	0.006	1.036	0.012	0.577	0.184	313,20	45.8/13.3	75,55	16.1/9.3
PA08	Monzodiorite	Predazzo	46°18'23"N	11°36'09"E	8	3.72E-02	1.004	0.003	1.013	0.006	1.018	0.006	0.496	0.286	226,17	39.4/7.7	123,37	10.2/8.1
PA09	Monzodiorite	Predazzo	46°18'46"N	11°37'40"E	8	3.11E-02	1.015	0.003	1.009	0.004	1.024	0.003	-0.244	0.283	79,2	12.6/4.1	344,71	12.3/3.7
PA10	Monzonites	Predazzo	46°18'38"N	11°37'59"E	8	7.39E-03	1.01	0.007	1.007	0.005	1.017	0.012	-0.204	0.262	132,48	13.1/4	323,41	9.2/5.2
PA11	Monzonites to Syenite	Predazzo	46°18'52"N	11°39'26"E	9	2.91E-02	1.025	0.01	1.02	0.09	1.046	0.012	-0.099	0.265	251,81	18.9/7.4	151,2	16.6/7.1
PA12	Clinopyroxenite	Predazzo	46°18'16"N	11°36'11"E	8	1.63E-01	1.003	0.01	1.044	0.015	1.052	0.015	0.858	0.318	83,32	68.5/18.3	185,19	18.4/12.6
PA13	Biotite granite	Predazzo	46°18'29"N	11°36'17"E	4	1.63E-03	1.008	0.007	1.027	0.017	1.037	0.015	0.542	0.423	174,3	37.2/11.8	81,46	17.6/9.4
PA14	Monzodiorite	Monzoni	46°19'33"N	11°35'54"E	9	2.57E-02	1.017	0.004	1.006	0.009	1.024	0.006	-0.495	0.409	357,9	13.9/6.9	104,63	40.1/9.6
PA15	Gabbros	Monzoni	46°23'25"N	11°45'07"E	9	7.34E-02	1.003	0.013	1.037	0.039	1.045	0.046	0.850	0.55	348,82	70.6/14.9	139,7	24.5/15.0
PA16	Gabbros (cumulate)	Monzoni	46°23'25"N	11°45'04"E	9	1.63E-03	1.01	0.012	1.034	0.025	1.047	0.028	0.532	0.36	30,40	25.4/6.5	137,19	12.0/4.8
PA17	Albitized granite	Predazzo	46°23'20"N	11°44'57"E	9	1.02E-04	1.003	0.004	1.006	0.004	1.010	0.007	0.334	0.413	70,32	35.2/15.9	177,25	24.7/17.8
PA18	Olivine gabbros	Monzoni	46°23'41"N	11°44'39"E	8	7.68E-02	1.017	0.009	1.036	0.01	1.055	0.011	0.351	0.272	118,36	18.4/6.3	322,51	16.4/3.8
PA19	Olivine gabbros	Monzoni	46°23'40"N	11°44'40"E	8	3.07E-02	1.022	0.005	1.026	0.003	1.049	0.006	0.084	0.12	315,17	7.3/3.2	128,73	6.4/3.8
PA20	Olivine gabbros	Monzoni	46°23'30"N	11°44'30"E	9	5.26E-02	1.024	0.01	1.049	0.017	1.075	0.015	0.344	0.239	110,7	17.8/11.0	243,78	18.6/7.6
PA21	Monzogabbros	Monzoni	46°23'34"N	11°44'10"E	9	6.22E-02	1.014	0.014	1.032	0.018	1.048	0.01	0.383	0.481	335,15	19.1/11.9	227,50	25.0/10.1
PA22	Monzonites	Monzoni	46°23'30"N	11°43'24"E	6	3.73E-02	1.029	0.007	1.013	0.011	1.043	0.016	-0.364	0.185	130,72	5.7/4.4	4,11	37.6/2.8
PA23	Monzonites	Monzoni	46°23'30"N	11°43'08"E	8	7.36E-02	1.019	0.007	1.019	0.015	1.038	0.013	-0.02	0.47	141,55	10.8/7.1	26,16	14.8/7.8
PA24	Monzonites	Monzoni	46°23'31"N	11°43'03"E	9	8.14E-02	1.016	0.007	1.031	0.014	1.049	0.021	0.325	0.149	102,19	22.4/11.7	0,30	17.3/11.0

Table 5.1. Location of sampling sites in the Predazzo and Monzoni plutons and measured magnetic parameters. N = number of specimens; K_m = (k_{max} + k_{int} + k_{min}) / 3 (mean susceptibility, in SI units); L=k₁ /k₂; F=k₃ /k₁ Pj = exp {2[(η₁ - η)² + (η₂ - η)² + (η₃ - η)²]}^{1/2} (corrected anisotropy degree; Jelinek. 1981); T = 2(η₂ - η₃) / (η₁ - η₃) - 1 (shape factor; Jelinek. 1981); η₁ = lnk₁; η₂ = lnk₂; η₃ = lnk₃; η = (η₁ + η₂ + η₃) / 3; D, I (k₁) = declination and inclination of the maximum susceptibility axis (geographic coordinates); D,I (k₃) = declination and inclination of the minimum susceptibility axis (geographic coordinates); α₉₅: confidence angles; std: standard deviation. Samples PR10, PR11a,b,c and PR12, not investigated for AMS, were taken close to sample PA12, whereas sample PR14c was taken close to sample PA08.

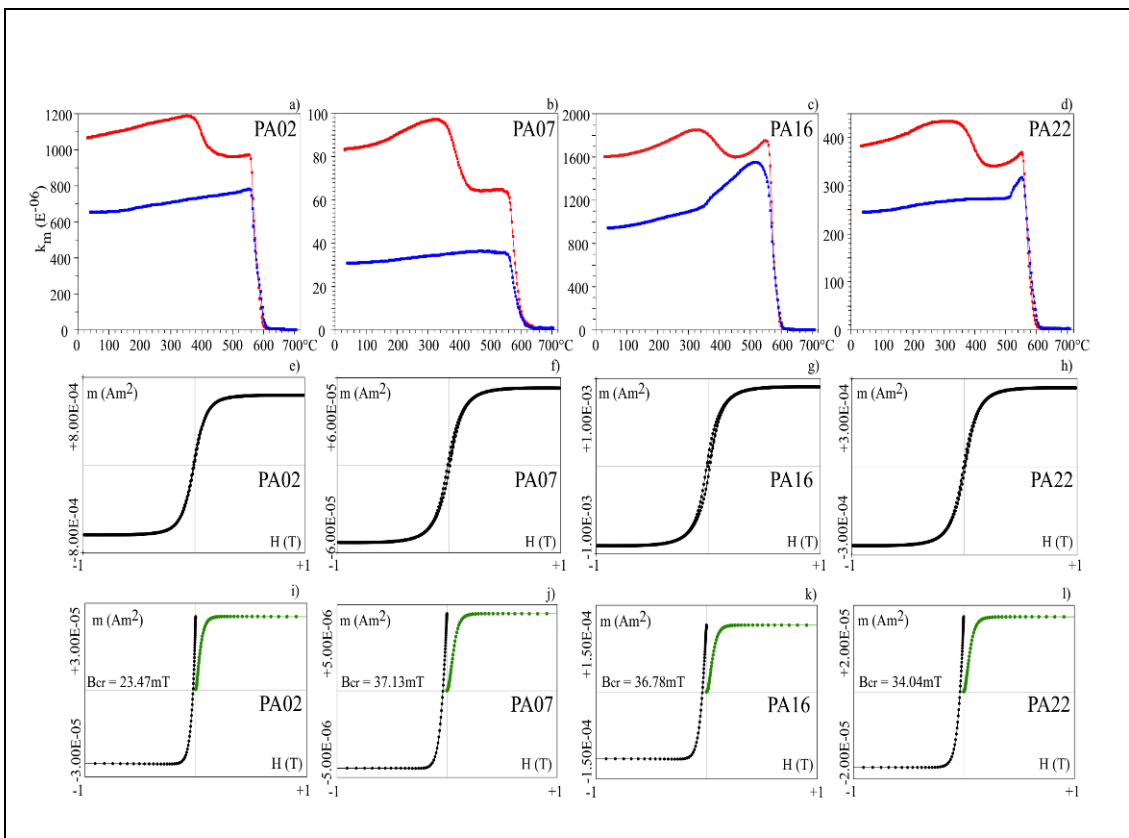


Fig. 5.13. Magnetic mineralogy results for selected samples from Predazzo and Monzoni plutons. a-d) Thermomagnetic curves; red and blue lines represent the heating-cooling cycle respectively. e-h) Hysteresis loops, corrected for the paramagnetic linear trend. i-l) IRM acquisition curves (green lines) and backfield applications (black lines).

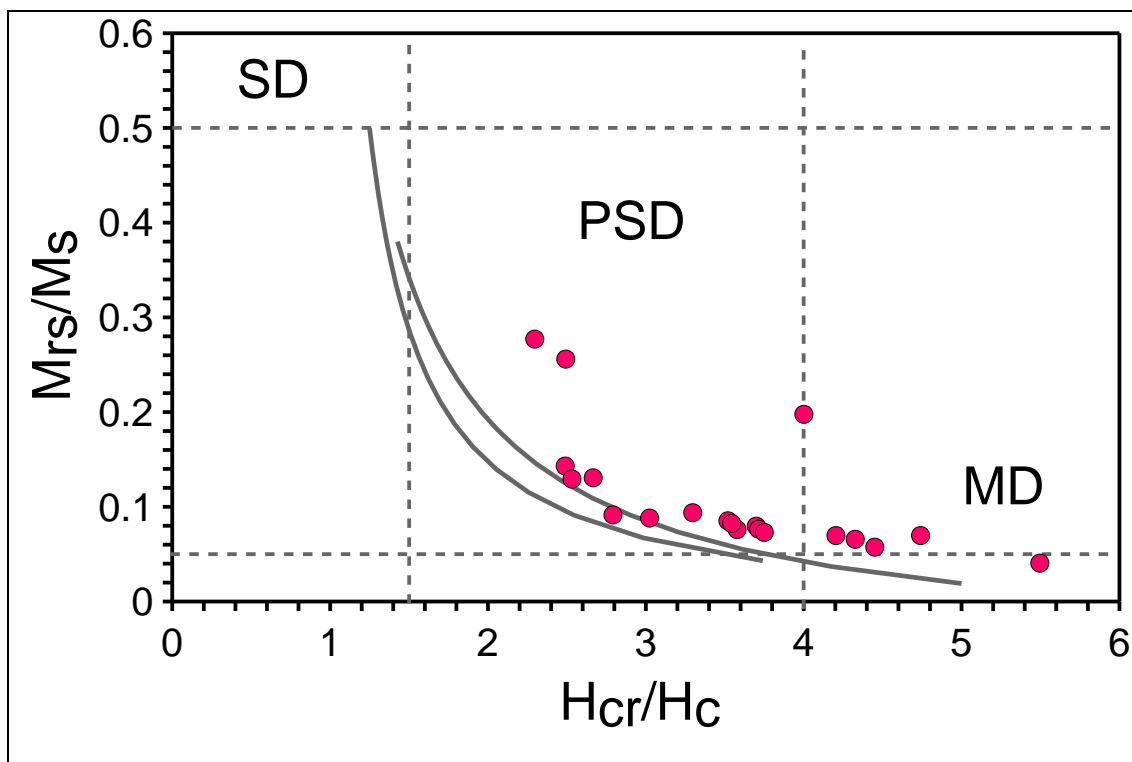


Fig. 5.14. Day et al. (1977) type plot for the determination of magnetic grain size (M_r , remanent magnetization; M_s , saturation magnetization; H_{cr} , remanent magnetic coercivity; H_c , magnetic coercivity). Different fields in the figure refer to the domain state of magnetite, SD: single domain, PSD: pseudo-single domain, MD: multi-domain. Grey curved lines represent theoretical SD-MD mixing curves for magnetite (after Dunlop, 2002).

5.4. AMS Shape Parameters (T)

In most of the sites from Predazzo and Monzoni plutons, the magnetic foliation is well developed and its values (F) are greater than those of the magnetic lineation (Table 5.1). Magnetic shape factors (T) in most of the samples show a dominant oblate shape, and for few samples, it shows prolate and triaxial shape (Figs. 5.15, 5.16, 5.19a, b).

5.5. Degree of anisotropy (P_j)

In Predazzo pluton, degree of anisotropy (P_j) ranges from 1.017 to 1.052 in Monzonitic units M1, M2 and M3. The granitic unit displays anisotropies ranging from 1.01 to 1.036. In the Monzoni pluton, P_j ranges from 1.024 to 1.075 in gabbroic rocks, whereas P_j ranges from 1.038 to 1.049 in monzonite rocks (Fig. 5.17, 5.18). Generally, P_j does not correlate with the magnetic susceptibility (K_m ; Fig. 5.19c). Also, no systematic lateral variations of P_j have been observed on the maps (Fig. 5.17, 5.18).

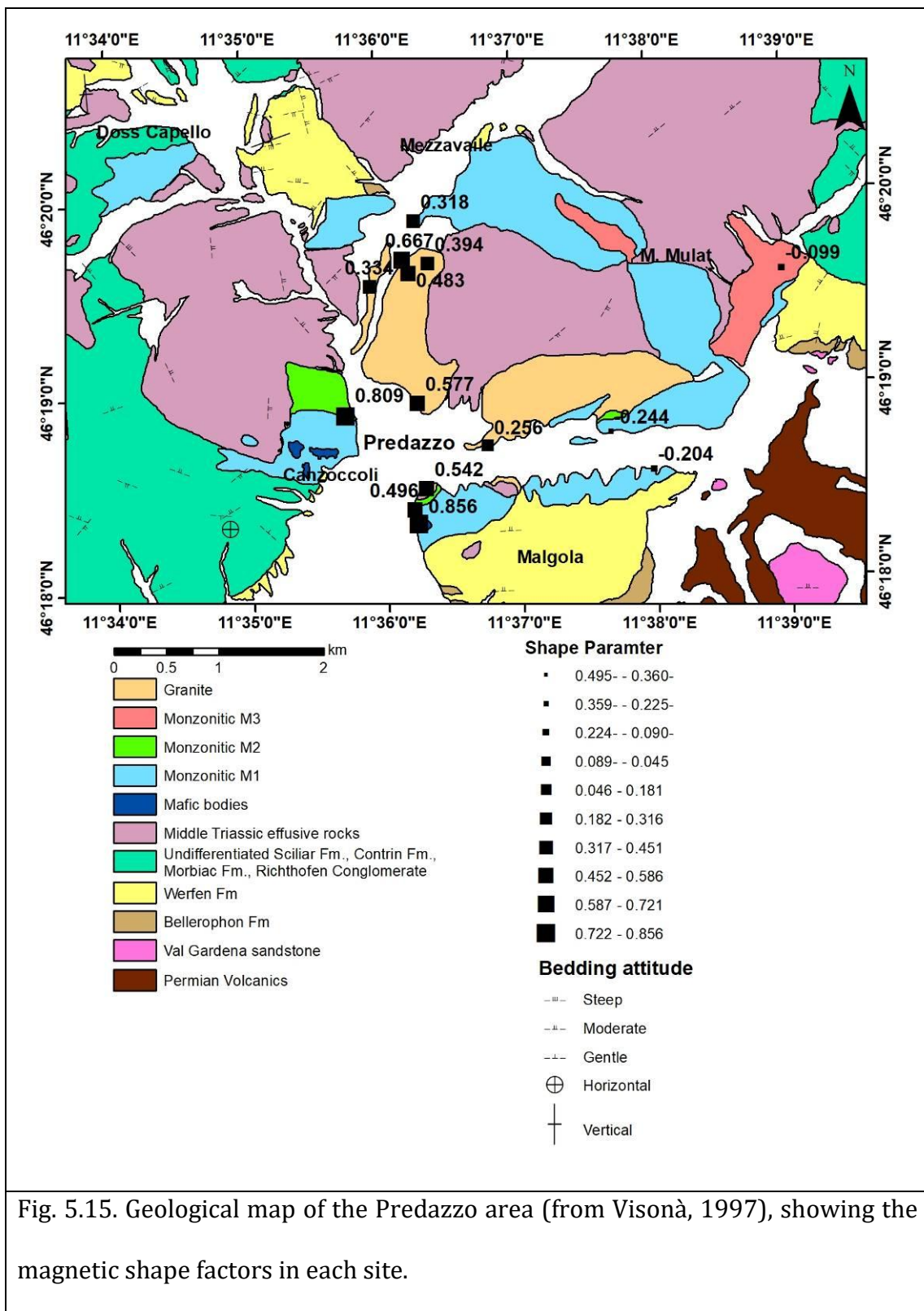


Fig. 5.15. Geological map of the Predazzo area (from Visonà, 1997), showing the magnetic shape factors in each site.

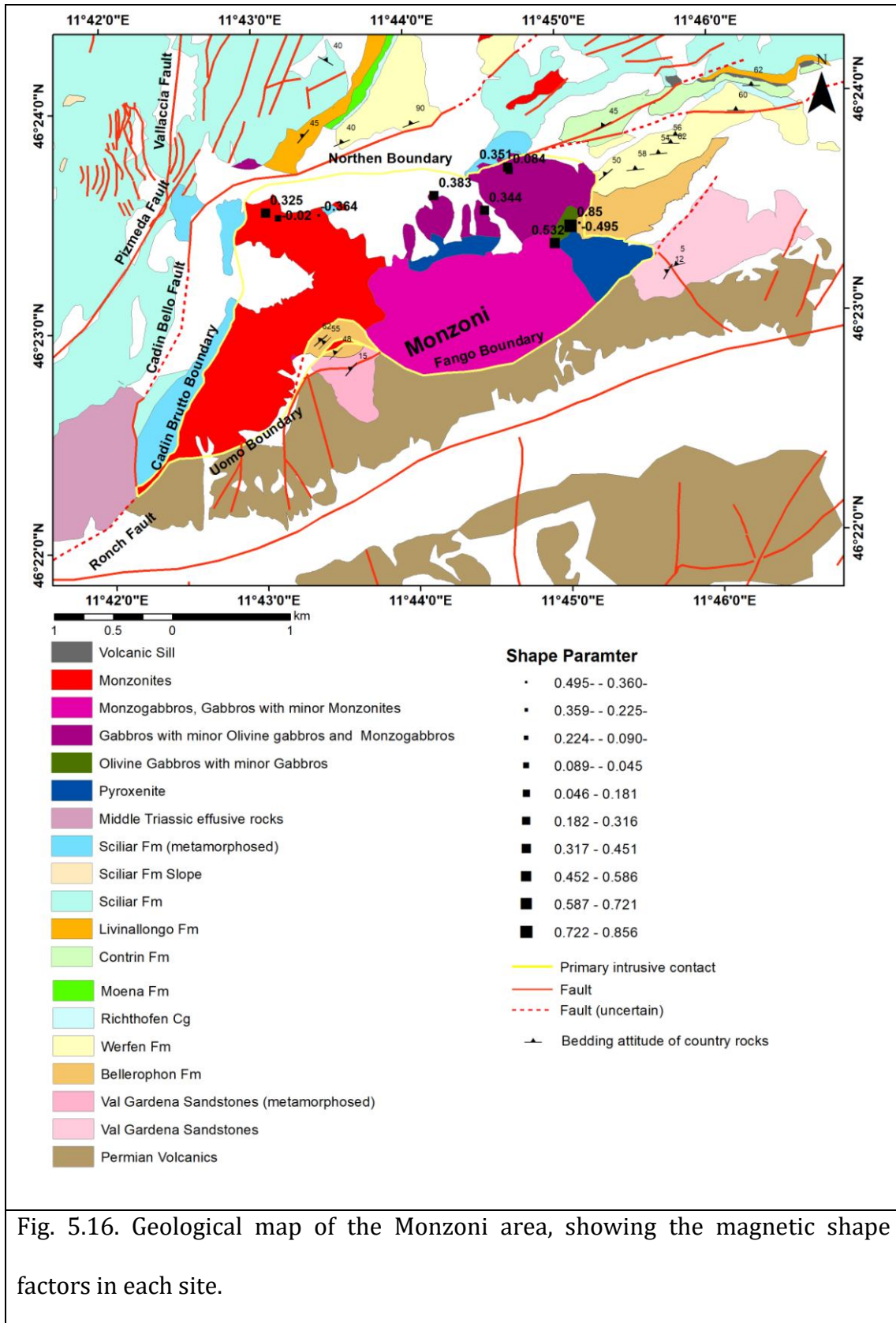


Fig. 5.16. Geological map of the Monzoni area, showing the magnetic shape factors in each site.

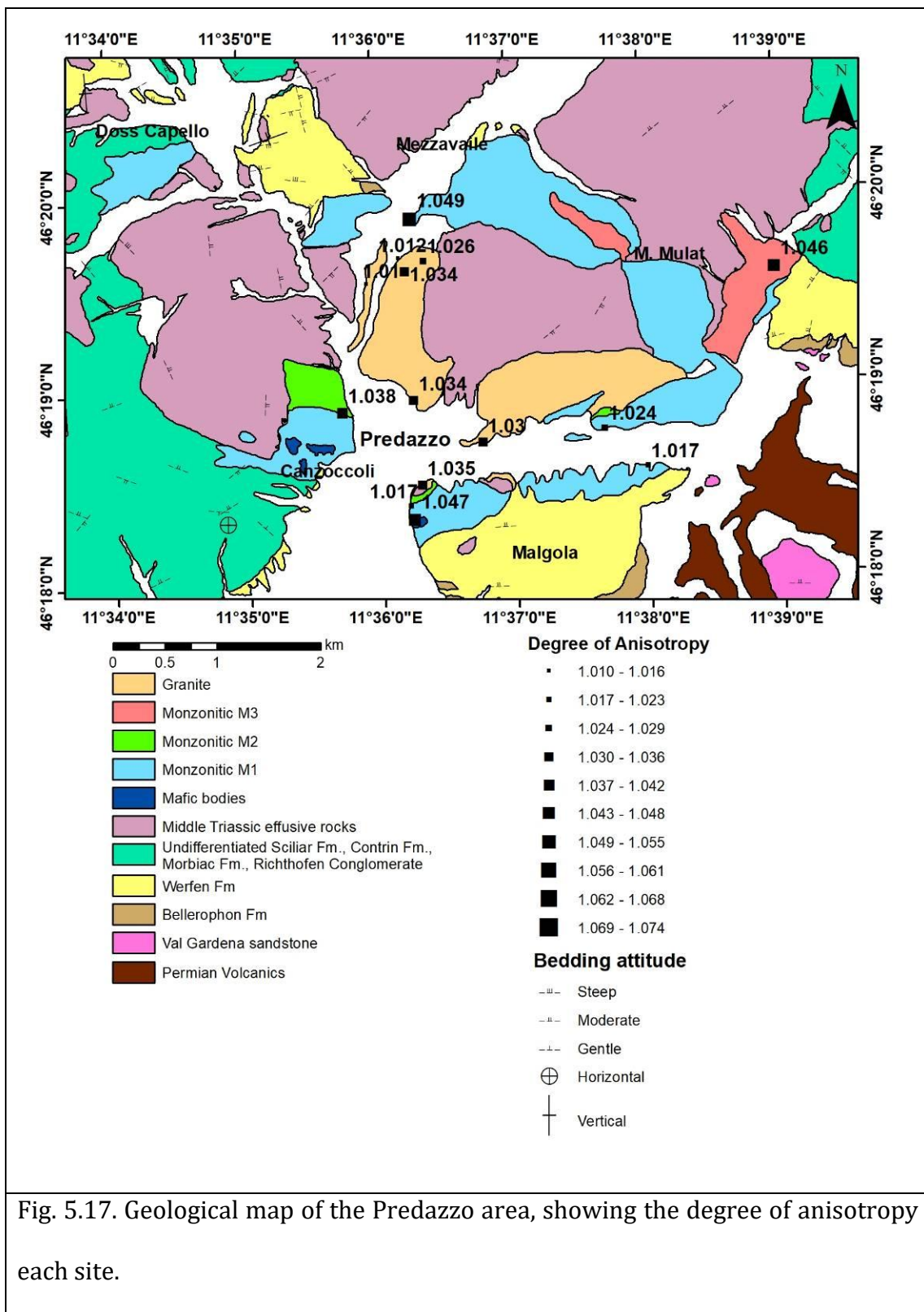


Fig. 5.17. Geological map of the Predazzo area, showing the degree of anisotropy each site.

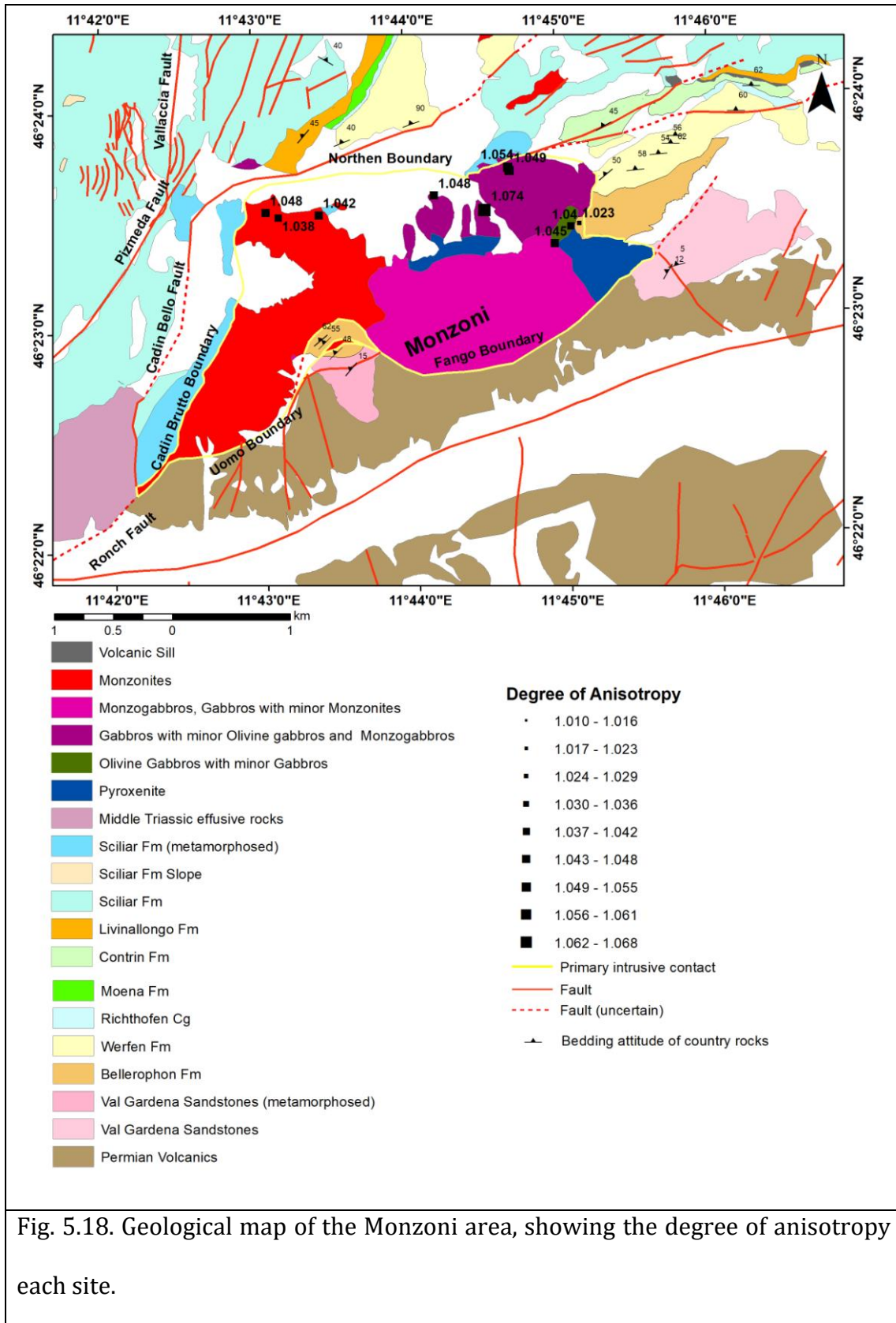
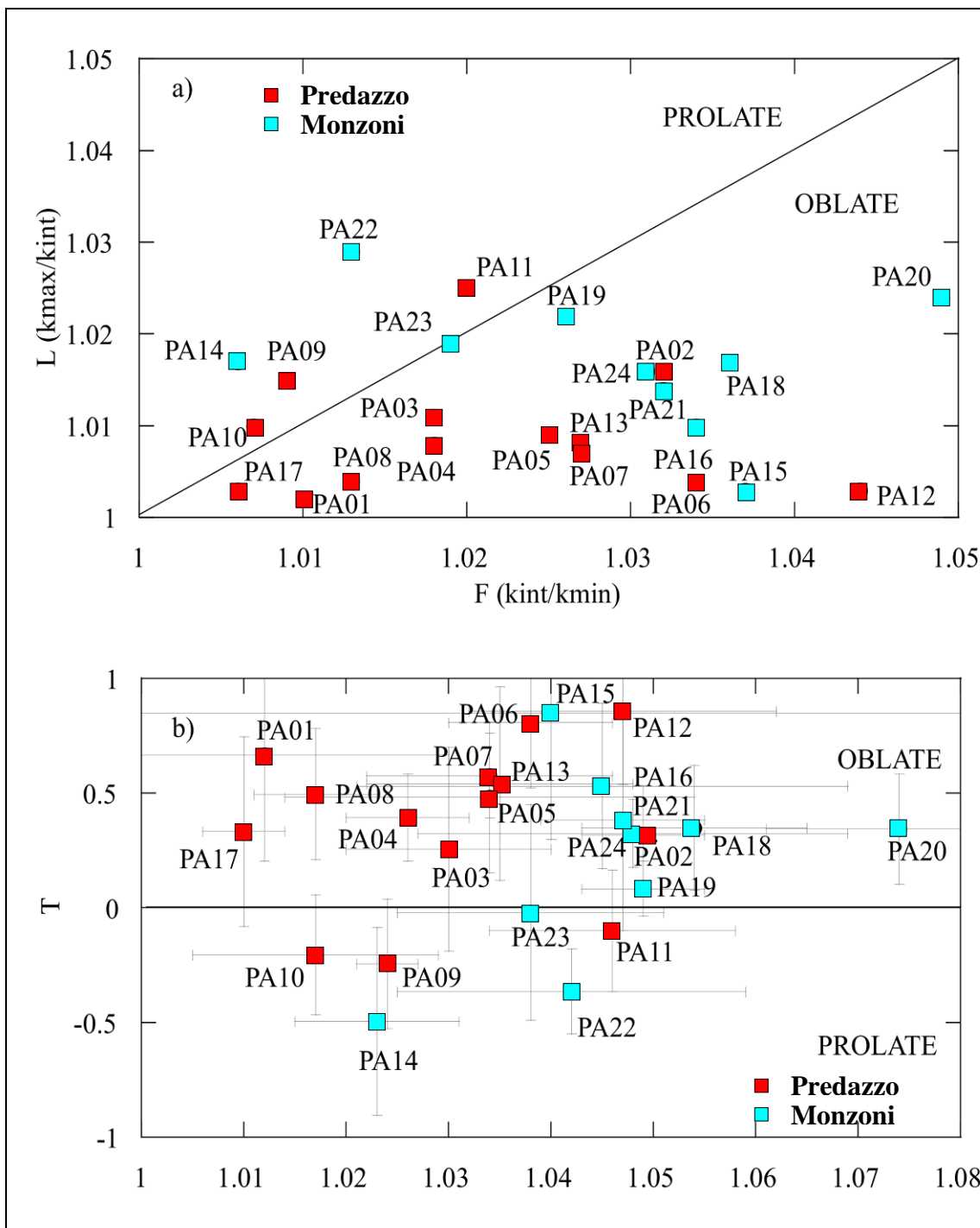


Fig. 5.18. Geological map of the Monzoni area, showing the degree of anisotropy each site.



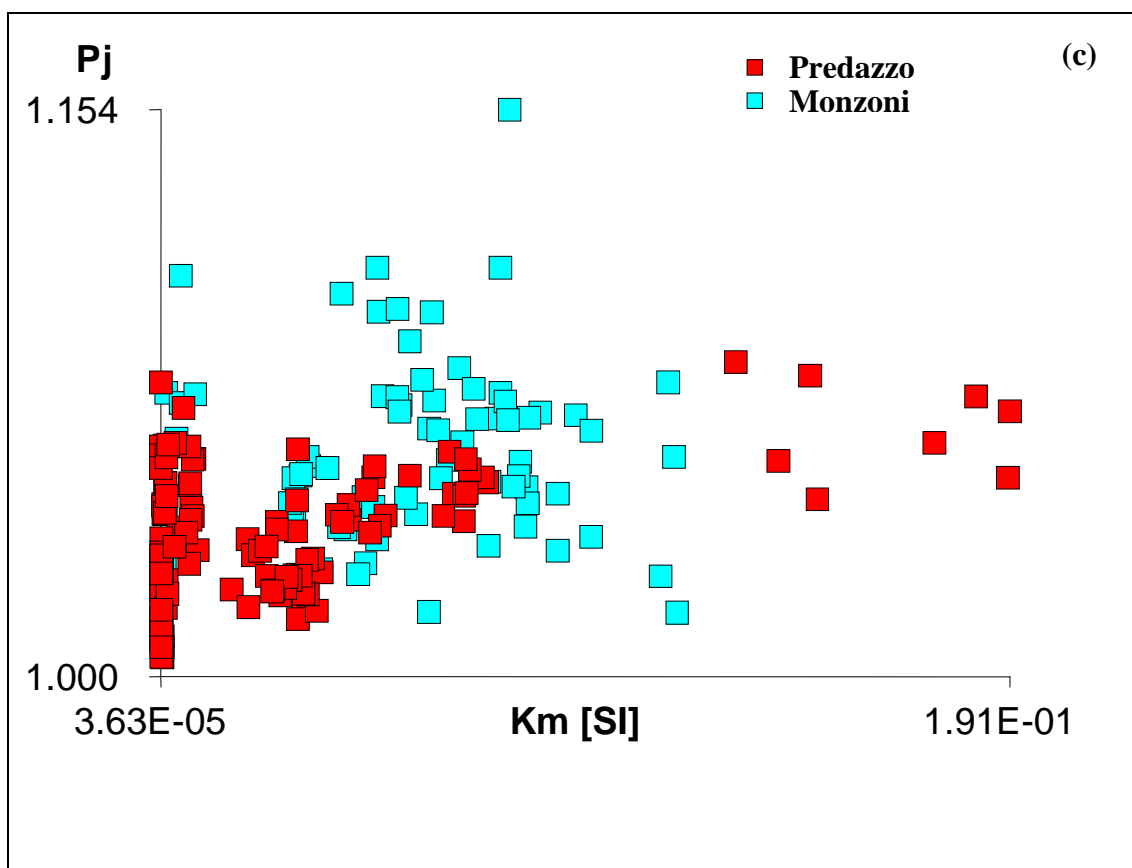


Fig. 5.19. Shape parameters for the analysed sites from the Predazzo and Monzoni plutons: a) F-L diagram; b) Pj-T diagram; c) the relation between magnetic susceptibility (Km) and degree of anisotropy (Pj).

5.6. AMS foliation and lineation

In the Predazzo pluton, the Monzonitic Unit M1 has been sampled in different sites along the southern (PA08, PA09, PA10), the south-western (PA06) and north-western (PA02) borders of the plutonic body (Fig. 5.1). In all these sites AMS shows a well-defined magnetic foliation, which ranges from moderately dipping (35°) to vertical (88°) and strikes almost parallel to the intrusive borders. In particular the magnetic foliation is oriented WSW-ENE at sites PA08, PA09, and PA10, WNW-ESE at site PA06, and N-S at site PA02 (Figs. 5.20 and 5.22a, e, f). Furthermore, we sampled a site (PA12) in one of the mafic bodies

that crops out along the western part of the pluton. The magnetic foliation dips outward the intrusive body at sites PA02, PA09 and PA10 and toward the boundary within Monzonitic Unit M2 at sites PA06, PA08 and in the mafic body site PA12. The magnetic lineation shows gentle to sub-horizontal dipping, and is variably oriented respect to the intrusive body, ranging from sub parallel to the boundary (PA02, PA06, PA08, PA09) to orthogonal to it (PA10) to disperse around a great circle (PA12). The Monzonitic Unit M3 has been sampled at one site (PA11), located in the eastern part of the pluton. In this site, magnetic foliation is very well defined and is sub-vertical with a WSW-ENE direction, parallel to the elongation of this unit. Magnetic lineation is also well defined and sub-vertical (Figs. 5.20 and 5.22d).

The granite unit of the Predazzo pluton has been sampled in 7 sites, located in the north-western (PA01, PA04, PA05 and PA17), in the south and south-western (PA03, PA07 and PA08) boundaries of the body (Fig. 5.1). The magnetic foliation is well defined in all the sites, but in site PA01 where it shows a significant dispersion around an E-W direction. In the north-western part of the intrusion magnetic foliation is oriented NNE-SSW at sites PA04 and PA05, where it is sub-vertical and dips toward the internal and external border of the intrusive body, respectively (Figs. 5.20a and 5.22b, c), whereas at site PA17 the magnetic foliation is E-W oriented and dips toward the north. In the south-western part of the granitic body, the magnetic foliation is also parallel to the border of the intrusion, being W-E oriented at site PA03 and NW-SE at site PA07. In both sites, the foliation is dipping toward the external part of the intrusion. The magnetic lineation is very poorly defined at sites PA01 and PA07, whereas is

sub-vertical at sites PA04 and PA07. At sites PA03 and PA17 the magnetic lineation is poorly grouped or not well-clustered with a sub-horizontal E-W orientation (Figs. 5.20b and 5.22a-f).

In the Monzoni pluton we sampled mafic rocks in the eastern part of the pluton, and monzonites in the western part of the body (Fig. 5.2). In the monzonite sites (PA22, PA23, and PA24), the magnetic foliation is well defined, with a W-E orientation and a sub-vertical attitude. In these sites, the magnetic lineation is well defined and mostly shows sub-vertical dip (Figs. 5.21 and 5.22j). In the mafic rocks, the magnetic foliation is well defined and varies from gently dipping toward the SE (PA18) to sub-horizontal (PA19, PA20, PA21). In all these sites, the magnetic lineation is well defined with a WNW-ESE orientation (Figs. 5.21 and 5.22i, k, l). At sites located in the eastern part of the pluton, the magnetic foliation is well defined at sites PA15 and PA16, where it shows a NE-SW orientation and a step dipping to NW. At site PA14 the magnetic foliation is poorly defined, being dispersed in a E-W direction. Magnetic lineation is well defined at sites PA14 and PA16, where it is sub-horizontal and N-S oriented respectively, whereas it is poorly defined at site PA15 (Figs. 5.21 and 5.22g-i).

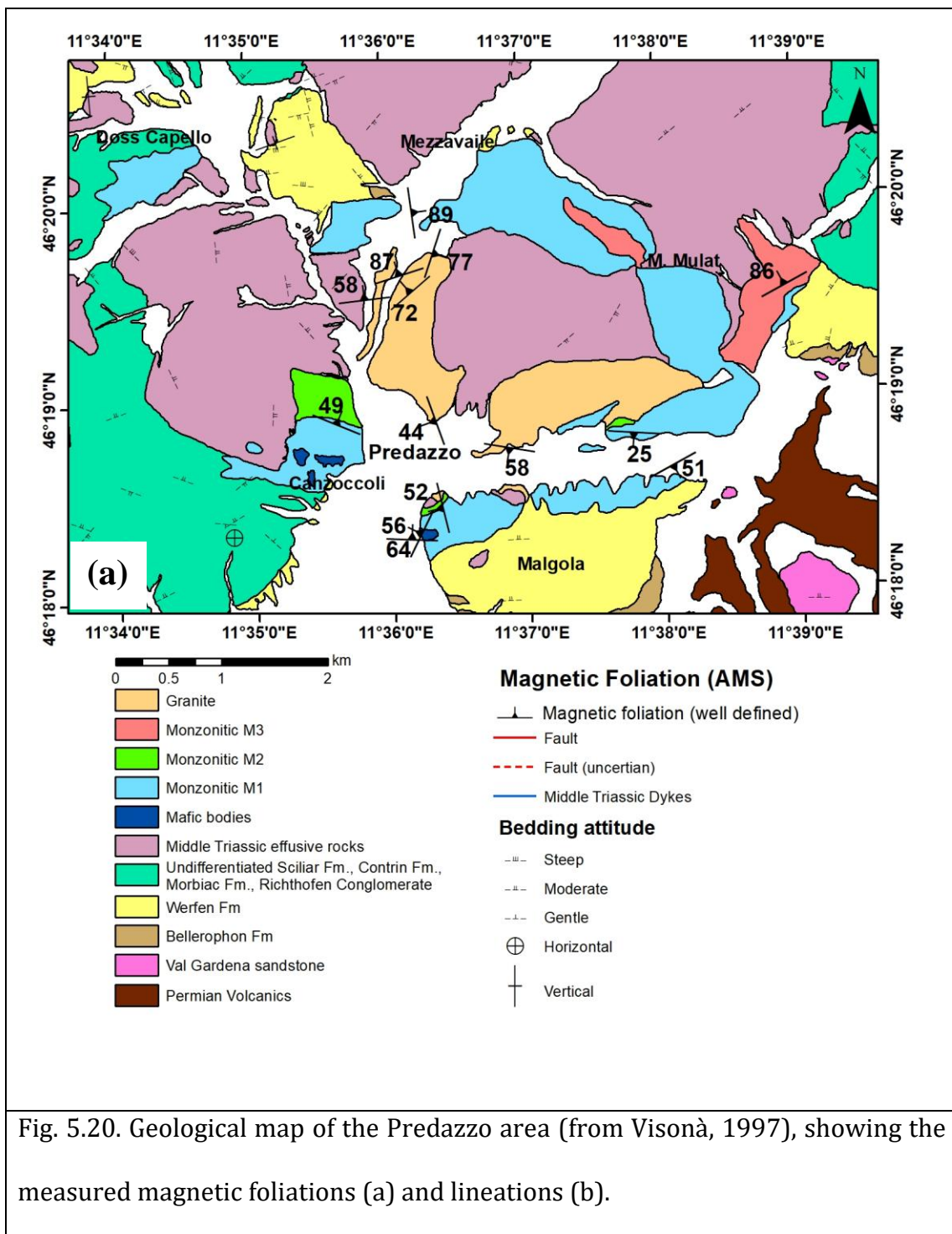
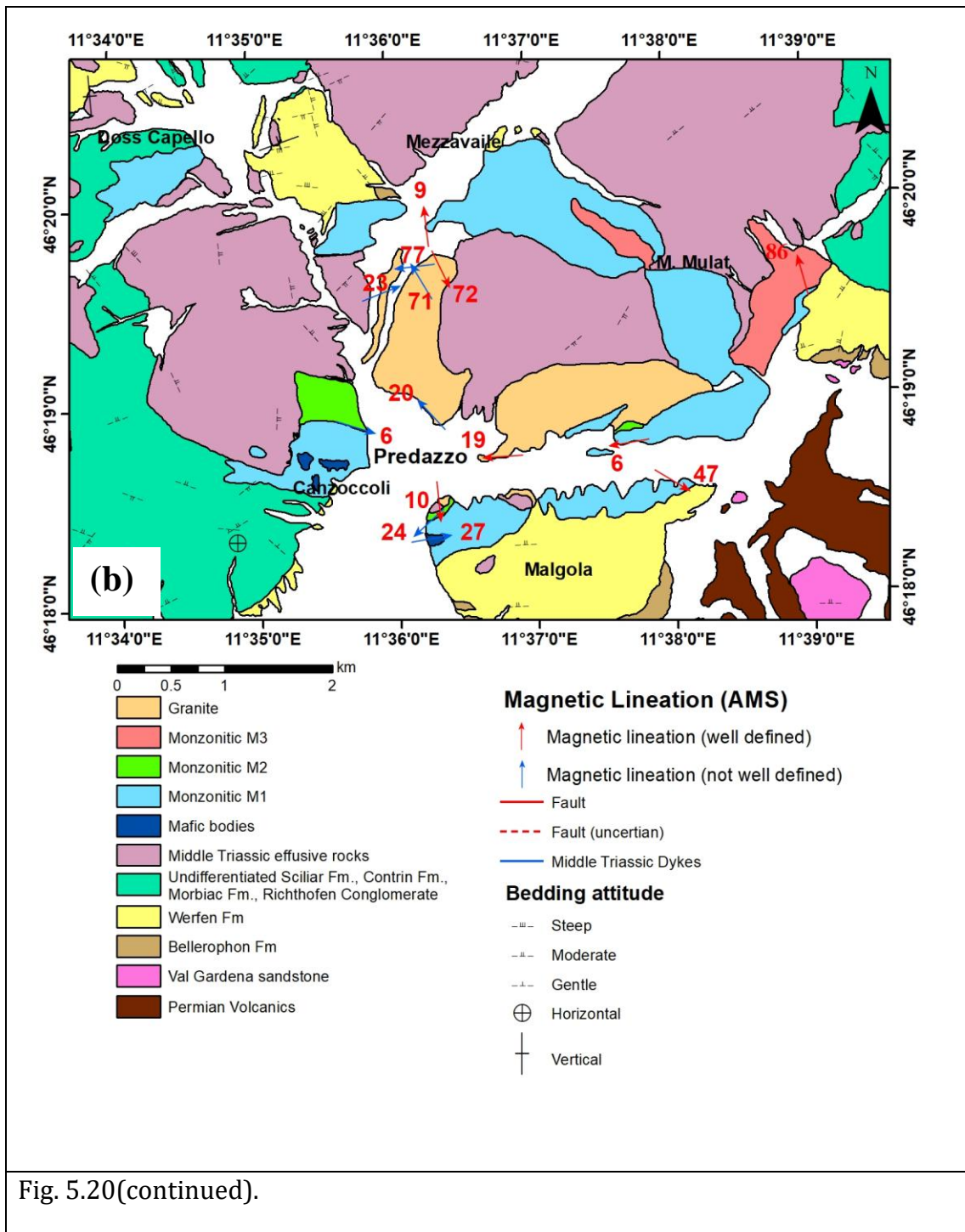


Fig. 5.20. Geological map of the Predazzo area (from Visonà, 1997), showing the measured magnetic foliations (a) and lineations (b).



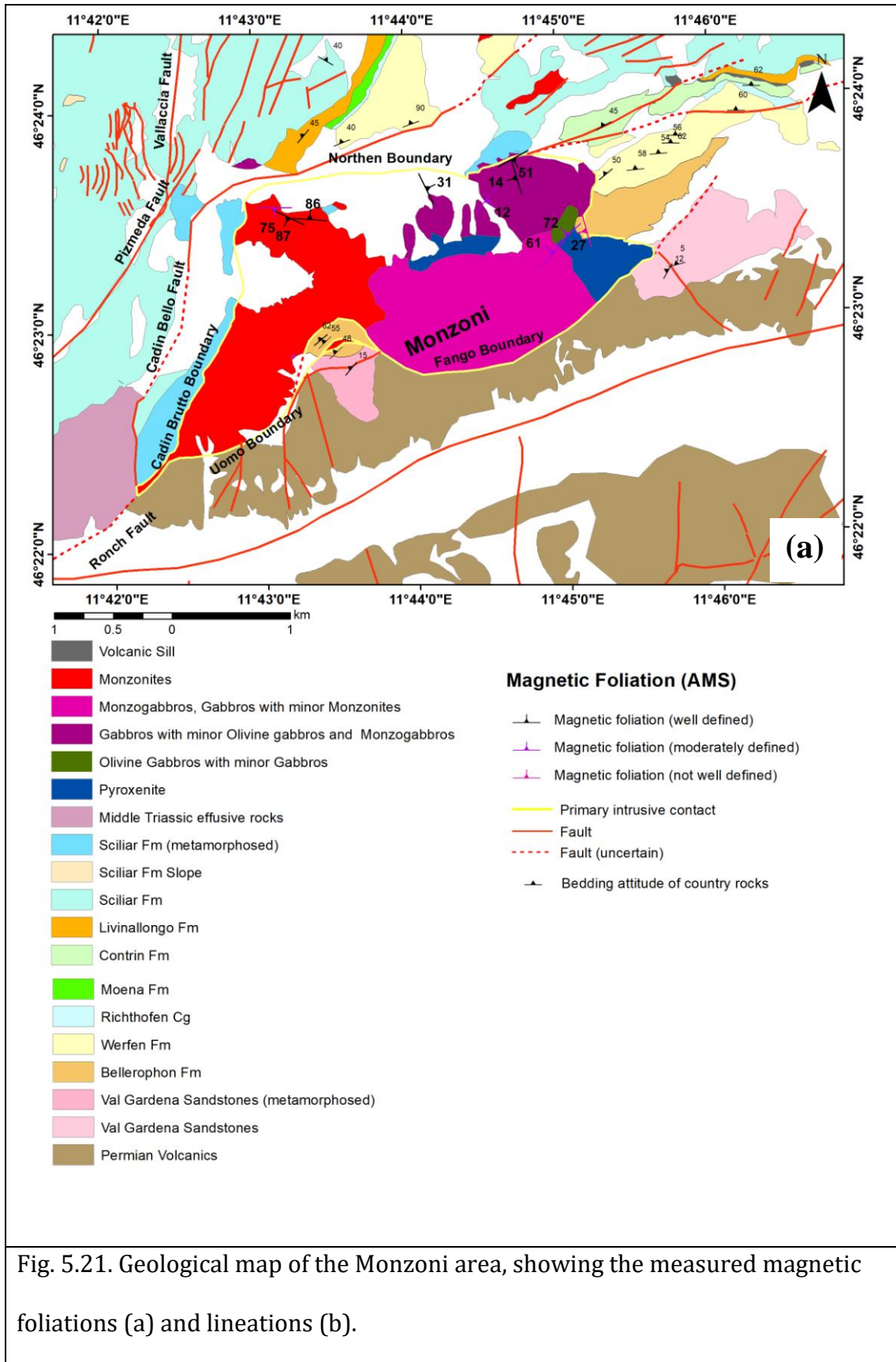


Fig. 5.21. Geological map of the Monzoni area, showing the measured magnetic foliations (a) and lineations (b).

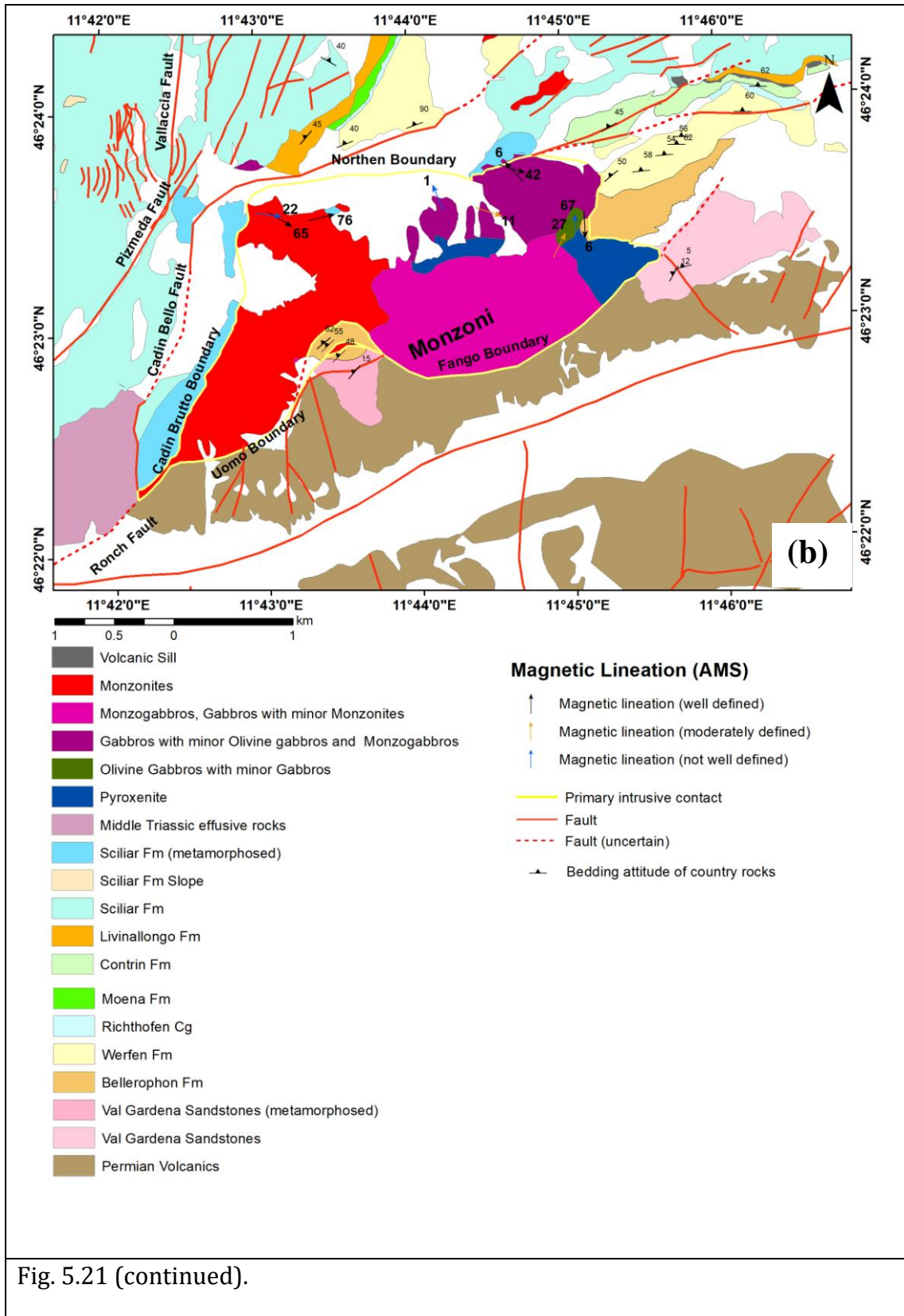


Fig. 5.21 (continued).

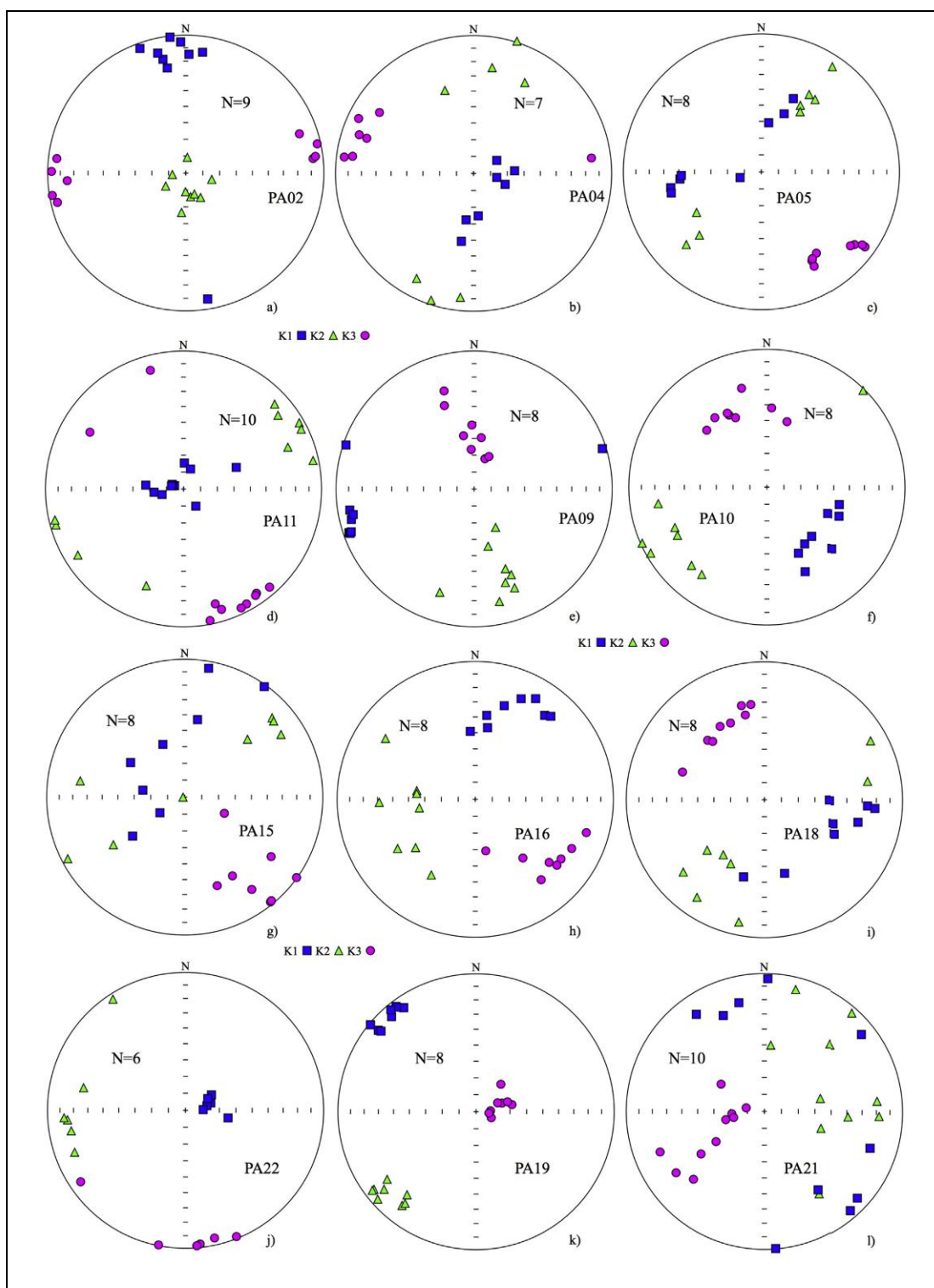


Fig. 5.22. Low-field AMS plots for representative sites in the Predazzo (a-f) and Monzoni (g-l) intrusive bodies. Data are plotted on lower hemisphere, equal area projections. Squares, triangles and circles represent maximum, intermediate and minimum axes, respectively, plotted relative to geographic coordinates.

5.7. HF-AMS fabric

HF-AMS measurements indicate that, for most of the samples, the observed magnetic fabric is dominated by the ferromagnetic component (Fig. 5.23) in most of the sites and a very good correspondence between the orientation of the principal axes of the ellipsoid at low-field and those of the ferromagnetic ellipsoid in high-field exists. This suggests that the magnetic fabric can be described in terms of the orientation of the ferromagnetic minerals. In samples where the HF-paramagnetic fraction is significant (>50%), there is a good correlation between low-field and high-field (ferromagnetic and paramagnetic) magnetic ellipsoids whereas in samples where the paramagnetic fraction is very low its orientation cannot be determined with the necessary accuracy.

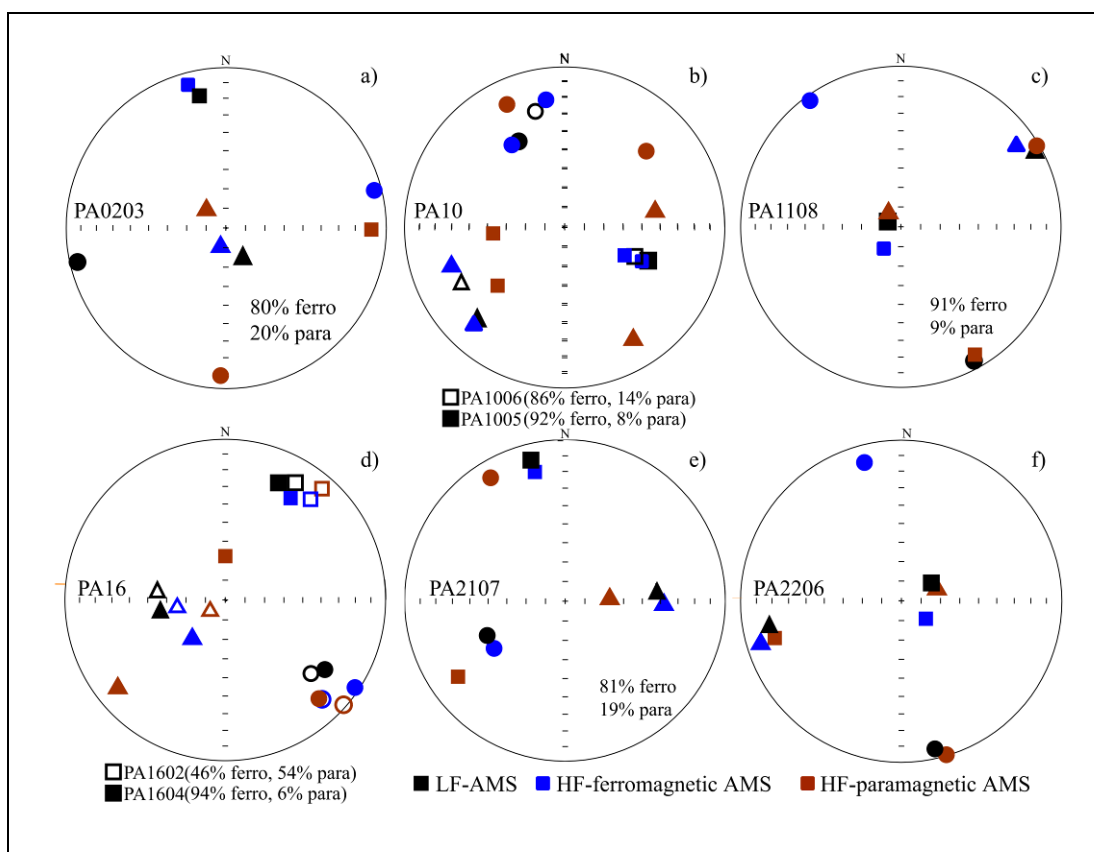


Fig. 5.23. HF-AMS measurements for representative samples from Predazzo and Monzoni plutons. Lower hemisphere equal area projections of the principal axes of the low-field/room temperature (black symbols), high-field paramagnetic (brown symbols) and high-field ferromagnetic (blue symbols) susceptibility ellipsoids. Percentages of the relative contribution of ferromagnetic and paramagnetic susceptibility to the magnetic fabric is also reported for each specimen.

**CHAPTER SIX
DISCUSSION****6.1. Petrological analysis**

The petrological data presented here are discussed with three approaches, the first addressed to define the origin of the inter- and intra-district geochemical variations, the second trying to constrain the composition of the mantle source(s) and the third aiming to define a geotectonic model in a large scale geological framework.

6.1.1. Inter- and intra-district geochemical variations.

As a whole, the 62 samples of volcanic and plutonic rocks from the Dolomites (including Predazzo and Monzoni plutons) and Vicentinian Alps sectors here investigated define relatively coherent trends in Harker-type diagrams. This is particularly surprising, considering the large time span of magma emplacement (from ~237 to ~230 Ma), the common subaqueous emplacement, with associated variable degrees of deuteric alteration, the very large outcrop area of the various districts (>4000 km²; Fig.2.1) and the thick crust in which the various magma batches intruded. The new data plot in the field defined by literature data for the various districts (Appendix 2); in many cases the data presented here are the first for specific areas or specific elements or isotopic ratios.

When major elements of the Southern Alps igneous rocks are plotted against differentiation parameters such as SiO₂, MgO or D.I. some important considerations can be made:

1) Figures 4.5 and 4.6 show the major oxide and trace element variation of the four investigated districts (Dolomites volcanics, Predazzo and Monzoni plutonic

rocks and Vicentinian Alps) against D.I. Despite being a nearly 60 year-old concept, this parameter is still a useful tool to indicate the evolution of liquid lines of descent. With a few exceptions, the investigated rocks define sharp positive (SiO_2 , $\text{Na}_2\text{O}+\text{K}_2\text{O}$) and negative correlations (TiO_2 , $\text{Fe}_2\text{O}_{3\text{tot}}$, MnO , MgO , CaO , $\text{CaO}/\text{Al}_2\text{O}_3$) with D.I. (Fig. 4.5). Only Al_2O_3 does not show any clear trend with this index, with a rough bell-shaped pattern, being mostly confined in the 14.5-19 wt% interval with D.I. ranging from ~ 5 to ~ 60 .

2) The samples with the lowest and highest D.I. values are plutonic rocks, the Monzoni samples being mostly concentrated in the poorly- to medium-evolved sectors. Predazzo samples spread the largest whole-rock variation for all the major oxides ($\text{SiO}_2 = 40.2\text{-}78.3$ wt%; $\text{MgO} = 0.0\text{-}11.9$ wt%; Alkalis = 0.7-12.0 wt%). Despite being the sector with the largest number of analysed samples, the Dolomites volcanic rocks show a rather restricted compositional range compared to the other districts.

3) The Monzoni and Predazzo samples with the lowest D.I. show similar compositions, resembling accumulation/fractionation of clinopyroxene ($\text{CaO} = 15.6\text{-}16.2$ wt%; $\text{Na}_2\text{O}+\text{K}_2\text{O} = 1.5\text{-}1.6$ wt%) and variable accumulation of Fe-Ti oxides ($\text{Fe}_2\text{O}_{3\text{tot}} = 14.7\text{-}22.9$ wt%; $\text{TiO}_2 = 1.3\text{-}1.5$ wt%) and minor amounts of intercumulus plagioclase ($\text{CaO}/\text{Al}_2\text{O}_3 = 0.9\text{-}3.0$; Fig. 4.5), coherently with the interpretation provided in the literature for the same rocks (Bonadiman et al., 1994; Casetta et al., 2018a).

4) In the existing literature, the Predazzo plutonic rocks have been subdivided into four (SiO_2 -saturated and SiO_2 -oversaturated shoshonite, potassic and calcalkaline; Visonà, 1997) or three groups (SiO_2 -saturated shoshonite, SiO_2 -

undersaturated shoshonite and granitic; Casetta et al., 2018a), but no substantial differences are observable in Appendix 2. With the exception of a small Na₂O enrichment for a restricted sub-group (Casetta et al., 2018a), the rest of the Predazzo rocks follows a rather continuous liquid line of descent, with most evolved samples displaying strong SiO₂ and K₂O enrichment, and Al₂O₃ and Na₂O decrease, questioning the actual existence of different serial affinities in this pluton. The transition from gabbroic to syenitic composition has been modelled by Casetta et al (2018a) with mass balance invoking two/three steps closed system fractionation of gabbroic (mostly plagioclase-clinopyroxene plus lower amounts – <2 wt% – of biotite, olivine and other minerals), monzo-dioritic (mostly plagioclase-clinopyroxene-biotite-alkali feldspar and minor magnetite) to monzonitic (plagioclase-alkali feldspar-clinopyroxene plus quartz, biotite and other accessory phases) assemblages. Our new data are qualitatively coherent with these results. Worth noting, however, none of these three hypothetical fractionating assemblages reflect the composition of the cumulitic clinopyroxenites, characterized by <10% plagioclase.

5) The most differentiated syenogranitic samples of Predazzo are not considered cogenetic with the rest of the plutonic rocks because of the impossibility to model fractional crystallization processes (Casetta et al., 2018a). As a consequence, the existence of three distinct magma batches has been proposed in literature (Visonà, 1997; Casetta et al., 2018a). The large amount of granitic magma (~1 km³) renders quite improbable its derivation from less differentiated melts via prolonged fractional crystallization. The granitic unit of Predazzo is considered to share more similarities with the volcanic rocks of the

Tarvisian (e.g., Gianolla, 1992) and Vicentinian Alps (e.g., De Vecchi and Sedeà, 1983; this study) than with the other Predazzo lithologies or the bulk of the Dolomites volcanic rocks (Casetta et al., 2018b). As a general consideration, however, the Vicentinian Alps data presented in this study fill the gap between Predazzo shoshonitic and granitic magmas, and plot within the main trend shown also by the latitic magmatism of the Dolomites (Fig. 4.6).

6) The Mg# range and major oxide variation of Dolomites volcanic rocks (Mg# = 63-36) qualitatively indicate fractional crystallization of Mg-bearing phases such as olivine and clinopyroxene. No quantitative approach can be made because of the absence of clear correlations of major oxides and trace elements with D.I. The rough correlation of Al₂O₃ vs. D.I. and the strong negative correlation of CaO/Al₂O₃ vs. D.I. of Ladinian volcanic rocks indicate only a minor role of plagioclase in the fractionating assemblage, despite its common presence among the phenocryst phases and the Eu/Eu* [Eu/Eu*=(Eu711/0.074)/(((Sm711/0.195)*(Gd711/0.259))^0.5)] <1 (1.01-0.75). The Dolomites volcanic rocks seem to define two parallel arrays in Al₂O₃ vs. D.I., with the low-Al group showing also low TiO₂ content. However, the existence of two sub-groups in this district is not corroborated by the concentrations and variations of other major oxides and trace elements.

7) The definition of the serial affinity of the Southern Alps Triassic igneous rocks (SATIR) is not as straightforward as it could be assumed. All the SATIR plot in the calcalkaline field in the AFM diagram (Fig. 4.4d). On the other hand, in the Miyashiro (1974) FeO_{tot}/MgO vs. SiO₂ diagram, modified by Arculus (2003), more than two thirds of the SATIR (with <70 wt% SiO₂) show relatively high

$\text{FeO}_{\text{tot}}/\text{MgO}$, clustering in the tholeiitic field (mostly “Medium-Fe field” of Arculus, 2003). However, strictly speaking, the AFM and $\text{FeO}_{\text{tot}}/\text{MgO}$ vs. SiO_2 diagrams should not be used because they are built for subalkaline compositions, while more than 80% of the SATIR fall in the alkaline field of the TAS diagram (Fig.4.4a).

At the same time, it is worth noting that the K_2O vs. SiO_2 diagram, widely used to discriminate between tholeiitic, calcalkaline and shoshonitic affinities, can lead to different classifications adopting the fields and the names proposed by different authors (Middlemost, 1975; Peccerillo and Taylor, 1976; Ewart, 1982; Le Maitre 2002). The mildly alkaline composition of most of the SATIR (Fig. 4.4a), coupled with a variable $\text{K}_2\text{O}/\text{Na}_2\text{O}$ ratio (mostly in the 0.3-1.6 range; average 1.16 ± 0.58 , over 628 samples) and the common mobility of alkalis, with widespread leakage of Na_2O and enrichment of K_2O (e.g., De Vecchi and Seda, 1983), render the definition of the magmatic affinity not an easy task. Despite these caveats, we agree with the common use of “shoshonitic affinity” for the SATIR, whose near primitive compositions have $\sim 1.0\text{-}4.5$ wt% K_2O in the SiO_2 48-56 wt% interval.

7) A limited to moderate amount (2-10 wt%) of assimilation of Permian kinzigitic/dioritic/rhyolitic/carbonate country rocks can explain the inter-group Sr and Nd isotopic variation of Predazzo plutonic rocks (Casetta et al., 2018b). The positive $^{143}\text{Nd}/^{144}\text{Nd}$ - $^{87}\text{Sr}/^{86}\text{Sr}$ correlation of silica-undersaturated shoshonitic group of Predazzo (albeit defined by three samples only) is at odd with crustal contamination process, but Casetta et al. (2018b) interpreted the spread of Sr isotopic ratios with local fluid mobilization at the intrusion borders.

8) The high Rb/Sr of the most differentiated plutonic rocks of Predazzo does not allow precise recalculation of the initial $^{87}\text{Sr}/^{86}\text{Sr}$ isotopic ratios (Casetta et al., 2018b). Initial Nd isotopic ratios of Predazzo granites ($^{143}\text{Nd}/^{144}\text{Nd} = 0.51222\text{-}0.51230$) overlap with those of the less differentiated composition ($0.51219\text{-}0.51229$). More in detail, on the basis of the differences in Nd isotopes, Casetta et al. (2018b) propose and confirm an earlier hypothesis about the existence of two independent magma batches for the least differentiated rocks with silica-undersaturated ($^{143}\text{Nd}/^{144}\text{Nd} = 0.51223\text{-}0.51229$) and silica-saturated shoshonitic groups ($0.51219\text{-}0.51225$) being the most striking difference. Our Predazzo granitic rocks have not been analyzed for isotopic ratios, but qualitatively they could be interpreted as the most extreme differentiation products of the basic compositions (gabbros). The major oxide variation seen in Fig. 4.5 indicates the possible involvement of feldspars in the latest crystallization phases, causing an abrupt change in the pattern of Al_2O_3 , Na_2O and, less evident, K_2O . The strong depletion of Sr and Ba in the most differentiated samples of Predazzo is compatible with such a process, as well as the strong depletion of Hf and Zr could involve zircon fractionation. In any case, volumetric considerations on the evolved and nearly primitive igneous compositions speak against simple direct derivation via fractional crystallization processes.

9) The number of samples for which both Sr-Nd isotopes and whole-rock analyses are available is currently limited (5 for Monzoni, 8 for Predazzo, 8 for Karawanken, 8 for Valsugana). Our samples are the first volcanic lava reported in literature (7 samples) for the entire Dolomites area. The situation for Pb isotopes

is even worse, being the data presented here (7 samples) the first for the entire SATIR, with the exception of the recent work of Bianchini et al. (2018; Valsugana dykes). Excluding the few Monzoni data (Bonadiman et al., 1994) and two 218 Myr-old basaltic and andesitic lavas from Brescian Alps (Cassinis et al., 2008), all the SATIR plot along a typical parabolic trend in the $^{143}\text{Nd}/^{144}\text{Nd}$ vs. $^{87}\text{Sr}/^{86}\text{Sr}$ diagram (Fig. 4.9a). This is classically interpreted as the result of interaction of mantle melts with ancient continental crust or the derivation from ancient mantle sources that have experienced variable degrees of melt extractions and/or modifications in the form of digestion of subducted material (e.g., Lustrino et al., 2011; Lustrino and Anderson, 2015, and references therein). In the latter case, the isotopic ratios are expected not to vary or to vary without any correlation with evolutionary degrees, while in the case of continental crust contamination clear trends should emerge with major oxides.

The $^{87}\text{Sr}/^{86}\text{Sr}$ values for the Dolomites volcanic rocks presented in this study (0.70432-0.70577 in the 49.8-58.1 wt% SiO_2 range) do not show any correlation with D.I. ($R^2 = 0.03$), with SiO_2 ($R^2 = 0.001$) or MgO ($R^2 = 0.14$). The spread of isotopic data can be, therefore, interpreted as characteristic of the mantle sources, only little modified, if any, by interaction with local crust. Interestingly, also the Predazzo rocks ($^{87}\text{Sr}/^{86}\text{Sr} = 0.70399$ - 0.70636 in the 45.1-67.8 wt% SiO_2 range) do not show any correlation with D.I. ($R^2 = 0.02$). Also the Monzoni rocks, with the exception of the SiO_2 -richest composition ($^{87}\text{Sr}/^{86}\text{Sr} = 0.70786$ at 69.7 wt% SiO_2) do not show any correlation with D.I. ($R^2 = 0.0004$). The same conclusions can be obtained for the (fewer) $^{143}\text{Nd}/^{144}\text{Nd}$ vs. D.I. trends. In conclusion, most of the isotopic variation seen in the SATIR is here related to

mantle source heterogeneities rather than to post-melting interaction with upper crustal lithologies.

6.1.2. Constraints on the mantle source(s)

Magmas generated by subduction-modified mantle sources are usually characterized by strongly fractionated incompatible element concentrations, manifested as peaks at U, K and Pb, troughs at Nb, Ta, Ti and, less marked, at Hf and Zr. Other key features are a general LILE enrichment relative to HFSE in primitive mantle-normalized diagrams (Fig. 4.8a). The Dolomites lava shows high Ba/Nb (32.8-93.9), low Ce/Pb (1.8-10.4) and low U/Nb (0.11-0.33) coupled with low HFSE (e.g., Nb = 6-12 ppm) with low Nb/Nb* ratio (0.1-0.35), resembling the typical characteristics of magmas generated by subduction-modified mantle sources (Turner and Langmuir, 2015; Kimura, 2017; Schmidt and Jagoutz, 2017; Zheng and Zhao, 2017).

Several are the geochemical tools to infer derivation from a subduction-modified mantle source, and the Th/Yb vs. Ta/Yb diagram is one of the most widely used. It is based on the – experimentally demonstrated – assumption that Th is highly mobile in fluids released during the metamorphic reactions in a sinking slab, while Ta is substantially immobile in the same conditions (Pearce, 1982; Pearce and Peate, 1995). Moreover, Ta and other HFSE are forced to remain in the subducting slab where titanates with very high K_d^{HFSE} easily stabilize (e.g., Foley et al., 2000; Kimura, 2017). The Yb at the denominator is used to buffer the absolute Th and Ta values to the same degree of evolution. In Fig. 6.1a the Dolomites lava samples are located outside mantle array, displaced towards high

Th/Yb ratios (1.3-4.9) for given Ta/Yb values (0.22-0.45). This can be interpreted as an additional evidence for the derivation from subduction-modified mantle sources.

The Dolomites lavas are characterized by $Eu/Eu^* < 1$ also in the least differentiated terms. The absence of correlation of this parameter with SiO_2 , MgO or D.I. indicates source characteristics that could be ultimately related to the digestion of subduction-related recycling of continental crust material in their mantle sources, confirming the previous hypothesis.

A quantitative approach to define the intensive and extensive variables that had a role in the genesis of the middle Triassic volcanic rocks of the Dolomites (and in arc magmas in general) is impossible. Only qualitative or semi-quantitative geochemical modeling can be drafted, hypothesizing fundamental parameters responsible for the chemical composition of mantle wedge partial melts.

One of the most important hard-to-constrain parameters is the evaluation of the degree of evolution of the least differentiated melt. Indeed, in the Dolomites lava case – as in nearly all the igneous district cases – even the most primitive compositions are not in equilibrium with mantle rocks (Mg# = ranges from 63 to 35 and Cr from 30 to 330 ppm, Ni from 20 to 80 ppm), indicating subtraction of mafic and sialic phases from melt (usually olivine, clinopyroxene, amphibole, plagioclase, spinel) and, at least in theory, also continental crust digestion enhancing fractional crystallization due to the release of latent enthalpy to country rocks and the adiabatic cooling *en route* to the surface. The typical approach to calculate primitive melt compositions in equilibrium with mantle rocks is to add back to the whole-rock compositions given amounts of the

fractionated minerals. This requires iterative addition of little amounts of olivine (usually in steps of 0.1 wt%) to the most primitive composition until a Mg# for the calculated melt reaches values (usually ~75-78; Frey et al., 1978) in equilibrium with upper mantle mineralogy (characterized as average by Mg# 90-92). This procedure can result in the addition of several % (up to >10%) of olivine, strongly modifying the composition of the calculated melts, based on the assumption that the only mineral fractionating at high T and P is olivine (e.g., Kimura and Ariskin, 2014, Herzberg and Asimow, 2015). Dealing with the Dolomites lavas, it is not possible to infer the composition of the mineral(s) fractionating from a parental magma to produce the melts that eventually crystallized to give the most primitive melt found in the area. For this reason, all the following calculations are performed on the most primitive melt, emphasizing that it does not represent the original geochemical budget of the original melt separated from the mantle.

The fundamental unknown variables playing a role during arc-magma genesis include: 1) the mineralogical and chemical composition of mantle wedge, as well as its thermal state before being metasomatized by subduction-related agents – fundamental parameters to evaluate the liquidus temperature and the composition of partial melts; 2) the lithological heterogeneity of the subducting slab (e.g., the composition and the relative thickness of the sediment cover, variably altered oceanic crust, fresh MORB, cumulitic gabbros); 3) the style and type of prograde dehydration metamorphic reactions responsible of liquid release from the subducting slab; 4) the style and type of hydration and carbonation metamorphic reactions occurring in the percolated mantle wedge

matrix; 5) the amount of mantle wedge sole scraped off and subducted coupled with the slab; 6) the slab-surface temperature and the slab-liquid fraction – mostly controlled by the style of subduction in terms of temperature, age of the subducting ocean, subduction dip; 7) the distribution coefficients between minerals and liquids, and their possible changes as a function of temperature; 8) the chromatographic exchanges of upwelling liquids passing through the slab and the mantle wedge; 9) the degree of melting of the metasomatized mantle. As anticipated above, further variables and uncertainties are related to the possible interaction of mantle melts with continental crustal lithologies in shallow level magma chambers.

The most powerful tool to investigate the processes acting in a supra-subduction mantle wedge from a geochemical and petrological point of view is the Arc Basalt Simulator software, now available in its version 5 (ABS5, Kimura, 2017). This is an easy-to-use macro working in MS Excel that takes into consideration nearly all the intensive and extensive parameters playing a role in the genesis of arc magmas. After choosing the composition of the primitive melt to match, and after assuming some basic starting conditions (e.g., Depleted Mantle-like composition of the pristine mantle wedge or the T-P style of subduction), the software calculates with Monte Carlo method thousands of multi-parameter solutions to match the calculated composition with the target melt.

As input parameters, we have assumed an original mantle source (pristine mantle wedge) with a depleted mantle composition (Salters et al., 2011), with an additional 0.8% MORB extraction from Depleted MORB Mantle (DMM), the P-T path of Solomon subduction zone (#32 in Kimura, 2017), slab-derived flux

originating at $P = 3$ GPa, with slab surface temperature = 792 °C (calculated by ABS5 on the basis of the selected P and P - T path of subduction zone). The slab liquid is assumed to derive 20% from the 0.3 km thick sedimentary cover, and 80% from 0.3 km thick altered oceanic crust in a reactive porous flow regime (%R slab = 90; Kimura 2017). Without the involvement of zone refining processes, open system partial melting is assumed at $P = 2.1$ GPa, at $T = 1280$ °C and 2% slab melting, 1.1% peridotite wedge melting, with slab melt containing 1.9 wt% H_2O and basaltic melt containing 2.1 wt% H_2O , all reasonable values.

The composition of the hypothetical liquid produced, together with the composition of the slab-derived metasomatizing fluid, the hypothetical DMM source and LAT5 potassic basalt sample (representing the most primitive basalt from the Dolomites lava group of rocks of this study) are shown in Fig. 6.1b. Bearing in mind the highly speculative approach, the model indicates a close match between the calculated melt and the target melt (LAT5). The calculated degree of melting of the mantle wedge is low (1.1), likely due to the effect of non-primitive composition of the target melt (LAT5). Indeed, during fractional crystallization, incompatible elements tend to be concentrated in the residual melts, and this process (i.e., incompatible element enrichment) is modelled by ABS5 reducing the degree of melting. The overlap between the calculated melt and LAT5 sample is nearly total in terms of incompatible element budget, with slight differences only in very mobile elements such as Rb, Th and K. In conclusion, the results obtained with ABS5 software indicate, with the necessary caveats reported above, that it is possible to obtain a basaltic liquid with incompatible element fractionation and absolute content closely resembling that

of basalt sample LAT5 assuming typical subduction settings from a peridotitic mantle wedge source.

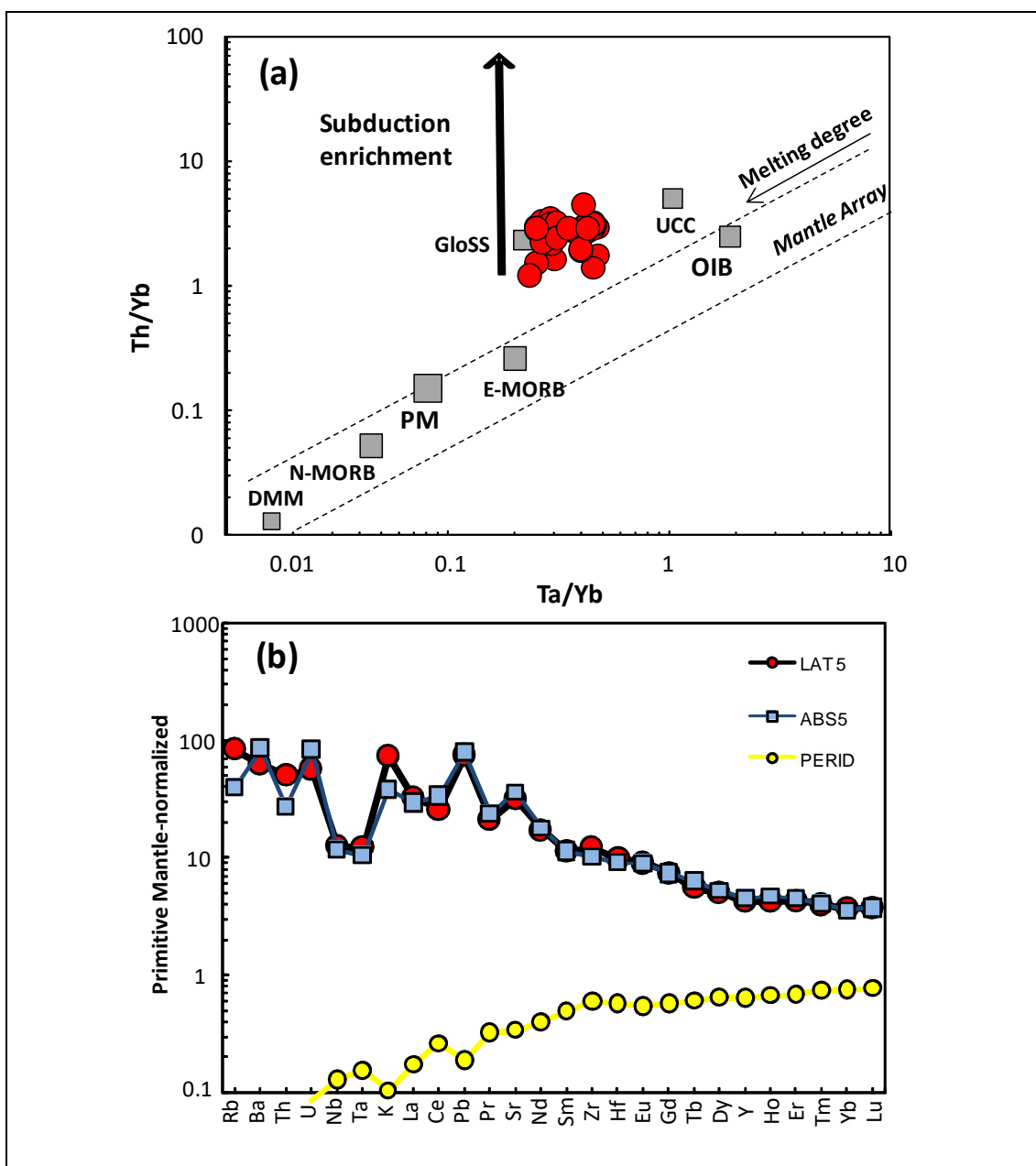


Fig. 6.1. a) Th/Yb vs. Ta/Yb (Pearce, 1982; Pearce and Peate, 1995) diagram for the studied rocks. Depleted MORB Mantle (DMM), N-MORB (normal MORB), E-MORB (enriched MORB) and OIB fields are from Sun and McDonough (1989). GloSS, Global Subducted Sediments (Plank, 2014); UCC, Upper Continental Crust (values from Taylor and McLennan, 1985). (b) Primitive mantle-normalized diagrams for three compositions: LAT5 represents the most primitive basalt from Dolomites (this study); ABS5 represents the best fit composition obtained using Arc Basalt Simulator 5 (Kimura, 2017); PERID = Composition of the pre-metasomatism mantle wedge calculated by Arc Basalt Simulator software.

6.1.3. Geodynamic and tectonic setting. Geochemistry vs. geology.

A common approach in Earth sciences is to consider as definitive the “quantitative” results of geochemical modelling and petrological considerations converging towards a specific petrogenetic process and tectonic setting. This is particularly true for example, when geochemical “evidence” is used to invoke the presence of mantle plumes and the thermal state of the mantle mixing concepts of geophysics, mineral chemistry and petrology (e.g., Lustrino and Anderson, 2015). In a broader view, paleotectonic environments have been often proposed using geochemical tools (a.o., Pearce and Cann, 1973; Meschede, 1986; Saccani, 2015), in some cases little questioning whether the results are really compatible with the actual geological evolution of the investigated area. The approach of identifying geological paleoenvironments is, however, very dangerous. A first comment is that all the “quantitative” geochemical modelling results are always based on poorly constrained (or completely unconstrained) parameters (e.g., the mineralogical and chemical composition of mantle sources, the geothermal gradient, the potential temperature, the elemental mineral/melt distribution coefficients, the styles of partial melting and melt-matrix interaction, the presence of a large amount of processes that can modify the composition of partial melts before transforming as the study objects of Earth scientists – FC (Fractional Crystallization), AFC (Assimilation and Fractional Crystallization), MASH (Melting, Assimilation, Storage and Homogenization), and so on). The “quantitative” results brought by geochemical modelling should be better defined as “qualitative” or “semi-quantitative” at best, even when precise figures with many decimals are presented in tables and diagrams.

Moreover, many are the cases of at least dubious tectonic settings proposed using specific trace element ratios, and a warm caveat seems to emerge in recent literature in using tectonic discrimination diagrams (e.g., Li et al., 2015). In the Mediterranean, several are the igneous districts with geochemical signature completely in contrast with local geology (e.g., Lustrino et al., 2016). In other cases, subduction modifications of mantle sources have been related to ancient metasomatic processes, not directly related with coeval tectonic setting (e.g., Lustrino et al., 2011; Mazzeo et al., 2014; Gaeta et al., 2016; Di Giuseppe et al., 2018) or to contamination of mantle melts with upper crustal lithologies (e.g., Esperança et al., 1992).

In the Southern Alps case, the late Middle-early Late Triassic igneous activity was associated with extensional and wrench tectonics (Doglioni 1984, 1987; Brandner et al., 2016, Abbas et al., 2018). This observation suggests that subduction-related (e.g., volcanic arc) settings (as proposed by Castellarin et al., 1988; Garzanti 1985; Zanetti et al. 2013; Bianchini et al., 2018) can be excluded. In line of principle, magmatism with subduction affinity and extensional tectonics could occur in back-arc settings, as proposed by some authors (Marinelli et al. 1980; Viel, 1982; Cassinis et al., 2008). However, back-arc basins develop due to slab roll-back and are characterized by progressive migration of extensional tectonics and magmatism. Typical examples of migrating magmatism are described for the Tyrrhenian Sea, associated with the Apennines subduction (Carminati et al., 2012), for the Lau Basin, associated with the Tonga subduction (e.g., Hawkins, 1995) and for the Parece Vela Basin, associated with the Marianas subduction (Ishizuka et al., 2010). The migration trend of magmatism in present-

day back-arc basins is at odd with the ages of volcanic deposits in the Southern Alps, which show no geographic trends. Actually, the oldest deposits occur in the central part of the 450 km wide volcanic area, and subsequently magmatism occurred to the east and to the west with no clear trends (Fig. 2.1). In addition, in back-arc basins magmas have both MORB and subduction affinities, differently from the Southern Alps case (Taylor and Martinez, 2003). Both these observations exclude a back-arc origin for the Triassic magmatism of the Southern Alps.

Being the geochemical message of the igneous rocks completely at odd with the geological evidence (i.e., subduction instead of continental rifting setting), we should invoke a decoupling between geochemistry and geology. The most likely model to be proposed in this case is the derivation of partial melts by post-collisional processes associated with the development of the Adria passive margin from mantle sources previously modified by infiltration of subduction-derived agents released by the north-directed Rheic oceanic lithosphere before the Gondwana-Laurussia collision in late Carboniferous. More subtle is the discrimination, via our petrographic and geochemical data, between the post-Hercynian collision processes proposed in the literature such as continental rifting (Bechstadt, et al., 1977; Brandner et al., 2016) or pull-apart extension associated with wrench tectonics (Blendinger, 1985; Doglioni, 1987, 1988; Brandner and Keim, 2011; Abbas et al., 2018).

6.2. Structural analysis

The structural and AMS data are discussed with two approaches, the first to discuss the origin of magnetic fabric and the second to define the emplacement modes of the two Dolomites intrusive igneous bodies (Predazzo and Monzoni).

6.2.1. The origin of magnetic fabric in the Predazzo and Monzoni rocks

Magnetic fabric in intrusions can be purely magmatic (related to internal magma chamber processes, such as convection, magma surges, and dyke injection) or it can be the result of regional deformation (syn- to post-tectonic strain) or a combination of these two processes (Paterson et al., 1998). In the Predazzo and Monzoni bodies, thin section analyses show that the microstructures are either purely magmatic or, in few cases, occurred in the subsolidus stage (i.e., just after the complete crystallization of magma).. The absence of evident solid-state deformation suggests that the magnetic fabric is not related to tectonic deformation after cooling, but it rather developed during magma emplacement and cooling (Büttner, 1999). Hydrothermal fluids can also modify the magnetic fabric orientation and parameters acquired during magma emplacement and cooling, thus complicating the interpretation of magnetic fabric data (e.g., Just et al. 2004; Petronis et al. 2011; Nédélec et al. 2015; Tomek et al., 2017). Although some samples from the northern part of the Predazzo granite body (PA01, PA04, PA05, and PA17) showed evidence of hydrothermal alteration, in most of these sites magnetic foliations are generally tangent to the ring shape of the pluton. This suggests that hydrothermal alteration had no or minor effect on the magnetic fabric, with the exception of sample PA17, that is

strongly hydrothermally altered and fractured and shows a distinctive magnetic fabric. Therefore, this sample will be no longer considered in the discussion of the emplacement mode of the Predazzo pluton. Sample PA11, belonging to Monzontic Unit M3 of the Predazzo body, is highly altered and transformed as a result of hydrothermal solutions. However, the magnetic fabric orientation is concordant with NE-SW elongation shape of Monzontic Unit M3 and shows well-clustered magnetic fabric. The compatibility of the magnetic fabric with the elongation shape of this unit could be explained as the hydrothermal fluid was likely coeval with the emplacement as a single event (e.g., Nédélec et al., 2015). Moreover, the NE-SW orientation of the magnetic fabric and elongation of the Monzontic Unit M3 suggests that the emplacement of this unit was controlled by NE-SW Middle Triassic (Ladinian) tectonic structures.

In the following, the Predazzo and Monzoni plutons will be discussed separately. However, Figure 2.2 shows that these intrusive bodies may be parts of a single large and rather continuous body, as suggested by the outcrop of a small volume of intrusive rocks between the plutons and by the continuity of a metamorphic aureole from west of the Predazzo body to the Monzoni body. The emplacement of Ladinian intrusive bodies likely occurred along a fractured zone associated with previous strike-slip tectonics (Fig. 6.3a), as suggested by the parallelism between Ladinian intrusives and Middle Triassic faults (e.g., StavaTrodena line, Fig. 2.2b).

The Predazzo and Monzoni plutonic rocks show distinct shapes, the first being roughly round shaped and characterized by ring-type successive intrusions, the second being markedly NE-SW elongated, sub-parallel to the Middle Triassic

Stava-Trodona line. Similarly, the AMS analyses show markedly different results for the two intrusive bodies, suggesting different emplacement modes. Both the Predazzo and Monzoni bodies are the result of multiple intrusions, as indicated by the variety of lithologies described above.

6.2.2. Emplacement modes of the Dolomites igneous bodies

6.2.2.1. Emplacement mode of the Predazzo pluton

In the Predazzo body, AMS has been measured in the different intrusive units that form the pluton, showing distinctive pattern of magnetic fabric. The Monzonitic Units M1 and M2, representing the older portion of the pluton, are characterized by an annular ellipsoidal shape, gently elongated in a ENE-WSW direction. In these two units, the magnetic foliation is generally oriented parallel to the borders of the intrusion (i.e., parallel to its perimeter). In sites that are located along the external rim, the foliations are predominantly steeply or shallowly dipping radially away from the pluton. On the contrary, in sites located along the internal rim of the annular intrusion the foliations radially dip towards the center of the pluton. The magnetic lineation is generally gently dipping to sub-horizontal and parallel to the border of the intrusion. In the granite body the magnetic foliation is almost parallel to the rims of the pluton and dips away from the intrusion, whereas the magnetic lineation varies from sub-vertical to sub-horizontal. The rough ring shape of the Predazzo multistage intrusive complex and the presence of volcanic rocks at the center of the ring (suggesting a caldera collapse of this area), led Castellarin et al. (1982b) to suggest a ring-dyke emplacement mode. Ring-dykes are cylindrical sheet intrusions occurring at

subvolcanic levels characterized by outward-dipping walls on all sides. They develop due to magma ascent along steep outward-dipping ring-fractures, induced by the collapse of the central block subsidence (e.g., O'Driscoll et al., 2006; Fig. 6.2). The development of caldera ring-faults and the related subsidence of a central block are the main structural processes that permit the intrusion of ring-dykes (Roche et al., 2000).

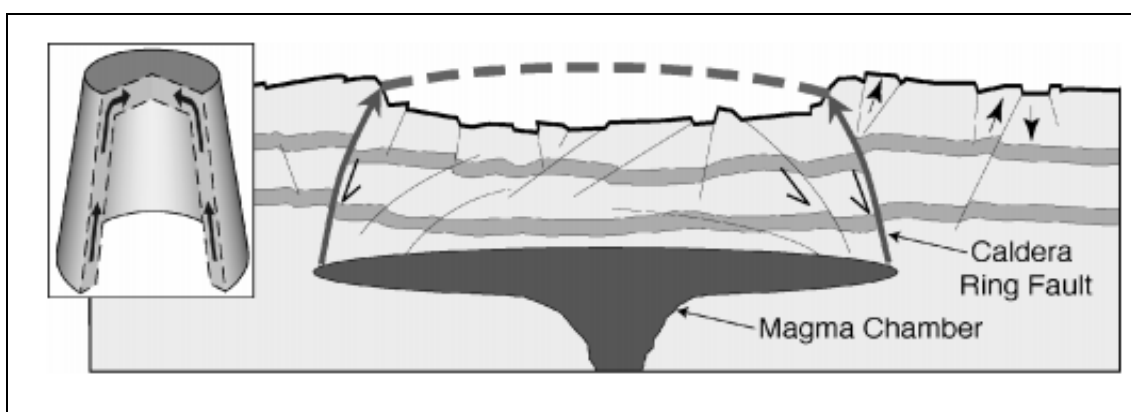


Fig. 6.2. Simplified sketch showing ring-fault system along which ring-dikes are emplaced (Walter and Troll, 2001; O'Driscoll et al., 2006). Inset: Bell-jar geometry of ring dike intrusion and directions of magma flow during emplacement.

Our AMS data are consistent with the ring dyke emplacement mode. In particular magnetic foliation in the Monzonitic units is dominantly parallel to the boundaries of the intrusion and prevalently dips away from the intrusion. Only in samples collected close to the internal boundary of the Monzonitic units, the foliation is very steep and dipping toward the internal rim, describing a symmetrical pattern of the magnetic foliation with respect to the dyke rims. This geometry has been widely recognized in volcanic dykes, where it has been interpreted as related to embrication of the magnetic foliation along the dyke

margins, related to upward flow of the magma (Aubourg et al., 2002). In this mechanism, the horizontal magnetic lineation can be interpreted as an intersection lineation between differently oriented foliation planes, which is oriented orthogonal to the magma flow. In sites far from the pluton margins (e.g., PA11), the steep lineations associated with steeply dipping foliations are likely related to ascent paths of magma, in particular with laminar flow and wall friction during injection (Andersson et al., 2016). On the other hand, in sites far from the intrusive rims (e.g., PA02) the occurrence of sub-horizontal lineations (tangential to the shape of the pluton) could be related to lateral flow of magma induced by "roll-over" at propagating sheet tips (Emeleus et al., 2012; Andersson et al., 2016) or to semi-chaotic particle movement during ring fissure flow observed in analogue models (Kennedy et al., 2008). The occurrence in some samples of magmatic layering steeply dipping inward and magnetic lineations plunging toward the center of the intrusion suggests that the shape of the walls was not as regular (i.e., constantly outward dipping) as assumed in ring dyke-models (complex flow due to complex sheet geometry of Andersson et al., 2016). The steep attitude of inward dipping foliations is not consistent with a lopolithic geometry of the Predazzo intrusion.

The degree of anisotropy (P) varies between 1.01 and 1.07 and is not controlled by lithology (i.e., low and high values are found both in monzonites and granites). More remarkably, the values do not show a pattern (e.g., high values aligned along WSW-ENE directions, typical of Ladinian tectonics) but are rather randomly distributed. This confirms a primary (i.e., emplacement-related) nature of magnetic anisotropy. Moreover, the nonlinear relationship between

Km and P supports the idea that the obtained low P values indicate the existence of low strain during the emplacement (Fig. 5.19c).

Finally, also the orientation of the dykes (mainly trending NNW-SSE) crosscutting intrusive rocks is at odds with sinistral strike-slip tectonics along WSW-ENE structures, that would be rather associated with NE-SW trending dilational (extensional) structure. NE-SW trending dykes are rather found in the host rocks of the pluton, suggesting that they utilized previous extensional structures associated with sinistral strike-slip faulting. Thus, their emplacement and the emplacement of the pluton were post-tectonic.

In summary, field, petrographic, microstructural and AMS data are consistent with a multistage ring-dyke emplacement mode, similar to the piston-floor subsidence mechanism (Tomek et al., 2014), likely post-tectonic. In particular, AMS data suggest that areas of upward flow of the magma are located in the NW and ESE part of the Monzonitic intrusion, whereas in the southern part of the pluton data suggests prevalently horizontal flows. Generally, the Predazzo sheets were emplaced via either updip magma flow or along-strike lateral magma transport (Fig. 6.3b).

6.2.2.2. Emplacement mode of the Monzoni pluton

The shape of the Monzoni pluton was clearly controlled by Middle Triassic tectonics, being it elongated WSW-ENE, parallel to the Stava-Trodona strike-slip fault. It remains to be discussed whether this control was direct (syn-tectonic emplacement of the pluton) or indirect (emplacement along pre-existing tectonic structures). The host rocks of the Monzoni pluton are affected on all sides by contact metamorphism. This suggests that the host rock-pluton contacts are primary, thus no or very poorly affected by post-emplacement tectonics.

Comparing magnetic and deformation fabrics in the pluton with strain markers in the country rocks one can determine whether the magnetic fabric in pluton is primary or reflects regional tectonic strain (Benn et al., 1998, 2001; Talbot et al., 2005; Raposo et al., 2012). Three different areas, with distinct magnetic fabric can be recognized in the Monzoni body. In the NW side, the magnetic foliation is well defined, sub-vertical, and parallel to the E-W oriented boundaries of the igneous body in this area, with a very steep magnetic lineation. Along the NE side of the intrusive body the magnetic foliation and magnetic lineation vary from very gently dipping to sub-horizontal. Along the SE side the magnetic foliation is almost parallel to the boundary of the intrusive and gently to strongly dipping toward the internal part of the pluton, whereas the magnetic lineation is prevalently gently plunging.

Our AMS results suggest that the magnetic fabric in Monzoni pluton was not directly controlled by Middle Triassic or post-tectonic deformation. This conclusion is supported by the absence of solid state deformation, by the general steeply magnetic fabric on the two sides of the pluton with absence of the NE-SW

horizontal magnetic lineation and by the low degree of anisotropy (P), suggesting that magnetic fabric developed during magma emplacement and cooling and was likely controlled by the shape of the magma chamber.

The magnetic fabric can be read in terms of direction of flow and can help to infer the location and geometry of the feeding or root zones for magmatic bodies (e.g., Marre, 1986; Djouadi et al., 1997; Callot et al., 2001; Petronis et al., 2005; O'Driscoll et al., 2006; Maes et al., 2007). Magma originating from a planar dyke generates a parallel flow pattern with lineations pointing to opposing, but consistent directions, on either sides of the dyke (Knight and Walker, 1988; Ernst and Baragar, 1992; Maes et al., 2007). Generally, the magnetic lineation, which represents the magma flow, plunges toward the magma source (Knight and Walker, 1988; Ernst and Baragar, 1992; Maes et al., 2007). In case of magma fed from a sub-vertical conduit, radial magma flow pattern is expected. Multiple feeders can produce more complex patterns of magma flow (Maes et al., 2007). In the Monzoni pluton, the magnetic lineations converge towards the north-eastern part of the pluton (PA15, PA16, PA18, PA22, PA23, and PA24), suggesting that the root zone was not located at the center of the pluton but rather towards NE. This interpretation is also consistent with the magmatic evolution of the pluton. Indeed, the most evolved rocks are located at the south-western edge of the pluton, while the less evolved rocks are located at the north-eastern part of the pluton.

In the Monzoni pluton, steep to moderate foliations and lineations at the western and eastern borders of the pluton leave space to shallowly dipping fabric in its intermediate parts. This fabric may have been induced by shear of

magma along the host-rocks at the top of the pluton. This inference is in agreement with field host-rocks above the pluton, in agreement with geological observations that allow to infer that the top boundary of the pluton was located just above the mountain peaks in the central part of the pluton (Castellarin et al., 1982b).

In summary, field, petrographic and AMS data and the ENE-WSW elongated shape indicate that the emplacement location and shape of the Monzoni pluton were controlled by strike-slip faults associated with Ladinian tectonics (Fig. 6.3c). However, the absence of deformation at the field- and micro- scale is consistent with a post Ladinian tectonics emplacement, as for the Predazzo body.

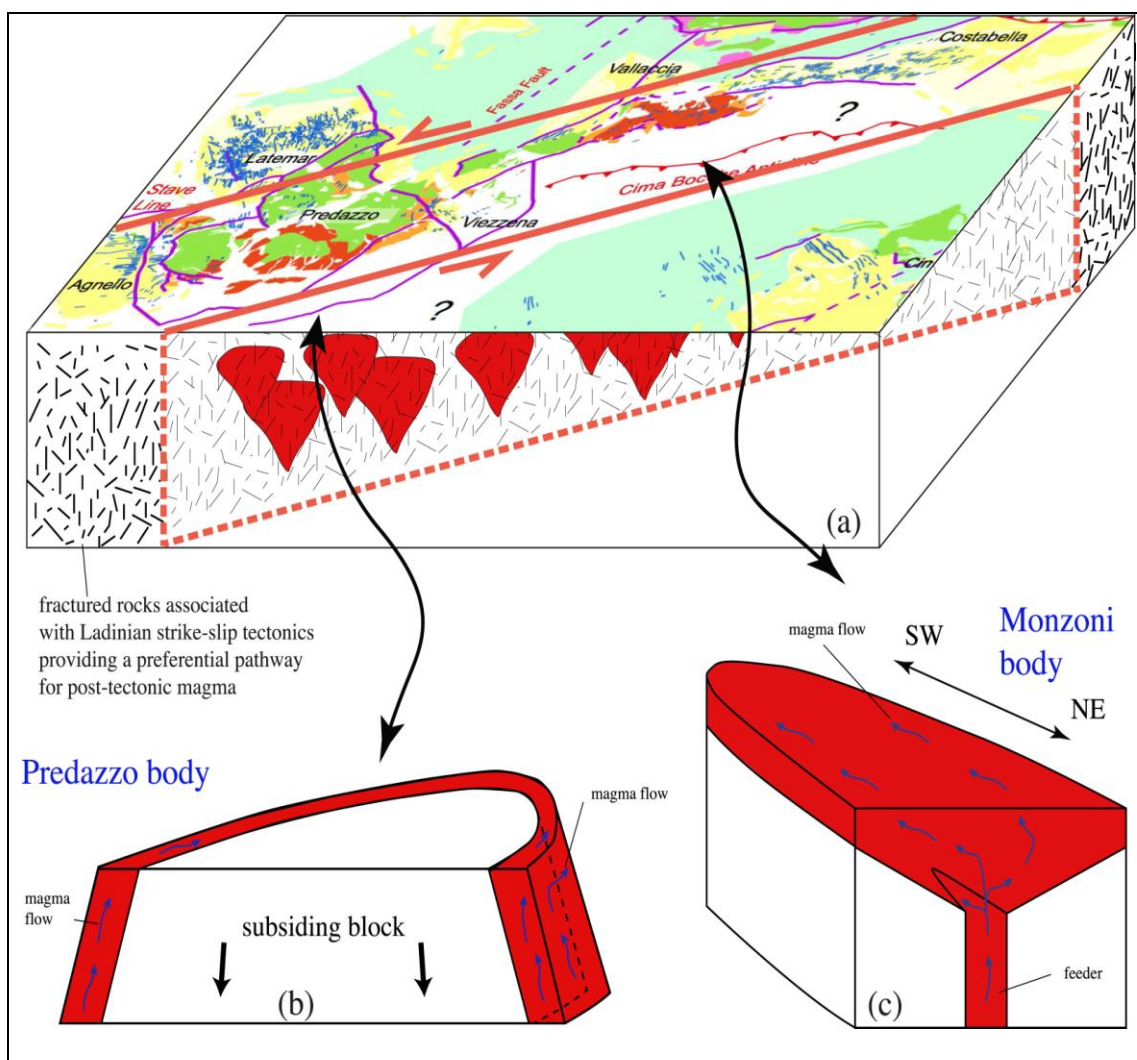


Fig. 6.3. a) Sketch showing the emplacement of Ladinian Dolomites intrusive bodies along a wide fractured zone associated with previous strike-slip tectonics. b) Sketch of the emplacement mode for the Predazzo body; c) Sketch of the emplacement mode for the Monzoni body.

**CHAPTER SEVEN
CONCLUSIONS**

During late Middle-early Late Triassic, a large area in the Southern Alps (N. Italy) was interested by an intense and diffuse igneous activity. This magmatism developed after the Devonian-Carboniferous subduction of the Rheic Ocean and the Carboniferous collision between the northern margin of Gondwana with the southern sectors of Laurussia. The last subduction stages and the collisional events are associated with abundant Permian calcalkaline volcanic and plutonic activity in large sectors of the Hercynian/Variscan Chain.

During the early Mesozoic the assembled Pangea super-continent started to suffer gravitational instabilities and in Early Triassic the first phases indicating the development of extensional tectonics were recorded, with formation of intra-montane rifts and the development of horst-and-graben structures. During these extensional movements, which ultimately evolved into the formation of passive continental margin with huge limestone factories and, eventually to the oceanization stage of the Alpine Tethys phase, the Triassic igneous activity took place in Southern Alps, mostly confined at 240 ± 5 Ma.

This activity is represented by volcanoclastic and epiclastic deposits up to 150 m thick, massive lava flows, dyke swarms and rare plutonic complexes. The igneous products are characterized by a wide compositional spectrum with compositions ranging from metaluminous basalt/gabbros to peraluminous rhyolites/leucogranites, including also cumulitic lithologies such as ultrabasic clinopyroxenites.

The petrography, mineral chemistry, whole-rock chemistry and Sr-Nd-Pb isotope ratios point to the derivation of the least differentiated melts from a subduction-modified mantle source. Shoshonitic affinities are the most abundant, followed by high-K calcalkaline. The mildly to strongly evolved compositions are generically linked with the least differentiated terms by closed system fractional crystallization of gabbroic to monzonitic assemblages, even if the SiO₂-richest magmas likely require a separate origin (the relation between granite and other Predazzo units is still uncertain and need more studies).

The studied rocks show a sharp positive (SiO₂, Na₂O+K₂O) and negative correlation (TiO₂, Fe₂O_{3tot}, MnO, MgO, CaO, CaO/Al₂O₃) with D.I. The Dolomites Lava exhibit enrichment of LILE relative to HFSE and high Ba/Nb (32.8-93.9), low Ce/Pb (1.8-10.4) and low U/Nb (0.11-0.33) coupled with low HFSE (e.g., Nb = 6-12 ppm) with low Nb/Nb* ratio (0.1-0.35), resembling the typical characteristics of magmas generated by subduction-modified mantle sources.

The fractional crystallization of Mg-bearing phases such as olivine and clinopyroxene with only a minor role of plagioclase controlled Dolomites volcanic rocks evolution.

The ⁸⁷Sr/⁸⁶Sr for the Dolomites volcanic rocks ranges from 0.70432 to 0.70577 and do not show any correlation with D.I., with SiO₂ or MgO which indicates that the mantle sources, only little modified, if any, by interaction with local crust. The ¹⁴³Nd/¹⁴⁴Nd_(i) ranges from 0.51227 to 0.51237, with εNd_(i) values slightly lower to slightly higher than ChUR_(230 Ma) (from -1.4 to +0.5). The Pb isotopic compositions are homogeneous, with ²⁰⁶Pb/²⁰⁴Pb clustered around 18.26 and 18.41, ²⁰⁷Pb/²⁰⁴Pb from 15.62 to 15.67 and ²⁰⁸Pb/²⁰⁴Pb from 38.36 to 38.89. The

isotopic variation of the Southern Alps Triassic rocks is related to mantle source heterogeneities rather than interaction with upper crustal lithologies.

The results of ABS5 software analyses of less evolved basaltic sample, indicates that the origin of these rocks is related with the melting of a peridotitic mantle wedge source as at typical subduction settings.

At a large scale, no substantial differences can be recorded in the four districts investigated in this study (Dolomites lavas, Predazzo, Monzoni and Vicentinian Alps), all sharing similar geochemical affinity and likely similar mantle sources, identified in a depleted mantle metasomatized by subduction event(s).

The geochemical message from these products is at odds with the geological, sedimentological and structural evidence indicating that magmatism occurred in association with tectonic and geodynamic processes (rifting and/or wrench tectonics) that will eventually lead to the development of the Adria passive margins. The apparent paradox can be easily solved invoking the activation of upper mantle sources contaminated during the previous Hercynian subduction when local geotherms were raised due to the passive upwelling of asthenospheric mantle along the rifted margin.

Microstructural, petrographic and AMS data, coupled with field geological data allowed us to investigate the emplacement modes of the Predazzo and Monzoni bodies and define the space and time relationship with the Middle Triassic strike-slip faulting in the Dolomites. Although these plutons are considered in the literature as separated bodies, the outcropping of a small volume of intrusive rocks between the bodies and the continuity of metamorphic aureole from west of the Predazzo body to east of the Monzoni body suggest that they are parts of a

~20 km long SW-NE oriented continuous pluton, sub-parallel to Ladinian strike-slip faults. However, our results suggest a variable control of Ladinian tectonic structures on the emplacement modes of the two bodies.

In the Predazzo pluton, lithologies vary from cumulitic clinopyroxenites to cumulitic gabbros, diorites, monzonites, monzodiorites, monzogabbros, albitized granite and biotite granite. The samples from Monzoni pluton are classified into two main groups: gabbroic rocks (monzogabbros, gabbros, cumulitic gabbros and olivine gabbros) and monzonites. The samples from both plutons show purely magmatic structures with no evidence of high strain solid-state deformation. This suggests that the magnetic fabric is not related to tectonic deformation after cooling, but it rather developed during magma emplacement and cooling. Magmatic foliation has been observed in the studied rocks both at the meso- and micro-scales.

The magnetic susceptibility values of the studied rocks suggest a major contribution of ferromagnetic minerals to the magnetic susceptibility. Low-Ti content titanomagnetite and magnetite are the main ferromagnetic minerals both in the Predazzo and Monzoni intrusive bodies with the presence of a small amount of maghemite which converted to hematite.

The degree of anisotropy (P) is low and not controlled by lithology in the two plutons. This confirms a primary (i.e., emplacement-related) nature of magnetic anisotropy. Moreover, the nonlinear relationship between K_m and P supports the idea that the obtained low P values indicate the existence of low strain during the emplacement.

AMS, microstructural and petrographic data from the Predazzo body are consistent with a multistage ring-dyke emplacement mode, with areas of upward flow of the magma located in the NW and ESE part of the intrusion, whereas in the southern part of the pluton our data suggest prevalently horizontal flows. Generally, the Predazzo sheets were emplaced via either updip magma flow or along-strike lateral magma transport, and the rounded shape suggests no influence of Ladinian tectonic structures.

On the contrary, the ENE-WSW elongated shape of the Monzoni body was controlled by strike-slip faults associated with Ladinian-tectonics, the feeder being likely located at the NE edge of the body. However, the absence of deformation at the field- and micro- scale is consistent with a post-Ladinian tectonics age of emplacement, as for the Predazzo pluton. Finally, The Ladinian strike-slip tectonics provided a preferential pathway for post-tectonic magma.

APPENDIX

Appendix 1 (Mineral chemistry analysis)

Sample	SiO ₂	TiO ₂	Al ₂ O ₃	MnO	FeO	CaO	Na ₂ O	K ₂ O	BaO	SrO	Total:	Si	Ti	Al	Mn	Fe ^{III}	Ca	Na	K	Ba	Sr	Sum	An	Ab	Or
AS2 pl gm 1-7	50.40	0.05	30.53	0.00	0.83	14.87	2.93	0.41	0.03	0.14	100.19	9.23	0.006	6.59	0.00	0.09	2.92	1.04	0.10	0.00	0.01	19.99	71.96	25.69	2.35
AS2 pl gm 1-8	52.04	0.02	29.74	0.02	0.74	13.52	3.55	0.55	0.00	0.19	100.36	9.48	0.003	6.38	0.00	0.08	2.64	1.25	0.13	0.00	0.02	19.98	65.64	31.17	3.20
AS2 pl interstitial in cpx glomerule 1-9	48.21	0.03	32.09	0.00	0.97	16.53	2.12	0.22	0.00	0.09	100.26	8.87	0.004	6.96	0.00	0.10	3.26	0.76	0.05	0.00	0.01	20.00	80.13	18.58	1.29
AS2 pl interstitial in cpx glomerule 1-10	47.38	0.03	32.45	0.00	0.88	17.20	1.68	0.22	0.00	0.23	100.07	8.75	0.004	7.07	0.00	0.09	3.40	0.60	0.05	0.00	0.02	19.99	83.92	14.81	1.27
AS2 pl gm 2-2	53.07	0.04	29.10	0.05	0.78	13.05	3.70	0.61	0.02	0.14	100.56	9.63	0.005	6.22	0.01	0.08	2.54	1.30	0.14	0.00	0.01	19.94	63.73	32.72	3.55
AS2 pl in glomerule rim 3-1	52.95	0.03	29.15	0.00	0.79	12.89	3.78	0.68	0.02	0.22	100.51	9.62	0.004	6.24	0.00	0.08	2.51	1.33	0.16	0.00	0.02	19.96	62.72	33.32	3.96
AS2 same pl in glomerule core 3-2	47.48	0.03	31.78	0.03	1.21	16.55	1.69	0.20	0.00	0.10	99.06	8.84	0.004	6.98	0.00	0.13	3.30	0.61	0.05	0.00	0.01	19.93	83.38	15.39	1.22
AS2 pl in glomerule rim 3-3	52.62	0.03	29.12	0.00	0.86	13.24	3.55	0.67	0.06	0.07	100.20	9.59	0.003	6.26	0.00	0.09	2.58	1.25	0.16	0.00	0.01	19.94	64.71	31.38	3.91
AS2 same pl in glomerule core 3-4	47.28	0.01	32.59	0.00	0.86	17.13	1.68	0.20	0.03	0.21	99.98	8.74	0.001	7.10	0.00	0.09	3.39	0.60	0.05	0.00	0.02	19.99	83.97	14.87	1.16
AS2 pl in glomerule core 3-5	46.28	0.00	33.24	0.04	0.96	17.68	1.43	0.17	0.00	0.14	99.95	8.58	0.000	7.26	0.01	0.10	3.51	0.51	0.04	0.00	0.02	20.02	86.37	12.63	1.00
AS2 pl pheno rim 5-1	47.13	0.01	32.60	0.02	0.84	17.25	1.70	0.18	0.03	0.12	99.87	8.72	0.002	7.11	0.00	0.09	3.42	0.61	0.04	0.00	0.01	20.01	83.97	14.97	1.06
AS2 pl pheno rim 5-2	55.03	0.07	26.98	0.00	0.82	10.60	4.79	0.98	0.04	0.20	99.51	10.04	0.009	5.81	0.00	0.08	2.07	1.70	0.23	0.00	0.02	19.96	51.86	42.42	5.72
AS2 same pl pheno core 5-3	49.46	0.07	31.16	0.01	0.83	15.36	2.65	0.38	0.00	0.17	100.07	9.09	0.009	6.75	0.00	0.08	3.02	0.94	0.09	0.00	0.02	20.00	74.57	23.26	2.17
AS2 pl in cpx pheno 5-4	46.19	0.02	32.50	0.02	2.41	17.15	1.40	0.25	0.00	0.15	100.07	8.60	0.002	7.13	0.00	0.25	3.42	0.50	0.06	0.00	0.02	19.99	85.88	12.66	1.46
AS3 pl gm 1-7	53.97	0.03	28.42	0.01	0.92	11.99	4.12	0.86	0.03	0.18	100.52	9.78	0.004	6.07	0.00	0.09	2.33	1.45	0.20	0.00	0.02	19.95	58.58	36.40	5.02
AS3 pl gm 1-8	54.35	0.05	28.01	0.04	0.70	11.47	4.40	0.95	0.00	0.17	100.13	9.87	0.007	6.00	0.01	0.07	2.23	1.55	0.22	0.00	0.02	19.97	55.78	38.71	5.51
AS3 pl gm 2-1	59.74	0.04	24.91	0.04	0.56	7.38	6.77	0.58	0.05	0.01	100.08	10.68	0.006	5.25	0.01	0.06	1.41	2.35	0.13	0.00	0.00	19.90	36.31	60.27	3.42
AS3 pl gm 2-5	57.84	0.06	25.82	0.04	0.68	8.43	5.74	1.27	0.03	0.02	99.91	10.43	0.008	5.49	0.01	0.07	1.63	2.01	0.29	0.00	0.00	19.93	41.48	51.10	7.41
AS7 pl gm 1-9	52.13	0.05	29.41	0.02	0.98	13.48	3.50	0.65	0.07	0.11	100.39	9.50	0.007	6.32	0.00	0.10	2.63	1.24	0.15	0.01	0.01	19.97	65.51	30.74	3.75
AS7 pl gm 1-11	53.56	0.08	28.52	0.02	0.92	12.19	3.95	0.93	0.04	0.21	100.41	9.73	0.011	6.11	0.00	0.09	2.37	1.39	0.21	0.00	0.02	19.96	59.65	34.96	5.40
AS7 pl gm 1-13	51.96	0.05	29.50	0.03	0.86	13.63	3.52	0.64	0.13	0.02	100.34	9.48	0.007	6.35	0.00	0.09	2.66	1.24	0.15	0.01	0.00	19.99	65.66	30.66	3.68
AS7 pl gm 2-5	52.69	1.81	28.69	0.00	0.84	12.38	3.97	0.77	0.04	0.22	101.41	9.51	0.246	6.10	0.00	0.08	2.39	1.39	0.18	0.00	0.02	19.93	60.44	35.09	4.47
AS8 pl gm 1-4	52.33	0.02	28.89	0.02	2.23	12.64	3.81	0.65	0.06	0.13	100.76	9.55	0.003	6.21	0.00	0.23	2.47	1.35	0.15	0.00	0.01	19.98	62.25	33.97	3.78
AS8 pl pheno rim 1-7	48.59	0.00	31.87	0.03	0.85	16.42	2.23	0.29	0.00	0.07	100.34	8.92	0.000	6.90	0.00	0.09	3.23	0.79	0.07	0.00	0.01	20.01	78.94	19.39	1.68
AS8 same pl pheno mantle 1-8	47.37	0.03	32.31	0.00	0.90	17.21	1.66	0.21	0.01	0.13	99.84	8.77	0.003	7.05	0.00	0.09	3.41	0.60	0.05	0.00	0.01	19.98	84.07	14.68	1.24
AS8 same pl pheno core 1-9	47.05	0.03	32.67	0.01	0.90	17.31	1.48	0.18	0.00	0.06	99.69	8.71	0.004	7.13	0.00	0.09	3.43	0.53	0.04	0.00	0.01	19.96	85.68	13.23	1.08
AS8 pl gm 2-5	53.75	0.07	28.44	0.00	0.87	12.35	3.96	0.81	0.05	0.15	100.47	9.75	0.010	6.09	0.00	0.09	2.40	1.39	0.19	0.00	0.02	19.94	60.27	35.01	4.72
AS8 pl micropheno 2-6	48.54	0.05	31.83	0.01	0.82	16.33	2.13	0.29	0.00	0.13	100.12	8.93	0.007	6.90	0.00	0.08	3.22	0.76	0.07	0.00	0.01	19.99	79.52	18.81	1.67
AS8 pl glomerule rim 3-1	50.78	0.07	29.52	0.03	0.89	13.74	3.28	0.59	0.02	0.14	99.05	9.39	0.010	6.44	0.01	0.09	2.72	1.18	0.14	0.00	0.01	19.99	67.44	29.14	3.42
AS8 same pl glomerule core 3-2	48.54	0.03	31.74	0.00	0.89	15.97	2.21	0.30	0.01	0.08	99.78	8.95	0.004	6.90	0.00	0.09	3.16	0.79	0.07	0.00	0.01	19.98	78.52	19.70	1.78
MAR1pl gm 1-4	51.84	0.07	29.32	0.08	0.86	13.19	3.62	0.63	0.03	0.00	99.64	9.51	0.010	6.34	0.01	0.09	2.59	1.29	0.15	0.00	0.00	19.99	64.37	31.96	3.67
MAR1pl pheno core 1-5	52.91	0.06	28.50	0.01	0.67	12.05	4.10	0.84	0.02	0.05	99.20	9.71	0.008	6.17	0.00	0.07	2.37	1.46	0.20	0.00	0.01	19.99	58.90	36.23	4.87
MAR1pl gm 1-6	53.26	0.10	28.42	0.00	0.93	12.32	4.02	0.86	0.06	0.14	100.11	9.71	0.014	6.11	0.00	0.09	2.41	1.42	0.20	0.00	0.02	19.98	59.78	35.27	4.95
MAR1pl pheno rim 2-1	51.86	0.04	29.21	0.00	0.84	13.36	3.58	0.51	0.07	0.08	99.53	9.52	0.005	6.32	0.00	0.09	2.63	1.27	0.12	0.00	0.01	19.97	65.37	31.66	2.97
MAR1pl same pheno core 2-2	52.92	0.07	28.65	0.00	0.72	12.42	3.92	0.75	0.00	0.08	99.52	9.69	0.010	6.18	0.00	0.07	2.43	1.39	0.18	0.00	0.01	19.96	60.86	34.75	4.39
MAR1pl gm 2-3	53.56	0.11	28.75	0.00	1.03	12.39	3.94	0.88	0.00	0.04	100.69	9.70	0.014	6.14	0.00	0.10	2.40	1.38	0.20	0.00	0.00	19.96	60.21	34.68	5.11
MAR1pl pheno rim 4-1	52.21	0.07	29.47	0.01	0.86	13.16	3.85	0.72	0.09	0.08	100.52	9.51	0.009	6.33	0.00	0.09	2.57	1.36	0.17	0.01	0.01	20.04	62.69	33.22	4.08
MAR1pl same pheno mantle 4-2	52.90	0.11	28.59	0.00	0.69	12.50	3.86	0.75	0.00	0.08	99.49	9.69	0.015	6.17	0.00	0.07	2.45	1.37	0.18	0.00	0.01	19.95	61.31	34.30	4.39
MAR1pl same pheno core 4-3	53.81	0.06	28.65	0.04	0.60	12.25	4.02	0.83	0.02	0.08	100.37	9.76	0.008	6.12	0.01	0.06	2.38	1.41	0.19	0.00	0.01	19.95	59.72	35.45	4.83
MAR1pl pheno rim 4-4	51.56	0.05	29.77	0.00	0.86	13.61	3.48	0.60	0.14	0.07	100.15	9.43	0.007	6.42	0.00	0.09	2.67	1.23	0.14	0.01	0.01	20.00	65.99	30.52	3.49
MAR1pl same pheno core 4-5	51.91	0.06	29.37	0.06	0.80	13.30	3.69	0.63	0.09	0.19	100.09	9.50	0.008	6.33	0.01	0.08	2.61	1.31	0.15	0.01	0.02	20.02	64.16	32.22	3.62
MAR1pl micropheno 4-6	52.77	0.07	29.03	0.04	0.71	12.86	3.81	0.68	0.06	0.01	100.05	9.62	0.010	6.24	0.01	0.07	2.51	1.35	0.16	0.00	0.00	19.97	62.53	33.53	3.94
MAR1pl gm 4-7	54.90	0.09	27.15	0.00	1.02	10.64	4.59	1.27	0.08	0.15	99.89	10.01	0.012	5.83	0.00	0.10	2.08	1.62	0.30	0.01	0.02	19.97	51.99	40.61	7.40
MAR1pl gm 5-5	55.28	0.12	27.70	0.00	1.33	10.89	4.56	0.86	0.14	0.05	100.95	9.96	0.017	5.88	0.00	0.13	2.10	1.59	0.20	0.01	0.01	19.91	54.00	40.92	5.08

Plagioclase (continued)

LAT2 pl pheno rim 2-1	53.31	0.12	28.72	0.00	0.79	12.50	4.05	0.53	0.02	0.08	100.12	9.69	0.017	6.16	0.00	0.08	2.44	1.43	0.12	0.00	0.01	19.95	61.10	35.81	3.09
LAT2 same pl pheno mantle 2-2	51.15	0.06	30.63	0.00	0.71	14.76	3.08	0.31	0.02	0.09	100.83	9.29	0.009	6.56	0.00	0.07	2.87	1.09	0.07	0.00	0.01	19.97	71.27	26.93	1.80
LAT2 same pl pheno core 2-3	50.89	0.05	30.68	0.00	0.67	14.66	2.95	0.28	0.00	0.08	100.26	9.28	0.007	6.60	0.00	0.07	2.87	1.04	0.07	0.00	0.01	19.93	72.11	26.24	1.65
LAT2 pl gm 2-4	53.89	0.06	28.99	0.03	1.29	10.75	4.47	0.77	0.01	0.05	100.31	9.76	0.008	6.19	0.00	0.13	2.09	1.57	0.18	0.00	0.00	19.94	54.39	40.95	4.66
LAT2 pl gm 2-5	56.31	0.08	27.37	0.02	0.86	8.98	5.25	1.32	0.01	0.10	100.30	#####	0.011	5.818	0.002	0.087	1.735	1.837	0.304	0.000	0.011	19.955	44.77	47.40	7.84
LAT2 pl pheno rim 2-8	57.73	0.03	26.46	0.03	0.48	9.14	5.62	0.96	0.12	0.00	100.56	#####	0.004	5.589	0.004	0.048	1.754	1.952	0.220	0.008	0.000	19.921	44.67	49.71	5.61
LAT2 same pl pheno core 2-9	49.82	0.04	31.22	0.00	0.69	15.42	2.80	0.26	0.03	0.04	100.33	9.114	0.005	6.732	0.000	0.071	3.023	0.993	0.061	0.002	0.004	20.007	74.14	24.36	1.50
LAT2 pl gm 3-4	54.32	0.09	27.98	0.00	0.64	11.34	4.60	0.74	0.04	0.13	99.86	9.879	0.012	5.999	0.000	0.064	2.209	1.624	0.171	0.003	0.013	19.974	55.18	40.55	4.27
LAT2 pl gm 3-5	55.24	0.10	28.11	0.04	0.72	11.42	4.50	0.65	0.03	0.00	100.81	9.930	0.013	5.958	0.007	0.073	2.200	1.569	0.149	0.002	0.000	19.900	56.16	40.05	3.79
LAT2 pl micropheno rim 3-6	53.79	0.06	28.72	0.00	0.70	12.46	4.31	0.54	0.05	0.00	100.64	9.728	0.009	6.123	0.000	0.070	2.415	1.512	0.125	0.004	0.000	19.985	59.60	37.31	3.09
LAT2 same pl micropheno rim 3-7	50.40	0.05	30.92	0.00	0.66	14.93	2.99	0.27	0.06	0.00	100.27	9.206	0.007	6.658	0.000	0.067	2.922	1.058	0.062	0.004	0.000	19.985	72.28	26.18	1.55
LAT5 pl pheno rim 1-1	52.27	0.07	29.91	0.07	0.96	13.51	3.64	0.47	0.03	0.04	100.97	9.464	0.010	6.384	0.011	0.097	2.622	1.276	0.109	0.002	0.004	19.979	65.42	31.85	2.73
LAT5 same pl pheno cribr mantle 1-2	50.67	0.05	30.87	0.00	0.79	15.01	2.83	0.35	0.00	0.00	100.57	9.228	0.007	6.627	0.000	0.080	2.929	0.999	0.082	0.000	0.000	19.952	73.03	24.92	2.05
LAT5 same pl pheno mantle2 1-3	47.99	0.05	32.77	0.01	0.79	17.01	1.85	0.16	0.00	0.05	100.67	8.784	0.007	7.072	0.001	0.080	3.336	0.655	0.038	0.000	0.005	19.980	82.79	16.26	0.95
LAT5 same pl pheno mantle3 1-4	48.55	0.07	32.41	0.08	0.71	16.67	1.97	0.25	0.04	0.09	100.82	8.869	0.009	6.980	0.012	0.072	3.264	0.698	0.058	0.003	0.009	19.973	81.20	17.36	1.43
LAT5 same pl pheno core1 1-5	48.53	0.08	32.52	0.00	0.68	16.66	2.04	0.19	0.06	0.09	100.85	8.860	0.011	7.000	0.000	0.069	3.258	0.723	0.044	0.004	0.010	19.979	80.94	17.95	1.11
LAT5 same pl pheno core2 1-6	47.62	0.04	32.82	0.00	0.68	17.12	1.76	0.17	0.00	0.08	100.29	8.752	0.006	7.112	0.000	0.069	3.371	0.627	0.040	0.000	0.008	19.985	83.49	15.53	0.98
LAT5 pl gm 1-7	54.33	0.10	28.22	0.02	0.69	11.42	4.66	0.69	0.03	0.12	100.27	9.845	0.013	6.030	0.002	0.070	2.218	1.637	0.160	0.002	0.012	19.990	55.24	40.76	4.00
LAT5 pl gm 2-2	55.00	0.09	27.95	0.00	0.64	10.99	4.88	0.84	0.06	0.05	100.49	9.934	0.013	5.951	0.000	0.064	2.127	1.707	0.193	0.004	0.006	19.997	52.81	42.40	4.79
LAT5 pl gm 2-4	51.41	0.06	30.29	0.03	0.74	14.27	3.18	0.40	0.00	0.05	100.42	9.359	0.012	6.502	0.004	0.075	2.783	1.124	0.092	0.000	0.005	19.952	69.61	28.10	2.29
LAT5 pl gm 3-4	53.47	0.06	28.68	0.02	0.67	12.29	4.21	0.61	0.13	0.09	100.22	9.719	0.008	6.146	0.003	0.067	2.393	1.482	0.141	0.009	0.010	19.978	59.58	36.91	3.51
LAT5 pl pheno rim 3-5	53.50	0.02	28.76	0.02	0.64	12.20	4.33	0.61	0.14	0.11	100.33	9.714	0.003	6.158	0.003	0.065	2.373	1.526	0.142	0.010	0.011	20.005	58.72	37.76	3.52
LAT5 same pl pheno clear mantle 3-7	51.99	0.08	29.63	0.00	0.66	13.63	3.49	0.52	0.00	0.13	100.04	9.486	0.011	6.372	0.000	0.067	2.665	1.236	0.121	0.000	0.003	19.962	66.26	30.72	3.02
LAT5 same pl pheno core1 3-8	48.00	0.03	32.16	0.04	0.70	16.75	2.06	0.19	0.00	0.00	99.94	8.848	0.005	6.988	0.006	0.072	3.309	0.736	0.044	0.000	0.000	20.007	80.93	17.99	1.08
LAT5 same pl pheno core2 3-9	46.57	0.01	33.22	0.02	0.71	17.57	1.66	0.16	0.04	0.08	100.03	8.609	0.002	7.240	0.003	0.073	3.480	0.594	0.038	0.003	0.008	20.049	84.64	14.44	0.92
BEL1 same pl pheno mantle2 1-3	53.69	0.05	28.92	0.00	0.65	12.96	3.70	0.62	0.09	0.06	100.75	9.702	0.007	6.161	0.000	0.066	2.510	1.297	0.142	0.007	0.007	19.897	63.56	32.84	3.60
BEL1 same pl pheno outer core 1-4	53.49	0.07	28.98	0.03	0.64	13.01	3.84	0.63	0.00	0.07	100.76	9.670	0.010	6.177	0.004	0.065	2.520	1.345	0.146	0.000	0.007	19.944	62.83	33.54	3.63
BEL1 same pl pheno inner core1-5	51.00	0.04	30.45	0.09	0.73	14.98	2.80	0.38	0.15	0.03	100.65	9.289	0.005	6.540	0.014	0.075	2.924	0.990	0.089	0.010	0.003	19.938	73.04	24.74	2.22
BEL1 pl gm 2-3	54.03	0.10	28.77	0.02	0.80	12.67	4.02	0.62	0.00	0.01	101.02	9.734	0.013	6.110	0.002	0.080	2.446	1.403	0.142	0.000	0.001	19.930	61.30	35.15	3.55
BEL1 pl in cpx pheno 2-9	53.77	0.15	28.57	0.03	1.62	12.18	4.05	0.57	0.00	0.00	100.94	9.721	0.020	6.089	0.005	0.163	2.359	1.419	0.131	0.000	0.000	19.907	60.35	36.30	3.35
BEL1 pl inclusion in cpx pheno 2-10	53.09	0.07	29.01	0.02	0.78	13.04	3.93	0.55	0.00	0.00	100.48	9.632	0.009	6.204	0.002	0.079	2.535	1.383	0.128	0.000	0.000	19.972	62.66	34.18	3.16
BEL1 pl inclusion in cpx pheno 2-12	53.43	0.07	28.99	0.00	0.76	12.95	3.79	0.59	0.09	0.00	100.66	9.670	0.010	6.184	0.000	0.076	2.510	1.330	0.137	0.006	0.000	19.923	63.12	33.44	3.44
BEL1 pl gm 2-14	54.21	0.06	28.45	0.00	0.79	12.62	3.93	0.69	0.01	0.00	100.76	9.787	0.008	6.056	0.000	0.080	2.440	1.374	0.159	0.001	0.000	19.904	61.42	34.58	4.01
BUF4 pl gm 1-5	54.84	0.04	27.99	0.00	0.91	12.02	4.07	0.81	0.12	0.03	100.82	8.993	0.005	5.952	0.000	0.091	2.323	1.424	0.186	0.008	0.003	19.886	59.06	36.20	4.74
BUF4 pl cribose pheno rim 1-6	48.70	0.01	32.00	0.03	0.90	16.68	1.81	0.22	0.07	0.02	100.43	8.927	0.002	6.914	0.004	0.092	3.276	0.644	0.051	0.005	0.002	19.916	82.52	16.21	1.27
BUF4 pl cribose pheno core 1-7	51.79	0.04	29.88	0.01	0.94	14.61	2.98	0.39	0.02	0.03	100.70	9.411	0.006	6.402	0.001	0.095	2.844	1.049	0.091	0.002	0.004	19.904	71.38	26.33	2.29
BUF4 pl cribose glomerule rim 2-1	50.03	0.08	31.11	0.02	1.03	15.82	2.31	0.30	0.04	0.04	100.77	9.123	0.010	6.688	0.003	0.105	3.092	0.817	0.069	0.003	0.004	19.913	77.74	20.54	1.73
BUF4 same pl cribose glomerule core 2-2	50.52	0.03	30.99	0.01	0.95	15.69	2.33	0.29	0.02	0.04	100.88	9.186	0.004	6.643	0.002	0.096	3.058	0.823	0.067	0.001	0.005	19.885	77.46	20.84	1.70
BUF4 same pl cribose glomerule rim 2-3	50.20	0.06	30.83	0.01	0.93	15.54	2.29	0.27	0.00	0.04	100.17	9.186	0.009	6.651	0.001	0.095	3.048	0.814	0.062	0.000	0.004	19.870	77.67	20.74	1.59
BUF4 same pl cribose glomerule core 2-4	49.73	0.00	31.27	0.03	0.93	16.18	2.07	0.28	0.11	0.02	100.61	9.086	0.000	6.736	0.005	0.095	3.169	0.733	0.065	0.008	0.002	19.897	79.89	18.47	1.63
BUF4 same pl cribose glomerule core 2-5	47.59	0.01	32.34	0.06	0.85	17.53	1.50	0.17	0.01	0.01	100.07	8.777	0.001	7.032	0.010	0.088	3.464	0.535	0.040	0.001	0.001	19.949	85.77	13.25	0.98
BUF4 pl pheno rim 3-3	49.73	0.06	30.93	0.01	1.02	15.51	2.42	0.30	0.06	0.00	100.04	9.131	0.008	6.696	0.001	0.104	3.052	0.861	0.071	0.004	0.000	19.928	76.60	21.62	1.79
BUF4 same pl pheno core 3-4	49.15	0.02	31.25	0.03	0.92	16.00	2.21	0.26	0.13	0.02	100.00	9.044	0.003	6.778	0.005	0.094	3.154	0.790	0.062	0.010	0.002	19.942	78.74	19.71	1.55
BUF4 pl micropheno 4-3	48.84	0.02	31.58	0.01	0.89	16.52	1.98	0.21	0.05	0.00	100.10	8.978	0.003	6.843	0.001	0.091	3.255	0.705	0.050	0.004	0.000	19.929	81.18	17.58	1.24
BUF4 pl gm 6-3	47.96	0.02	32.00	0.00	1.02	16.92	1.75	0.22	0.00	0.01	99.91	8.852	0.002	6.964	0.000	0.105	3.347	0.625	0.053	0.000	0.001	19.950	83.15	15.53	1.31
BUF4 pl pheno cribose rim 6-5	48.50	0.06	31.88	0.02	0.92	16.87	1.81	0.21	0.05	0.02	100.35	8.906	0.008	6.902	0.003	0.094	3.320	0.646	0.050	0.004	0.002	19.935	82.68	16.08	1.24
BUF4 pl gm 7-4	54.77	0.06	27.38	0.00	1.32	11.35	4.17	1.03	0.00	0.08	100.17	9.954													

Plagioclase (continued)

BUF2 same pl pheno core 3-2	48.32	0.03	32.33	0.04	0.89	17.06	1.67	0.17	0.19	0.00	100.69	8.851	0.004	6.980	0.006	0.091	3.347	0.591	0.040	0.013	0.000	19.925	84.13	14.86	1.01
BUF2 pl in cpx 3-9	49.57	0.02	30.99	0.00	0.99	15.62	2.41	0.30	0.08	0.04	100.01	9.110	0.003	6.714	0.000	0.101	3.077	0.858	0.070	0.005	0.004	19.943	76.83	21.43	1.74
BUF2 pl pheno rim 4-1	48.29	0.04	31.76	0.04	1.06	16.57	1.90	0.20	0.00	0.00	99.86	8.909	0.005	6.908	0.006	0.109	3.275	0.679	0.047	0.000	0.000	19.940	81.84	16.97	1.18
BUF2 same pl pheno mantle 4-2	48.02	0.02	32.03	0.04	0.85	16.96	1.72	0.20	0.17	0.00	100.01	8.857	0.003	6.964	0.006	0.087	3.351	0.616	0.048	0.012	0.000	19.946	83.46	15.35	1.20
BUF2 same pl pheno outer core 4-3	47.61	0.03	32.64	0.00	0.77	17.66	1.33	0.11	0.13	0.08	100.35	8.756	0.004	7.077	0.000	0.079	3.480	0.473	0.025	0.009	0.009	19.911	87.48	11.88	0.64
BUF2 same pl pheno inner core 4-4	47.89	0.01	32.36	0.00	0.80	17.55	1.39	0.14	0.15	0.00	100.28	8.809	0.001	7.016	0.000	0.082	3.458	0.497	0.033	0.011	0.000	19.907	86.70	12.46	0.84
GAR3 pl gm 1-7	51.13	0.07	29.88	0.06	1.08	14.60	2.86	0.47	0.00	0.04	100.18	9.356	0.009	6.445	0.009	0.110	2.862	1.014	0.109	0.000	0.004	19.919	71.82	25.46	2.72
GAR3 pl gm 1-8	54.45	0.05	27.78	0.00	1.06	12.34	3.82	0.87	0.11	0.10	100.59	9.867	0.007	5.936	0.000	0.107	2.396	1.343	0.201	0.008	0.011	19.876	60.82	34.08	5.11
GAR3 pl pheno rim 1-9	52.81	0.03	29.21	0.05	1.06	13.94	3.21	0.57	0.05	0.00	100.94	9.564	0.004	6.237	0.008	0.107	2.704	1.129	0.133	0.003	0.000	19.890	68.20	28.46	3.34
GAR3 same pl pheno core 1-10	52.81	0.04	29.22	0.00	0.92	13.85	3.18	0.59	0.01	0.00	100.63	9.578	0.006	6.249	0.000	0.093	2.691	1.117	0.137	0.001	0.000	19.872	68.21	28.31	3.48
GAR3 pl gm 3-5	52.47	0.09	28.99	0.00	1.01	13.68	3.35	0.60	0.00	0.08	100.27	9.566	0.012	6.231	0.000	0.103	2.673	1.184	0.140	0.000	0.009	19.918	66.87	29.63	3.50
GAR3 pl gm 6-6	54.17	0.06	28.51	0.04	1.07	12.73	3.69	0.81	0.07	0.00	101.14	9.764	0.008	6.058	0.006	0.108	2.458	1.291	0.185	0.005	0.000	19.883	62.48	32.81	4.71
GAR3 pl micropheno 6-7	53.25	0.04	29.10	0.00	1.06	13.66	3.23	0.66	0.07	0.02	101.09	9.620	0.006	6.197	0.000	0.106	2.644	1.132	0.152	0.005	0.002	19.865	67.31	28.82	3.87
PR3 pl pheno rim 1-8	54.09	0.02	28.83	0.00	0.67	12.88	3.83	0.57	0.23	0.06	101.15	9.738	0.002	6.119	0.000	0.067	2.485	1.336	0.131	0.016	0.006	19.900	62.88	33.80	3.31
PR3 same pl pheno core 1-9	54.62	0.04	28.93	0.00	0.70	12.58	3.98	0.36	0.15	0.02	101.37	9.782	0.005	6.108	0.000	0.070	2.414	1.380	0.082	0.011	0.002	19.854	62.27	35.61	2.12
PR3 pl pheno rim 1-10	51.66	0.01	30.39	0.00	0.75	14.57	2.85	0.33	0.12	0.08	100.76	9.372	0.002	6.501	0.000	0.076	2.833	1.001	0.077	0.008	0.008	19.877	72.44	25.59	1.97
PR3 same pl pheno core 1-11	53.98	0.00	28.63	0.02	0.69	12.80	3.80	0.59	0.18	0.00	100.69	9.757	0.001	6.101	0.003	0.070	2.479	1.333	0.136	0.013	0.000	19.892	62.79	33.77	3.45
PR3 pl pheno rim 2-1	55.30	0.03	28.20	0.08	0.56	12.14	4.14	0.72	0.14	0.08	101.37	9.908	0.004	5.956	0.012	0.056	2.330	1.440	0.164	0.010	0.009	19.885	59.23	36.60	4.16
PR3 same pl pheno mantle 2-2	54.97	0.03	28.58	0.02	0.61	12.06	3.86	0.66	0.00	0.00	100.78	9.875	0.004	6.053	0.003	0.061	2.321	1.343	0.150	0.000	0.000	19.811	60.84	35.22	3.94
PR3 same pl pheno core 2-3	54.75	0.02	28.44	0.00	0.66	12.02	4.09	0.63	0.10	0.10	100.81	9.858	0.003	6.038	0.000	0.066	2.318	1.429	0.144	0.007	0.010	19.874	59.56	36.73	3.71
PR3 pl pheno rim 3-6	53.55	0.01	29.23	0.00	0.61	12.55	3.55	0.69	0.14	0.02	100.35	9.697	0.002	6.241	0.000	0.062	2.435	1.247	0.159	0.010	0.002	19.853	63.40	32.47	4.13
PR3 pl pheno rim 3-7	53.62	0.04	29.46	0.00	0.78	13.11	3.64	0.48	0.10	0.02	101.25	9.640	0.006	6.245	0.000	0.078	2.525	1.270	0.110	0.007	0.002	19.883	64.66	32.53	2.81
PR3 pl pheno rim 3-8	54.79	0.03	28.21	0.00	0.65	11.94	4.09	0.72	0.15	0.00	100.59	9.886	0.004	6.001	0.000	0.066	2.309	1.431	0.166	0.011	0.000	19.874	59.12	36.65	4.24
PR3 pl pheno rim 4-1	51.93	0.03	30.03	0.00	0.78	14.00	3.03	0.31	0.09	0.09	100.28	9.449	0.003	6.442	0.000	0.079	2.729	1.070	0.071	0.006	0.009	19.858	70.50	27.66	1.84
PR3 same pl pheno core 4-2	53.75	0.07	28.84	0.00	0.59	12.72	3.71	0.63	0.28	0.07	100.64	9.725	0.009	6.152	0.000	0.059	2.465	1.300	0.145	0.019	0.007	19.882	63.05	33.24	3.71
PR3 pl pheno rim 4-3	54.14	0.01	28.22	0.00	0.66	12.08	4.01	0.78	0.07	0.00	99.97	9.838	0.002	6.045	0.000	0.067	2.351	1.414	0.180	0.005	0.000	19.901	59.60	35.84	4.55
PR3 same pl pheno core 4-4	54.53	0.03	28.13	0.00	0.61	12.00	4.28	0.73	0.11	0.09	100.51	9.862	0.004	5.998	0.000	0.062	2.326	1.502	0.169	0.008	0.009	19.940	58.20	37.57	4.23
PR20 pl micropheno rim 1-7	52.76	0.07	29.43	0.00	0.74	13.59	3.42	0.48	0.08	0.06	100.64	9.563	0.010	6.289	0.000	0.075	2.639	1.201	0.112	0.005	0.006	19.901	66.78	30.39	2.83
PR20 pl micropheno rim 1-8	53.12	0.03	29.26	0.00	0.75	13.06	3.40	0.56	0.07	0.00	100.26	9.639	0.004	6.260	0.000	0.076	2.540	1.197	0.128	0.005	0.000	19.851	65.70	30.97	3.32
PR20 pl micropheno 1-9	54.06	0.08	28.13	0.00	0.79	12.42	3.88	0.65	0.08	0.07	100.15	9.818	0.011	6.023	0.000	0.080	2.417	1.365	0.151	0.006	0.007	19.878	61.45	34.70	3.85
PR20 pl gm 2-14	52.57	0.06	29.18	0.00	0.77	13.39	3.40	0.53	0.11	0.05	100.06	9.584	0.008	6.271	0.000	0.079	2.616	1.202	0.124	0.008	0.005	19.896	66.36	30.49	3.15
PR20 pl micropheno 2-15	52.11	0.07	29.59	0.00	0.77	14.01	3.29	0.45	0.00	0.06	100.35	9.485	0.009	6.350	0.000	0.078	2.732	1.162	0.104	0.000	0.006	19.926	68.33	29.06	2.61

Sanidine																									
AS2 san gm 2-1	66.70	0.14	18.86	0.00	0.41	0.61	4.04	10.47	0.00	0.00	101.22	11.955	0.019	3.984	0.000	0.040	0.116	1.403	2.394	0.000	0.000	19.912	2.97	35.86	61.17
AS2 san gm 2-4	66.07	0.15	18.71	0.02	0.52	0.91	4.10	10.12	0.03	0.00	100.64	11.923	0.021	3.980	0.004	0.053	0.176	1.435	2.330	0.002	0.000	19.922	4.46	36.40	59.14
AS2 san gm 2-5	64.67	0.09	19.55	0.00	0.42	1.04	3.98	9.81	1.08	0.03	100.66	11.754	0.013	4.188	0.000	0.042	0.203	1.403	2.275	0.077	0.003	19.957	5.22	36.15	58.62
AS2 san gm 4-4	65.12	0.14	18.97	0.00	0.35	0.79	3.41	11.28	0.03	0.00	100.09	11.863	0.019	4.075	0.000	0.036	0.155	1.203	2.622	0.002	0.000	19.975	3.89	30.23	65.88
AS3 san interstitial 1-6	63.24	0.08	20.32	0.06	0.58	1.70	3.80	9.13	1.30	0.00	100.20	11.570	0.012	4.384	0.009	0.059	0.333	1.346	2.131	0.093	0.000	19.936	8.73	35.34	55.93
AS3 san gm 2-2	65.31	0.14	19.02	0.05	0.42	0.87	3.61	10.44	0.24	0.00	100.09	11.872	0.019	4.076	0.008	0.042	0.169	1.272	2.421	0.017	0.000	19.896	4.38	32.93	62.69
AS3 san gm 2-3	65.25	0.15	19.09	0.00	0.37	0.98	3.69	10.50	0.07	0.00	100.10	11.854	0.020	4.089	0.000	0.038	0.191	1.299	2.433	0.005	0.000	19.929	4.86	33.12	62.02
AS3 san gm 2-4	64.98	0.00	18.66	0.00	0.15	0.04	0.28	16.10	0.31	0.17	100.68	11.959	0.000	4.048	0.000	0.015	0.008	0.098	3.779	0.022	0.018	19.948	0.20	2.53	97.27
AS7 san gm 1-10	64.74	0.13	19.02	0.00	0.64	0.88	2.83	11.43	0.60	0.00	100.27	11.835	0.017	4.098	0.000	0.065	0.173	1.003	2.666	0.043	0.000	19.901	4.50	26.11	69.39
AS7 san gm 1-12	64.88	0.01	18.23	0.00	0.21	0.02	0.24	16.45	0.02	0.00	100.06	12.004	0.002	3.977	0.000	0.022	0.004	0.086	3.882	0.002	0.000	19.979	0.09	2.18	97.73
AS7 san gm 2-4	64.05	0.13	19.36	0.00	0.59	1.24	3.10	10.84	0.90	0.00	100.22	11.736	0.018	4.182	0.000	0.061	0.244	1.102	2.535	0.065	0.000	19.943	6.29	28.39	65.32
AS7 san gm 2-7	63.75	0.18	19.03	0.00	1.43	1.32	3.62	9.65	0.09	0.00	99.06	11.743	0.025	4.133	0.000	0.147	0.260	1.293	2.267	0.006	0.000	19.873	6.81	33.86	59.34
AS7 san gm 2-8	64.80	0.20	19.22	0.05	0.54	1.20	3.27	11.10	0.24	0.00	100.61	11.782	0.027	4.120	0.008	0.055	0.234	1.151	2.575	0.017	0.000	19.968	5.90	29.06	65.03
AS7 san gm 2-9	65.02	0.15	19.15	0.00	0.46	1.10	3.23	11.02	0.18	0.00	100.31	11.827	0.021	4.106	0.000	0.046	0.215	1.138	2.558	0.013	0.000	19.924	5.49	29.09	65.41
AS7 pl pheno core 2-11	64.36	0.23	18.47	0.00	0.02	0.02	0.47	15.84	0.18	0.00	99.59	11.946	0.033	4.042	0.000	0.002	0.005	0.169	3.751	0.013	0.000	19.959	0.12	4.30	95.58
AS8 san gm 3-3	64.21	0.24	20.06	0.00	0.42	1.47	4.45	9.13	0.20	0.00	100.19	11.648	0.033	4.290	0.000	0.043	0.286	1.566	2.113	0.014	0.000	19.992	7.21	39.50	53.29
AS8 san gm 3-4	63.08	0.14	19.20	0.00	0.61	0.95	2.98	11.13	0.48	0.00	98.56	11.735	0.020	4.210	0.000	0.063	0.189	1.073	2.642	0.035	0.000	19.967	4.85	27.48	67.67
AS8 san gm 3-5	64.14	0.11	18.91	0.00	0.74	1.08	2.92	11.21	0.17	0.00	99.28	11.816	0.015	4.106	0.000	0.076	0.212	1.044	2.636	0.012	0.000	19.918	5.45	26.83	67.71
AS8 san gm 3-8	64.80	0.15	19.14	0.01	0.32	0.70	3.31	11.25	0.38	0.00	100.06	11.833	0.021	4.121	0.001	0.032	0.137	1.171	2.620	0.027	0.000	19.965	3.49	29.82	66.69
LAT5 san gm 1-8	66.99	0.21	18.56	0.01	0.66	0.32	5.20	9.05	0.00	0.00	101.00	11.987	0.028	3.915	0.002	0.066	0.061	1.803	2.067	0.000	0.000	19.929	1.56	45.86	52.58
LAT5 san gm 1-9	66.29	0.13	19.03	0.03	0.29	0.67	4.88	9.24	0.02	0.00	100.58	11.914	0.017	4.032	0.005	0.029	0.130	1.702	2.118	0.001	0.000	19.948	3.28	43.08	53.64
LAT5 san gm 2-1	65.86	0.17	19.11	0.00	0.29	0.76	4.01	10.57	0.18	0.00	100.95	11.871	0.023	4.062	0.000	0.030	0.147	1.402	2.430	0.013	0.000	19.976	3.69	35.23	61.08
LAT5 san gm 2-5	66.45	0.17	18.74	0.00	0.25	0.55	4.24	10.34	0.00	0.00	100.74	11.959	0.023	3.976	0.000	0.025	0.107	1.478	2.374	0.000	0.000	19.943	2.70	37.34	59.97
BEL1 pl inclusion in cpx pheno 2-11	65.34	0.10	20.57	0.00	0.39	2.59	4.85	7.51	0.00	0.00	101.35	11.629	0.013	4.315	0.000	0.039	0.494	1.675	1.706	0.000	0.000	19.872	12.76	43.22	44.03

Clinopyroxene

Sample	SiO ₂	TiO ₂	Al ₂ O ₃	Cr ₂ O ₃	MgO	CaO	MnO	FeO	Na ₂ O	Total:	Si	Ti	Al _(tot)	Al _(T)	Al _(M1)	Fe ³⁺ _(T)	Fe ³⁺ _(M1)	Fe ²⁺	Mn	Mg	Ca	Na	Cr	Sum	En	Fs	Wo	
AS2 cpx pheno rim 1-1	50.78	0.62	3.22	0.01	13.63	21.72	0.37	10.12	0.30	100.78	1.881	0.017	0.141	0.119	0.021	0.000	0.084	0.229	0.012	0.753	0.862	0.021	0.000	4.000	38.81	16.75	44.44	Aluminian Augite
AS2 same cpx pheno core 1-2	50.83	0.46	3.03	0.04	13.95	20.91	0.41	10.90	0.36	100.89	1.880	0.013	0.132	0.120	0.012	0.000	0.106	0.231	0.013	0.769	0.829	0.025	0.001	4.000	39.50	17.96	42.54	Aluminian Ferrian Augite
AS2 cpx glomerule 1-3	50.07	0.60	3.71	0.04	13.43	21.21	0.41	10.53	0.31	100.31	1.865	0.017	0.163	0.135	0.027	0.000	0.095	0.233	0.013	0.745	0.846	0.022	0.001	4.000	38.57	17.64	43.79	Aluminian Augite
AS2 cpx gm 1-11	51.67	0.50	2.03	0.02	13.61	21.08	0.46	11.54	0.27	101.18	1.916	0.014	0.089	0.084	0.004	0.000	0.070	0.287	0.014	0.752	0.837	0.019	0.001	4.000	38.34	18.97	42.68	Augite
AS2 cpx gm 2-3	50.42	0.69	3.00	0.02	12.31	21.02	0.48	12.31	0.28	100.52	1.892	0.019	0.133	0.108	0.025	0.000	0.064	0.322	0.015	0.688	0.845	0.021	0.000	4.000	35.58	20.75	43.67	Aluminian Augite
AS2 cpx gm 2-6	52.30	0.47	1.86	0.00	13.52	20.51	0.40	12.19	0.25	101.49	1.937	0.013	0.081	0.063	0.018	0.000	0.036	0.341	0.012	0.747	0.814	0.018	0.000	4.000	38.28	19.99	41.73	Augite
AS2 cpx pheno rim 4-1	50.34	0.63	3.00	0.00	12.94	20.74	0.43	11.53	0.28	99.89	1.892	0.018	0.133	0.108	0.025	0.000	0.068	0.295	0.014	0.725	0.835	0.021	0.000	4.000	37.44	19.44	43.13	Aluminian Augite
AS2 same cpx pheno core 4-2	51.30	0.43	2.60	0.00	14.69	20.46	0.38	10.02	0.33	100.22	1.903	0.012	0.114	0.097	0.016	0.000	0.081	0.229	0.012	0.812	0.813	0.024	0.000	4.000	41.70	16.56	41.74	Aluminian Augite
AS2 cpx pheno rim 5-7	51.14	0.48	2.12	0.03	13.55	21.19	0.51	11.43	0.26	100.71	1.904	0.013	0.093	0.093	0.000	0.003	0.087	0.266	0.016	0.752	0.845	0.019	0.001	4.000	38.18	18.89	42.93	Augite
AS2 same cpx pheno core 5-8	50.92	0.52	3.37	0.01	14.10	21.74	0.35	9.67	0.35	101.03	1.875	0.014	0.146	0.125	0.021	0.000	0.101	0.197	0.011	0.774	0.857	0.025	0.000	4.000	39.89	15.91	44.20	Aluminian Ferrian Augite
AS3 cpx pheno rim 1-1	50.76	0.56	3.22	0.00	14.14	21.67	0.32	9.47	0.27	100.42	1.880	0.016	0.141	0.120	0.021	0.000	0.088	0.206	0.010	0.781	0.860	0.020	0.000	4.000	40.16	15.60	44.24	Aluminian Augite
AS3 same cpx pheno core 1-2	50.93	0.52	3.71	0.00	14.05	20.82	0.27	10.19	0.35	100.83	1.880	0.014	0.161	0.120	0.041	0.000	0.076	0.239	0.008	0.773	0.823	0.025	0.000	4.000	40.29	16.82	42.89	Aluminian Augite
AS3 cpx pheno core 1-3	51.08	0.49	3.19	0.02	14.17	21.89	0.26	9.60	0.27	100.97	1.882	0.014	0.139	0.118	0.021	0.000	0.089	0.207	0.008	0.778	0.864	0.019	0.001	4.000	39.99	15.61	44.40	Aluminian Augite
AS3 cpx pheno rim 2-6	49.99	0.83	3.10	0.01	11.98	20.81	0.38	13.28	0.36	100.74	1.877	0.023	0.137	0.123	0.014	0.000	0.088	0.328	0.012	0.670	0.837	0.026	0.000	4.000	34.62	22.15	43.22	Aluminian Augite
AS3 same cpx pheno core 2-7	51.27	0.45	3.03	0.01	14.29	21.46	0.42	9.69	0.29	100.91	1.890	0.012	0.132	0.110	0.022	0.000	0.084	0.215	0.013	0.785	0.848	0.021	0.000	4.000	40.39	16.03	43.58	Aluminian Augite
AS7 cpx pheno rim 1-4	51.31	0.44	2.58	0.01	13.85	21.78	0.37	10.24	0.28	100.86	1.899	0.012	0.113	0.101	0.011	0.000	0.086	0.232	0.012	0.764	0.863	0.020	0.000	4.000	39.05	16.80	44.14	Aluminian Augite
AS7 same cpx pheno core 1-5	50.56	0.49	3.35	0.00	13.87	21.04	0.47	10.31	0.38	100.45	1.875	0.014	0.146	0.125	0.022	0.000	0.103	0.217	0.015	0.767	0.836	0.027	0.000	4.000	39.58	17.26	43.16	Aluminian Ferrian Augite
AS7 cpx pheno rim 1-6	50.59	0.53	3.85	0.02	14.18	21.58	0.26	9.35	0.32	100.68	1.866	0.015	0.167	0.134	0.033	0.000	0.094	0.194	0.008	0.780	0.853	0.023	0.001	4.000	40.42	15.37	44.21	Aluminian Augite
AS7 same cpx pheno core 1-7	51.22	0.52	2.85	0.01	14.24	21.31	0.39	10.14	0.31	100.99	1.889	0.014	0.124	0.111	0.013	0.000	0.090	0.223	0.012	0.783	0.842	0.022	0.000	4.000	40.15	16.66	43.18	Aluminian Augite
AS7 cpx micropheno 1-8	53.48	0.22	1.70	0.08	16.75	23.50	0.14	4.35	0.18	100.40	1.945	0.006	0.073	0.055	0.018	0.000	0.035	0.097	0.004	0.908	0.916	0.013	0.002	4.000	46.32	6.96	46.72	Diopside
AS7 cpx micropheno rim 2-1	49.82	0.57	3.32	0.02	13.96	21.69	0.30	9.75	0.27	99.69	1.860	0.016	0.146	0.140	0.006	0.000	0.121	0.183	0.009	0.777	0.868	0.019	0.001	4.000	39.68	16.02	44.30	Aluminian Ferrian Augite
AS7 same cpx micropheno core 2-2	49.98	0.47	3.37	0.03	14.10	22.10	0.29	8.91	0.28	99.51	1.864	0.013	0.148	0.136	0.012	0.000	0.117	0.160	0.009	0.784	0.883	0.020	0.001	4.000	40.12	14.68	45.20	Aluminian Ferrian Diopside
AS7 cpx gm 2-3	51.04	0.57	2.78	0.00	13.84	21.47	0.37	10.34	0.29	100.69	1.892	0.016	0.121	0.108	0.014	0.000	0.083	0.238	0.012	0.765	0.853	0.021	0.000	4.000	39.22	17.03	43.74	Aluminian Augite
AS7 cpx gm 2-6	51.20	0.58	2.06	0.02	13.43	19.77	0.52	12.95	0.26	100.79	1.913	0.016	0.091	0.087	0.004	0.000	0.069	0.336	0.016	0.748	0.791	0.019	0.001	4.000	38.16	21.47	40.37	Augite
AS8 cpx gm 1-5	50.36	0.74	3.73	0.00	13.10	21.26	0.38	11.33	0.25	101.15	1.867	0.021	0.163	0.133	0.030	0.000	0.080	0.271	0.012	0.724	0.845	0.018	0.000	4.000	37.47	18.81	43.72	Aluminian Augite
AS8 cpx gm 1-6	50.05	0.67	3.70	0.00	13.42	21.55	0.33	10.56	0.27	100.55	1.860	0.019	0.162	0.140	0.022	0.000	0.100	0.229	0.010	0.744	0.858	0.019	0.000	4.000	38.33	17.45	44.22	Aluminian Augite
AS8 cpx pheno rim 1-10	50.80	0.56	3.11	0.04	13.81	21.76	0.37	10.07	0.29	100.82	1.879	0.016	0.136	0.121	0.015	0.000	0.094	0.217	0.012	0.762	0.863	0.021	0.001	4.000	39.11	16.59	44.29	Aluminian Augite
AS8 same cpx pheno core 1-11	51.43	0.46	3.15	0.01	14.10	20.84	0.51	10.57	0.33	101.39	1.892	0.013	0.137	0.108	0.028	0.000	0.078	0.247	0.016	0.773	0.821	0.024	0.000	4.000	39.94	17.63	42.43	Aluminian Augite
AS8 cpx pheno rim 2-1	50.03	0.75	4.13	0.00	13.66	21.54	0.39	10.25	0.26	101.00	1.848	0.021	0.180	0.152	0.027	0.000	0.103	0.214	0.012	0.752	0.852	0.019	0.000	4.000	38.90	17.01	44.09	Aluminian Ferrian Augite
AS8 same cpx pheno core 2-2	49.97	0.53	4.05	0.01	13.57	21.26	0.34	10.28	0.33	100.34	1.856	0.015	0.177	0.144	0.034	0.000	0.104	0.215	0.011	0.751	0.846	0.024	0.000	4.000	38.98	17.13	43.89	Aluminian Ferrian Augite
AS8 cpx gm 2-3	51.04	0.54	3.14	0.07	14.04	21.55	0.34	9.51	0.35	100.60	1.888	0.015	0.137	0.112	0.024	0.000	0.081	0.213	0.011	0.774	0.854	0.025	0.002	4.000	40.05	15.77	44.18	Aluminian Augite
AS8 cpx glomerule core 3-6	50.02	0.53	3.37	0.01	13.82	21.44	0.38	10.15	0.32	100.04	1.863	0.015	0.148	0.137	0.011	0.000	0.120	0.196	0.012	0.768	0.855	0.023	0.000	4.000	39.34	16.82	43.84	Aluminian Ferrian Augite
MAR1cpx pheno rim 1-1	49.65	0.82	3.90	0.03	14.03	21.34	0.25	9.63	0.38	100.03	1.845	0.023	0.171	0.155	0.016	0.000	0.120	0.179	0.008	0.777	0.849	0.027	0.001	4.000	40.18	15.89	43.93	Aluminian Ferrian Augite
MAR1cpx same pheno core 1-2	49.91	0.93	4.01	0.01	13.88	21.64	0.29	9.25	0.40	100.31	1.849	0.026	0.175	0.151	0.024	0.000	0.104	0.182	0.009	0.767	0.859	0.029	0.000	4.000	39.90	15.39	44.70	Aluminian Ferrian Augite
MAR1cpx gm 1-3	48.45	1.20	5.38	0.00	12.69	20.39	0.31	10.99	0.58	99.99	1.811	0.034	0.237	0.189	0.047	0.000	0.116	0.227	0.010	0.707	0.816	0.042	0.000	4.000	37.68	18.83	43.49	Aluminian Ferrian Augite
MAR1cpx micropheno 2-4	49.51	1.08	3.99	0.04	13.54	21.43	0.38	10.19	0.40	100.54	1.837	0.030	0.175	0.163	0.012	0.000	0.119	0.197	0.012	0.749	0.852	0.029	0.001	4.000	38.83	17.00	44.17	Aluminian Ferrian Augite
MAR1cpx pheno rim 3-1	49.59	0.93	4.20	0.09	13.86	21.55	0.27	9.62	0.44	100.54	1.833	0.026	0.183	0.167	0.017	0.000	0.127	0.170	0.008	0.764	0.854	0.032	0.003	4.000	39.73	15.89	44.38	Aluminian Ferrian Augite
MAR1cpx glomerule core 3-2	49.17	0.94	5.63	0.22	14.60	21.97	0.15	7.21	0.33	100.23	1.808	0.026	0.244	0.192	0.052	0.000	0.105	0.117	0.005	0.800	0.866	0.023	0.006	4.000	42.28	11.97	45.74	Aluminian Ferrian Diopside
MAR1cpx gm 3-3	49.39	1.12	4.33	0.01	13.91	20.46	0.29	10.59	0.35	100.43	1.833	0.031	0.189	0.167	0.023	0.000	0.106	0.223	0.009	0.769	0.814	0.025	0.000	4.000	40.05	17.59	42.36	Aluminian Ferrian Augite
MAR1cpx pheno rim 5-1	49.79	0.95	4.42	0.04	13.87	22.39	0.27	8.85	0.33	100.91	1.832	0.026	0.192	0.168	0.024	0.000	0.113	0.159	0.009	0.761	0.883	0.024	0.001	4.000	39.53	14.59	45.88	Aluminian Ferrian Diopside
MAR1cpx same pheno mantle 5-2	49.80	1.00	4.42	0.02	13.65																							

Clinoptyroxene (continued)

LAT2 cpx large pheno line rime to core 1-3	50.88	1.10	3.53	0.05	14.42	21.36	0.26	9.16	0.31	101.06	1.871	0.030	0.153	0.129	0.024	0.000	0.065	0.217	0.008	0.790	0.842	0.022	0.001	4.000	41.12	15.09	43.79	Aluminian Augite
LAT2 cpx large pheno line rime to core 1-4	50.76	1.08	3.64	0.00	14.20	21.10	0.39	9.81	0.35	101.33	1.865	0.030	0.158	0.135	0.023	0.000	0.077	0.225	0.012	0.778	0.831	0.025	0.000	4.000	40.48	16.32	43.21	Aluminian Augite
LAT2 cpx large pheno line rime to core 1-6	51.30	1.10	3.35	0.04	14.30	21.58	0.36	8.83	0.37	101.24	1.883	0.030	0.145	0.117	0.028	0.000	0.054	0.217	0.011	0.783	0.849	0.027	0.001	4.000	40.90	14.75	44.35	Aluminian Augite
LAT2 cpx large pheno line rime to core 1-7	50.28	1.11	4.36	0.03	13.76	20.95	0.30	8.72	0.49	99.99	1.867	0.031	0.191	0.133	0.058	0.000	0.047	0.224	0.009	0.762	0.834	0.035	0.001	4.000	40.62	14.93	44.45	Aluminian Augite
LAT2 cpx large pheno line rime to core 1-9	49.55	1.16	5.33	0.04	13.86	21.53	0.17	9.19	0.40	101.23	1.817	0.032	0.230	0.183	0.048	0.000	0.098	0.184	0.005	0.758	0.846	0.028	0.001	4.000	40.07	15.18	44.75	Aluminian Augite
LAT2 cpx large pheno line rime to core 1-10	50.01	1.18	4.65	0.00	13.99	21.61	0.30	8.90	0.46	101.09	1.836	0.033	0.201	0.164	0.037	0.000	0.094	0.179	0.009	0.765	0.850	0.032	0.000	4.000	40.33	14.89	44.78	Aluminian Augite
LAT2 cpx large pheno line rime to core 1-11	50.48	1.12	4.11	0.07	14.33	21.99	0.25	8.36	0.33	101.02	1.853	0.031	0.178	0.147	0.031	0.000	0.076	0.181	0.008	0.784	0.865	0.023	0.002	4.000	40.98	13.81	45.20	Aluminian Diopside
LAT2 cpx large pheno line rime to core 1-12	50.38	1.20	4.44	0.00	14.00	21.29	0.21	9.25	0.41	101.19	1.850	0.033	0.192	0.150	0.043	0.000	0.070	0.214	0.007	0.766	0.838	0.029	0.000	4.000	40.45	15.33	44.21	Aluminian Augite
LAT2 cpx large pheno line rime to core 1-13	50.08	1.13	4.51	0.05	14.03	21.57	0.28	8.78	0.37	100.80	1.844	0.031	0.196	0.156	0.040	0.000	0.078	0.192	0.009	0.770	0.851	0.027	0.001	4.000	40.53	14.69	44.79	Aluminian Augite
LAT2 cpx large pheno line rime to core 1-14	49.91	1.26	5.25	0.04	13.34	21.29	0.20	8.88	0.39	100.57	1.846	0.035	0.229	0.154	0.075	0.000	0.035	0.240	0.006	0.736	0.844	0.028	0.001	4.000	39.54	15.11	45.36	Aluminian Diopside
LAT2 cpx large pheno line rime to core 1-15	50.67	1.01	3.79	0.02	14.34	21.26	0.20	8.88	0.35	100.53	1.870	0.028	0.165	0.130	0.035	0.000	0.063	0.211	0.006	0.789	0.841	0.025	0.000	4.000	41.31	14.69	44.01	Aluminian Augite
LAT2 cpx gm 2-6	48.52	1.97	4.28	0.00	11.92	20.88	0.46	12.05	0.46	100.54	1.822	0.056	0.189	0.178	0.011	0.000	0.090	0.288	0.015	0.667	0.840	0.033	0.000	4.000	35.12	20.68	44.19	Aluminian Augite
LAT2 cpx gm 2-7	46.67	2.46	5.66	0.00	12.15	21.05	0.37	11.65	0.42	100.44	1.749	0.069	0.250	0.250	0.000	0.001	0.143	0.221	0.012	0.679	0.845	0.031	0.000	4.000	35.71	19.83	44.46	Aluminian Ferrrian subsilicic Augite
LAT2 cpx gm 2-10	51.75	0.95	2.25	0.00	14.75	20.13	0.36	10.49	0.28	100.95	1.911	0.027	0.098	0.089	0.010	0.000	0.046	0.278	0.011	0.812	0.797	0.020	0.000	4.000	41.77	17.24	40.99	Augite
LAT2 cpx pheno rim 3-1	51.62	0.99	2.57	0.07	15.02	21.16	0.33	9.08	0.34	101.19	1.893	0.027	0.111	0.107	0.005	0.000	0.070	0.209	0.010	0.821	0.832	0.024	0.002	4.000	42.30	14.87	42.83	Aluminian Augite
LAT2 same cpx pheno mantle 3-2	51.35	0.89	3.10	0.00	14.71	20.42	0.35	10.01	0.38	101.21	1.887	0.024	0.134	0.113	0.021	0.000	0.071	0.237	0.011	0.806	0.804	0.027	0.000	4.000	41.79	16.52	41.70	Aluminian Augite
LAT2 same cpx pheno core 3-3	51.46	0.90	2.77	0.00	14.42	21.85	0.36	8.68	0.34	100.79	1.896	0.025	0.120	0.104	0.017	0.000	0.062	0.206	0.011	0.792	0.863	0.025	0.000	4.000	40.97	14.41	44.62	Aluminian Augite
LAT2 cpx gm 3-8	51.77	1.00	2.24	0.02	14.68	20.00	0.41	10.74	0.27	101.13	1.911	0.028	0.097	0.089	0.009	0.000	0.043	0.289	0.013	0.808	0.791	0.020	0.001	4.000	41.58	17.72	40.71	Augite
LAT2 cpx gm 3-9	51.80	0.97	2.37	0.00	14.95	21.11	0.44	10.40	0.26	101.31	1.906	0.027	0.103	0.094	0.008	0.000	0.051	0.269	0.014	0.820	0.793	0.019	0.000	4.000	42.11	17.15	40.74	Aluminian Augite
LAT2 cpx pheno rim 3-11	51.30	1.02	2.70	0.02	14.69	21.20	0.34	9.69	0.30	101.26	1.885	0.028	0.117	0.115	0.002	0.000	0.078	0.220	0.011	0.804	0.835	0.022	0.001	4.000	41.30	15.84	42.85	Aluminian Augite
LAT2 same cpx pheno core 3-12	50.79	1.03	3.30	0.00	14.49	21.62	0.32	8.93	0.30	100.78	1.872	0.029	0.143	0.128	0.015	0.000	0.078	0.197	0.010	0.796	0.853	0.022	0.000	4.000	41.15	14.75	44.11	Aluminian Augite
LAT5 cpx pheno line rim to core 2-6	51.30	0.90	2.81	0.05	15.06	21.12	0.31	8.68	0.28	100.50	1.892	0.025	0.122	0.108	0.014	0.000	0.063	0.205	0.010	0.828	0.835	0.020	0.001	4.000	42.68	14.29	43.03	Aluminian Augite
LAT5 cpx pheno line rim to core 2-7	51.03	0.85	3.20	0.07	15.30	21.11	0.19	8.39	0.36	100.50	1.876	0.023	0.139	0.124	0.015	0.000	0.086	0.172	0.006	0.839	0.832	0.026	0.002	4.000	43.36	13.65	42.99	Aluminian Augite
LAT5 cpx pheno line rim to core 2-8	50.49	1.00	3.83	0.09	14.59	20.60	0.31	9.65	0.41	100.97	1.857	0.028	0.166	0.143	0.023	0.000	0.091	0.205	0.010	0.800	0.812	0.029	0.003	4.000	41.70	15.97	42.32	Aluminian Augite
LAT5 cpx pheno line rim to core 2-9	50.94	0.85	3.01	0.07	14.93	21.06	0.41	8.99	0.32	100.59	1.878	0.024	0.131	0.122	0.009	0.000	0.087	0.190	0.013	0.821	0.832	0.023	0.002	4.000	42.24	14.93	42.83	Aluminian Augite
LAT5 cpx pheno line rim to core 2-10	50.48	0.95	3.38	0.14	14.69	21.35	0.23	8.64	0.34	100.19	1.867	0.026	0.148	0.133	0.015	0.000	0.086	0.181	0.007	0.810	0.846	0.024	0.004	4.000	41.97	14.21	43.82	Aluminian Augite
LAT5 cpx pheno line rim to core 2-12	52.18	0.52	3.42	0.11	12.78	19.83	0.37	10.09	0.30	99.60	1.963	0.015	0.151	0.037	0.114	0.000	0.000	0.317	0.012	0.717	0.799	0.022	0.003	4.000	38.85	17.83	43.33	Aluminian Augite
LAT5 cpx pheno line rim to core 2-13	50.58	0.94	3.95	0.24	14.64	22.00	0.30	8.00	0.31	100.96	1.855	0.026	0.171	0.145	0.026	0.000	0.082	0.163	0.009	0.800	0.865	0.022	0.007	4.000	41.70	13.26	45.04	Aluminian Diopside
LAT5 cpx pheno line rim to core 2-14	49.76	1.18	4.56	0.05	14.09	21.55	0.27	8.49	0.39	100.35	1.839	0.033	0.199	0.161	0.037	0.000	0.085	0.177	0.008	0.776	0.853	0.028	0.002	4.000	40.85	14.25	44.90	Aluminian Augite
LAT5 cpx pheno line rim to core 2-15	49.55	1.27	4.87	0.00	14.00	21.55	0.17	8.98	0.43	100.80	1.824	0.035	0.211	0.176	0.035	0.000	0.101	0.175	0.005	0.768	0.850	0.030	0.000	4.000	40.44	14.82	44.73	Aluminian Ferrrian Augite
LAT5 cpx pheno line rim to core 2-16	49.24	1.25	4.90	0.11	14.05	21.35	0.25	9.23	0.38	100.75	1.815	0.035	0.213	0.185	0.028	0.000	0.112	0.172	0.008	0.772	0.843	0.027	0.003	4.000	40.47	15.32	44.21	Aluminian Ferrrian Augite
LAT5 cpx pheno rim 3-1	49.88	1.15	4.54	0.09	13.83	21.20	0.24	9.29	0.40	100.63	1.843	0.032	0.198	0.157	0.041	0.000	0.078	0.209	0.007	0.762	0.839	0.029	0.003	4.000	40.18	15.54	44.28	Aluminian Augite
LAT5 same cpx pheno core 3-2	50.69	0.78	3.09	0.08	15.13	21.25	0.21	8.39	0.33	99.94	1.875	0.022	0.135	0.125	0.010	0.000	0.093	0.166	0.006	0.834	0.842	0.024	0.002	4.000	42.94	13.69	43.37	Aluminian Augite
LAT5 cpx gm 3-3	51.84	0.84	1.91	0.00	14.69	21.04	0.38	9.93	0.28	100.90	1.914	0.023	0.083	0.083	0.000	0.003	0.059	0.244	0.012	0.809	0.832	0.020	0.000	4.000	41.27	16.25	42.48	Augite
BEL1 cpx gm 1-7	49.73	1.92	4.56	0.05	12.58	21.55	0.24	9.73	0.42	100.77	1.849	0.054	0.200	0.151	0.049	0.000	0.025	0.278	0.007	0.697	0.858	0.031	0.001	4.000	37.38	16.61	46.01	Aluminian Diopside
BEL1 cpx gm 1-6	49.91	1.79	4.90	0.02	13.15	21.85	0.20	9.10	0.38	101.29	1.839	0.050	0.213	0.161	0.052	0.000	0.037	0.244	0.006	0.722	0.863	0.027	0.000	4.000	38.59	15.32	46.10	Aluminian Diopside
BEL1 cpx pheno rim 2-4	52.40	1.02	2.35	0.00	13.44	21.82	0.26	9.61	0.30	101.19	1.937	0.028	0.103	0.063	0.040	0.000	0.000	0.297	0.008	0.741	0.864	0.021	0.000	4.000	38.78	15.97	45.25	Aluminian Diopside
BEL1 same cpx pheno mantle1 2-5	52.09	1.17	2.66	0.03																								

Clinopyroxene (continued)

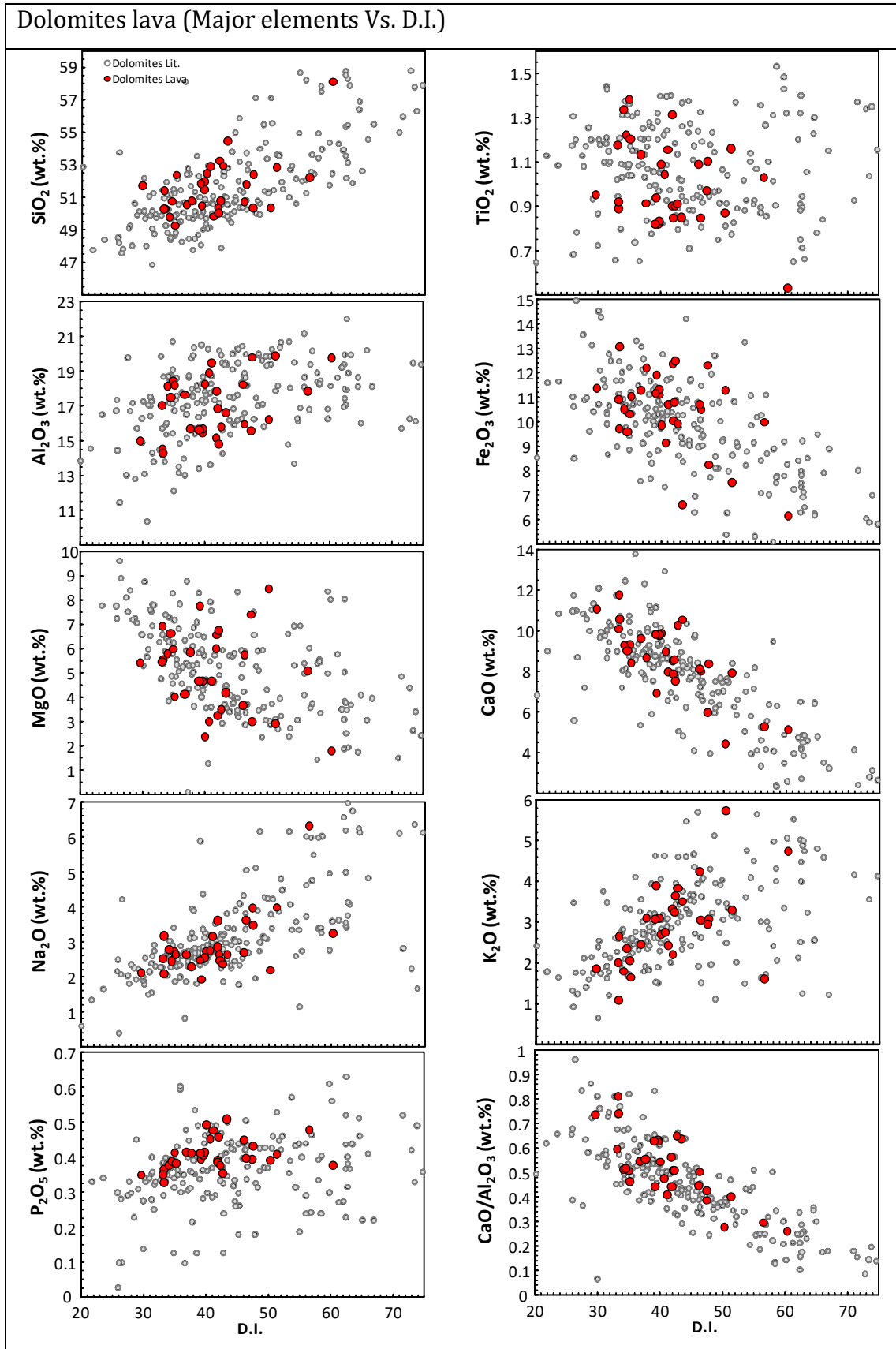
BUF4 cpx pheno rim 8-4	49.99	0.72	3.98	0.00	14.13	21.99	0.18	8.69	0.36	100.05	1.852	0.020	0.174	0.148	0.026	0.000	0.108	0.161	0.006	0.780	0.873	0.026	0.000	4.000	40.47	14.26	45.27	Aluminian ferrian Diopside
BUF4 cpx pheno core 8-5	49.78	0.76	3.66	0.00	14.18	21.79	0.21	8.81	0.38	99.57	1.853	0.021	0.161	0.147	0.014	0.000	0.117	0.157	0.007	0.787	0.869	0.027	0.000	4.000	40.62	14.51	44.87	Aluminian ferrian Augite
BUF2 cpx pheno rim 1-1	50.96	0.52	3.05	0.02	14.17	21.57	0.30	8.97	0.28	99.84	1.896	0.015	0.134	0.104	0.030	0.000	0.064	0.215	0.009	0.786	0.860	0.020	0.001	4.000	40.64	14.91	44.45	Aluminian Augite
BUF2 cpx pheno mantle 1-2	50.54	0.55	3.32	0.04	14.47	21.98	0.21	8.30	0.30	99.70	1.877	0.015	0.145	0.123	0.022	0.000	0.090	0.167	0.006	0.801	0.875	0.021	0.001	4.000	41.28	13.63	45.09	Aluminian Diopside
BUF2 cpx pheno core 1-3	51.75	0.38	2.81	0.13	15.03	23.08	0.16	6.53	0.27	100.14	1.904	0.011	0.122	0.096	0.026	0.000	0.064	0.137	0.005	0.825	0.910	0.019	0.004	4.000	42.49	10.61	46.89	Aluminian Diopside
BUF2 cpx pheno rim 2-1	51.05	0.59	3.05	0.03	14.44	21.25	0.24	9.19	0.27	100.12	1.894	0.016	0.133	0.106	0.027	0.000	0.065	0.220	0.007	0.799	0.845	0.020	0.001	4.000	41.26	15.11	43.63	Aluminian Augite
BUF2 same cpx pheno mantle1 2-2	50.10	0.61	3.91	0.04	14.15	22.42	0.21	7.88	0.24	99.56	1.864	0.017	0.171	0.136	0.035	0.000	0.084	0.161	0.007	0.785	0.893	0.017	0.001	4.000	40.66	13.04	46.30	Aluminian Diopside
BUF2 same cpx pheno mantle2 2-3	52.96	0.19	1.48	0.45	16.46	23.60	0.09	4.36	0.20	99.78	1.941	0.005	0.064	0.059	0.005	0.000	0.045	0.089	0.003	0.899	0.927	0.014	0.013	4.000	45.82	6.95	47.23	Chromian Diopside
BUF2 same cpx pheno mantle3 2-4	50.32	0.56	3.60	0.03	14.66	22.84	0.15	7.18	0.27	99.61	1.864	0.016	0.157	0.136	0.021	0.000	0.102	0.121	0.005	0.810	0.906	0.019	0.001	4.000	41.67	11.69	46.64	Aluminian ferrian Diopside
BUF2 cpx pheno rim 3-3	50.71	0.53	3.06	0.01	14.45	21.45	0.25	9.42	0.31	100.19	1.879	0.015	0.134	0.121	0.013	0.000	0.100	0.192	0.008	0.798	0.852	0.022	0.000	4.000	40.94	15.39	43.67	Aluminian ferrian Augite
BUF2 same cpx pheno mantle 3-4	50.76	0.53	2.90	0.03	14.41	21.24	0.29	9.10	0.30	99.55	1.893	0.015	0.128	0.107	0.020	0.000	0.079	0.205	0.009	0.801	0.848	0.022	0.001	4.000	41.24	15.08	43.68	Aluminian Augite
BUF2 same cpx pheno core 3-5	50.89	0.52	3.12	0.01	14.57	21.76	0.18	8.44	0.29	99.77	1.889	0.014	0.136	0.111	0.025	0.000	0.078	0.184	0.006	0.806	0.865	0.021	0.000	4.000	41.58	13.80	44.63	Aluminian Augite
BUF2 cpx glomerule rim 5-1	51.28	0.50	3.07	0.01	14.04	21.20	0.19	9.43	0.36	100.07	1.905	0.014	0.135	0.095	0.040	0.000	0.053	0.240	0.006	0.777	0.844	0.026	0.000	4.000	40.49	15.56	43.95	Aluminian Augite
BUF2 cpx glomerule core 5-2	51.84	0.41	2.53	0.18	14.91	21.72	0.21	8.04	0.35	100.18	1.914	0.011	0.110	0.086	0.024	0.000	0.059	0.189	0.007	0.821	0.859	0.025	0.005	4.000	42.42	13.17	44.41	Aluminian Augite
GAR3 cpx pheno rim 1-1	51.30	0.72	3.49	0.04	13.90	20.86	0.22	10.30	0.29	101.12	1.893	0.020	0.152	0.107	0.044	0.000	0.043	0.275	0.007	0.764	0.825	0.021	0.001	4.000	39.94	16.97	43.09	Aluminian Augite
GAR3 cpx pheno rim 1-3	51.96	0.57	2.94	0.04	14.92	20.79	0.25	9.32	0.38	101.17	1.904	0.016	0.127	0.096	0.031	0.000	0.059	0.227	0.008	0.815	0.816	0.027	0.001	4.000	42.34	15.24	42.41	Aluminian Augite
GAR3 cpx gm 1-5	51.70	0.61	3.00	0.06	14.70	20.64	0.19	9.43	0.29	100.61	1.908	0.017	0.131	0.092	0.039	0.000	0.038	0.253	0.006	0.809	0.816	0.021	0.002	4.000	42.08	15.44	42.48	Aluminian Augite
GAR3 cpx corona around quartz xenolith 2-3	54.83	0.19	0.34	0.00	15.74	21.55	0.22	8.40	0.24	101.50	2.001	0.005	0.014	0.000	0.014	0.000	0.000	0.256	0.007	0.857	0.843	0.017	0.000	4.000	43.65	13.41	42.95	Augite
GAR3 cpx pheno line rime to core 3-1	51.93	0.69	3.65	0.08	14.45	20.78	0.22	9.32	0.31	101.42	1.902	0.019	0.157	0.098	0.060	0.000	0.019	0.266	0.007	0.789	0.815	0.022	0.002	4.000	41.60	15.41	42.99	Aluminian Augite
GAR3 cpx pheno line rime to core 3-3	51.72	0.58	3.36	0.10	14.49	21.01	0.19	9.17	0.31	100.93	1.903	0.016	0.146	0.097	0.048	0.000	0.036	0.246	0.006	0.794	0.828	0.022	0.003	4.000	41.59	15.08	43.34	Aluminian Augite
GAR3 cpx pheno line rime to core 3-4	51.82	0.63	3.60	0.23	14.81	21.53	0.17	8.13	0.26	101.18	1.896	0.017	0.155	0.104	0.051	0.000	0.030	0.219	0.005	0.808	0.844	0.019	0.007	4.000	42.38	13.32	44.29	Aluminian Augite
GAR3 cpx pheno line rime to core 3-5	51.65	0.63	3.43	0.16	14.47	20.91	0.23	9.21	0.31	100.99	1.900	0.017	0.149	0.100	0.048	0.000	0.035	0.248	0.007	0.793	0.824	0.022	0.005	4.000	41.59	15.23	43.19	Aluminian Augite
GAR3 cpx pheno line rime to core 3-6	51.63	0.61	3.34	0.06	14.59	21.06	0.29	9.19	0.34	101.10	1.895	0.017	0.145	0.105	0.040	0.000	0.054	0.229	0.009	0.798	0.828	0.024	0.002	4.000	41.63	15.18	43.19	Aluminian Augite
GAR3 cpx pheno line rime to core 3-7	51.16	0.70	3.65	0.14	14.31	20.40	0.23	9.74	0.32	100.66	1.890	0.019	0.159	0.110	0.049	0.000	0.041	0.260	0.007	0.788	0.808	0.023	0.004	4.000	41.40	16.19	42.42	Aluminian Augite
GAR3 cpx pheno line rime to core 3-8	51.00	0.68	3.54	0.15	14.11	21.03	0.25	9.40	0.33	100.49	1.888	0.019	0.154	0.112	0.042	0.000	0.052	0.239	0.008	0.778	0.834	0.023	0.004	4.000	40.72	15.64	43.63	Aluminian Augite
GAR3 cpx pheno line rime to core 3-9	51.24	0.62	3.85	0.09	14.30	20.66	0.27	9.71	0.36	101.10	1.883	0.017	0.167	0.117	0.050	0.000	0.055	0.244	0.008	0.784	0.814	0.026	0.003	4.000	41.16	16.11	42.73	Aluminian Augite
GAR3 cpx pheno line rime to core 3-10	50.60	0.69	4.07	0.04	14.32	20.40	0.32	10.15	0.35	100.93	1.864	0.019	0.177	0.136	0.041	0.000	0.080	0.232	0.010	0.786	0.805	0.025	0.001	4.000	41.07	16.87	42.06	Aluminian Augite
GAR3 cpx pheno cribose clean rim 4-1	50.65	0.73	3.80	0.08	14.47	21.10	0.16	9.50	0.29	100.79	1.866	0.020	0.165	0.134	0.031	0.000	0.081	0.212	0.005	0.795	0.833	0.021	0.002	4.000	41.28	15.46	43.26	Aluminian Augite
GAR3 same cpx pheno cribose clean rim 4-2	51.92	0.57	3.09	0.08	14.83	21.48	0.20	8.87	0.31	101.35	1.899	0.016	0.133	0.101	0.032	0.000	0.057	0.214	0.006	0.808	0.842	0.022	0.002	4.000	41.94	14.40	43.67	Aluminian Augite
GAR3 same cpx pheno cribose mantle1 4-3	52.38	0.45	2.10	0.11	16.20	18.61	0.32	9.97	0.35	100.48	1.928	0.012	0.091	0.072	0.019	0.000	0.049	0.258	0.010	0.889	0.734	0.025	0.003	4.000	45.83	16.33	37.84	Augite
GAR3 same cpx pheno cribose mantle2 4-4	51.61	0.47	2.69	0.08	15.26	20.81	0.28	9.15	0.32	100.66	1.898	0.013	0.117	0.102	0.015	0.000	0.082	0.200	0.009	0.837	0.820	0.023	0.002	4.000	42.97	14.90	42.13	Aluminian Augite
GAR3 same cpx pheno cribose mantle3 4-5	52.03	0.49	2.64	0.09	15.26	20.82	0.29	9.15	0.32	101.07	1.907	0.014	0.114	0.093	0.021	0.000	0.065	0.215	0.009	0.834	0.817	0.022	0.002	4.000	42.97	14.91	42.12	Aluminian Augite
GAR3 same cpx pheno cribose outer core 4-6	50.81	0.59	3.36	0.02	14.58	21.14	0.23	9.07	0.34	100.12	1.881	0.016	0.146	0.119	0.028	0.000	0.082	0.199	0.007	0.805	0.839	0.024	0.001	4.000	41.66	14.92	43.42	Aluminian Augite
GAR3 same cpx pheno cribose outer core 4-6	51.21	0.58	3.33	0.06	14.67	21.54	0.27	9.42	0.34	101.42	1.874	0.016	0.144	0.126	0.017	0.000	0.100	0.189	0.008	0.800	0.844	0.024	0.002	4.000	41.23	15.28	43.49	Aluminian Augite
GAR3 same cpx pheno cribose outer core 4-7	50.75	0.52	3.29	0.03	14.89	21.63	0.25	8.91	0.33	100.59	1.868	0.014	0.142	0.132	0.010	0.000	0.116	0.158	0.008	0.817	0.853	0.023	0.001	4.000	41.85	14.45	43.70	Aluminian ferrian Augite
GAR3 same cpx pheno cribose middle core 4-9	52.03	0.54	3.14	0.10	14.47	21.27	0.21	9.25	0.33	101.34	1.907	0.015	0.136	0.093	0.043	0.000	0.041	0.242	0.007	0.790	0.835	0.024	0.003	4.000	41.26	15.15	43.60	Aluminian Augite
GAR3 same cpx pheno cribose inner core 4-11	51.74	0.57	3.38	0.02	14.73	21.48	0.22	8.96	0.30	101.40	1.892	0.016	0.146	0.108	0.038	0.000	0.060	0.214	0.007	0.803	0.841	0.021	0.001	4.000	41.70	14.59	43.71	Aluminian Augite
GAR3 cpx glomerule 6-2	52.03	0.61	3.54	0.07	14.66																							

Spinel																		
Sample	TiO ₂	Al ₂ O ₃	Cr ₂ O ₃	MgO	MnO	FeO	Total:	Ti	Al	Fe ^{III}	Fe ^{II}	Mn	Mg	Cr	Sum	Usp	Mg#	Cr#
AS2 sp in cpx glomerule 1-4	7.10	5.30	0.25	2.51	0.46	79.63	95.24	0.23	0.27	1.38	1.04	0.02	0.16	0.01	3.12	0.25	0.13	0.03
AS2 sp in cpx glomerule 1-5	6.72	5.87	0.09	3.65	0.46	78.60	95.39	0.22	0.30	1.39	0.97	0.02	0.24	0.00	3.13	0.24	0.19	0.01
AS2 sp gm 1-6	10.87	3.58	0.05	1.14	0.66	79.73	96.03	0.36	0.18	1.24	1.22	0.02	0.07	0.00	3.10	0.37	0.06	0.01
AS2 sp gm 2-7	11.15	3.52	0.01	1.04	0.66	79.90	96.28	0.36	0.18	1.23	1.23	0.02	0.07	0.00	3.10	0.37	0.05	0.00
AS2 sp in pl glomerule 3-6	2.16	18.97	0.09	4.99	0.35	68.32	94.87	0.06	0.88	1.13	0.79	0.01	0.29	0.00	3.18	0.10	0.27	0.00
AS2 sp in pl glomerule 3-7	7.40	3.57	0.24	1.65	0.41	81.09	94.37	0.25	0.19	1.42	1.10	0.02	0.11	0.01	3.10	0.26	0.09	0.04
AS2 sp in pl glomerule 3-8	3.49	14.22	0.08	4.56	0.45	72.19	94.98	0.11	0.68	1.24	0.84	0.02	0.28	0.00	3.17	0.15	0.24	0.00
AS2 sp in cpx pheno 4-3	6.09	6.81	0.09	3.12	0.45	78.86	95.42	0.20	0.35	1.38	0.98	0.02	0.20	0.00	3.13	0.22	0.17	0.01
AS2 sp in cpx pheno 5-5	7.44	5.15	0.24	2.27	0.47	79.53	95.10	0.25	0.27	1.36	1.07	0.02	0.15	0.01	3.12	0.27	0.12	0.03
AS2 sp gm 5-6	10.33	3.99	0.16	1.21	0.66	78.64	95.00	0.34	0.21	1.24	1.20	0.02	0.08	0.01	3.10	0.35	0.06	0.03
AS3 sp in cpx pheno 1-4	7.20	5.17	0.14	2.73	0.51	78.16	93.90	0.24	0.27	1.37	1.03	0.02	0.18	0.00	3.12	0.26	0.15	0.02
AS3 sp in cpx pheno 1-5	7.20	5.16	0.17	2.66	0.43	78.15	93.76	0.24	0.27	1.37	1.04	0.02	0.18	0.01	3.12	0.26	0.14	0.02
AS7 sp in cpx glomerule 1-1	8.48	4.73	0.29	2.84	0.43	76.76	93.53	0.28	0.25	1.31	1.07	0.02	0.19	0.01	3.12	0.30	0.15	0.04
AS7 sp in cpx glomerule 1-2	7.96	4.92	0.99	2.97	0.51	76.18	93.53	0.26	0.26	1.31	1.04	0.02	0.20	0.03	3.13	0.29	0.16	0.12
AS7 sp in cpx glomerule 1-3	8.43	4.78	0.28	2.92	0.50	76.37	93.29	0.28	0.25	1.31	1.06	0.02	0.19	0.01	3.12	0.30	0.15	0.04
AS7 sp gm 2-12	8.42	4.64	0.16	2.40	0.59	77.49	93.69	0.28	0.24	1.32	1.08	0.02	0.16	0.01	3.12	0.30	0.13	0.02
AS7 sp gm 2-13	8.42	4.33	0.10	1.78	0.48	77.98	93.09	0.29	0.23	1.33	1.12	0.02	0.12	0.00	3.11	0.30	0.10	0.02
AS8 sp micropheno rim 1-1	7.65	4.90	0.31	2.87	0.46	79.32	95.52	0.25	0.25	1.36	1.04	0.02	0.19	0.01	3.12	0.27	0.15	0.04
AS8 same micropheno core 1-2	7.37	5.18	0.23	3.20	0.45	79.10	95.52	0.24	0.27	1.37	1.01	0.02	0.21	0.01	3.13	0.26	0.17	0.03
AS8 sp gm 1-3	8.25	3.87	0.03	1.29	0.51	80.05	94.00	0.28	0.21	1.36	1.14	0.02	0.09	0.00	3.10	0.29	0.07	0.01
AS8 sp gm 2-4	7.79	4.85	0.23	2.93	0.38	79.70	95.88	0.25	0.25	1.36	1.04	0.01	0.19	0.01	3.12	0.27	0.15	0.03
AS8 sp in cpx glomerule 3-7	6.44	5.64	0.27	3.20	0.42	78.84	94.80	0.21	0.29	1.40	0.99	0.02	0.21	0.01	3.13	0.23	0.17	0.03
MAR1 sp gm 1-7	11.20	5.31	1.31	3.94	0.54	71.03	93.32	0.36	0.27	1.11	1.08	0.02	0.25	0.04	3.13	0.39	0.19	0.14
MAR1 sp in cpx pheno 5-4	8.77	6.44	0.97	2.89	0.57	72.63	92.27	0.29	0.33	1.20	1.07	0.02	0.19	0.03	3.13	0.33	0.15	0.09
LAT5 sp gm 1-10	19.86	2.72	0.65	0.13	2.07	68.93	94.35	0.63	0.13	0.71	1.50	0.07	0.01	0.02	3.08	0.64	0.01	0.14
LAT5 sp gm 2-3	20.77	2.12	0.00	0.66	2.26	67.85	93.67	0.66	0.11	0.70	1.49	0.08	0.04	0.00	3.08	0.65	0.03	0.00
AS3 sp in cpx 2-8	8.37	4.97	0.22	2.70	0.53	76.33	93.12	0.28	0.26	1.31	1.07	0.02	0.18	0.01	3.12	0.30	0.14	0.03
AS3 sp gm 2-9	10.61	3.19	0.01	0.64	0.68	77.66	92.80	0.36	0.17	1.24	1.25	0.03	0.04	0.00	3.09	0.37	0.03	0.00
BEL1 sp gm 1-8	21.32	2.77	0.11	0.46	3.04	64.84	92.54	0.68	0.14	0.62	1.50	0.11	0.03	0.00	3.07	0.69	0.02	0.03
BEL1 sp gm 2-1	20.31	3.66	0.65	1.30	2.61	62.97	91.50	0.65	0.18	0.62	1.43	0.09	0.08	0.02	3.08	0.68	0.05	0.11
BEL1 sp gm 2-2	19.57	3.61	0.64	0.66	2.53	65.31	92.32	0.62	0.18	0.67	1.45	0.09	0.04	0.02	3.08	0.65	0.03	0.11
BEL1 sp gm 2-15	19.94	3.18	0.46	0.32	2.76	64.87	91.52	0.64	0.16	0.66	1.48	0.10	0.02	0.02	3.08	0.66	0.01	0.09
BEL1 sp gm 2-16	20.68	2.86	0.09	0.35	2.96	64.22	91.14	0.67	0.14	0.63	1.50	0.11	0.02	0.00	3.07	0.68	0.01	0.02
BUF4 sp gm 4-4	9.13	5.13	0.96	2.97	0.44	74.07	92.69	0.30	0.27	1.23	1.08	0.02	0.20	0.03	3.13	0.33	0.15	0.11
BUF4 sp gm 5-1	7.64	6.01	1.29	3.59	0.37	73.55	92.45	0.25	0.31	1.27	1.00	0.01	0.24	0.04	3.14	0.28	0.19	0.13
BUF4 sp in cpx pheno 5-2	8.77	5.37	0.81	3.94	0.39	73.92	93.20	0.29	0.28	1.26	1.01	0.01	0.26	0.03	3.14	0.31	0.20	0.09
BUF4 sp in cpx pheno 5-3	7.76	5.12	0.38	3.05	0.49	75.78	92.57	0.26	0.27	1.33	1.03	0.02	0.20	0.01	3.13	0.28	0.16	0.05
BUF4 sp in cpx pheno 5-4	7.04	6.08	0.82	4.24	0.41	73.93	92.51	0.23	0.32	1.32	0.95	0.02	0.28	0.03	3.14	0.26	0.22	0.08
BUF4 sp gm 6-6	9.93	4.55	0.85	2.13	0.55	74.66	92.67	0.33	0.24	1.21	1.14	0.02	0.14	0.03	3.12	0.35	0.11	0.11
BUF4 sp in cpx pheno 8-1	8.35	5.64	0.68	4.03	0.45	73.18	92.32	0.28	0.29	1.27	1.00	0.02	0.26	0.02	3.14	0.30	0.21	0.07
BUF4 sp in cpx pheno 8-2	7.71	5.43	0.55	4.15	0.34	74.00	92.18	0.26	0.28	1.32	0.98	0.01	0.27	0.02	3.14	0.28	0.22	0.06
BUF4 sp in cpx pheno 8-3	7.84	5.41	0.65	4.26	0.29	74.59	93.06	0.26	0.28	1.31	0.97	0.01	0.28	0.02	3.14	0.28	0.22	0.08
BUF2 sp in cpx pheno 3-6	6.92	5.28	0.59	3.68	0.33	74.04	90.85	0.24	0.28	1.36	0.98	0.01	0.25	0.02	3.14	0.26	0.20	0.07
BUF2 sp in cpx pheno 3-6	7.18	5.38	0.60	3.34	0.32	75.80	92.62	0.24	0.28	1.35	1.01	0.01	0.22	0.02	3.13	0.26	0.18	0.07
BUF2 sp in cpx pheno 4-5	6.65	5.54	0.83	3.67	0.21	74.49	91.39	0.23	0.29	1.36	0.98	0.01	0.25	0.03	3.14	0.25	0.20	0.09
BUF2 sp in cpx glomerule 5-4	7.87	5.01	0.66	3.62	0.33	73.95	91.45	0.27	0.27	1.31	1.01	0.01	0.24	0.02	3.13	0.29	0.19	0.08
GAR3 sp gm 2-6	6.46	6.12	2.00	4.29	0.26	73.94	93.06	0.21	0.32	1.32	0.94	0.01	0.28	0.07	3.15	0.24	0.23	0.18
GAR3 sp in cpx pheno 3-1	6.78	5.99	2.69	4.43	0.31	72.30	92.48	0.22	0.31	1.29	0.94	0.01	0.29	0.09	3.15	0.26	0.23	0.23
GAR3 sp in cpx pheno 3-2	6.59	6.39	2.88	4.71	0.30	71.24	92.12	0.22	0.33	1.28	0.91	0.01	0.31	0.10	3.15	0.25	0.25	0.23
GAR3 sp in cpx pheno 3-3	6.61	5.97	1.95	4.67	0.21	72.18	91.59	0.22	0.31	1.31	0.92	0.01	0.31	0.07	3.15	0.25	0.25	0.18
GAR3 sp gm 3-4	6.49	6.16	1.89	4.23	0.26	73.53	92.55	0.21	0.32	1.32	0.94	0.01	0.28	0.07	3.15	0.25	0.23	0.17
PR3 big sp close to epidote 1-3	9.84	4.62	0.07	0.39	2.17	74.86	91.95	0.34	0.25	1.22	1.19	0.08	0.03	0.00	3.11	0.36	0.02	0.01
PR3 rounded big sp close to epidote 1-4	10.49	4.60	0.02	0.47	2.07	74.26	91.91	0.36	0.25	1.18	1.21	0.08	0.03	0.00	3.11	0.38	0.02	0.00
PR3 big sp around epidote 1-5	10.11	2.82	0.05	0.16	0.99	76.38	90.50	0.36	0.16	1.27	1.26	0.04	0.01	0.00	3.09	0.36	0.01	0.01
PR3 big sp around epidote 1-6	10.51	4.51	0.01	0.70	4.68	72.39	92.79	0.35	0.24	1.20	1.11	0.18	0.05	0.00	3.12	0.37	0.04	0.00
PR3 sp in pl pheno 1-7	9.01	4.95	0.00	0.06	3.16	74.76	91.93	0.31	0.27	1.25	1.15	0.12	0.00	0.00	3.11	0.33	0.00	0.00
PR3 big sp rim around epidote 3-3	9.92	2.47	0.00	0.08	0.41	79.84	92.73	0.34	0.13	1.31	1.27	0.02	0.01	0.00	3.08	0.34	0.00	0.00
PR3 big sp core around epidote 3-3	11.55	4.24	0.02	0.32	1.92	74.02	92.06	0.39	0.22	1.14	1.25	0.07	0.02	0.00	3.10	0.41	0.02	0.00
PR3 big sp around epidote 3-5	10.53	3.54	0.02	0.12	1.47	75.85	91.52	0.36	0.19	1.22	1.25	0.06	0.01	0.00	3.09	0.37	0.01	0.00
PR20 sp in cpx 1-10	10.12	5.51	0.83	3.65	0.43	72.37	92.91	0.33	0.28	1.17	1.07	0.02	0.24	0.03	3.13	0.36	0.18	0.09
PR20 sp in cpx 1-11	11.64	4.45	0.97	2.28	0.64	70.99	90.97	0.39	0.23	1.10	1.18	0.02	0.15	0.03	3.11	0.42	0.11	0.13

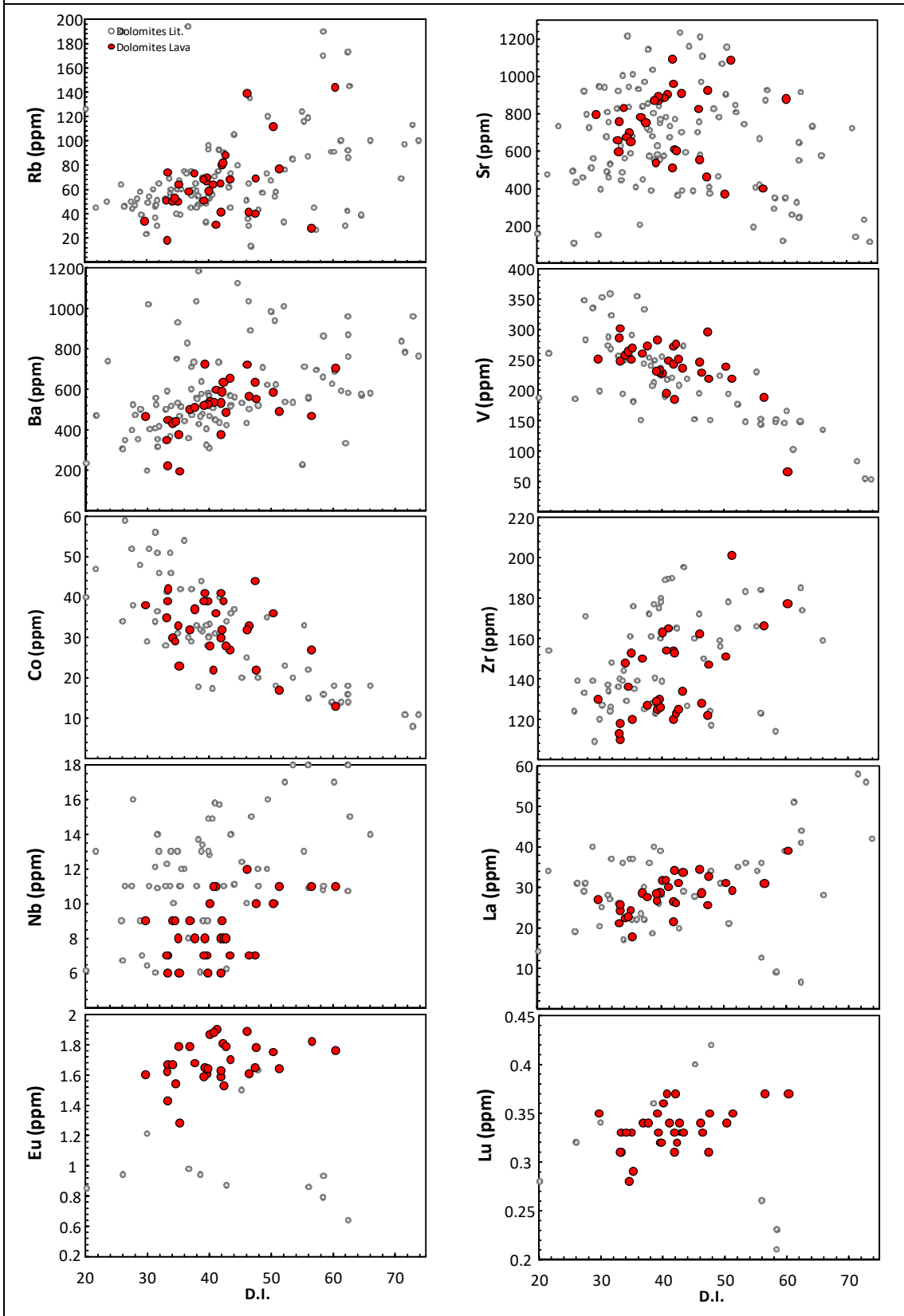
Olivine																
Sample	SiO ₂	MgO	CaO	MnO	FeO	NiO	Total:	Si	Fe ^{II}	Mn	Mg	Ca	Ni	Total	Fo	
BUF4 ol pheno relict 3-1	37.81	36.65	0.31	0.57	25.03	0.06	100.43	0.993	0.550	0.013	1.435	0.009	0.001	3.000	72.30	
BUF4 ol pheno core 4-1	37.54	36.25	0.33	0.57	25.15	0.02	99.86	0.992	0.556	0.013	1.429	0.009	0.000	3.000	71.98	
BUF4 ol pheno core 4-2	37.08	36.25	0.31	0.57	25.06	0.04	99.30	0.985	0.557	0.013	1.436	0.009	0.001	3.000	72.06	
BUF4 ol pheno core 6-1	37.65	37.09	0.33	0.55	23.38	0.05	99.04	0.996	0.517	0.012	1.463					

Glass																																										
Sample	SiO ₂	TiO ₂	Al ₂ O ₃	FeO	MnO	MgO	CaO	Na ₂ O	K ₂ O	P ₂ O ₅	SO ₃	F	Cl	Sum	Na ₂ O+K ₂ O	Q	C	or	ab	an	ne	Cpx	[Wo]	[En]	[Fs]	Opx	[En]	[Fs]	Ol	[Fo]	[Fa]	mt	il	ap	Sum	R1	R2	A	F	M	D.I.	
AS6 orange glass 1-1	63.56	0.44	19.00	1.82	0.00	0.40	2.82	3.62	8.64	0.43	0.02	0.13	0.02	100.90	12.26	3.34	0.00	51.06	30.62	10.08	0.00	0.93	0.46	0.16	0.32	2.54	0.84	1.70	0.00	0.00	0.00	0.35	0.84	1.01	104.25	866.90	693.99	12.26	1.82	0.40	85.02	
AS6 black glass 1-2	58.45	1.13	18.06	5.58	0.03	1.89	3.00	4.16	6.19	0.72	0.06	0.03	0.02	99.30	10.34	0.39	0.80	36.57	35.16	10.16	0.00	0.00	0.00	0.00	0.00	0.00	11.30	4.71	6.59	0.00	0.00	0.00	1.07	2.15	1.71	110.62	786.89	768.68	10.34	5.58	1.89	72.12
AS6 orange glass 1-3	63.05	0.30	18.86	1.97	0.00	0.07	2.61	3.06	9.80	0.57	0.00	0.00	0.02	100.31	12.86	2.63	0.00	57.92	25.87	8.79	0.00	0.38	0.18	0.01	0.19	2.45	0.17	2.28	0.00	0.00	0.00	0.38	0.57	1.35	103.18	760.28	653.15	12.86	1.97	0.07	86.42	
AS6 orange glass 1-4	56.91	0.47	17.38	5.53	0.00	3.69	2.08	3.60	8.45	0.88	0.02	0.10	0.02	99.13	12.05	0.00	0.62	49.96	24.27	4.58	3.35	0.00	0.00	0.00	0.00	0.00	0.00	0.00	12.28	6.45	5.84	1.06	0.90	2.08	111.40	370.10	746.91	12.05	5.53	3.69	77.58	
AS6 orange glass 1-5	62.33	0.53	18.85	3.00	0.07	0.18	2.84	3.68	8.71	0.50	0.03	0.00	0.02	100.75	12.39	1.30	0.00	51.45	31.16	9.18	0.00	1.42	0.68	0.08	0.66	3.48	0.37	3.11	0.00	0.00	0.00	0.57	1.01	1.19	105.65	711.80	682.27	12.39	3.00	0.18	83.91	
AS6 orange glass 2-1	62.93	0.37	19.07	2.21	0.00	0.13	3.03	3.51	8.85	0.47	0.03	0.18	0.01	100.79	12.36	2.44	0.00	52.28	29.70	10.14	0.00	1.64	0.78	0.09	0.77	2.18	0.22	1.96	0.00	0.00	0.00	0.42	0.70	1.10	104.44	805.62	704.96	12.36	2.21	0.13	84.42	
AS6 black glass 2-2	55.27	1.63	16.46	9.94	0.09	0.84	2.74	3.92	7.11	1.11	0.29	0.15	0.03	99.56	11.02	0.00	0.00	41.98	31.14	6.35	1.09	0.02	0.01	0.00	0.01	0.00	0.00	0.00	11.08	1.46	9.62	1.90	3.10	2.62	110.38	310.98	657.51	11.02	9.94	0.84	74.22	
AS6 black glass 2-3	58.84	1.39	17.83	7.01	0.11	0.10	2.51	4.01	7.88	0.82	0.05	0.10	0.02	100.67	11.89	0.00	0.09	46.56	33.95	7.12	0.00	0.00	0.00	0.00	0.00	0.00	1.12	0.03	1.09	5.88	0.16	5.72	1.34	2.63	1.94	107.64	422.17	623.84	11.89	7.01	0.10	80.51
AS6 black glass 2-4	61.48	1.24	18.45	3.71	0.06	0.10	2.98	3.96	8.20	0.75	0.06	0.00	0.02	100.99	12.16	1.31	0.00	48.45	33.53	8.34	0.00	1.36	0.64	0.04	0.67	3.18	0.20	2.98	0.00	0.00	0.00	0.71	2.35	1.78	105.54	636.76	685.45	12.16	3.71	0.10	83.30	
AS6 orange glass 2-5	61.03	0.57	18.63	3.98	0.00	0.97	2.82	3.14	8.69	0.52	0.00	0.00	0.00	100.35	11.83	1.17	0.17	51.33	26.60	10.60	0.00	0.00	0.00	0.00	0.00	0.00	7.47	2.40	5.07	0.00	0.00	0.00	0.76	1.09	1.23	107.90	792.33	714.87	11.83	3.98	0.97	79.11
AS6 orange glass 3-1	64.54	0.33	18.66	1.53	0.03	0.11	2.05	3.53	9.67	0.25	0.02	0.06	0.04	100.81	13.20	2.78	0.00	57.15	29.84	6.51	0.00	1.78	0.85	0.12	0.81	1.15	0.15	1.00	0.00	0.00	0.00	0.29	0.63	0.59	103.65	734.52	590.92	13.20	1.53	0.11	89.78	
AS6 black glass 3-2	56.35	1.84	16.38	7.79	0.05	0.30	3.85	3.12	8.86	1.56	0.06	0.07	0.02	100.25	11.99	0.00	0.00	52.38	23.49	4.49	1.58	3.93	1.86	0.16	1.91	0.00	0.00	0.00	5.74	0.41	5.33	1.49	3.49	3.69	109.95	309.94	748.33	11.99	7.79	0.30	77.45	
AS6 black glass 3-3	55.67	2.21	16.17	9.94	0.06	0.94	2.79	4.11	6.83	1.31	0.06	0.08	0.06	100.21	10.94	0.00	0.06	40.34	34.78	5.32	0.00	0.00	0.00	0.00	0.00	0.00	0.08	0.01	0.07	10.43	1.63	8.81	1.90	4.19	3.10	110.73	319.95	662.60	10.94	9.94	0.94	75.13
AS6 orange glass 4-1	61.91	0.49	19.14	3.27	0.03	0.09	3.53	3.36	8.62	0.43	0.07	0.03	0.02	100.98	11.97	1.67	0.00	50.91	28.42	11.71	0.00	2.63	1.24	0.07	1.32	3.02	0.16	2.86	0.00	0.00	0.00	0.63	0.93	1.02	106.57	813.51	757.19	11.97	3.27	0.09	81.00	
AS6 orange glass 5-1	60.66	0.84	18.41	4.08	0.06	0.13	3.45	3.50	8.42	0.76	0.08	0.00	0.07	100.46	11.92	0.98	0.00	49.76	29.58	9.68	0.00	2.21	1.05	0.07	1.10	4.02	0.24	3.77	0.00	0.00	0.00	0.78	1.60	1.80	106.63	695.84	736.92	11.92	4.08	0.13	80.32	
AS6 orange glass 5-2	61.25	0.71	18.37	3.42	0.00	0.03	3.23	2.66	10.03	0.97	0.12	0.12	0.04	100.93	12.69	1.60	0.00	59.27	22.49	8.56	0.00	1.01	0.47	0.01	0.52	3.52	0.06	3.46	0.00	0.00	0.00	0.66	1.35	2.30	105.29	677.67	707.24	12.69	3.42	0.03	83.37	
AS6 orange glass 5-3	62.30	1.52	17.71	3.25	0.01	0.43	2.38	4.03	8.32	0.68	0.06	0.19	0.02	100.89	12.35	2.48	0.00	49.19	34.06	5.68	0.00	1.46	0.72	0.23	0.51	2.73	0.84	1.88	0.00	0.00	0.00	0.62	2.89	1.60	104.89	645.97	623.54	12.35	3.25	0.43	85.72	

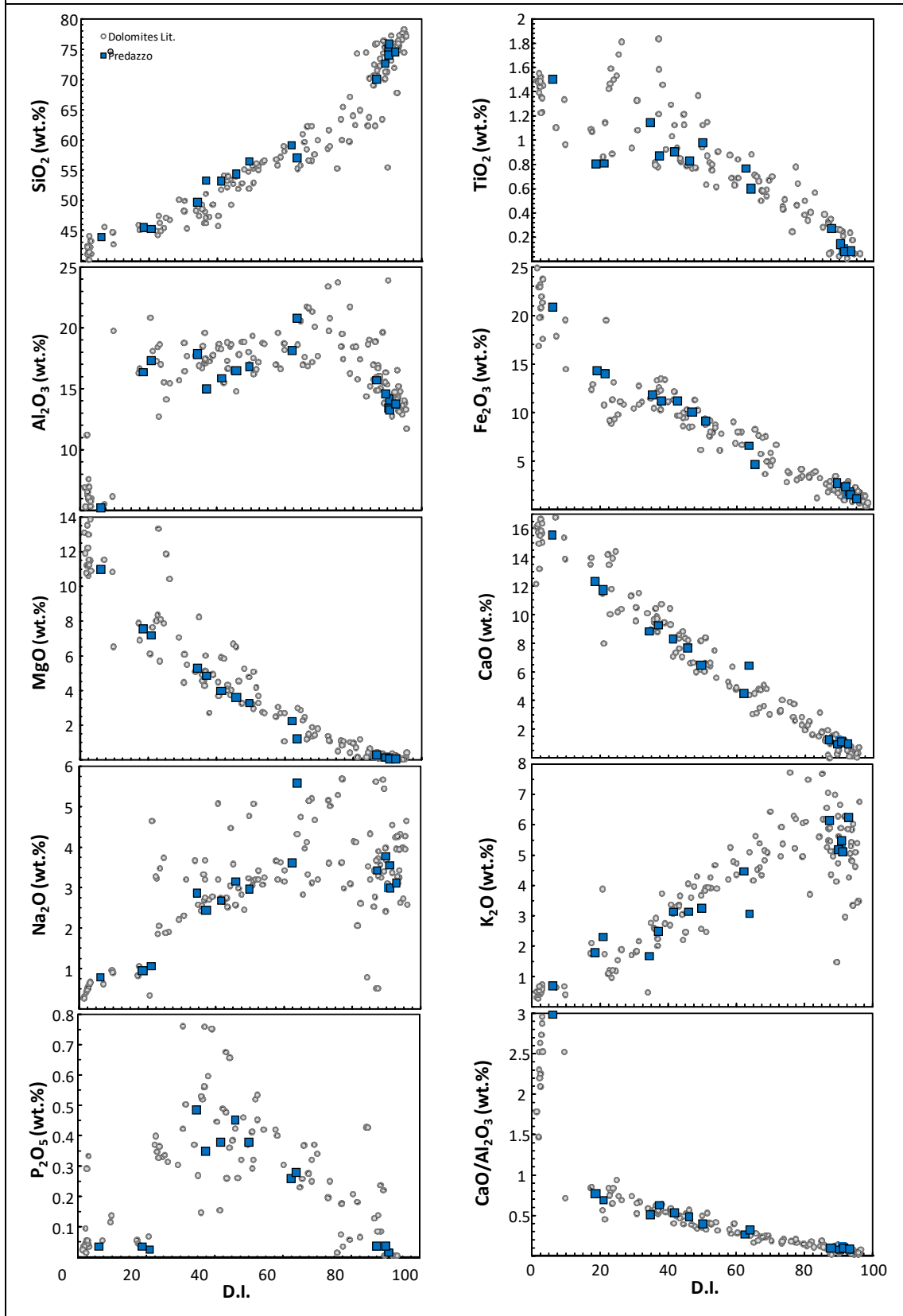
Appendix 2 (Major elements and Trace elements Vs. D.I.)



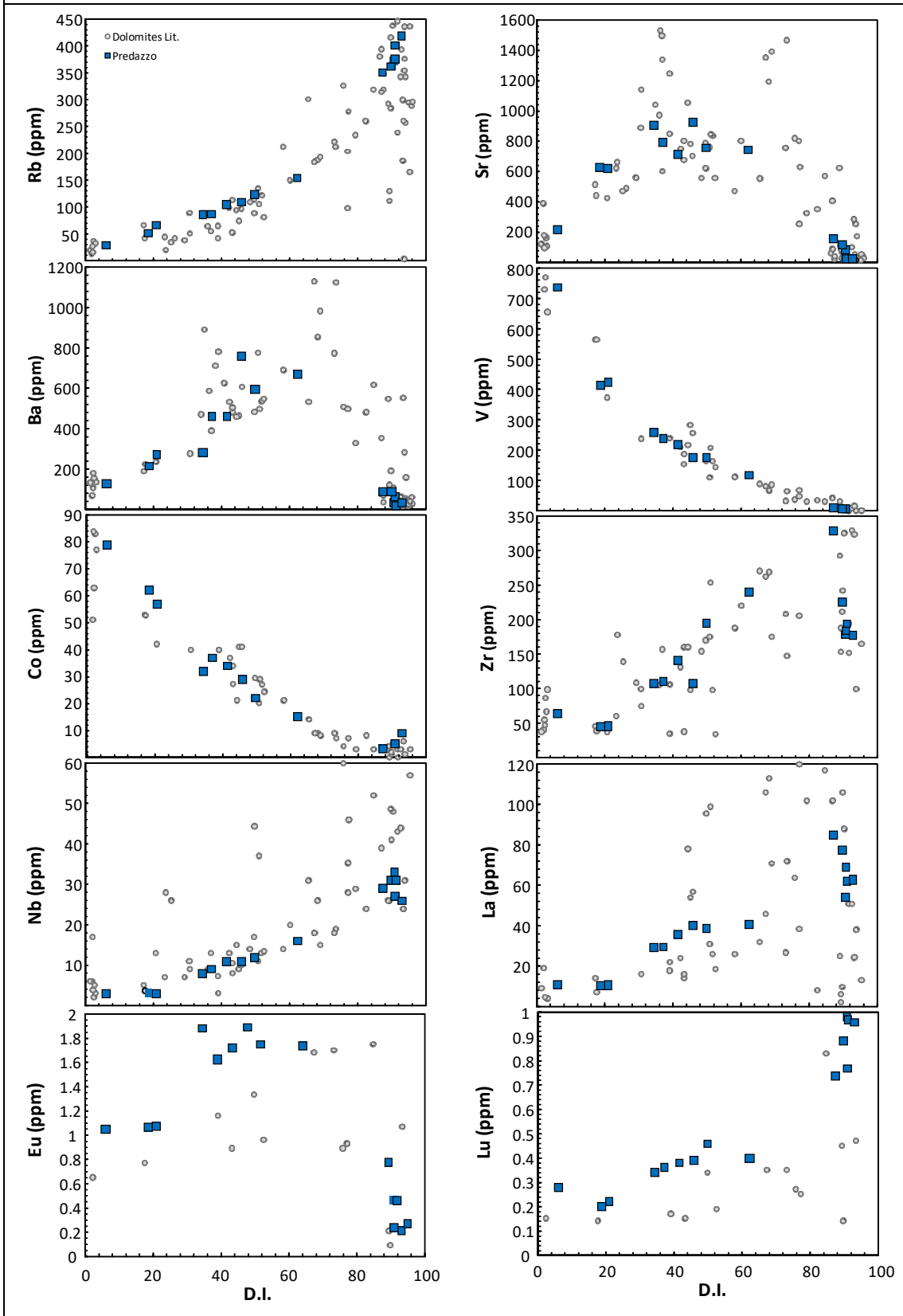
Dolomites lava (Minor elements Vs. D.I.)



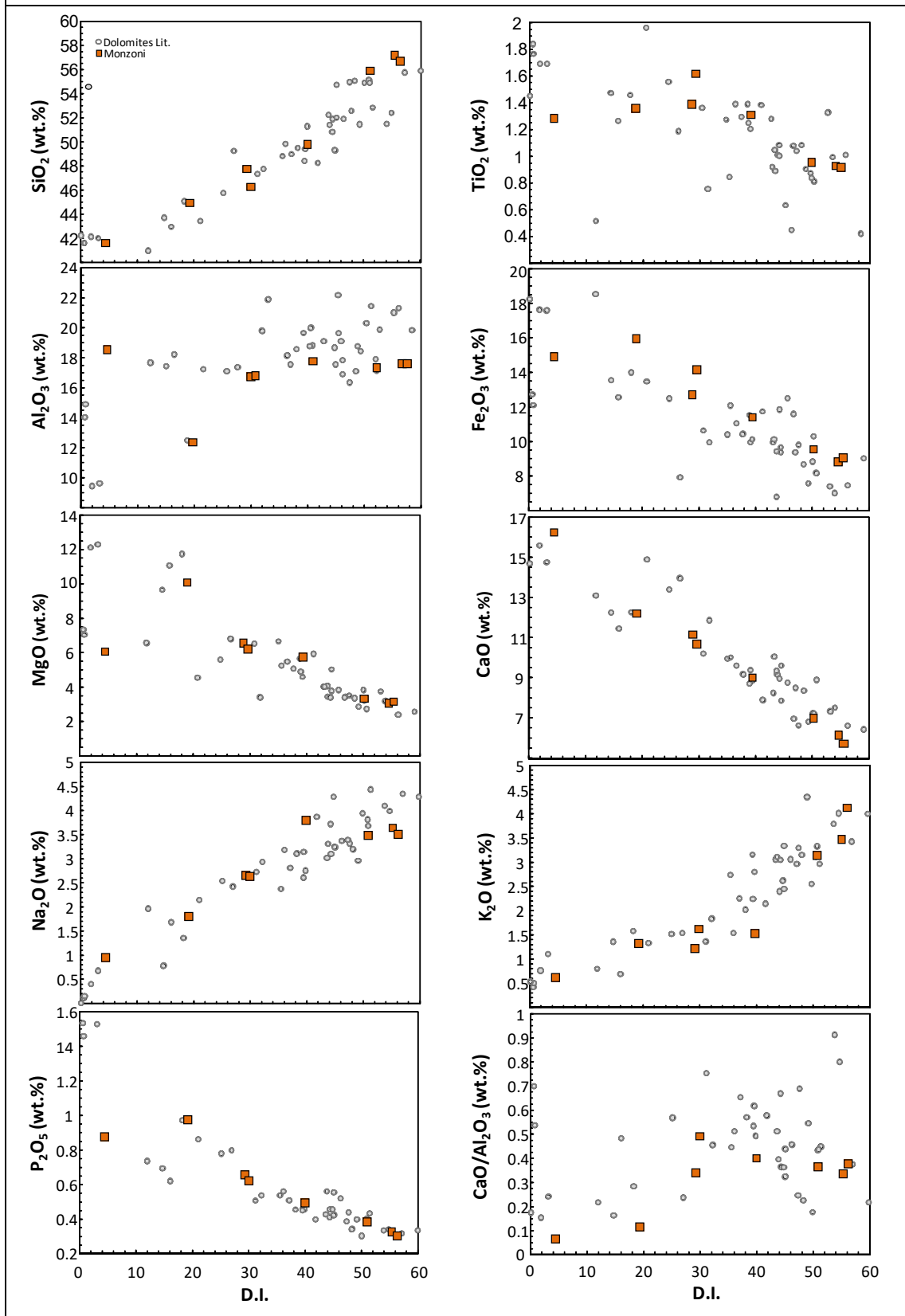
Predazzo (Major elements Vs. D.I.)



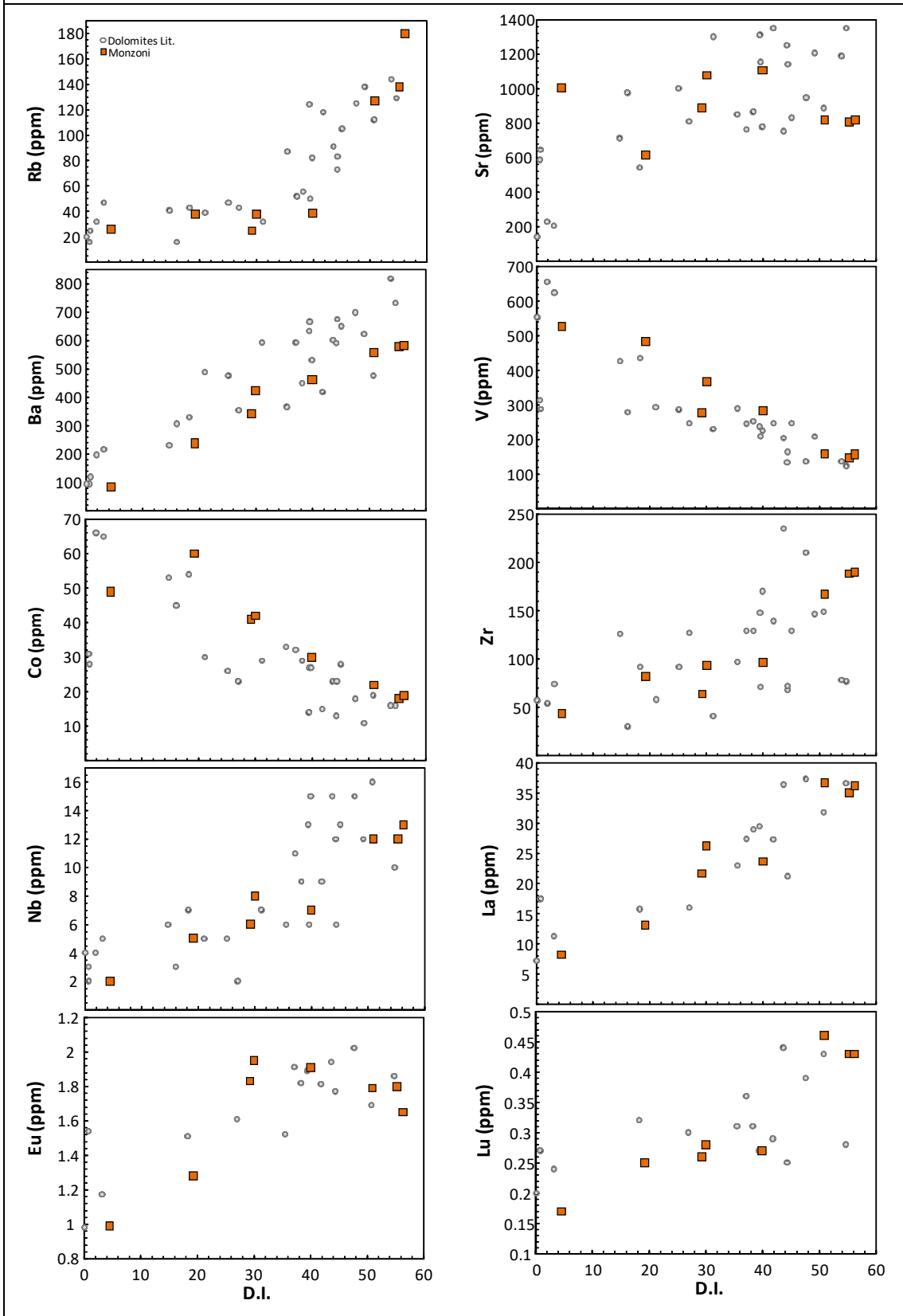
Predazzo (Minor elements Vs. D.I.)



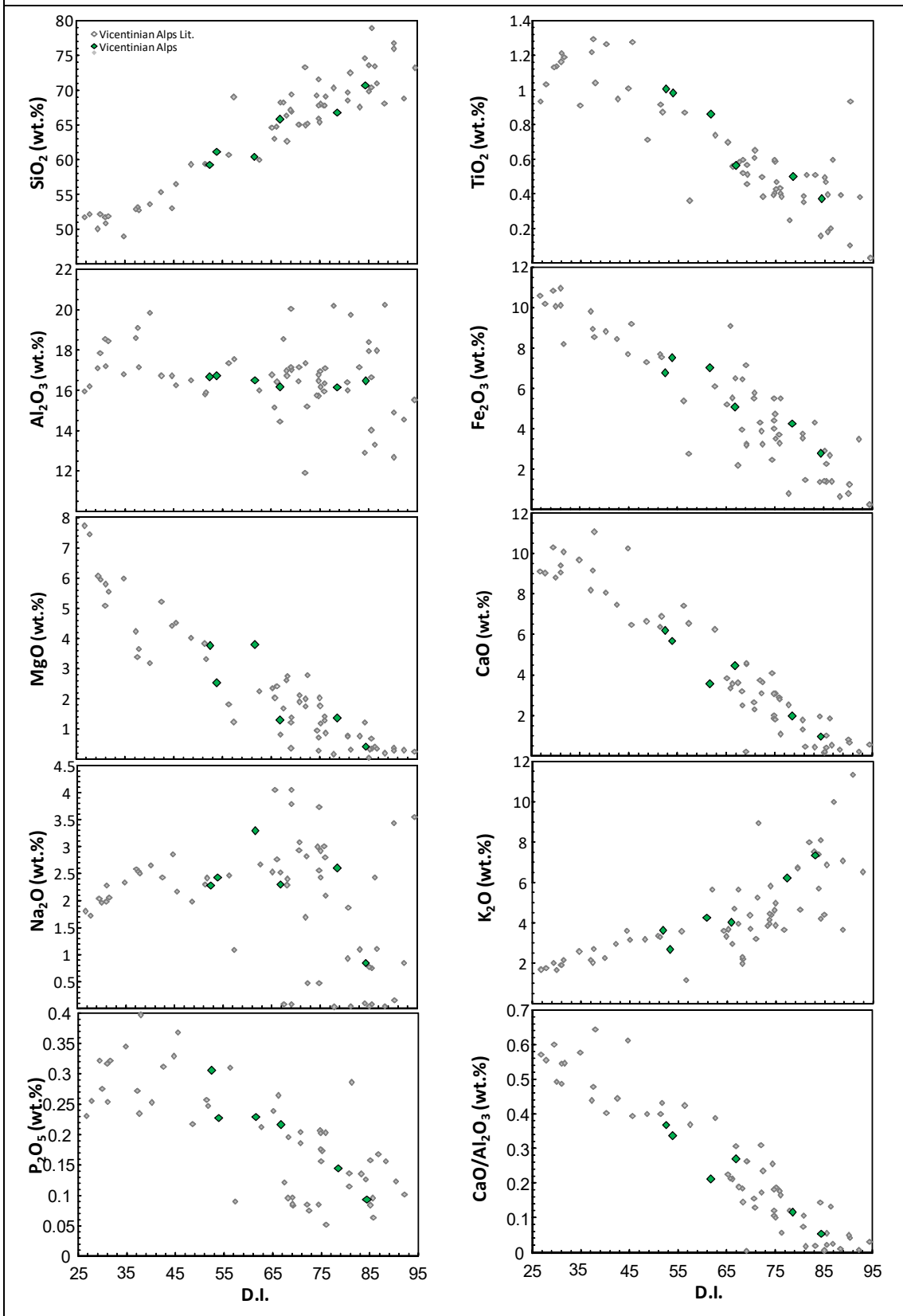
Monzoni (Major elements Vs. D.I.)



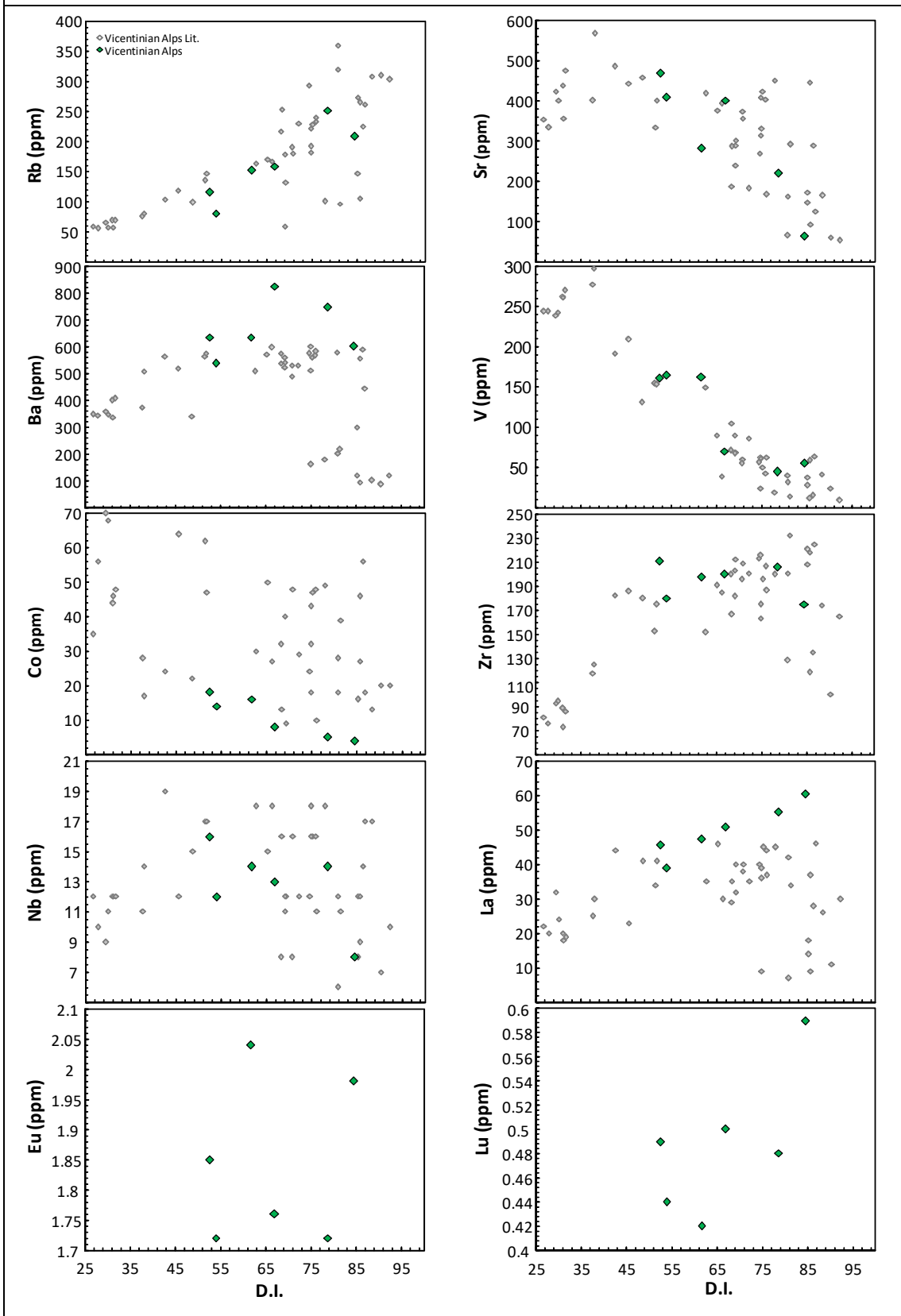
Monzoni (Minor elements Vs. D.I.)



Vicentinian Alps (Major elements Vs. D.I.)



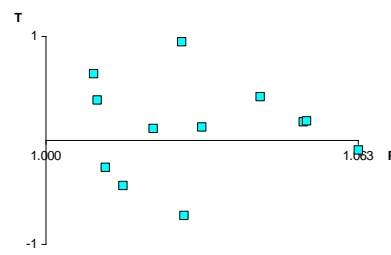
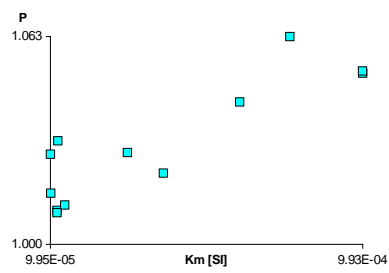
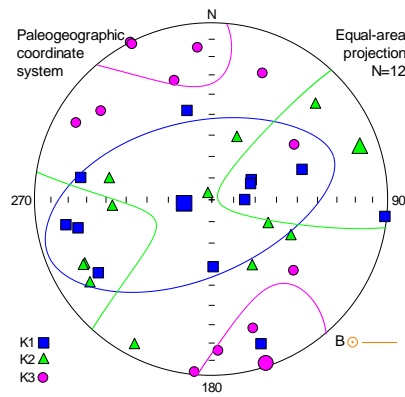
Vicentinian Alps (Minor elements Vs. D.I.)

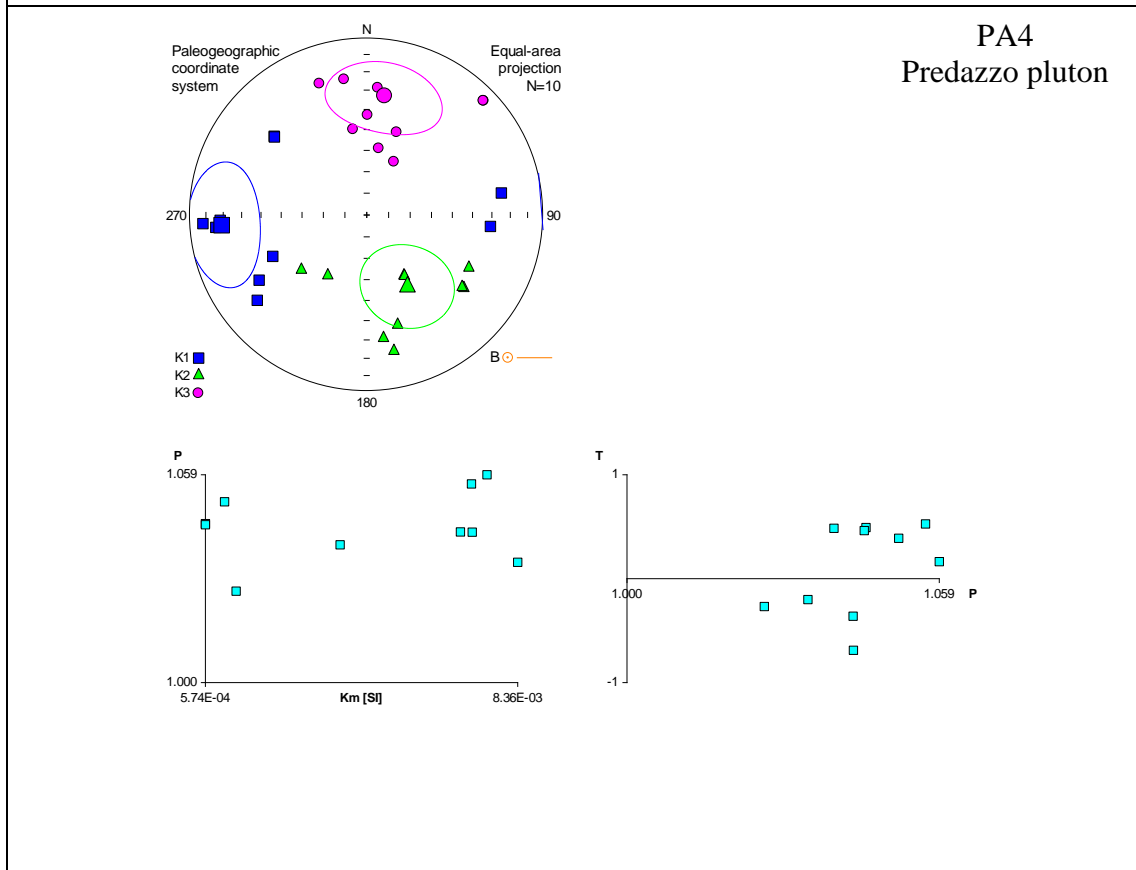
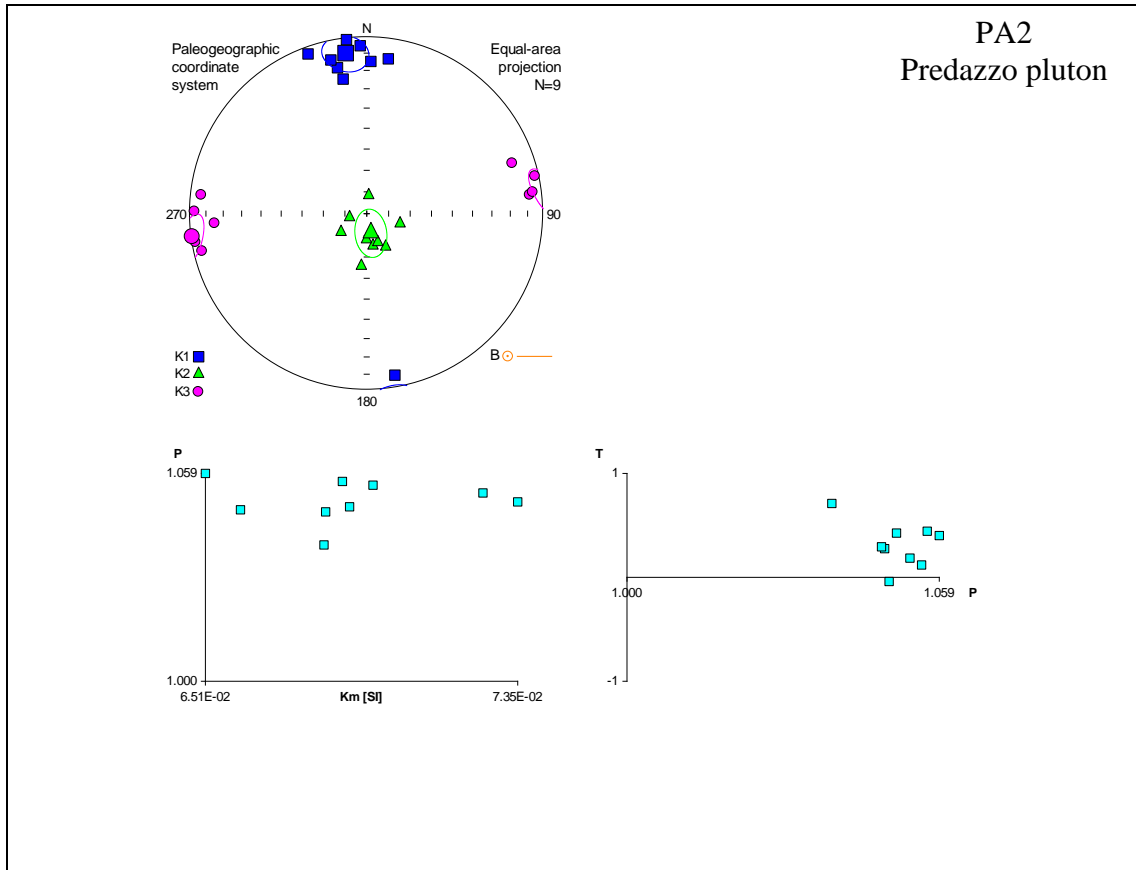


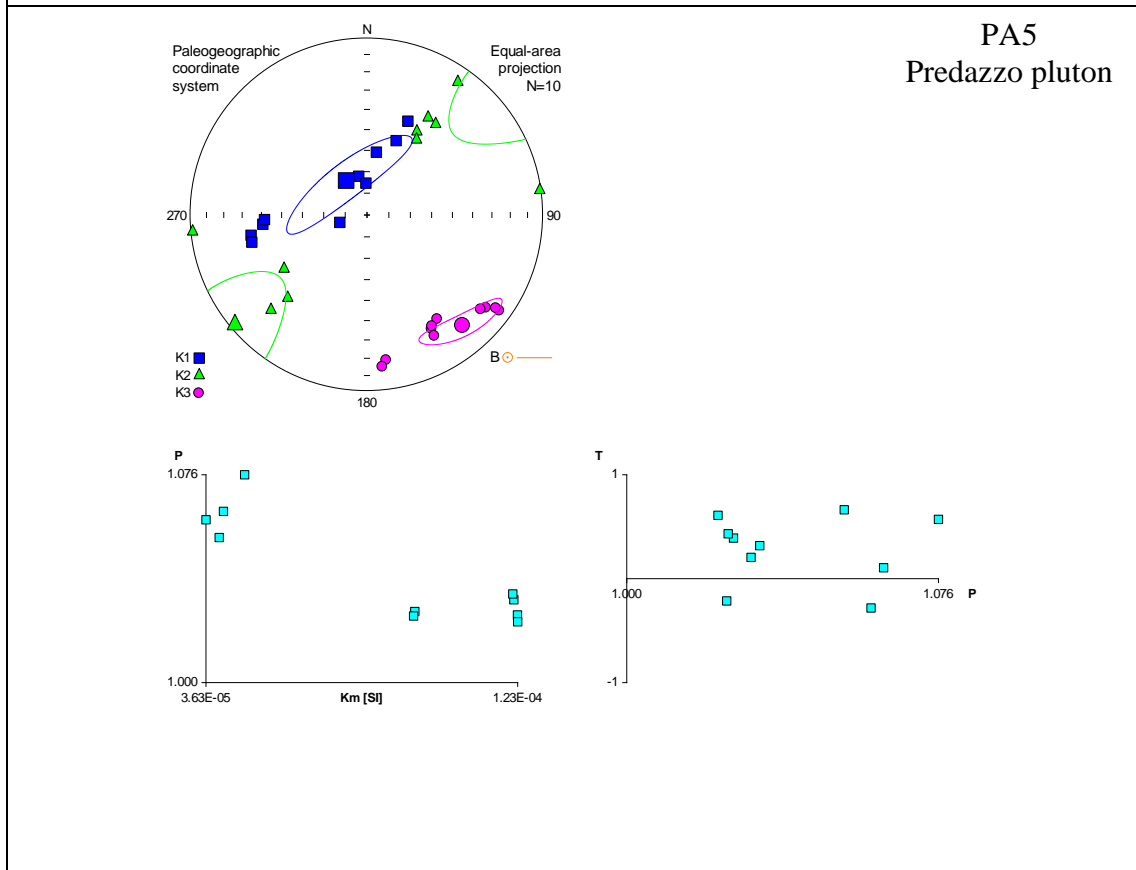
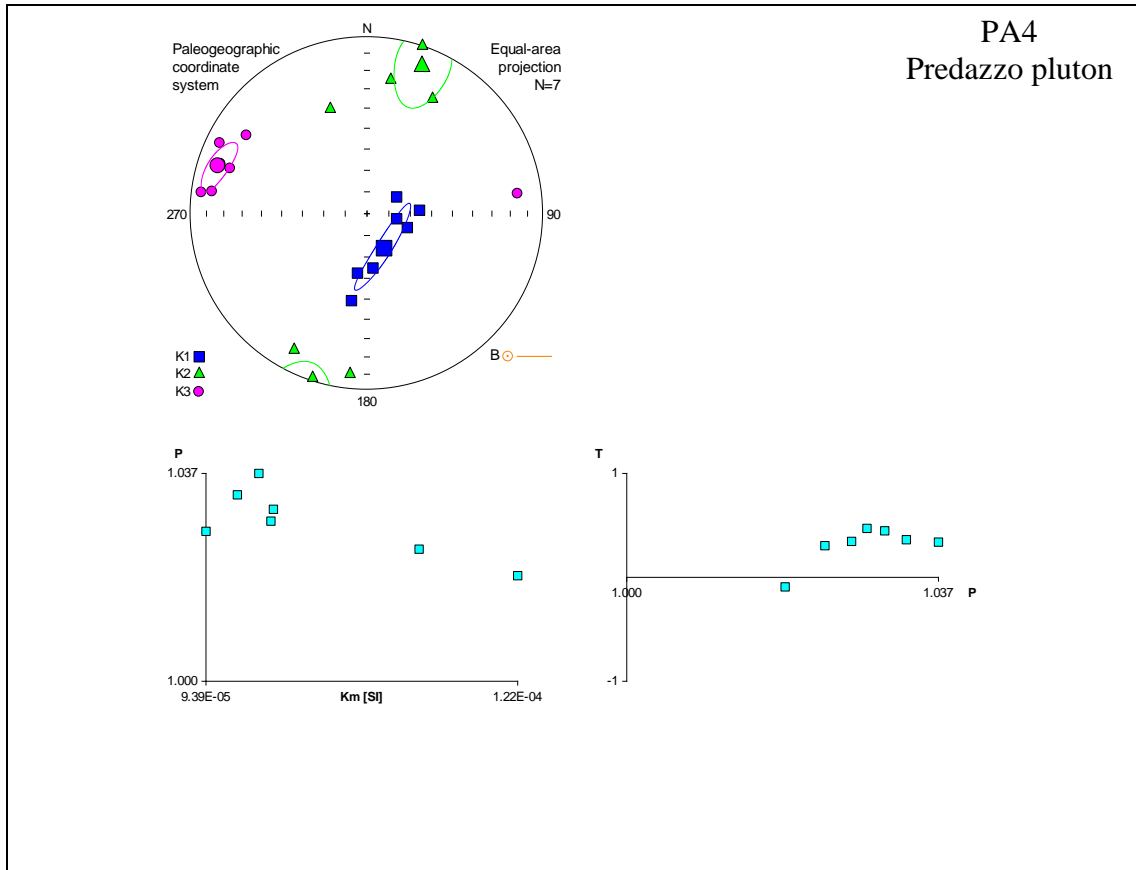
Appendix 3

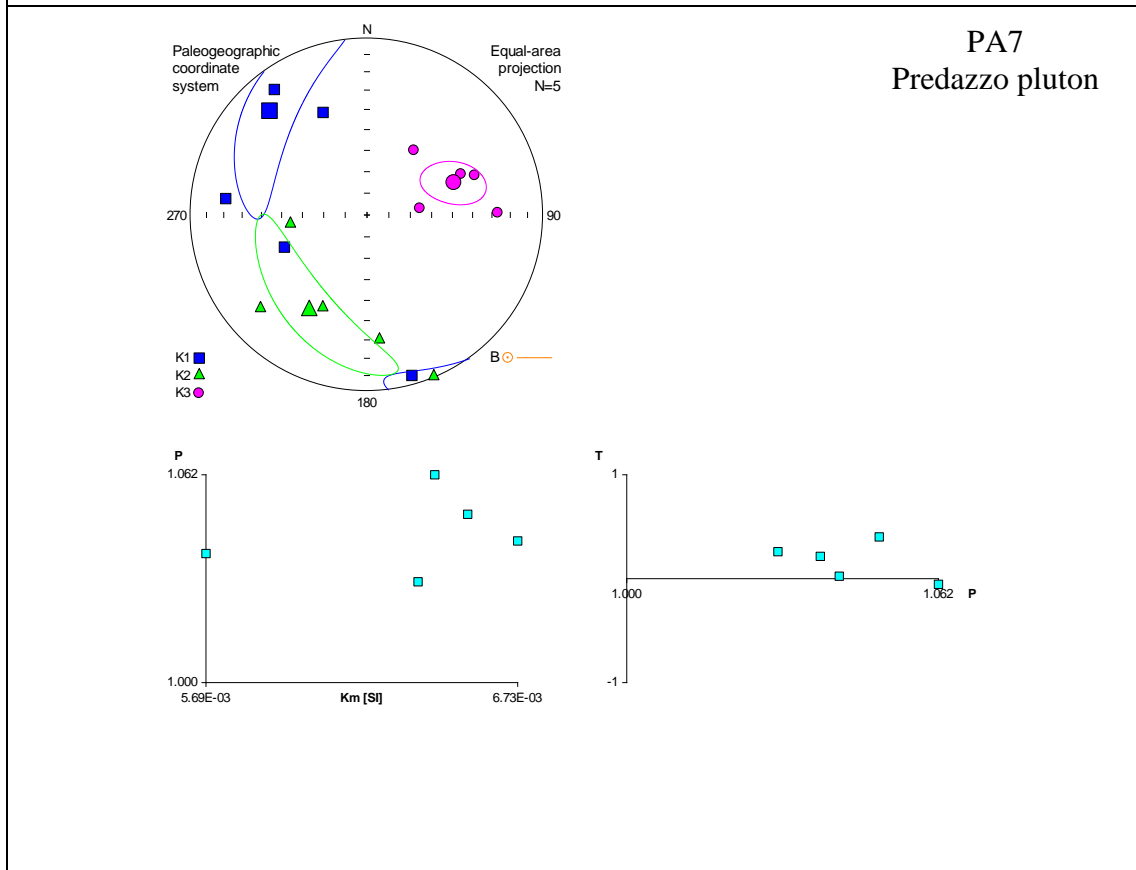
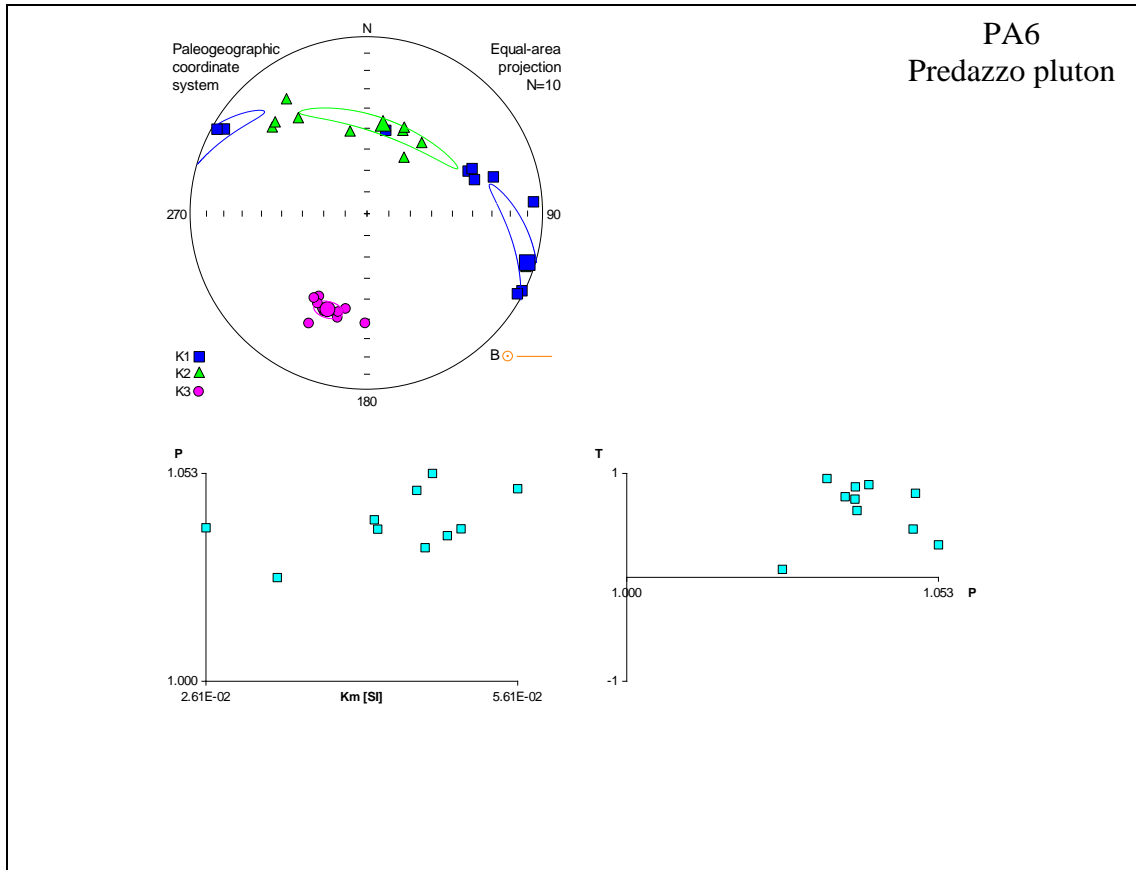
AMS parameter for each site

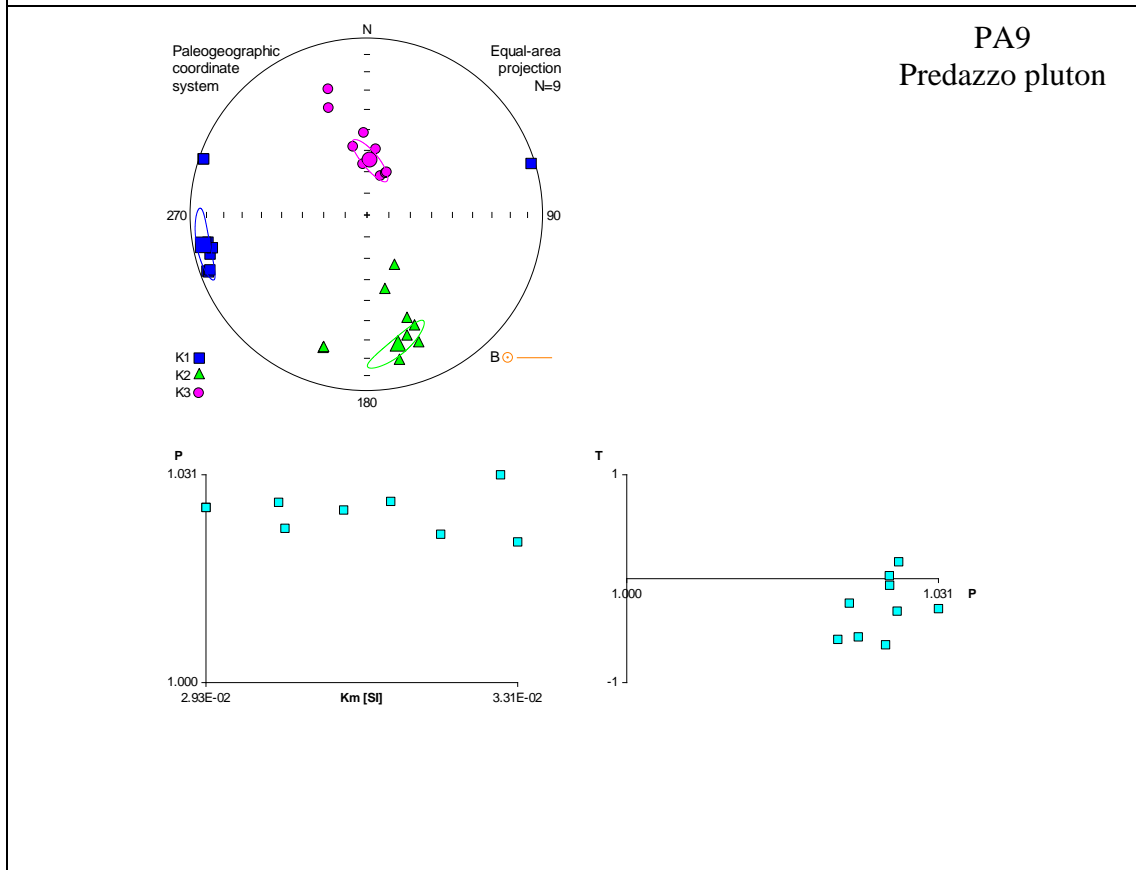
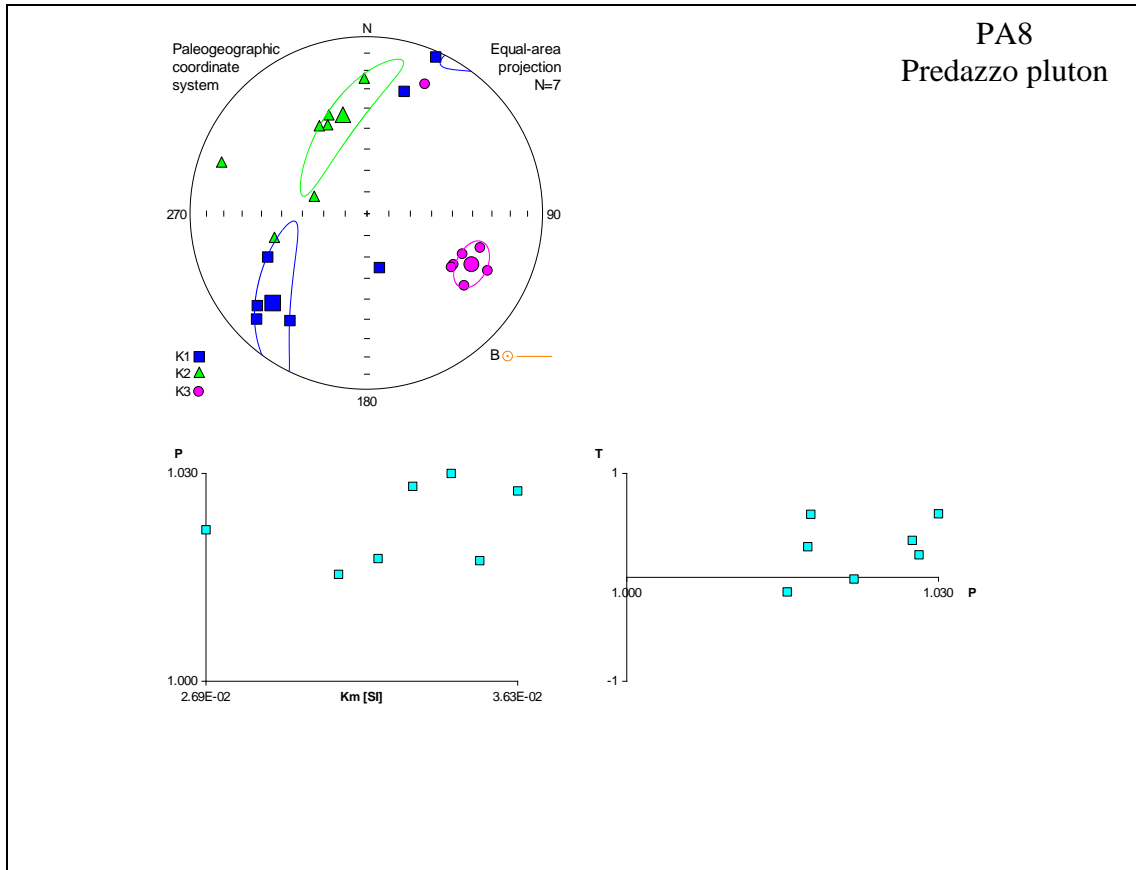
PA1
Predazzo pluton

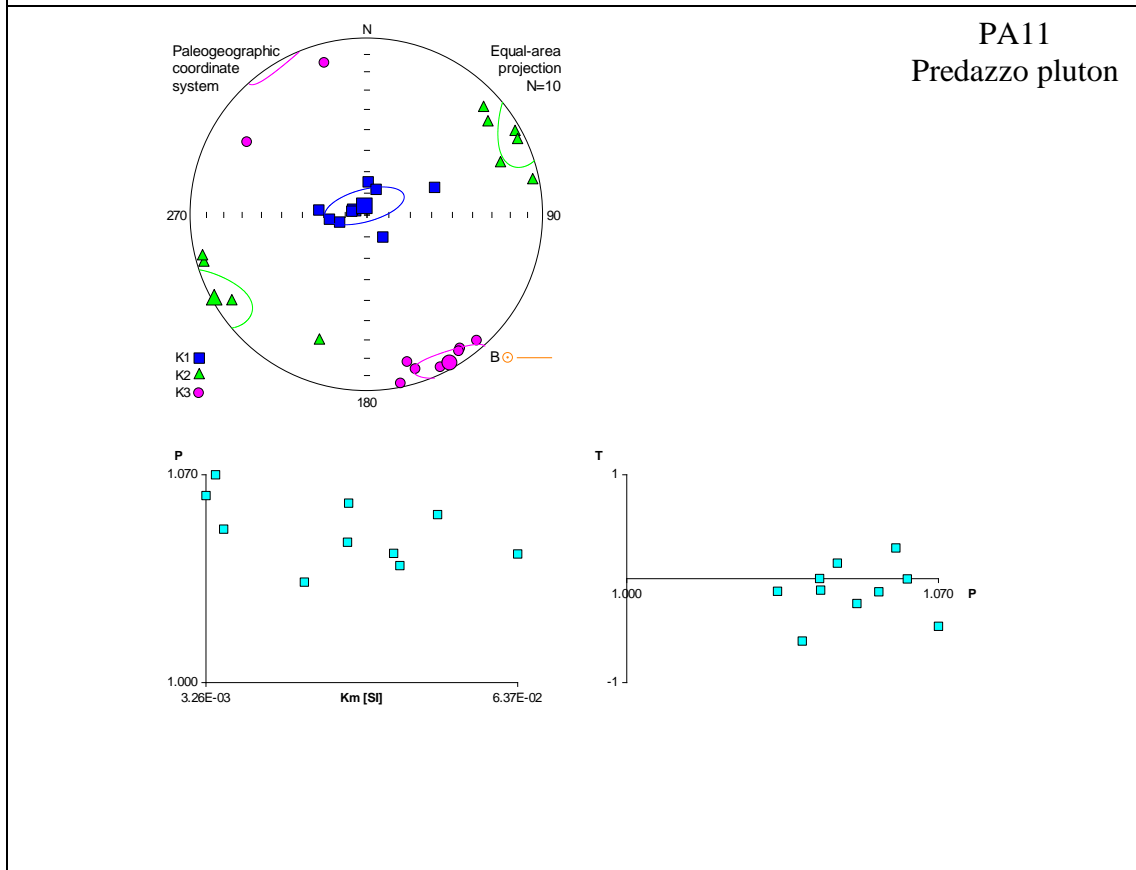
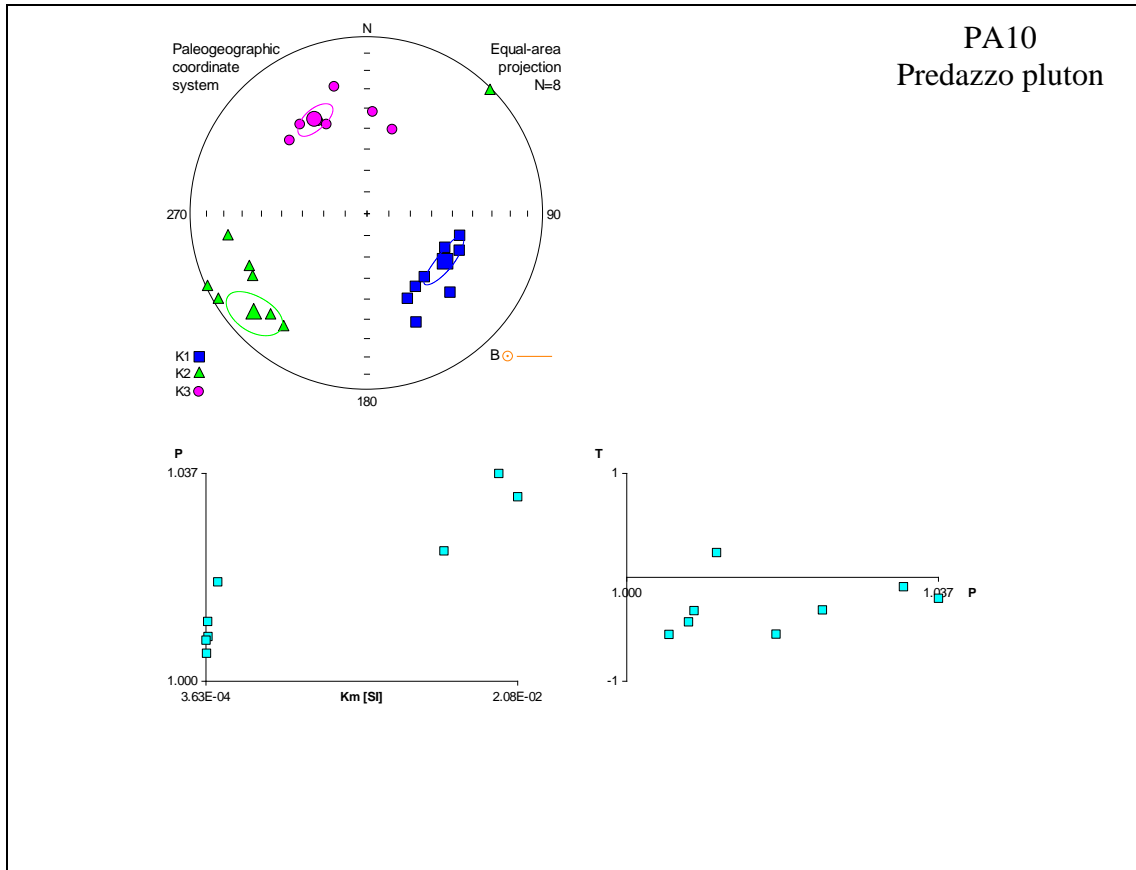


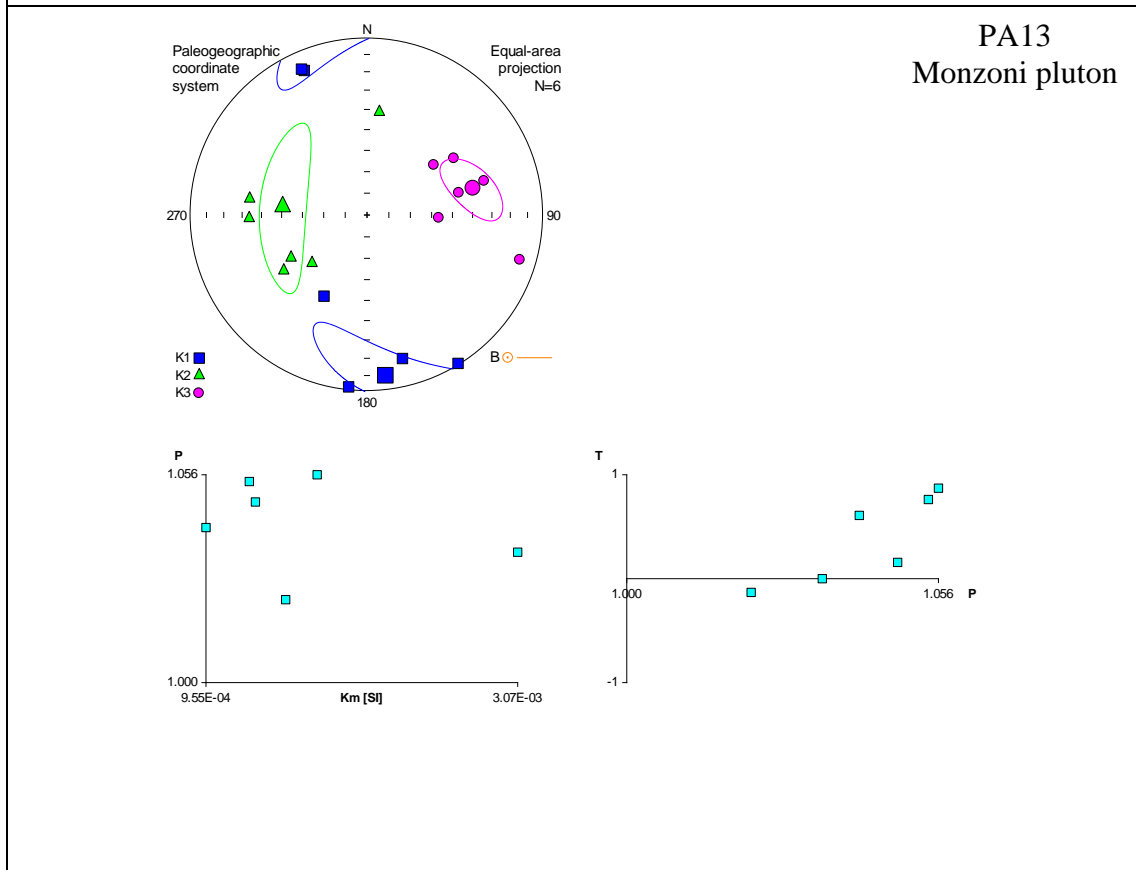
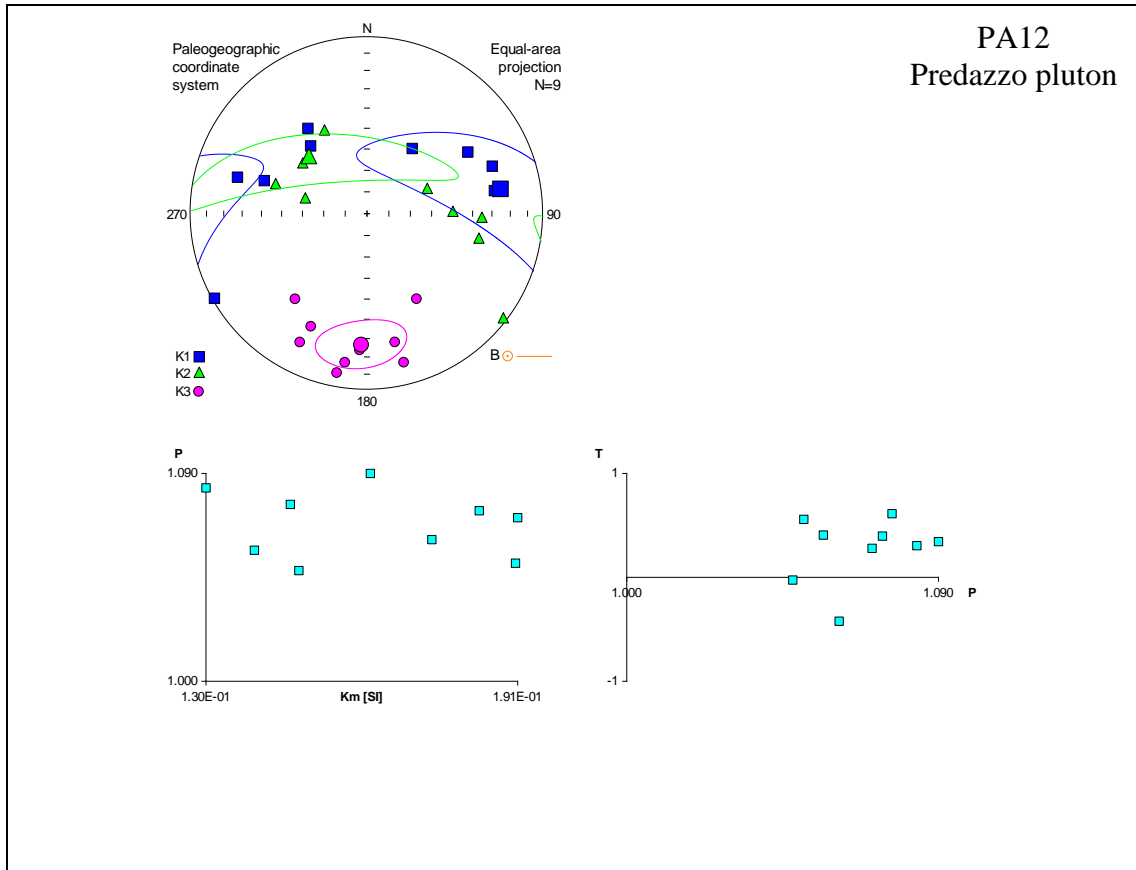




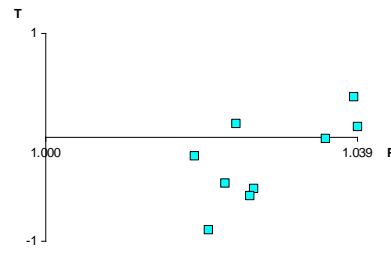
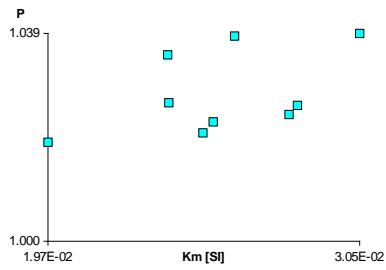
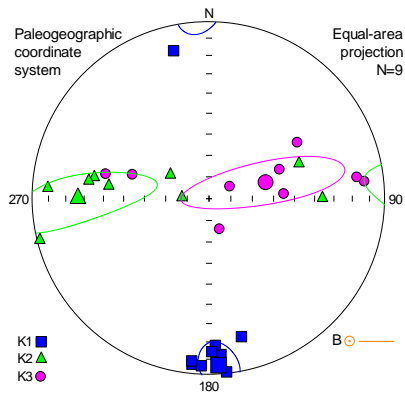




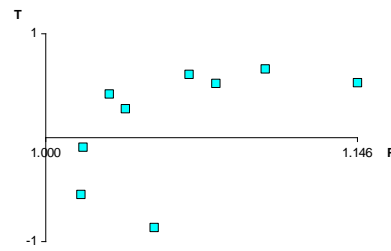
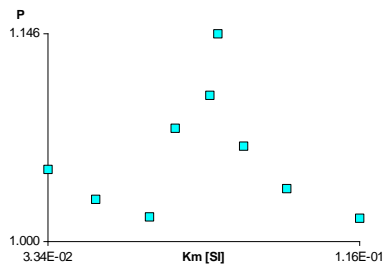
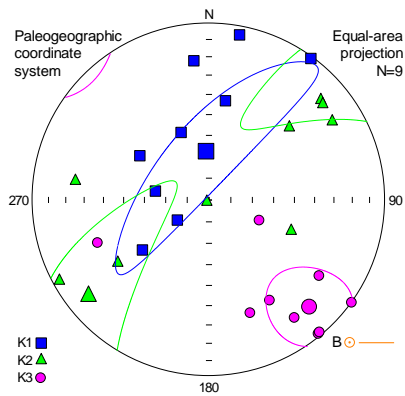


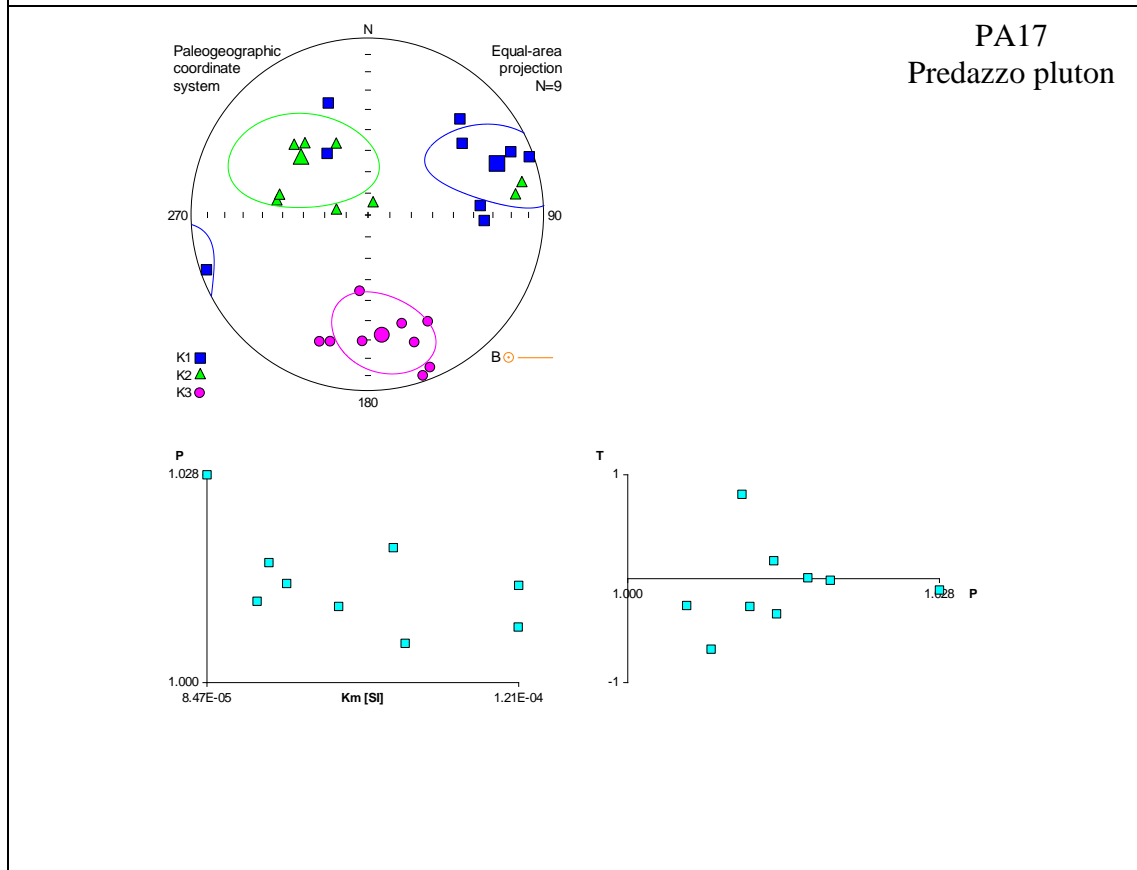
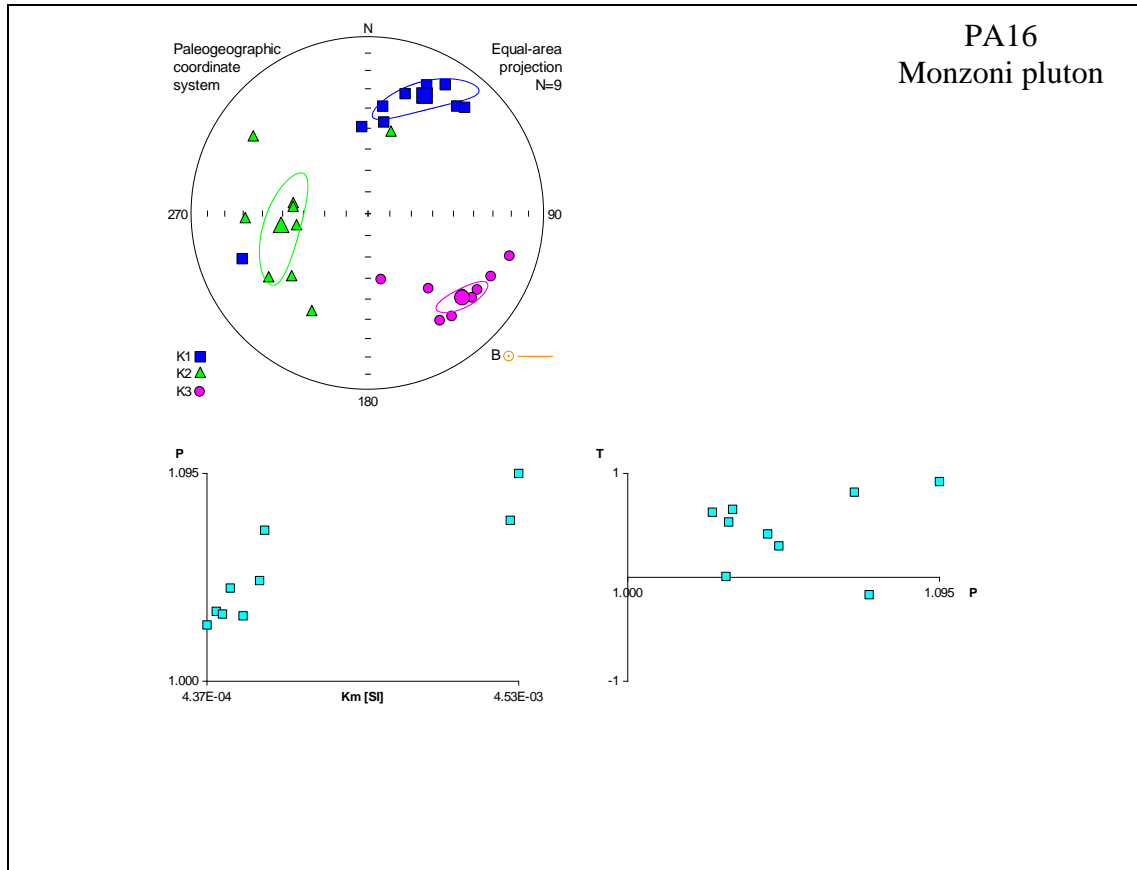


PA14
Monzoni pluton

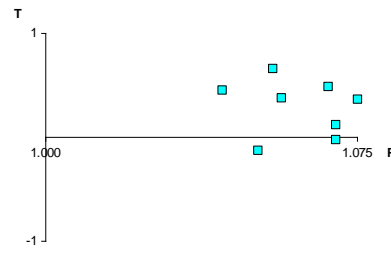
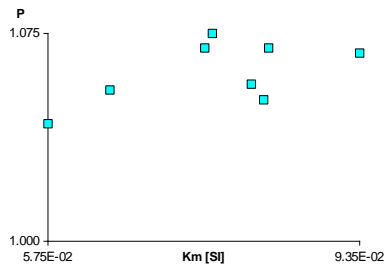
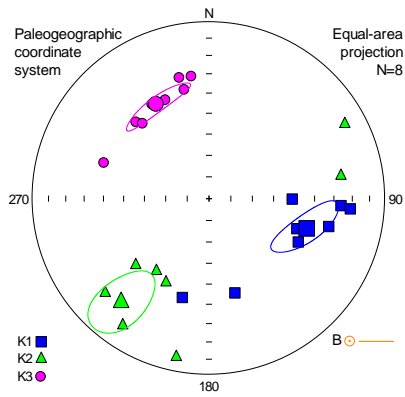


PA15
Monzoni pluton

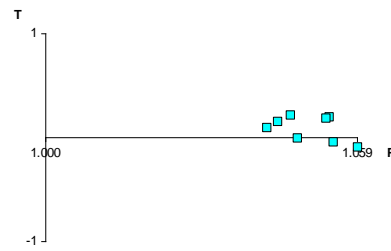
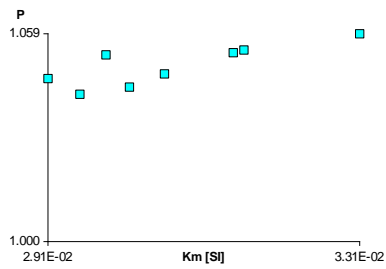
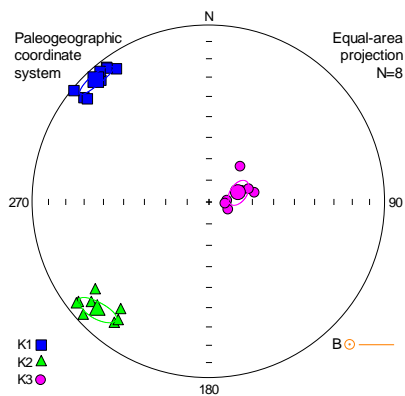




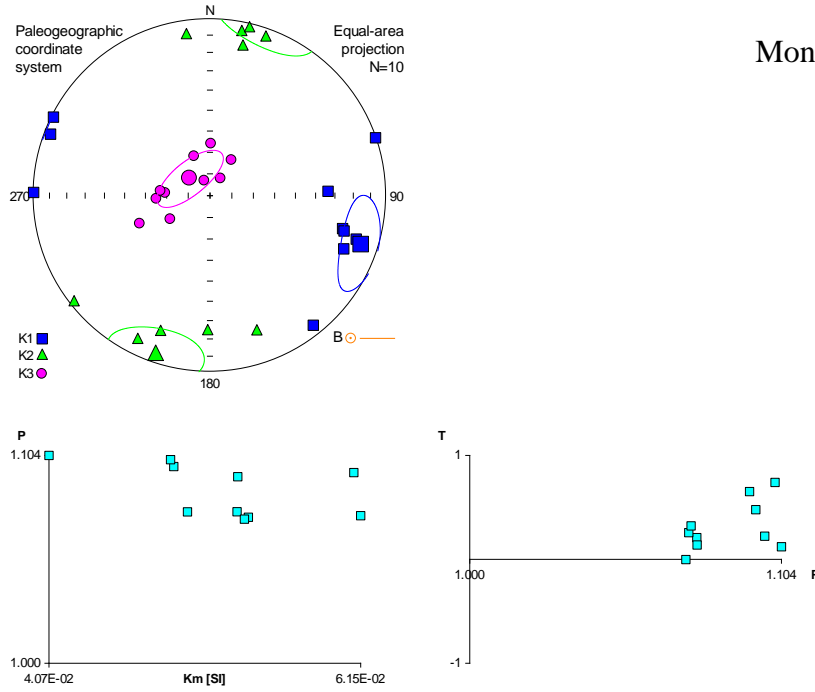
PA18
Monzoni pluton



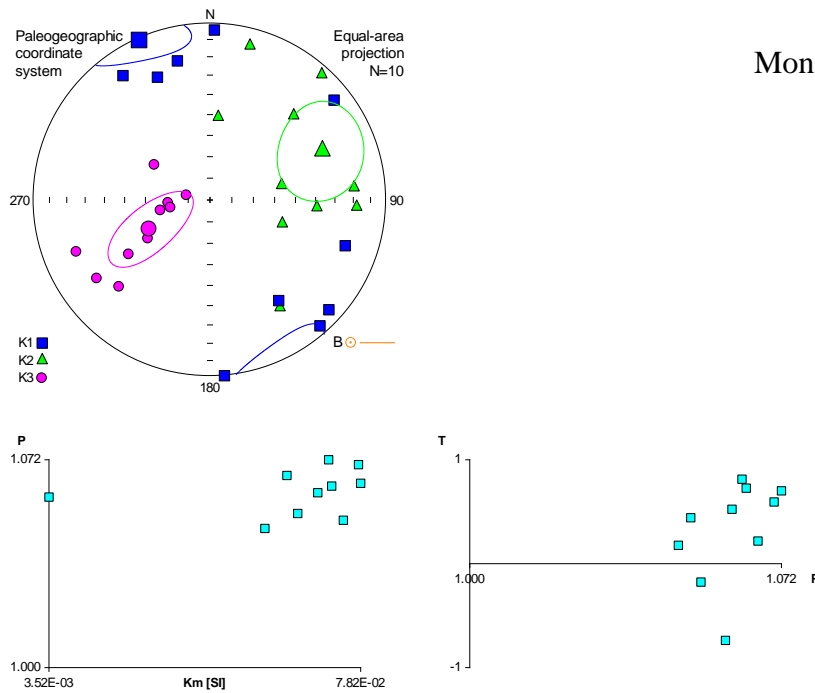
PA19
Monzoni pluton

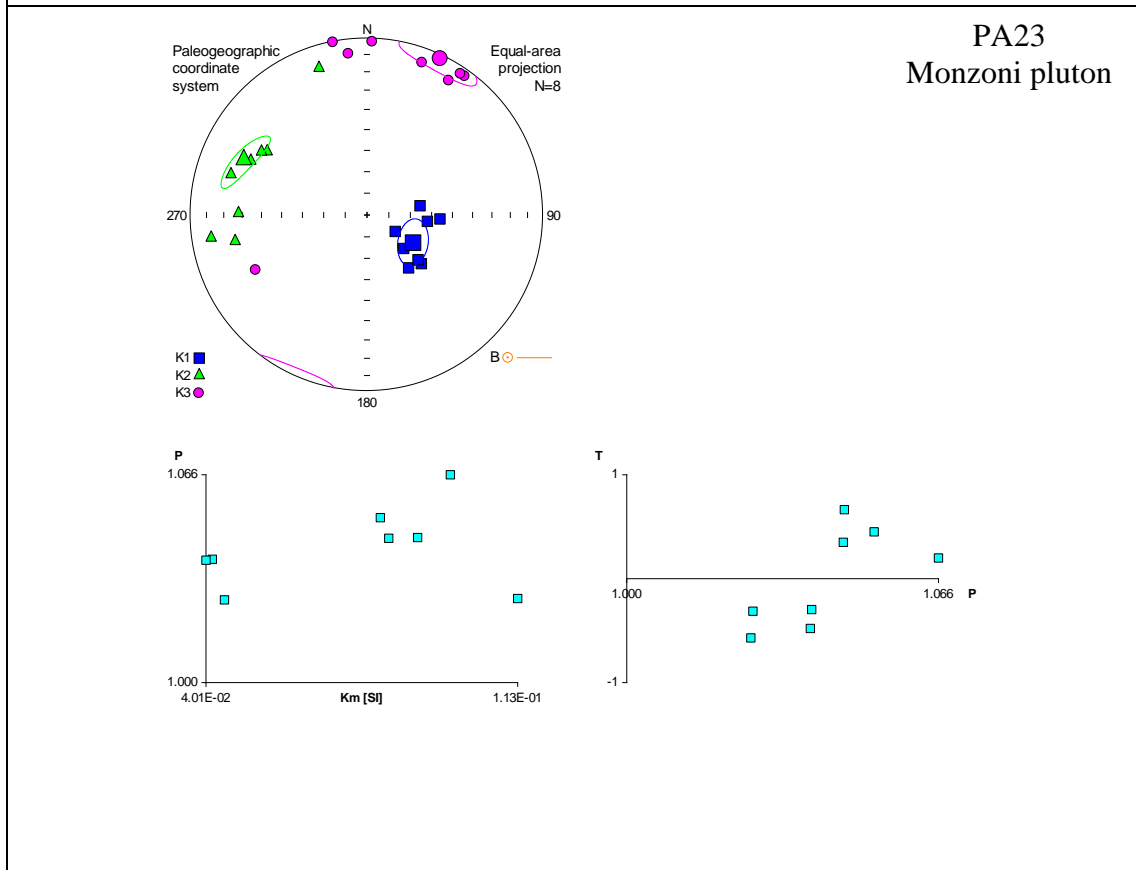
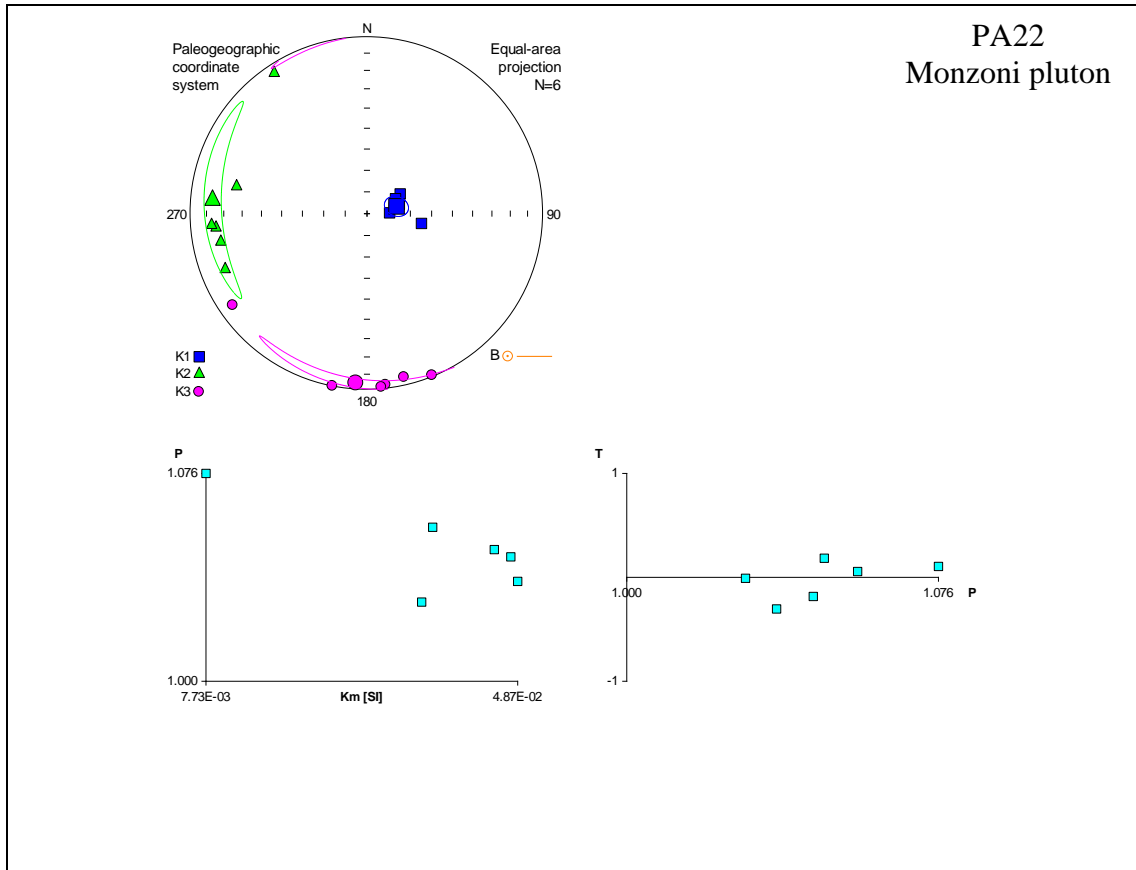


PA20
Monzoni pluton

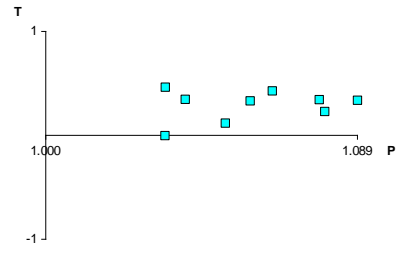
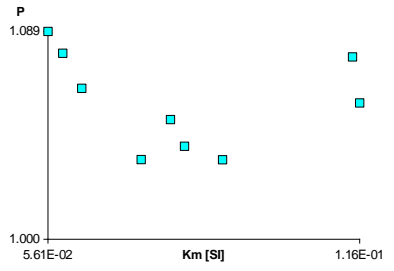
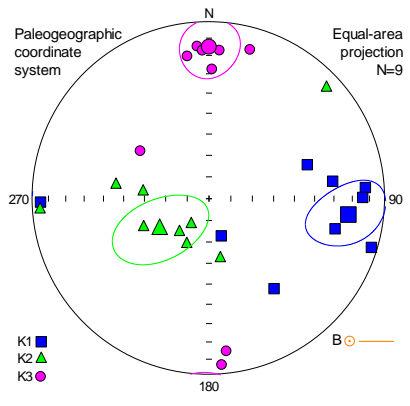


PA21
Monzoni pluton



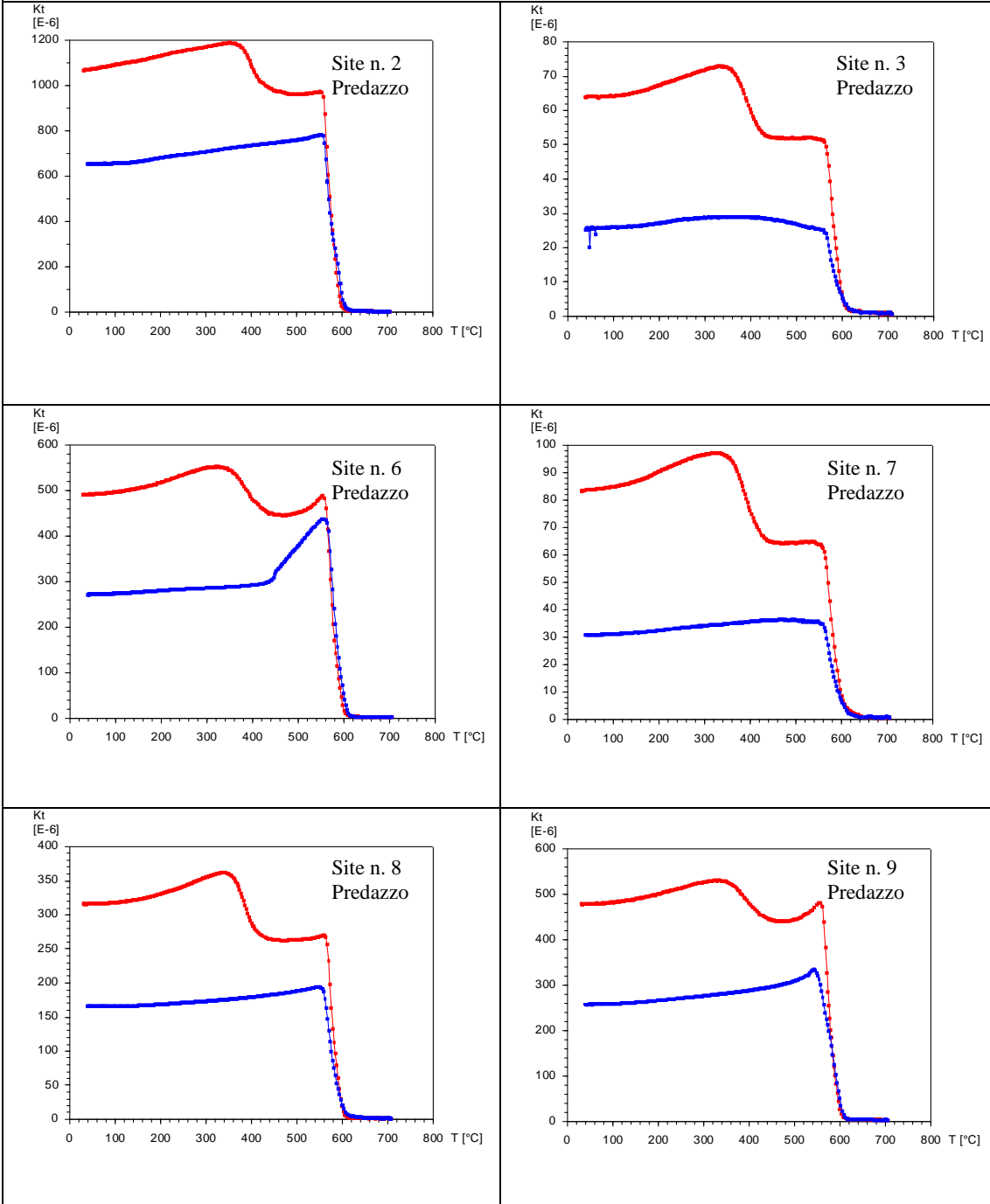


PA24
Monzoni pluton

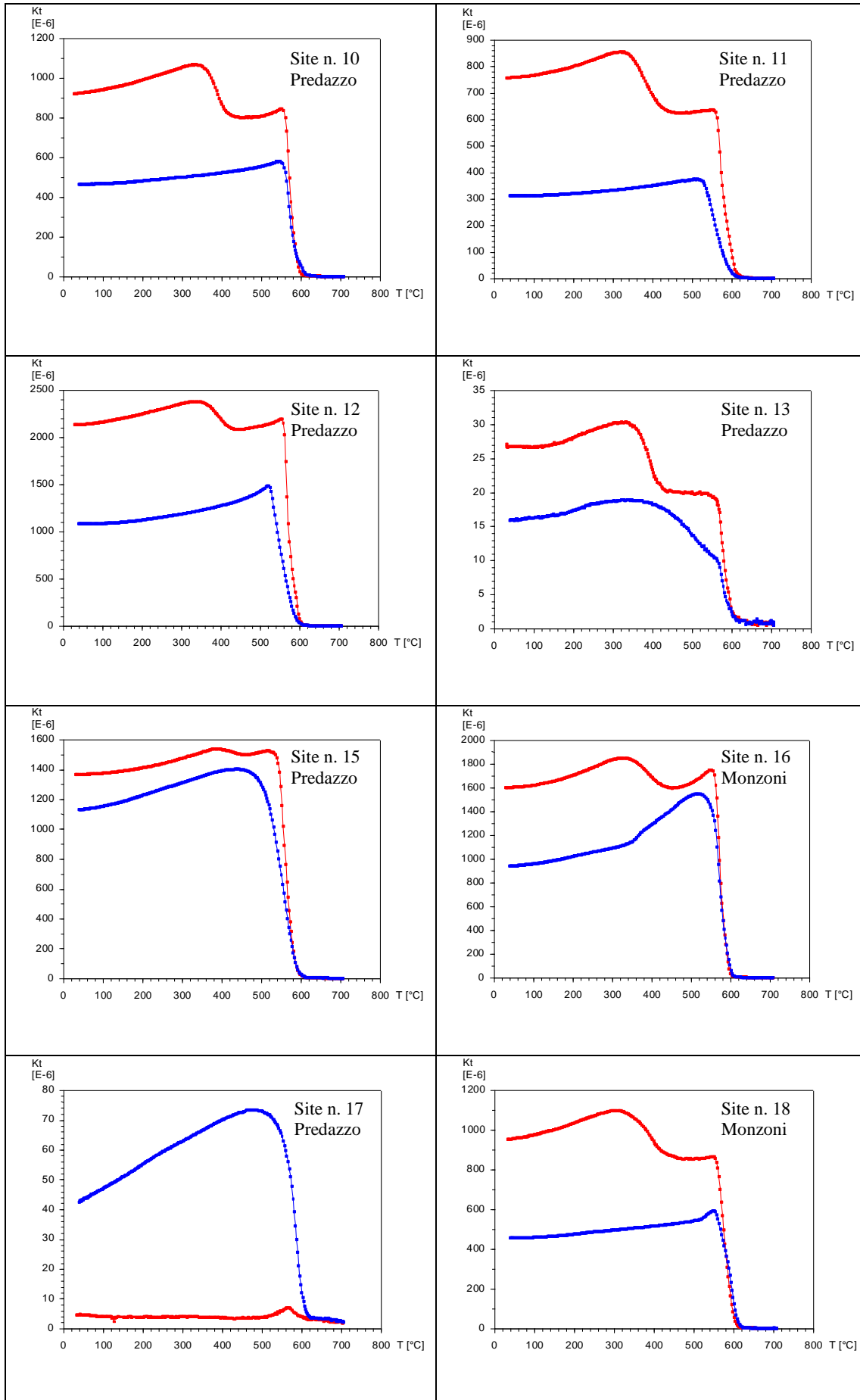


Appendix 4

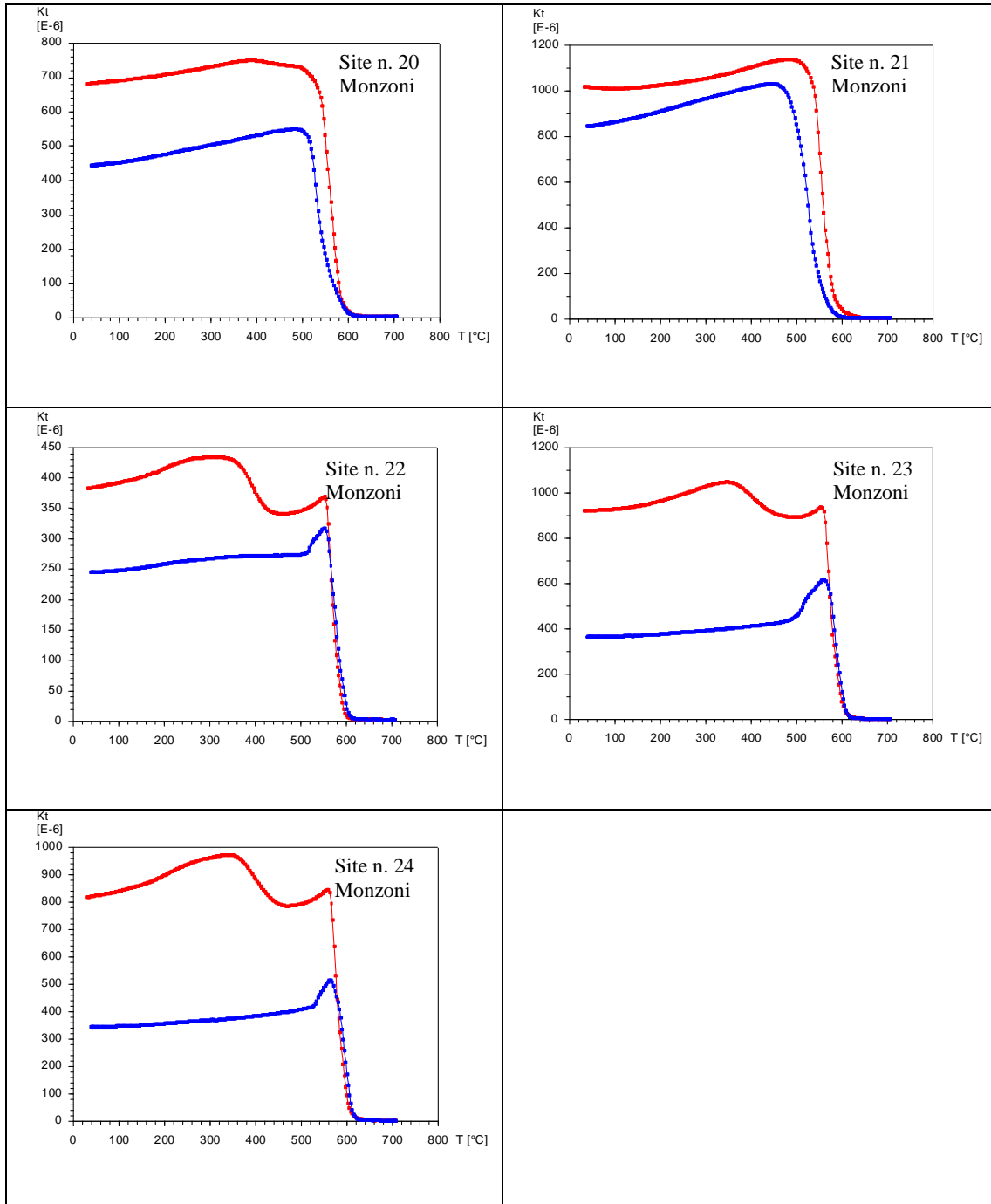
Thermomagnetic curves



APPENDIX

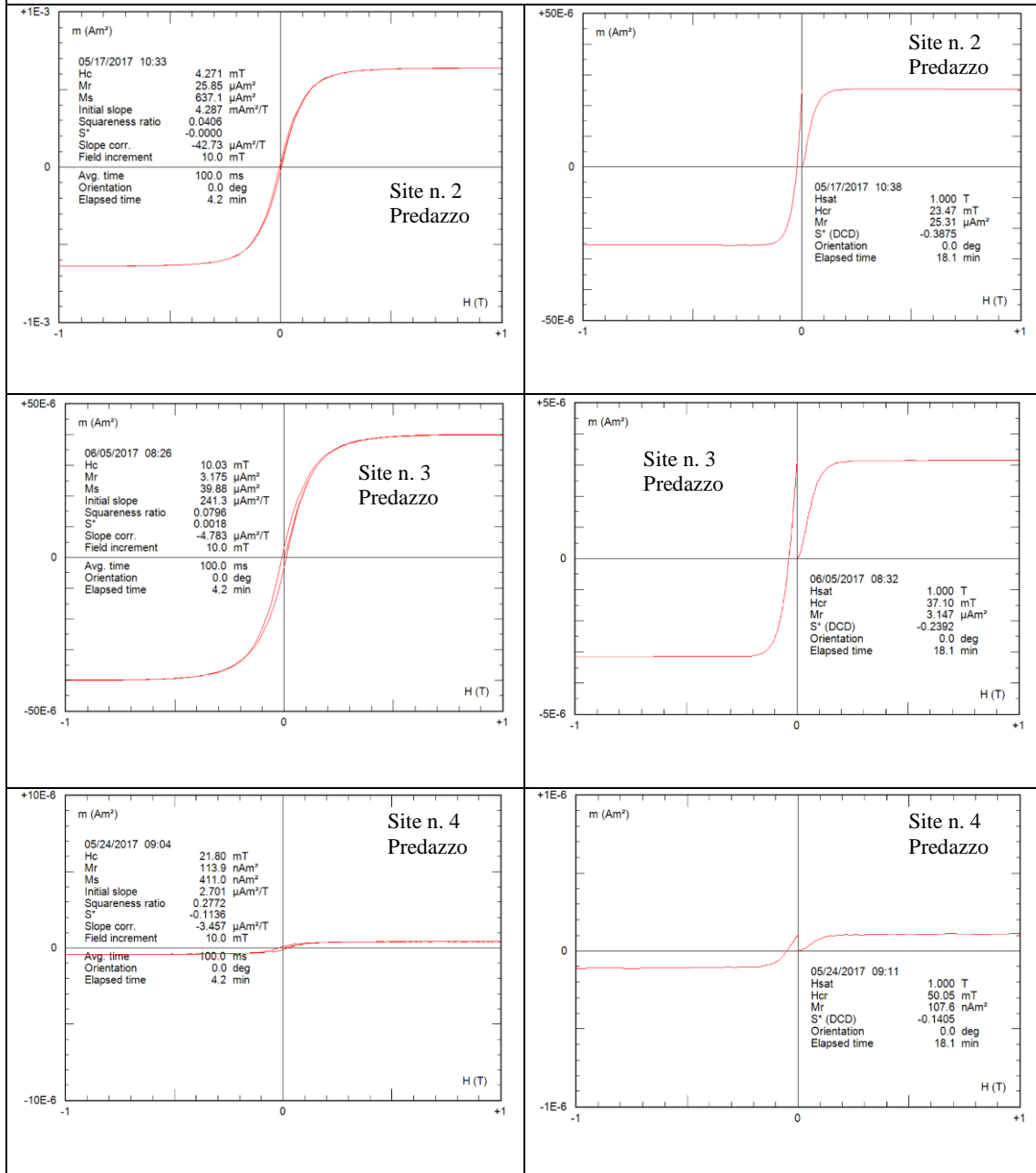


APPENDIX

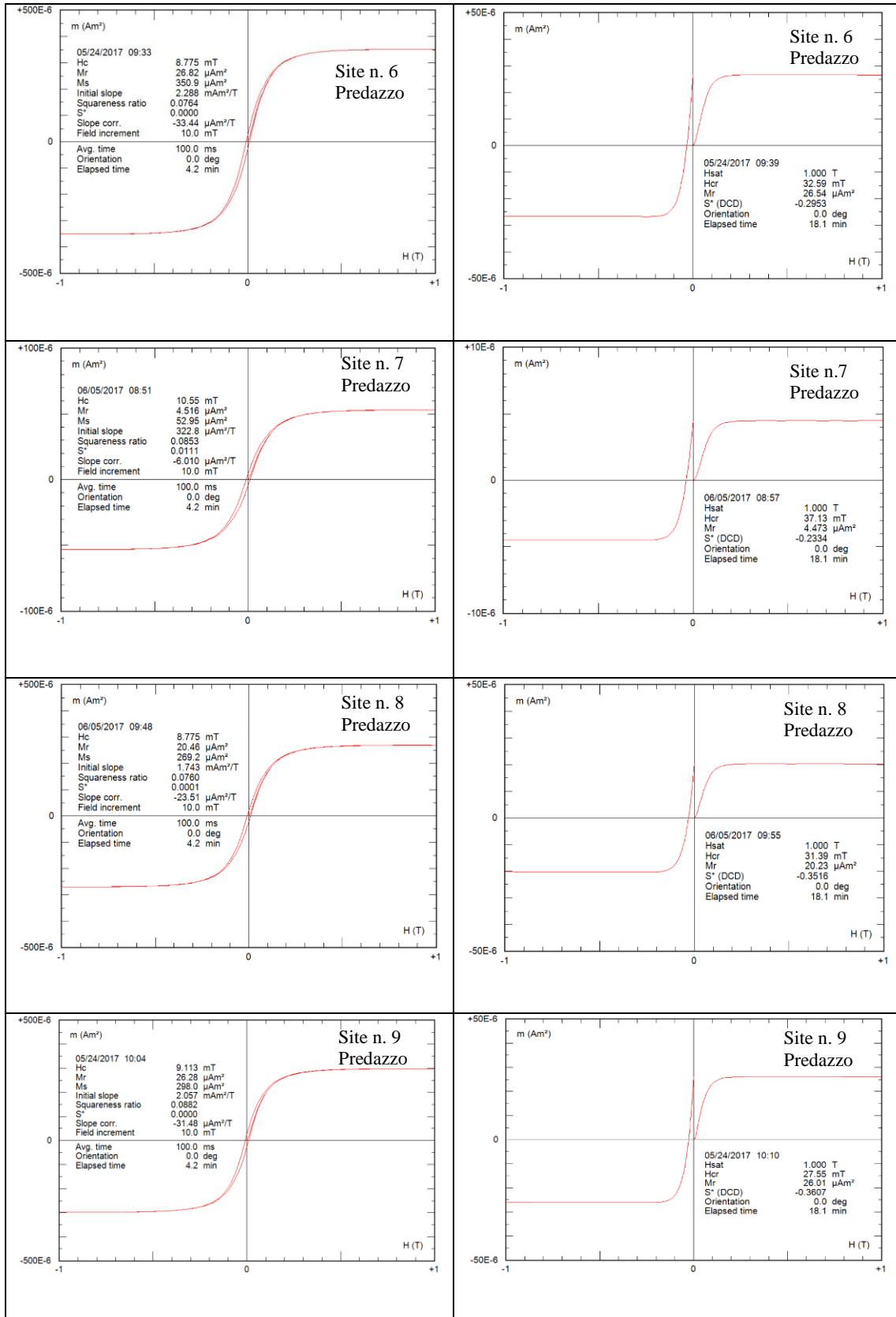


Appendix 5

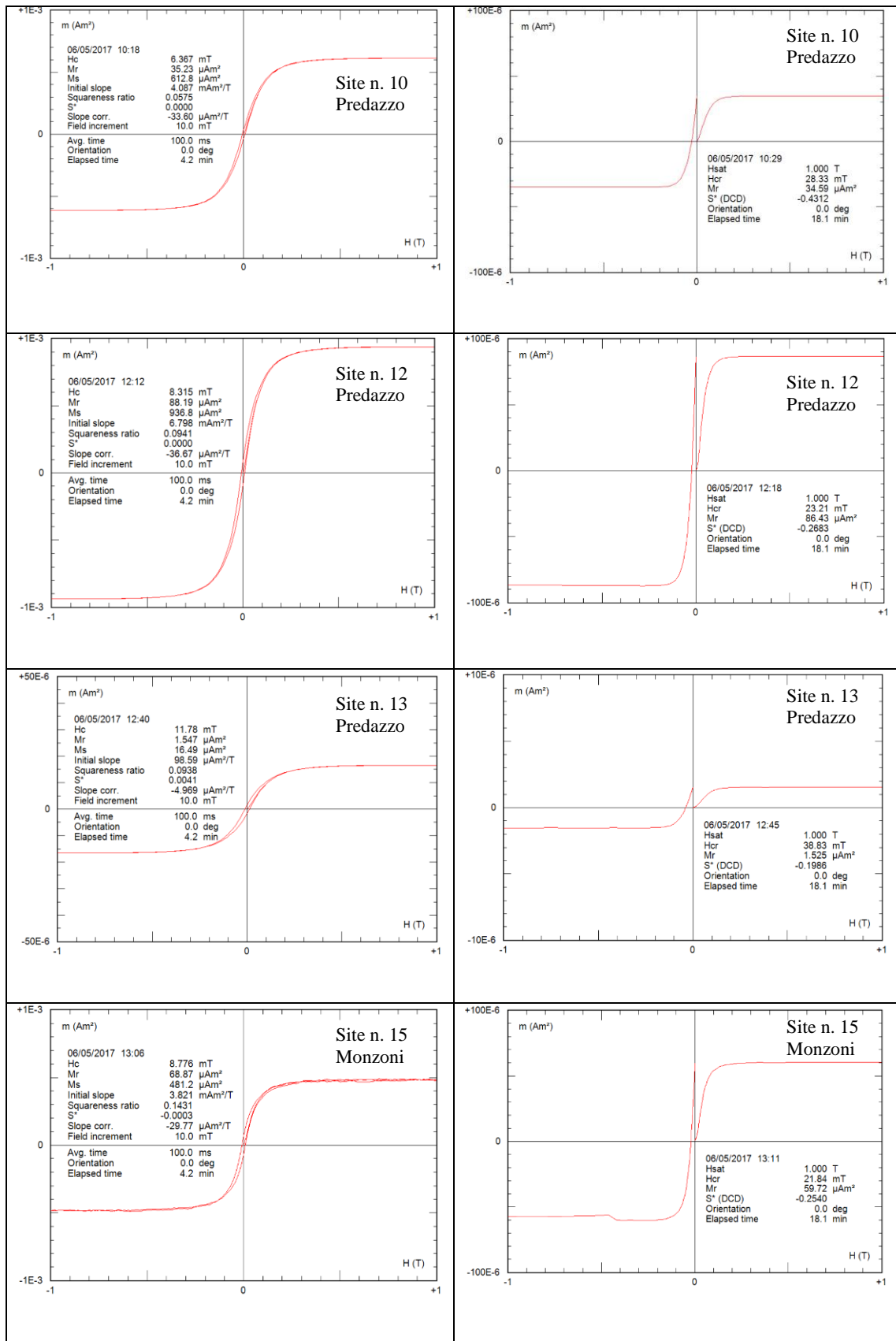
Hysteresis loops & IRM acquisition curves



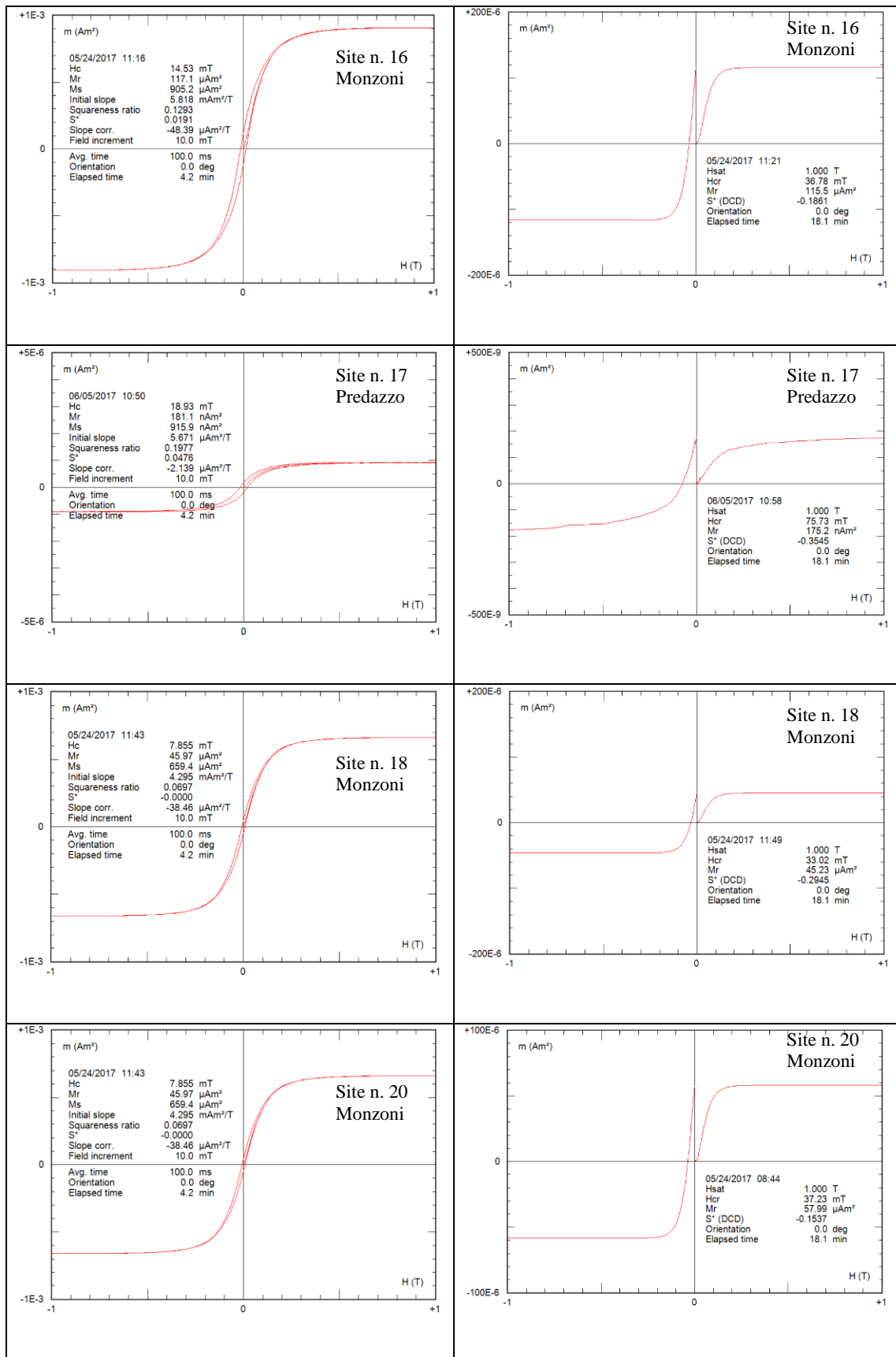
APPENDIX

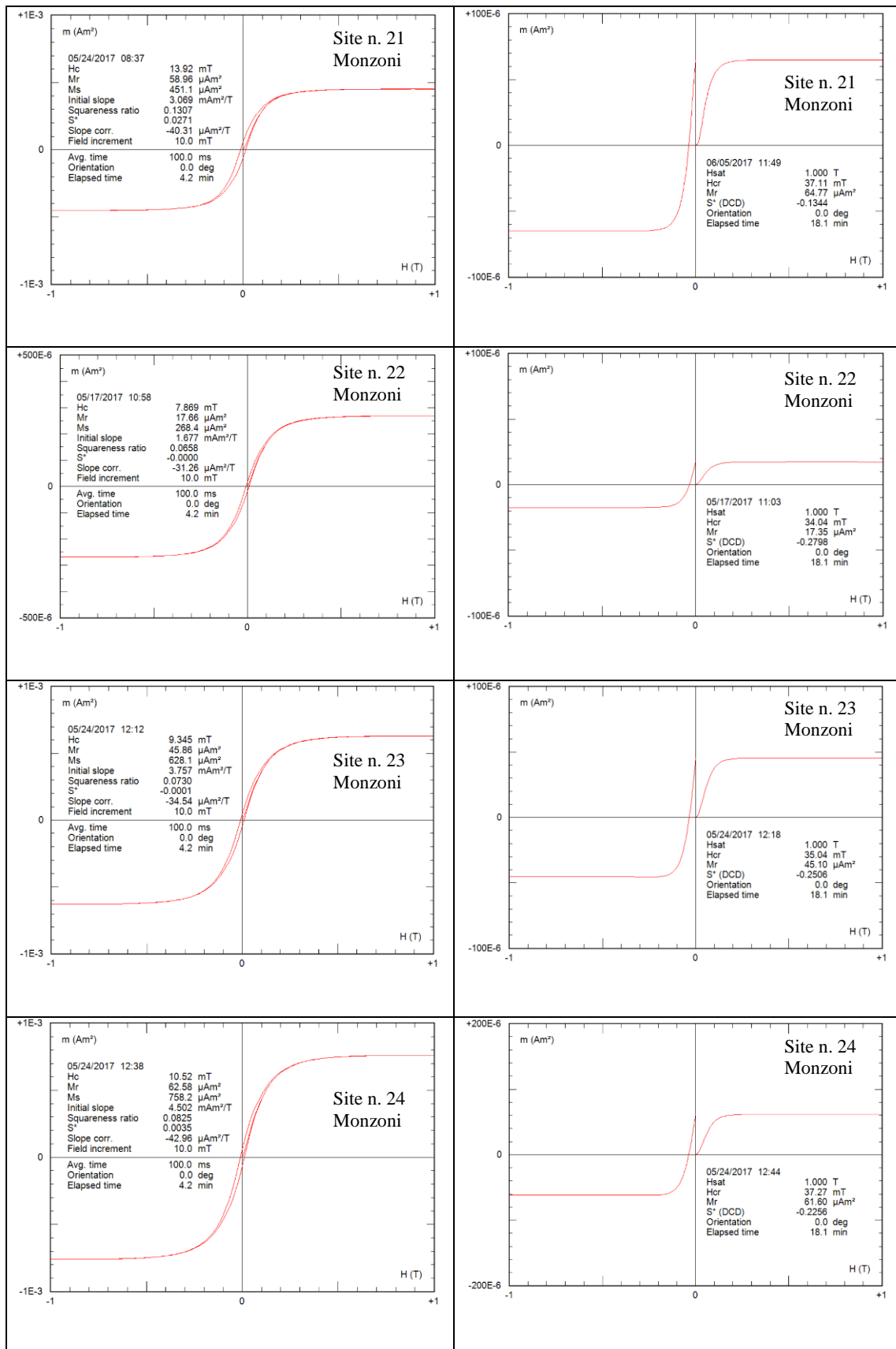


APPENDIX



APPENDIX





REFERENCES

REFERENCES

- Abbas, H., Michail, M., Cifelli, F., Mattei, M., Gianolla, P., Lustrino, M., Carminati, E., 2018. Emplacement modes of the Ladinian plutonic rocks of the Dolomites: insights from anisotropy of magnetic susceptibility. *J. Struct. Geol.*, 113, 42-61.
- Abbate, E., 1986. Apennines and Alps ophiolites and the evolution of the Western Tethys. *Mem. Soc. Geol. It.*, 31, 23-44.
- Andersson, M., Almqvist, B.S.G., Burchardt, S., Troll, V.R., Malehmir, A., Snowball, I., Kübler, L., 2016. Magma transport in sheet intrusions of the Alnö carbonatite complex, central Sweden. *Sci. Rep.*, 6, 1-13.
- Arculus, R.J., 2003. Use and abuse of the terms calcalkaline and calcalkalic. *J. Petrol.*, 44, 929-935.
- Armienti, P., Corazzato, C., Groppelli, G., Natoli, E., Pasquarè, G., 2003. Geological and petrographical study of Montecampione Triassic subvolcanic bodies (Southern Alps, Italy): preliminary geodynamic results. *Boll. Soc. Geol. It. Spec.*, 2, 67-78.
- Aubourg, C., Giordano, G., Mattei, M., Speranza, F., 2002. Magma flow in rhyolitic dikes inferred from magnetic fabric analysis (Ponza Island, W Italy). *Physics and Chemistry of the Earth*, 27, 1263-1272.
- Avanzini, M., Bargossi, G.M., Borsato, A., Castiglioni, G.B., Cucato, M., Morelli, C., Prosser, G., Sapezza, A., 2007. Note Illustrative - Foglio 026 Appiano, Carta Geologica d'Italia alla Scala 1:50000: Roma, ISPRA, p. 184.

REFERENCES

- Bébian, J., Blanchet, R., Cadet, J. P., Charvet, J., Chorowicz, J., Lapierre, H., Rampnoux, J. P., 1978. Le volcanisme triasique des din arides en yougoslavie: SA place dans l'evolution geotectonique peri-mediterraneenne. *Tectonophysics*, 47, 159-176.
- Beccaluva, L., Coltorti, M., Saccani, E., Siena, F., Zeda, O., 2005. Triassic magmatism and Jurassic ophiolites at the margins of the Adria Plate. In: I.R. Finetti (Ed.) CROP PROJECT: Deep seismic exploration of the central Mediterranean and Italy. Elsevier, 607-618.
- Bechstadt, T., Brandner, R., Mostler, H., Schmidt, K., 1977. Aborted rifting in the Triassic of the Eastern and Southern Alps. *N. Jb. Geol. Palaont. Abh.*, 156, 157-178.
- Bell, T.H., Newman, R., 2006. Appalachian orogenesis: the role of repeated gravitational collapse. *Geol. Soc. Am. Spec. Paper*, 414, 95-118.
- Bellieni, G., Fioretti, A.M., Marzoli, A., Visonà, D., 2010. Permo-Paleogene magmatism in the eastern Alps. *Rend. Lincei*, 21, 51-71.
- Beltrán-Triviño, A., Winkler, W., von Quadt, A., Gallhofer, D., 2016. Triassic magmatism on the transition from Variscan to Alpine cycles: evidence from U-Pb, Hf, and geochemistry of detrital minerals. *Swiss J. Geosci.*, 109, 309-328.
- Benn, K., Ham, N.M., Pignotta, G.S., Bleeker, W., 1998. Emplacement and deformation of granites during transpression: Magnetic fabrics of the Archean Sparrow pluton, Slave Province, Canada. *J. Struct. Geol.*, 20, 1247-1259.
- Benn, K., Paterson, S.R., Lund, S.P., Pignotta, G.S., Kruse, S., 2001. Magmatic fabrics in batholiths as markers of regional strains and plate kinematics: Example of cretaceous Mt. Stuart batholith. *Phys. Chem. Earth, Part A Solid Earth Geod.*, 26, 343-354.

REFERENCES

- Bergmüller, F., Bärlocher, C., Geyer, B., Grieder, M., Heller, F., & Zweifel, P., 1994. A torque magnetometer for measurements of the high-field anisotropy of rocks and crystals. *Measurement Science and Technology*, 5, 1466-1470.
- Bernoulli, D., 2007. The pre-Alpine geodynamic evolution of the Southern Alps: a short summary. *Bulletin für angewandte Geologie*, 12, 3-10.
- Bertotti, G., Picotti, V., Bernoulli, D., Castellarin, A., 1993. From rifting to drifting: tectonic evolution of the South-Alpine upper crust from the Triassic to the Early Cretaceous. *Sedim. Geol.*, 86, 53-76.
- Bianchini, G., Natali, C., Shibata, T., Yoshikawa, M., 2018. Basic dykes crosscutting the crystalline basement of Valsugana (Italy): new evidence of early Triassic volcanism in the Southern Alps. *Tectonics*, 37. <https://doi.org/10.1029/2017TC004950>
- Blendinger, W., 1985. Middle Triassic strike-slip tectonics and igneous activity of the Dolomites (Southern Alps). *Tectonophysics*, 113, 105-121.
- Bonadiman, C., Coltorti, M., Siena, F., 1994. Petrogenesis and T-fO₂ estimates of Mt. Monzoni complex (Central Dolomites, Southern Alps): a Triassic shoshonitic intrusion in a transcurrent geodynamic setting. *Eur. J. Mineral.*, 6, 943-966.
- Bonarelli-Marzocchi, L., Emiliani, F., Vespignani-Balzani, G.C., 1967. Fe, Mg and Mn distribution in the Predazzo granite (North Italy). *Mineral. Petrogr. Acta*, 13, 1-30.
- Bonarelli-Marzocchi, L., Emiliani, F., Vespignani-Balzani, G.C., 1965. Calcium distribution in the Predazzo Granite (North Italy). *Miner. Petrogr. Acta*, 11, 49-67.

REFERENCES

- Boriani, A., Caironi, V., Giobbi Origoni, E., Vannucci, R., 1992. The Permian intrusive rocks of Serie dei Laghi (Western Southern Alps). *Acta Vulcanol.*, 2, 73-86.
- Borsi, S., Ferrara, G., 1967. Determinazione dell'età delle rocce intrusive di Predazzo con i metodi del Rb/Sr e K/Ar. *Mineral. Petrogr. Acta*, 13, 45-66.
- Borsi, S., Ferrara, G., Paganelli, L., Simboli, G., 1968. Isotopic age measurements of the M. Monzoni intrusive complex. *Mineral. Petrogr. Acta*, 14, 171-183.
- Bosellini A., 1996. *Geologia delle Dolomiti*. Athesia, Bolzano, 192 pp.
- Bosellini, A., Castellarin, A., Doglioni, C., Guy, F., Lucch NI, F., Perri, M.C., Rossi, P.I., Simboli, G., Sommavill, E., 1982. Magmatismo e tettonica nel Trias delle Dolomiti. In: Castellarin, A. and Vai, G.B. (Eds) *Guida alla Geologia del Sudalpino centro-orientale*. *Soc. Geol. It.*, 189-210.
- Bosellini, A., Castellarin, A., Rossi, P.L., Simboli, G., Sommavilla, E., (1977). Schema sedimentologico e stratigrafico per il Trias medio della Val di Fassa ed aree circostanti (Dolomiti Centrali). *G. Geologia*, 42, 83-108.
- Bosellini, A., Gianolla P., Stefani M., 2003. *Geology of the Dolomites*. *Episodes*, 26, 181-185.
- Bouchez, J.L., Gleizes, G., Djouadi, T., & Rochette, P., 1990. Microstructure and magnetic susceptibility applied to emplacement kinematics of granites: the example of the Foix pluton (French Pyrenees). *Tectonophysics*, 184, 157-171.
- Brack, P., and Rieber, H., 1993, Towards a better definition of the Anisian/Ladinian boundary: new biostratigraphic data and correlations of boundary sections from the Southern Alps: *Heclogae Geologicae Helvetiae*, 86, 415-527.

REFERENCES

- Brack, P., Mundil, R., Oberli, F., Meier, M., Rieber, H., 1997. Biostratigraphic and radiometric age data question the Milankovitch characteristics of the Latemar
- Brack, P., Rieber, H., Mundil, R., Blendinger, W., Maurer, F., 2007. Geometry and chronology of growth and drowning of Middle Triassic carbonate platforms (Cernerera and Bivera/Clapsavon) in the Southern Alps (northern Italy). *Swiss J. Geosci.*, 100, 327-348.
- Brack, P., Rieber, H., Nicora, A., Mundil, R., 2005. The Global boundary Stratotype Section and Point (GSSP) of the Ladinian Stage (Middle Triassic) at Bagolino (Southern Alps, Northern Italy) and its implications for the Triassic time scale. *Episodes*, 28, 233-244.
- Brandner, R., 1984. Meeresspiegelschwankungen und Tektonik in der Trias der NW Tethys. *Jb. Geol.*, 126, 435-475.
- Brandner, R., Gruber, A., Morelli, C., Mair, V., 2016. Pulses of Neotethys-Rifting in the Permomesozoic of the Dolomites. *Geo. Alp.*, 13, 7-70.
- Brandner, R., Keim, L., 2011. A 4-day geological field trip in the Western Dolomites. *Geo. Alp.*, 8, 76-118.
- Brogger, W. C., 1895. Die Eruptivgesteine des Kristianiagebietes. II. Die Eruptionsfolge der triadischen Eruptivgesteine bei Predazzo in Siidtyrol: *Skr. Norske Vid.-Akad. i Oslo, I., Mat. Nat. Kl.*, 7, 123-153.
- Brusca, C., Gaetani, M., Jadoul, F., Viel, G., 1982. Paleogeografia Ladino- Carnica e metallogenesi nel Sudalpino: *Mem. Soc. Geol. It.*, 22, 65-82.
- Buser, S., 1980. Tolmač za list Celovec (Klagenfurt). Osnovna geološka karta SFRJ 1:100.000: Beograd, Zvezni geološki zavod, p. 62.
- Buser, S., 1986. Tolmač za list Tolmin in Videm (Udine). Osnovna geološka karta SFRJ 1:100.000: Beograd, Zvezni geološki zavod, p. 103.

REFERENCES

- Büttner, S.H., 1999. The geometric evolution of structures in granite during continuous deformation from magmatic to solid-state conditions: An example from the central European Variscan belt. *Am. Mineral.*, 84, 1781-1792.
- Calanchi, N., Lucchini, F., Rossi, P.L., 1978. The volcanic rocks from the Mount Agnello area (Fiemme Valley, Italy): A contribution to the knowledge of the mid-Triassic magmatism of the Southern Alps. *Tschermaks mineralogische und petrographische Mitteilungen*, 25, 131-143.
- Callot, J.P., Geoffroy, L., Aubourg, C., Pozzi, J.P., Mege, D., 2001. Magma flow directions of shallow dykes from the East Greenland volcanic margin inferred from magnetic fabric studies. *Tectonophysics*, 335, 313-329
- Caputo, R., Poli, M.E., Zanferrari, A., 2010. Neogene–Quaternary tectonic stratigraphy of the eastern Southern Alps, NE Italy. *J. Struct. Geol.*, 32, 1009-1027.
- Carminati, E., Doglioni, C., 2012. Alps vs. Apennines: the paradigm of a tectonically asymmetric Earth. *Earth-Sci. Rev.*, 112, 67-96.
- Carminati, E., Lustrino, M., Doglioni, C., 2012. Geodynamic evolution of the central and western Mediterranean: Tectonics vs. igneous petrology constraints. *Tectonophysics*, 579, 173-192.
- Casetta, F., Coltorti, M., Ickert, R.B., Bonadiman, C., Giacomoni, P.P., Ntaflos, T., 2018b. Intrusion of shoshonitic magmas at shallow crustal depth: T-P path, H₂O estimates, and AFC modeling of the Middle Triassic Predazzo Intrusive Complex (Southern Alps, Italy). *Contrib. Mineral. Petrol.*, 173, 57.
- Casetta, F., Coltorti, M., Marocchino, E., 2018a. Petrological evolution of the Middle Triassic Predazzo Intrusive Complex, Italian Alps. *Int. Geol. Rev.*, 60, 977-997.

REFERENCES

- Cashman, K.V., Sparks, R.S.J., 2013. How volcanoes work: A 25year perspective. *Geol. Soc. Am. Bull.*, 125, 664-690.
- Cassinis, G., Cortesogno, L., Gaggero, L., Perotti, C.R., Buzzi, L., 2008. Permian to Triassic geodynamic and magmatic evolution of the Brescian Prealps (eastern Lombardy, Italy). *Boll. Soc. Geol. It.*, 127, 501-518.
- Cassinis, G., Zezza, U., 1982. Dati geologici e petrografici sui prodotti del magmatismo triassico nelle Prealpi Bresciane. Guida alla geologia del subalpino centro-occidentale. *Guide Geol. Regionali Soc. Geol. It.*, 157-171.
- Castellarin, A., Cantelli, L., 2000. Neo-Alpine evolution of the Southern Eastern Alps. *J. Geodyn.*, 30, 251-274.
- Castellarin, A., Guy, F., Selli, L., 1982. Geologia dei dintorni del Passo di S. Nicolò e della Valle di Contrin (Dolomiti), in: Guida alla Geologia del Sudalpino Centro Orientale, pp. 231-242.
- Castellarin, A., Lucchini, F., Rossi, P. L., Selli, L., Simboli, G., 1988. The Middle Triassic magmatic-tectonic arc development in the Southern Alps. *Tectonophysics* 146, 79-89.
- Castellarin, A., Lucchini, F., Rossi, P.L., Sartori, R., Simboli, G., Somlavilla, E., 1982b. Note geologiche sulle intrusioni di Predazzo e dei Monzoni, in: Guida Alla Geologia Del Sudalpino Centro-Orientale, pp. 211-220.
- Castellarin, A., Lucchini, F., Row, P.L., Simboli, G., Bosellini, A., Somlavilla, E. 1980. Middle Triassic magmatism in Southern Alps: a geodynamic model. *Riv. Ital. Paleont.*, 85, 1111- 1124.
- Castellarin, A., Nicolich, R., Fantoni, R., Cantelli, L., Sella, M., Selli, L., 2006. Structure of the lithosphere beneath the Eastern Alps (southern sector of the TRANSALP transect). *Tectonophysics*, 414, 259-282.

REFERENCES

- Castellarin, A., Pisa, G., 1973. Le vulcaniti Ladiniche di Forni di Sopra (carnia occidentale): Mem. Museo Trident. Sc. Nat., 20, 99-136.
- Castellarin, A., Selli, L., Picotti, V., Cantelli, L., 1998. La tettonica delle Dolomiti nel quadro delle Alpi Meridionali orientali. Mem. della Soc. Geol. Ital., 53, 133-143.
- Castellarin, A., Selli, L., Picotti, V., Cantelli, L., 1998b. Tettonismo e diapirismo Medio Triassico delle Dolomiti. Mem. Soc. Geol. Ital., 53, 145-169.
- Castellarin, A., Vai, G.B., Cantelli, L., 2006. The Alpine evolution of the Southern Alps around the Giudicarie faults: A Late Cretaceous to Early Eocene transfer zone. Tectonophysics, 414, 203-223.
- Castro, A., 1987. On granitoid emplacement and related structures. A review. Geol. Rundsch., 76, 101-124.
- Celarc, B., Gorican, S., Kolar-Jurkovšek, T., 2013. Middle Triassic carbonate-platform break-up and formation of small-scale half-grabens (Julian and Kamnik-Savinja Alps, Slovenia). Facies, 9, 583-610.
- Cifelli, F., Minelli, L., Rossetti, F., Urru, G., Mattei, M., 2012. The emplacement of the Late Miocene Monte Capanne intrusion (Elba Island, Central Italy): constraints from magnetic fabric analyses. Int. J. Earth Sci. (Geol Rundsch) 101, 787-802.
- Crisci, C.M., Ferrara, G., Mazzuoli, R., Rossi, P.M., 1984. Geochemical and geochronological data on Triassic volcanism of the Southern Alps of Lombardy (Italy): genetic implications. Geol. Rund., 73, 279-292.
- Cros, P., 1980. Relations paleogeographiques entre la sedimentation tufacée et les apports terrigenes, Trias Moyen et Superieur des Dolomites et des Alpes Carniques. Riv. It. Paleont. Strat., 85, 953-982.

REFERENCES

- Dal Piaz, G.V., Bistacchi, A., Massironi, M., 2003. Geological outline of the Alps. *Episodes*, 26, 175-180.
- Davidson J.P., 1996. Deciphering mantle and crustal signatures in subduction zone magmatism. In Bebout, G.E., Scholl, D.W., Kirbyand, S.H., and Platt, J.P. (Eds.) *Subduction Top to Bottom*. Washington, D.C., American Geophysical Union, 251-262.
- Day, R., Fuller, M., Schmidt, V.A., 1977. Hysteresis properties of titanomagnetites: grain-size and compositional dependence. *Phys. Earth Planet. Int.*, 13, 260-267.
- De Vecchi, G., De Zanche, V., Sedea, R., 1974. Osservazioni preliminari sulle manifestazioni magmatiche triassiche nelle Prealpi Vicentine (area di Recoaro-Schio-Posina). *Boll. Soc. Geol. It.*, 93, 397-409.
- De Vecchi, G., Sedea, R. and Di Lallo, E., 1986. Note illustrative della carta geologica dell'area di Valli del Pasubio-Posina-Laghi: alla scala 1: 20.000. Soc. cooperativa tip.
- De Vecchi, G., Sedea, R., 1983. Il vulcanismo medio-triassico nelle prealpi vicentine (Italia settentrionale). *Mem. Sci. Geol. Univ. Padova*, 36, 14-169.
- De Zanche, V., Gianolla, P., Mietto, P., Siorpaes, C., Vail, P.R., 1993. Triassic sequence stratigraphy in the Dolomites (Italy). *Mem. Sci. Geol.*, 45, 1-27.
- Del Monte, M., Paganelli, L., & Simboli, G., 1967. The Monzoni intrusive rocks. A modal and chemical study. *Mineral Petrogr. Acta*, 13, 75-118.
- Del Monte, M., Paganelli, L., 1965. The syenitic outcrops in the Viezzena valley near Predazzo (North Italy). *Miner. Petrogr. Acta*, 11, 69-89.
- Di Giuseppe, P., Agostini, S., Lustrino, M., Karaoglu, O., Savasçin, M.Y., Manetti, P., Ersoy, Y., 2017. Transition from compression to strike-slip tectonics revealed

REFERENCES

- by Miocene-Pleistocene volcanism west of the Karliova Triple Junction (East Anatolia). *J. Petrol.*, 58, 2055-2087.
- Di Giuseppe, P., Agostini, S., Manetti, P., Savasçin, M.Y., Conticelli, S., 2018. Sub-lithospheric origin of Na-alkaline and calc-alkaline magmas in a post-collisional tectonic regime: Sr-Nd-Pb isotopes in recent monogenetic volcanism of Cappadocia, Central Turkey. *Lithos*, 316, 304-322.
- Djouadi, M.T., Gleizes, G., Ferré, E., Bouchez, J.L., Caby, R., Lesquer, A., 1997. Oblique magmatic structures of two epizonal granite plutons, Hoggar, Algeria: late-orogenic emplacement in a transcurrent orogen. *Tectonophysics*, 279, 351-374.
- Doglioni, C., 1983. Duomo medio-triassico nelle Dolomiti. *Rend. Soc. Geol. It.*, 6, 13-16.
- Doglioni, C., 1984. Triassic diapiric structures in the central Dolomites (northern Italy). *Eclogae Geol. Helv.*, 77, 261-285.
- Doglioni, C., 1987. Tectonics of the Dolomites (Southern Alps, Northern Italy). *J. Struct. Geol.*, 9, 181-193.
- Doglioni, C., 1988. Examples of strike-slip tectonics on platform-basin margins. *Tectonophysics*, 156, 293-302.
- Doglioni, C., 1992. Relationships between Mesozoic extensional tectonics, stratigraphy and Alpine inversion in the Southern Alps. *Eclogae Geol. Helv.*, 85, 105-126.
- Doglioni, C., 2007. Tectonics of the Dolomites. *Bull. Angew. Geol.*, 12, 11-15.
- Doglioni, C., Bosellini, A. 1987. Eoalpine and mesoalpine tectonics in the Southern Alps: *Geol. Rundsch.*, 76, 735-754.

REFERENCES

- Doglioni, C., Carminati E., 2008. Structural styles and Dolomites Field Trip. Mem. Mem. Descr. Carta Geol. It., 82, 296 pp.
- Dozet, S., Buser, S., 2009. Triassic, in Pleničar, M., Ogorelec, B., and Novak, M., eds., The geology of Slovenia: Lubiana, Geološki Zavod Slovenije, 161-214.
- Dunlop, D.J., 2002. Theory and application of the Day plot (Mrs/Ms versus Hcr/Hc) 1. Theoretical curves and tests using titanomagnetite data. J. Geophys. Res: Solid Earth, 107(B3).
- Emeleus, C.H., Troll, V.R., Chew, D.M., Meade, F.C., 2012. Lateral versus vertical emplacement in shallow-level intrusions? The Slieve Gullion Ring-complex revisited. J. Geol. Soc. London, 169, 157-171.
- Emiliani, F., Fabbri, B., Paganelli, L., Vespignani-Balzani, G.C., 1970. Sr, Ba, Fe, Mg, Mn and Ti distribution in the leucomozodiorite-syenite series in Predazzo intrusive complex. Miner. Petrogr. Acta, 16, 45-73.
- Emiliani, F., Vespignani-Balzani, G.C., 1964. An emission-spectrographic method for the determination of Sr and Ba in granites and other silicate rocks. Miner. Petrogr. Acta, 10, 43-56.
- Emiliani, F., Vespignani-Balzani, G.C., 1968. Titanium distribution in the Predazzo Granite (North Italy). Miner. Petrogr. Acta, 14, 1-21.
- Ernst, R.E., Baragar, W.R.A., 1992. Evidence from magnetic fabric for the flow pattern of magma in the Mackenzie giant radiating dyke swarm. Nature, 356, 511-513.
- Esperança, S., Crisci, G.M., de Rosa, R., Mazzuoli, R., 1992. The role of the crust in the magmatic evolution of the island of Lipari (Aeolian Islands, Italy). Contrib. Mineral. Petrol., 112, 450-462.

REFERENCES

- Ewart, A., 1982. The mineralogy and petrology of Tertiary-Recent orogenic volcanic rocks with special reference to the andesitic-basaltic compositional range. In: Thorpe R.S. (Ed.) *Andesites*. Chichester, UK, John Wiley, 26-87.
- Fabbri, b., Paganelli, L., 1973. Sr and Ba partitioning between phenocrysts and groundmass, and Sr, Ba, Cr, V, Mg, Fe, Ti, Mn abundance in the triassic volcanic rocks near Forno (Fiamme Valley). *Miner. Petrogr. Acta*, 19, 103.
- Fabbri, B., Paganelli, L., 1976. Studio geochimico-petrografico delle rocce intrusive dei M.ti Monzoni: distribuzione di Sr, Ba, Cr, V, Fe, Mg, Mn, e Ti. *Miner. Petrogr. Acta*, 21, 53-64.
- Fan, W.M., Guo, F., Wang, Y. J., Lin, G., 2003. Late Mesozoic calc-alkaline volcanism of post-orogenic extension in the northern Da Hinggan Mountains, northeastern China. *J. Volcanol. Geotherm. Res.*, 121, 115-135.
- Ferrara, G., Lucchini, F., Morten, L., Rita, F., Rossi, P. L., Simboli, G., 1974. Clinopyroxenite inclusions in the Triassic volcanic rocks from Latemar, Predazzo, North Italy. *Rend. Soc. It. Min. Petr.*, 30, 141-163.
- Ferry, J. M., Wing, B. A., Penniston-Dorland, S. C., & Rumble, D., 2002. The direction of fluid flow during contact metamorphism of siliceous carbonate rocks: new data for the Monzoni and Predazzo aureoles, northern Italy, and a global review. *Contrib. Mineral Petrol.*, 14, 679-699.
- Foley, S.F., Barth, M.G., Jenner, G.A., 2000. Rutile/melt partition coefficients for trace elements and an assessment of the influence of rutile on trace element characteristics of subduction zone magmas. *Geochim. Cosmochim. Acta*, 64, 933-938.

REFERENCES

- Fondriest, M., Smith, S.A.F., Di Toro, G., Zampieri, D., and Mittempergher, S., 2012. Fault zone structure and seismic slip localization in dolostones, an example from the Southern Alps, Italy, *J. Struct. Geol.*, 45, p. 52-67.
- Franke, W., Cocks, L.R.M., Torsvik, T.H., 2017. The Paleozoic Variscan oceans revisited. *Gondw. Res.*, 48, 257-284.
- Frey, F.A., Green, D.H., Roy, S.D., 1978. Integrated models of basalt petrogenesis: a study of quartz tholeiites to olivine melilitites from South Eastern Australia utilizing geochemical and experimental petrological data. *J. Petrol.*, 19, 463-513.
- Gaeta, M., Freda, C., Marra, F., Arienzo, I., Gozzi, F., Jicha, B., Di Rocco, T., 2016. Paleozoic metasomatism at the origin of Mediterranean ultrapotassic magmas: constraints from time-dependent geochemistry of Colli Albani volcanic products (Central Italy). *Lithos*, 244, 151-164.
- Gallien, F., Abart, R., & Wyhlidal, S., 2007. Contact metamorphism and selective metasomatism of the layered Bellerophon Formation in the eastern Monzoni contact aureole, northern Italy. *Mineralogy and Petrology*, 91, 25-53.
- Garzanti, E., 1985. The sandstone memory of the evolution of a Triassic volcanic arc in the Southern Alps, Italy. *Sedimentology*, 32, 423-433.
- Gasparotto, G., Simboli, G., 1991. Mineralogia, petrografia e schemi evolutivi delle magmatiti triassiche del complesso di Cima Pape (Dolomiti Orientali). *Miner. Petrogr. Acta*, 34, 205-234.
- Gianolla, P., 1992. Evoluzione mediotriassica del vulcanismo di Rio Freddo. (Alpi Giulie, Italia). *Mem. Sci. Geol.*, 44, 193-209.
- Gianolla, P., Avanzini, M., Breda, A., Kustatscher, E., Preto, N., Roghi, G., Furin, S., Massari, F., Picotti, V., Stefani, M., 2010. Field trip to the world heritage site of

REFERENCES

- the Tethysian Triassic, September 5-10, 2010, Dolomites, Southern Alps, Italy. 122 pp.
- Gianolla, P., Avanzini, M., Breda, A., Kustatscher, E., Preto, N., Roghi, G., Furin, S., Massari, F., Picotti, V., Stefani, M., 2010. Field trip to the world heritage site of the Tethysian Triassic, September 5-10, 2010, Dolomites, Southern Alps, Italy. 122 pp.
- Gianolla, P., De Zanche, V., Mietto, P., 1998. Triassic sequence stratigraphy in the Southern Alps (Northern Italy): definition of sequences and basin evolution. In: de Graciansky, P.-C., Hardenbol, J., Jacquin, T. and P.R. Vail (Eds.). Mesozoic and Cenozoic Sequence Stratigraphy of European Basins. SEPM Special Publications, 60, 719-747.
- Gianolla, P., Morelli, C., Cucato, M., and Siorpaes, C., in press, Note Illustrative - Foglio 016 Dobbiaco, Carta Geologica d'Italia alla Scala 1:50000: Roma, ISPRA.
- Gianolla, P., Neri, C., 2007. Formazione di Wengen. In: Cita Sironi, M.B., Abbate, E., Balini, M., Conti, M.A., Falorni, P., Germani, D., Gropelli, G., Manetti, P., Petti, F.M. (Eds.), Carta Geologica d'Italia 1:50.000, Catalogo delle Formazioni-Unità tradizionali (2), QUADERNI serie III, 7/VIII. S.E.L.CA, Firenze, 111-124.
- Graham, J.W., 1954. Magnetic susceptibility anisotropy, an unexploited petrofabric element. Geol. Soc. Am. Bull., 65, 1257-1258.
- Handy, M.R., Schmid, S.M., Bousquet, R., Kissling, E., Bernoulli, D., 2010. Reconciling plate-tectonic reconstructions of Alpine Tethys with the geological-geophysical record of spreading and subduction in the Alps. Earth-Sci. Rev., 102, 121-158.
- Hansel, V., 1878. Die petrographische Beschaffenheit des Monzonits von Predazzo. Jahrb. der Kais. Geol. Reichsanstalt, 28, 449-466.

REFERENCES

- Hart, S.R., 1984. A large-scale isotope anomaly in the Southern Hemisphere mantle. *Nature*, 309, 753-757.
- Hawkins, J.W., 1995. The geology of the Lau Basin. In *Back arc Basins* (pp. 63-138). Springer, Boston, MA.
- Herzberg, C., Asimow, P.D., 2015. PRIMELT MEGA.XLSM software for primary magma calculation: peridotite primary magma MgO contents from the liquids to the solidus. *Geochem. Geophys. Geosyst.*, 16, 563-578.
- Hörnès, R., 1912. Zur Geologie von Predazzo. *Sitzungsberichte der Akad. der Wissenschaften Math. Klasse*, 121, 3-31.
- Hrouda, F., 1982. Magnetic anisotropy of rocks and its application in geology and geophysics. *Geophys. Surv.*, 5, 37-82.
- Hrouda, F., Jelínek, V., 1990. Resolution of ferromagnetic and paramagnetic anisotropies, using combined low-field and high-field measurements. *Geophys. J. Int.*, 103, 75-84.
- Hrouda, F., Jelínek, V., Zapletal, K., 1997. Refined technique for susceptibility resolution into ferromagnetic and paramagnetic components based on susceptibility temperature-variation measurement. *Geophys. J. Int.*, 129, 715-719.
- Hutton, D.H.W., 1988. Granite emplacement mechanisms and tectonic controls: inferences from deformation studies. *Trans. R. Soc. Edinb. Earth Sci.*, 79, 245-255.
- Ishizuka, O., Yuasa, M., Tamura, Y., Shukuno, H., Stern, R. J., Naka, J., ... & Taylor, R. N. (2010). Migrating shoshonitic magmatism tracks Izu–Bonin–Mariana intra-oceanic arc rift propagation. *Earth and Planetary Science Letters*, 294, 111-122.

REFERENCES

- Jadoul, F., Galli, M.T., Berra, F., Cirilli, S., Ronchi, P., and Paganoni, A., 2004, The Late Triassic-Early Jurassic of the Lombardy Basin: Stratigraphy, Palaeogeography and Palaeontology, 32 IGC Florence August 20-28 2004, Excursion Guide book, Volume 68, p. 36.
- Jelinek, V., 1977. The statistical theory of measuring anisotropy of magnetic susceptibility of rocks and its application. Geofyzika Brno, pp. 77.
- Jelínek, V., 1981. Characterization of the magnetic fabric of rocks. Tectonophysics, 79, 63-67.
- Jelínek, V., Pokorný, J., 1997. Some new concepts in technology of transformer bridges for measuring susceptibility anisotropy of rocks. Physics and Chemistry of the Earth 22, 179-181.
- Just, J., Kontny, A., De Wall, H., Hirt, A.M. & Martín-Hernández, F., 2004. Development of magnetic fabrics during hydrothermal alteration in the Soultz-sous-Forets granite from the EPS-1 borehole, Upper Rhine Graben. In: Martín-Hernández, F., Lunebrg, C.M., Aubourg, C. & Jackson, M. (eds) Magnetic Fabric: Methods and Applications. Geological Society, London, Special Publications, 238, 509-526.
- Kawabata, H., Hanyu, T., Chang, Q., Kimura, J.I., Nichols, A.R.L., Tatsumi, Y., 2011. The petrology and geochemistry of St. Helena alkali basalts: evaluation of the oceanic crust-recycling model for HIMU OIB. Journal of Petrology, 22, 791-838.
- Keim, L., Brandner, R., Krystyn, L., Mette, W., 2001. Termination of carbonate slope progradation: an example from the Carnian of the Dolomites, Northern Italy. Sedim. Geol., 143, 303-323.

REFERENCES

- Kennedy, B.M., Mark Jellinek, A., Stix, J., 2008. Coupled caldera subsidence and stirring inferred from analogue models. *Nat. Geosci.*, 1, 385-389.
- Kimura, J.I., 2017. Modeling chemical geodynamics of subduction zones using the Arc Basalt Simulator version 5. *Geosphere*, 13, 992-1025.
- Kimura, J.-I., Ariskin, A.A., 2014. Calculation of water-bearing primary basalts and estimation of source mantle conditions beneath arcs: PRIMACALC2 model for WINDOWS. *Geochem. Geophys. Geosyst.*, 15, 1494-1514.
- Knight, M.D., Walker, G.P.L., 1988. Magma Flow Directions in Dikes of the Koolau Complex, Oahu, Determined From Magnetic Fabric Studies. *J. Geophys. Res.*, 93, 4301-4319.
- Kuno, H., 1968. Differentiation of basalt magmas. *Intersci.*, 2, 623-688.
- Kustatscher, E., Bernardi, M., Petti, F.M., Franz, M., van Konijnenburg-van Cittert, J.H.A., and Kerp, H., 2017, Sea-level changes in the Lopingian (late Permian) of the northwestern Tethys and their effects on the terrestrial palaeoenvironments, biota and fossil preservation: *Global and Planetary Change*, v. 148, p. 166-180.
- Lan, T. G., Fan, H. R., Santosh, M., Hu, F. F., Yang, K. F., Yang, Y. H., Liu, Y., 2012. Early Jurassic high-K calc-alkaline and shoshonitic rocks from the Tongshi intrusive complex, eastern North China Craton: implication for crust–mantle interaction and post-collisional magmatism. *Lithos*, 140, 183-199.
- Laurenzi, M. A., Visonà, D., 1996. $^{40}\text{Ar}/^{39}\text{Ar}$ Chronology of Predazzo magmatic complex (Southern Alps, Italy). 78^a Riunione Estiva Società Geologica Italiana, San Cassiano.
- Laurenzi, M. A., Visonà, D., Zantedeschi, C., 1994. High resolution Ar/Ar chronology of Predazzo Magmatic Complex (Southern Alps, Italy). Eighth

REFERENCES

- International Conference on Geochronology, Cosmochronology, and Isotope Geology, US Geological Survey Circular, 186.
- Le Maitre, R.W. (Ed.), 2002. Igneous rocks. A Classification of Igneous Rocks and Glossary of Terms. Cambridge Univ. Press., New York, 236 pp.
- Leonardi, P., 1967. Le Dolomiti. Geologia dei monti tra Isarco e Piave. Consiglio Nazionale delle Ricerche. Rome, 1019 pp. (2 volumes).
- Li, C., Arndt, N.T., Tang, Q., Ripley, E.M., 2015. Trace element indiscrimination diagrams. *Lithos*, 232, 76-83.
- Liegeois, J. P., Navez, J., Hertogen, J., Black, R., 1998. Contrasting origin of post-collisional high-K calc-alkaline and shoshonitic versus alkaline and peralkaline granitoids. The use of sliding normalization. *Lithos*, 45, 1-28.
- Lucchini, F., Mezzetti, R., Simboli, G., 1969. The lamprophyres of the area Predazzo-Monzoni: camptonites. *Miner. Petrogr. Acta*, 15, 109-145.
- Lucchini, F., Morten, L., 1977. An example of flow differentiation: clinopyroxenite of the Predazzo igneous complex (North Italy). *Lithos*, 10, 39-47.
- Lucchini, F., Morten, L., 1978. La clinopirossenite del Complesso Igneo di Predazzo: un esempio di differenziazione per flusso. Elementi minori ed in traccia. *Miner. Petrogr. Acta*, 22, 1-11.
- Lucchini, F., Rossi, P.L., Simboli, G., 1982. Il magmatismo triassico nell'area di Predazzo (Alpi Meridionali, Italia). Guida alla Geologia del Sudalpino centro-orientale", A. Castellarin & GB Vai, eds. SGI, Bologna, 211, 220.
- Lucchini, F., Rossi, P.L., Simboli, G., Viel, G., 1980. Dati petrochimici sulla serie vulcanica medio-triassica dell'area di Tarvisio (Carnia). *Miner. Petrogr. Acta*, 18, 183-211.

REFERENCES

- Lucchini, F., Simboli, G., 1970. Petrochemical research on Triassic Volcanic Rocks of St. Pellegrino Valley (Moena, North Italy). *Miner. Petrogr. Acta*, 16, 183-211.
- Lucchini, F., Simboli, G., 1972. Modal and petrochemical study on the Predazzo monzonitic rocks. *Miner. Petrogr. Acta*, 18, 43-82.
- Lustrino, M., Anderson, D.L., 2015. The mantle isotopic printer: Basic mantle plume geochemistry for seismologists and geodynamicists. *Geol. Soc. Am. Spec. Paper*, 514, 257-279.
- Lustrino, M., Duggen, S., Rosenberg, C.L., 2011. The Central-Western Mediterranean: anomalous igneous activity in an anomalous collisional tectonic setting. *Earth-Sci. Rev.*, 104, 1-40.
- Lustrino, M., Prelevic, D., Agostini, S., Gaeta, M., Di Rocco, T., Stagno, V., Capizzi, L.S., 2016. Ca-rich carbonates associated with ultrabasic-ultramafic melts: Carbonatite or limestone xenoliths? A case study from the late Miocene Morron de Villamayor volcano (Calatrava volcanic field, central Spain). *Geochim. Cosmochim. Acta*, 185, 477-497.
- Macera, P., Del Moro, A., Bargossi, G.M., Campana, R., Rottura, A., 1994. Polygenetic nature of the Cima d'Asta intrusive complex, Southern Alps, Italy. Inferences from petrological, geochemical and isotopic (Sr and Nd) data. *Lithos*, 32, 47-62.
- Maes, S.M., Tikoff, B., Ferré, E.C., Brown, P.E., Miller, J.D., 2007. The Sonju Lake layered intrusion, northeast Minnesota: Internal structure and emplacement history inferred from magnetic fabrics. *Precambrian Res.*, 157, 269-288.
- Magee, C., O'Driscoll, B., Petronis, M.S., Stevenson, C.T.E., 2016. Three-dimensional magma flow dynamics within subvolcanic sheet intrusions. *Geosphere*, 12, 842-866.

REFERENCES

- Marinelli, M., Viel, G., Farabegoli, E., 1980. Il Permo-Trias delle Alpi Meridionali: evoluzione tardo-ercinica di un bacino marginale di retroarco sialico. *Ind. Min.*, 6, 1-14.
- Marocchi, M., Morelli, C., Mair, V., Klötzli, U., Bargossi, G.M., 2008. Evolution of Large Silicic Magma Systems: New U-Pb Zircon Data on the NW Permian Athesian Volcanic Group (Southern Alps, Italy). *J. Geol.*, 116, 480-498.
- Marre, J., 1986. *The Structural Analysis of Granitic Rocks*. Elsevier, New York 123 pp.
- Martin Hernandez, F., & Hirt, A.M., 2001. Separation of ferrimagnetic and paramagnetic anisotropies using a high-field torsion magnetometer. *Tectonophysics*, 337, 209-221.
- Masetti, D., Trombetta, G.L., 1998, L'eredità anisica nella nascita ed evoluzione delle piattaforme medio-triassiche delle dolomiti occidentali: *Memorie di Scienze Geologiche*, 50, 213-237.
- Massari, F., Neri, C., 1997. The infill of a supradetachment (?) basin: the continental to shallow-marine Upper Permian succession in the Dolomites and Carnia (Italy). *Sedimentary Geology*, 110(3-4), pp.181-221.
- Bosellini, A. and Hardie, L.A., 1973. Depositional theme of a marginal marine evaporite. *Sedimentology*, 20, 5-27.
- Maurer, F., 2000, Growth mode of Middle Triassic carbonate platforms in the Western Dolomites (Southern Alps, Italy). *Sedim. Geol.*, 134, 275-286.
- Maurer, F., Schlager, W., 2003. Lateral variations in sediment composition and bedding in Middle Triassic interplatform basins (Buchenstein Formation, southern Alps, Italy). *Sedimentology*, 50, 1-22.

REFERENCES

- Mazzeo, F.C., D'Antonio, M., Arienzo, I., Aulinas, M., Di Renzo, V., Gimeno, D., 2014. Subduction-related enrichment of the Neapolitan volcanoes (Southern Italy) mantle source: new constraints on the characteristics of the slab-derived components. *Chem. Geol.*, 386, 165-183.
- Menegazzo, V., L., Visonà, D., Zantedeschi, C., 1995. Amphibole composition in rocks from Predazzo volcano-plutonic complex (Southern Alps, Italy). *Mem. Sci. Geol.*, 47, 87-94.
- Meschede, M., 1986. A method of discriminating between different types of mid-ocean ridge basalts and continental tholeiites with the Nb-Zr-Y diagram. *Chem. Geol.*, 56, 207-218.
- Middlemost, E.A.K., 1975. The basalt clan. *Earth-Sci. Rev.*, 11, 337-364.
- Mietto, P., Manfrin, S., Preto, N., Rigo, M., Roghi, G., Furin, S., Gianolla, P., Posenato, R., Muttoni, G., Nicora, A., Buratti, N., 2012. The global boundary stratotype section and point (GSSP) of the Carnian stage (Late Triassic) at Prati di Stuares/Stuares Wiesen section (Southern Alps, NE Italy). *Episodes*, 35, 414-430.
- Miller, C., Thoni, M., Goessler, W., Tessadri, R., 2011. Origin and age of the Eisenkappel gabbro to granite suite (Caringhia, SE Austrian Alps). *Lithos*, 125, 343-448.
- Miyashiro, A., 1974. Volcanic rock series in island arcs and active continental margins. *Amer. Jour. Sci.*, 274, 321-355.
- Moghazi, A.M., 2003. Geochemistry and petrogenesis of a high-K calc-alkaline Dokhan Volcanic suite, South Safaga area, Egypt: the role of late Neoproterozoic crustal extension. *Precamb. Res.*, 125, 161-178.

REFERENCES

- Morandi, N., Nannetti, M.C., Pirani, R., Resmi, U., 1981. Pegmatiti e Aputi nel granito di Predazzo. *Rend. Soc. Geol. It. Miner. Petrolog.*, 37, 793-811.
- Mundil, R., Brack, P., Meier, M., Rieber, H., Oberli, F., 1996. High resolution U-Pb dating of Middle Triassic volcanoclastics: Time scale calibration and verification of tuning parameters for carbonate sedimentation. *Earth Planet. Sci. Lett.*, 141, 137-151.
- Nédélec, A., Trindade, R., Peschler, A., Archanjo, C., Macouin, M., Poitrasson, F., Bouchez, J.L., 2015. Hydrothermally-induced changes in mineralogy and magnetic properties of oxidized A-type granites. *Lithos*, 212, 145-157.
- Neri, C., Gianolla, P., Furlanis, S., Caputo, R., Bosellini, A., 2007, Carta Geologica d'Italia alla scala 1:50000, Foglio 29 Cortina d'Ampezzo, APAT.
- Nimis, P., Omenetto, P., Giunti, I., Artioli, G., Angelini, I., 2012. Lead isotope systematics in hydrothermal sulphide deposits from the central-eastern Southalpine (northern Italy). *Eur. J. Mineral.*, 24, 23-37.
- O'Driscoll, B., Troll, V.R., Reavy, R.J., Turner, P., 2006. The Great Eucrite intrusion of Ardnamurchan, Scotland: Reevaluating the ring-dike concept. *Geology*, 34, 189-192.
- Obenholzner, J.H., Pfeiffer, J., 1991. "Pietra verde" - ein Diskussionsbeitrag zur Geodynamik der Südalpen: Jubiläumsschrift 20 Jahre Geologische Zusammenarbeit Österreich - Ungarn, 1, 221-245.
- Ogilvie Gordon, M.M., 1902. Monzoni and Upper Fassa. *Geol. Mag.*, dec. 10, vol. 9, p. 309, London.
- Ogilvie Gordon, M.M., 1902-1903. The Geological Structure of Monzoni and Fassa. *Transactions of the Edinburgh geological society*. v. VIII.

REFERENCES

- Paganelli, L., 1967. Studio petrográfico degli affioramenti stentici del Monte Mulat (Predazzo, Italia Settentrionale). *Miner. Petrogr. Acta*, 13, 195-215.
- Paganelli, L., Tiburtini, R., 1964. The Predazzo granite, North Italy. *Miner. Petrogr. Acta*, 10, 57-79.
- Pamic, J.J., 1984. Triassic magmatism of the Dinarides in Yugoslavia: *Tectonophysics*, 109, 273-307.
- Paterson S.R., Fowler T.K., 1993. Re-examining pluton emplacement processes. *J. Struct. Geol.*, 15, 191-206.
- Paterson, S.R., Fowler, T.K., Schmidt, K.L., Yoshinobu, A.S., Yuan, E.S., Miller, R.B., 1998. Interpreting magmatic fabric patterns in plutons. *Lithos*, 44, 53-82.
- Pearce, J.A., 1982. Trace element characteristics of lavas from destructive plate boundaries. *Andesites*, 8, 525-548.
- Pearce, J.A., Cann, J.R., 1973. Tectonic setting of basic volcanic rocks determined using trace element analyses. *Earth Planet. Sci. Lett.*, 19, 290-300.
- Pearce, J.A., Peate, D.W., 1995. Tectonic implications of the composition of volcanic arc magmas. *Annu. Rev. Earth Planet Sci.*, 23, 251-285.
- Peccerillo, A., Taylor, S.R., 1976. Geochemistry of Eocene calc-alkaline volcanic rocks from the Kastamonu area, northern Turkey. *Contrib. Mineral. Petrol.*, 58, 63-81.
- Penck, W., 1911. Der geologische Bau des Gebirges von Predazzo. *Neues Jahrb. f. Min., Geol. u. Paläont.*, 32, 239-382.
- Petersen, J.S., 1980. REE abundances in the Predazzo-Monzoni intrusive complex, Dolomites, North Italy. In: M. Gaetani (Editor), contribution to the Triassic stratigraphy. *Riv. Ital. Paleont.*, 85, 1065-1080.

REFERENCES

- Petronis, M.S., Delcamp, A., van Wyk de Vries, B., 2013. Magma emplacement into the Lemptégy scoria cone (Chaîne Des Puys, France) explored with structural, anisotropy of magnetic susceptibility, and paleomagnetic data. *Bull. Volcano.*, 75, 753.
- Petronis, M.S., Hacker, D.B., Holm, D.K., Geissman, J.W., Harlen, S.S., 2005. Magnetic flow paths and paleomagnetism of the Miocene Stoddard Mountain laccolith, Iron Axis region, southwest Utah, USA. In: Martín-Hernandez, F., Luneburg, C.M., Aubourg, C., Jackson, M. (Eds.), *Magnetic Fabric: Methods and Applications*. *Geol. Soc. Spec. Publ.*, 238, 251-283.
- Petronis, M.S., O'Driscoll, B., Lindline, J., 2011. Late stage oxide growth associated with hydrothermal alteration of the Western Granite, Isle of Rum, NW Scotland. *Geochemistry, Geophysics, Geosystems* 12, 1.
- Petrovský, E.D., Kapička, A., 2006. On determination of the Curie point from thermomagnetic curves. *J. Geophys. Res. Solid Earth*, 111, 1-10.
- Pinarelli, L., Del Moro, A., Boriani, A., Caironi, V., 2002. Sr, Nd isotope evidence for an enriched mantle component in the origins of the Hercynian gabbro-granite series of the "Serie dei Laghi" (Southern Alps, NW Italy). *Eur. J. Mineral.*, 14, 403-415.
- Pisa G., Castellarin A., Lucchini F., Rossi P.L., Simboli G., Bosellini A., Sommariva E., 1980. Middle Triassic magmatism in Southern Alps. I: a review of general data in the Dolomites. *Riv. It. Paleont. Strat.*, 85, 1093-1110.
- Plank, T., 2014. The chemical composition of subducting sediments. *Treat. Geochem.*, 4, 607-629.

REFERENCES

- Polteau, S., Ferré, E.C., Planke, S., Neumann, E.R., and Chevallier, L., 2008. How are saucer-shaped sills emplaced? Constraints from the Golden Valley Sill, South Africa. *J. Geophys. Res.*, 113, B12104.
- Preto, N., Franceschi, M., Gattolin, G., Massironi, M., Riva, A., Gramigna, P., Bertoldi, L., Nardon, S., 2011. The Latemar: A Middle Triassic polygonal fault-block platform controlled by synsedimentary tectonics: *Sedim. Geol.*, 234, 1-18.
- Preto, N., Spötl, C., Mietto, P., Gianolla, P., Riva, A., Manfrin, S., 2005. Aragonite dissolution, sedimentation rates and carbon isotopes in deep-water hemipelagites (Livinallongo Formation, Middle Triassic, northern Italy). *Sedim. Geol.*, 181, 173-194.
- Quick, J.E., Sinigoi, S., Peressini, G., Demarchi, G., Wooden, J.L., Sbisà, A., 2009. Magmatic plumbing of a large Permian caldera exposed to a depth of 25 km. *Geology*, 37, 603-606.
- Raposo, M.I.B., Gastal, P.M.P., 2009. The emplacement mechanism of the main granite Pluton of the Lavras does Sul intrusive complex, South Brazil, determined by magnetic anisotropies. *Tectonophysics*, 466, 18-31.
- Raposo, M.I.B., Pressi, L.F., de Assis Janasi, V., 2012. Magnetic fabrics and their relationship with the emplacement of the Piracaia pluton, SE Brazil. *Int. J. Earth Sci.*, 101, 773-786.
- Roche, O., Druitt, T.H., Merle, O., 2000. Experimental study of caldera formation. *J. Geophys. Res.*, 105, 395-416.
- Rochette, P., Fillion, G., Mollard, P., Vergne, R., 1983. Utilisation d'un magnétomètre à effet Josephson pour l'analyse de l'anisotropie magnétique des roches. *CR Acad. Sci. Paris*, 296, 557-559.

REFERENCES

- Rochette, P., Jackson, M., Aubourg, C., 1992. Rock magnetism and interpretation of anisotropy of magnetic susceptibility. *Review of Geophysics* 30, 209-226.
- Román-Berdiel, T., Gapais, D., Brun, J.P., 1997. Granite intrusion along strike-slip zones in experiment and nature. *Am. J. Sci.*, 297, 651-678.
- Rosenberg, C.L., 2004. Shear zones and magma ascent: A model based on a review of the Tertiary magmatism in the Alps. *Tectonics* 23, 21. doi:10.1029/2003TC001526.
- Rossi, D., 1973. Il conglomerato di Richthofen e la superficie di discordanza alla sua base: *Atti dell'Accademia Roveretana degli Agiati di Scienze, Lettere ed Arti*, 13, 3-20.
- Rossi, P.L., 1970. Vulcaniti e vulcanoclastiti dell'area di Mezzavalle-Forno (Predazzo-Nord Italia). *Miner. Petrogr. Acta*, 16, 155, 181.
- Rossi, P.L., Morten, L., Petersen, J.S., 1980. The Middle Triassic volcanic rocks from Non Valley, North Italy. *Riv. It. Paleont. Strat.*, 85, 1081-1092.
- Rossi, P.L., Simboli, G., Somnavilla, E., 1974. La serie vulcanica medio-triassica della catena del Padon (Gruppo della Marmolada, parte settentrionale). *Miner. Petrogr. Acta*, 20, 1-48.
- Rossi, P.L., Viel, G., Simboli, G., 1976. Significato paleogeografico e magmatico-tettonico della serie vulcanica vulcano-clastica Ladinica superiore nell'area del Monte Civetta. *Boll. Soc. Geol. It.*, 95, 433-458.
- Rottura, A., Bargossi, G.M., Caggianelli, A., Del Moro, A., Visona, D., Tranne, C.A., 1998. Origin and significance of the Permian high-K calc-alkaline magmatism in the central-eastern Southern Alps, Italy. *Lithos*, 45, 329-348.

REFERENCES

- Rottura, A., Del Moro, A., Caggianelli, A., Bargossi, G.M., Gasparotto, G., 1997. Petrogenesis of the Monte Croce granitoids in the context of Permian magmatism in the Southern Alps, Italy. *Eur. J. Mineral.*, 9, 1293-1310.
- Saccani, E., 2015. A new method of discriminating different types of post-Archean ophiolitic basalts and their tectonic significance using Th-Nb and Ce-Dy-Yb systematics. *Geosci. Front.*, 6, 481-501.
- Sacerdoti, M., Somnavilla, E., 1962. Pillowlave, laloclastiti e altre formazioni vulcanoclastiche nella Regione Dolomitica Occidentale. *Studi Trent. Sc. Nat.*, 39, 423-473.
- Salter, V.M., Mallick, S., Hart, S.R., Langmuir, C.H., Stracke, A., 2011. Domains of depleted mantle: new evidence from hafnium and neodymium isotopes. *Geochem. Geophys. Geosyst.*, 12, doi:10.1029/2011GC003617.
- Schaltegger, U., Brack, P., 2007. Crustal-scale magmatic systems during intracontinental strike-slip tectonics: U, Pb and Hf isotopic constraints from Permian magmatic rocks of the Southern Alps. *Int. J. Earth Sci.*, 96, 1131-1151.
- Schmidt, M.W., Jagoutz, O., 2017. The global systematics of primitive arc melts. *Geochem. Geophys. Geosyst.*, 18, 2817-2854.
- Selli, L., 1998. Il lineamento della Valsugana fra Trento e Cima d'Asta: cinematica neogenica ed eredità strutturali permo-mesozoiche nel quadro evolutivo del Sudalpino Orientale (NE-Italia). *Mem. Soc. Geol. It.*, 53, 503-541.
- Simboli, G., 1966. Ricerche petrochimiche e considerazioni petrologiche sulle formazioni vulcaniche triassiche di Val Gardonè,(Predazzo). *Miner. Petrogr. Acta*, 12, 37-60.
- Sloman, L.E., 1989. Triassic shoshonites from the dolomites, northern Italy: Alkaline arc rocks in a strike-slip setting. *J. Geophys. Res.*, 94, 4655-4666.

REFERENCES

- Spadea, P., 1970. Le ignimbriti riolitiche del membro superiore delle Vulcaniti di Rio Freddo, nel Trias medio della regione di Trivisio (Alpi Giulie Occidentali). *St. Trentini Sc. Nat.*, A, 47, 287-358.
- Sparks, R.S.J., 2003. Forecasting volcanic eruptions. *Earth and Planet. Sci. Lett.*, 210, 1-15.
- Stahle, V., Frenzel, G., Hess, J. C., Saupé, F., Schmidt, S. T., Schneider, W., 2001. Permian metabasalt and Triassic alkaline dykes in the northern Ivrea zone: clues to the post-Variscan geodynamic evolution of the Southern Alps. *Schweiz. Mineral. Petrogr. Mitt.*, 81, 1-21.
- Stefani, M., Caputo, R., 1998. Stratigrafia triassica e tettonica alpina nel Gruppo Marmolada-Costabella (Dolomiti centrali). *MEM.SOC. GEOL. IT.*, 53, 263-293.
- Stefani, M., Furin, S., Gianolla, P., 2010. The changing climate framework and depositional dynamics of Triassic carbonate platforms from the Dolomites. *Palaeogeogr. Palaeoclimat. Palaeoecol.*, 290, 43-57.
- Sun, S.S., McDonough, W.F., 1989. Chemical and isotopic systematics of oceanic basalts: implication for mantle composition and processes. In: Saunders, A.D., Norry, M.J. (Eds.), *Magmatism in the Ocean Basins*. *Geol. Soc. Spec. Publ.*, 42, 313-345.
- Talbot, J.Y., Chen, Y., Faure, M., 2005. A magnetic fabric study of the Aigoual-Saint Guiral-Liron granite pluton (French Massif Central) and relationships with its associated dikes. *J. Geophys. Res. Solid Earth*, 110, 1-14.
- Tarling, D.H., Hrouda, F., 1993. *The Magnetic Anisotropy of Rocks*. Chapman & Hall, London, pp. 217.
- Taylor, B., Martinez, F., 2003. Back-arc basin basalt systematics. *Earth Planet. Sci. Lett.*, 210, 481-497.

REFERENCES

- Taylor, S.R., McLennan, S.M., 1985. The Continental Crust; its Composition and Evolution; an Examination of the Geochemical Record Preserved in Sedimentary Rocks. Blackwell, Oxford, p. 312.
- Tibaldi, A., Pasquarè, F.A., 2008. A new mode of inner volcano growth: The “flower intrusive structure”. *Earth and Planet. Sci. Lett.*, 271, 202-208.
- Tikoff, B., Teyssier, C., 1992. Crustal-scale, en echelon “P-shear’ tensional bridges: a possible solution to the batholithic room problem. *Geology*, 20, 927-930.
- Tomek, F., Žák, J., Chadima, M., 2014. Magma flow paths and strain patterns in magma chambers growing by floor subsidence: a model based on magnetic fabric study of shallow-level plutons in the Štiavnica volcano-plutonic complex, Western Carpathians. *Bull. Volcanol.* 76. doi:10.1007/s00445-014-0873-z.
- Tomek, F., Žák, J., Verner, K., Holub, F. V., Sláma, J., Paterson, S. R., Memeti, V., 2017. Mineral fabrics in high-level intrusions recording crustal strain and volcano–tectonic interactions: the Shellenbarger pluton, Sierra Nevada, California. *J. Geol. Soc.* 174, 193-208.
- Trubelja, F., Burgath, K.P., Marchig, V., 2004. Triassic magmatism in the area of the Central Dinarides (Bosnia and Herzegovina): geochemical resolving of tectonic setting. *Geologia Croatica*, 57, 159-170.
- Turner, S., Arnaud, N., Liu, J., Rogers, N., Hawkesworth, G., Harris, N., Deng, W., 1996. Post-collision, shoshonitic volcanism on the Tibetan Plateau: implications for convective thinning of the lithosphere and the source of ocean island basalts. *J. Petrol.*, 37, 45-72.

REFERENCES

- Turner, S., Langmuir, C.H., 2015. What processes control the chemical compositions of arc front stratovolcanoes? *Geochem. Geophys. Geosyst.*, 16, 1865-1893.
- Van der Voo, R., Klootwijk, C.T., 1972. Paleomagnetic reconnaissance study of the Flamanville granite with a special reference to the anisotropy of its susceptibility. *Geol. Mijnbouw* 51, 609-617.
- Vardabasso, S., 1929. Rapporti tra attività magmatica e vicende tettoniche nella provincia petrografica di Predazzo: *Studi Trentini Di Scienze Naturali*, 11, 49-64.
- Vardabasso, S., 1930. Carta geologica del territorio eruttivo di Predazzo e Monzoni: Ufficio Idrografico del Magistrato alle Acque di Venezia. scale 1:25000, 2 sheet.
- Vecchi, G., Zanche, V., 1982. Potassium enrichment in Triassic volcanics. *N. Jb. Geol. Paläont. Mh*, 10, 573-579.
- Venturini, C., 2006. Evoluzione geologica delle Alpi Carniche: Udine, Museo Friulano di Storia Naturale, 208 p.
- Viel, G., 1979. Litostratigrafia ladinica: una revisione. Ricostruzione paleogeografica e paleostrutturale dell'area Dolomitica-Cadorina (Alpi Meridionali). *Riv. It. Paleont. Strat.*, 85, 85-125, 297-352.
- Viel, G., 1982. Polarità tettonica e vulcanismo ladino-carnici del Sudalpino. *Rend. Soc. Geol. It.* , 261-262, Roma.
- Visonà, D., 1997. The Predazzo multipulse intrusive body (Western Dolomites, Italy). Field and mineralogical studies. *Mem. Sci. Geol. Univ. Padova*, 49, 117-125.

REFERENCES

- Visonà, D., Zanferrari, A., 2000. Some constraints on geochemical features in the Triassic mantle of the easternmost Austroalpine–Southalpine domain: evidence from the Karawanken pluton (Carinthia, Austria). *Int. J. Earth Sci.*, 89, 40-51.
- Von Richthofen, F.F., 1860. *Geognostische Beschreibung der Umgebung von Predazzo, Sanct Cassian und der Seiser Alpe in Süd-Tyrol*. Verlag von Justus Perthes, Gotha.
- Walter, T.R., Troll, V.R., 2001. Formation of caldera periphery faults: An experimental study. *Bull. Volcanol.*, 63, 191-203.
- Wilson, M., Neumann, E.-R., Davies, G.R., Timmermann, M.J., Heeremans, M., Larsen, B.T. (Eds.), 2004. *Permo-Carboniferous Magmatism and rifting in Europe*. *Geol. Soc. London Spec. Publ.*, 223, 487 pp.
- Wotzlaw, J.-F., Brack, P., Storck, J.-C., 2017. High-resolution stratigraphy and zircon U–Pb geochronology of the Middle Triassic Buchenstein Formation (Dolomites, northern Italy): precession-forcing of hemipelagic carbonate sedimentation and calibration of the Anisian–Ladinian boundary interval, *J. Geol. Soc.*, 175, 71-85 .
- Zanetti, A., Mazzucchelli, M., Sinigoi, S., Giovanardi, T., Peressini, G., Fanning, M., 2013. SHRIMP U-Pb Zircon Triassic Intrusion Age of the Finero Mafic Complex (Ivrea-Verbano Zone, Western Alps) and its Geodynamic Implications. *J. Petrol.*, 54, 2235-2265.
- Zheng, Y-F., Zhao, Z-F., 2017. Introduction to the structures and processes of subduction zones. *J. Asian Earth Sci.*, 145, 1-15.